Karlsruher Institut für Technologie

Resonant nanophotonics with time-varying metamaterials

Zur Erlangung des akademischen Grades eines

DOKTORS DER NATURWISSENSCHAFTEN (Dr. rer. nat.)

von der KIT-Fakultät für Physik des
Karlsruher Instituts für Technologie (KIT)
angenommene

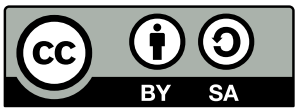
DISSERTATION

von

Puneet Garg

am Institut für Theoretische Festkörperphysik

Tag der mündlichen Prüfung: 6 Nov. 2026
Referent: Prof. Dr. Carsten Rockstuhl
Korreferent: Prof. Dr. Viktar Asadchy



This work (with the exception of reprinted or adapted tables and figures for which the copyright is held by the respective journal) is licensed under a Creative Commons "Attribution-ShareAlike 4.0 International" license. To view a copy of the license, visit https://creativecommons.org/licenses/by-sa/4.0/deed.en.

Abstract

Time-varying metamaterials are formed by modulating material properties as a function of time, often on time scales comparable to the oscillation period of light. In recent years, such metamaterials have increasingly gained attention because they enable novel optical phenomena such as time refraction, time reflection, and the emergence of momentum bandgaps. So far, however, a large body of existing work has focused on spatially homogeneous time-varying systems. Introducing spatial structuring into time-varying media provides a route to simultaneously harness spatial and temporal degrees of freedom for controlling light-matter interactions, which motivates their exploration.

Here, we theoretically and numerically study spatially structured time-varying metamaterials. We develop a comprehensive computational framework to model such complex scattering systems. Our framework is based on the transition (T-) matrix and scattering (S-) matrix methods. We employ these formalisms to study finite-sized time-varying particles, including homogeneous and multilayered spheres as well as cylinders. The framework also enables the study of time-varying metasurfaces formed by periodic two-dimensional arrangements of particles. It further accommodates multilayered structures obtained by stacking such metasurfaces, so that truly four-dimensional photonic materials can be explored.

We use the developed computational tools to study various intriguing physical phenomena. Utilizing the T-matrix formalism, we demonstrate the emergence of noticeable momentum bandgaps in time-varying metasurfaces that sustain resonances thanks to a suitable spatial structuring. We show that such bandgaps can be obtained at perturbative modulation amplitudes by exploiting the Mie and quasi-bound states in the continuum (qBIC) resonances of the metasurfaces. Furthermore, we establish that the threshold modulation amplitude required to open a momentum bandgap vanishes as the quality factor of the metasurface resonance diverges.

We then reveal the existence of unusual scattering phenomena such as exceptional points (EPs), coherent perfect absorption (CPA), and lasing in a wide class of time-varying scatterers. Utilizing the S-matrix description, we show the emergence of such scattering anomalies in resonant time-varying spheres, metasurfaces, and Fabry-Perot cavities. We further use the S-matrix formalism to engineer time-varying multilayered metasurfaces exhibiting a strong nonreciprocal response. Such metasurfaces support one-way monochromatic light transmission.

Finally, we exploit methods from the field of photonic inverse design to tailor the optical response of temporally modulated structures. We optimize a time-varying sphere to realize an anomalous Drexhage effect. Furthermore, by optimizing a time-varying metasurface for enhanced frequency upconversion, we realize asymmetric transmission of light.

In this thesis, we follow a systematic and step-by-step approach to studying the physics of time-varying media. With our work, we aim to advance the scientific understanding of resonant time-varying nanophotonics and facilitate future research in the field.

Publications

The author of this work contributed to the research published in the articles and conference contributions listed below. With the exception of Reference [P8], all of the listed contributions were developed as part of the author's doctoral research. Reference [P8] was based on research conducted during the author's Master's thesis.

Research articles as lead author

[P1] **P. Garg**, E. Almpanis, L. Zimmer, J. D. Fischbach, X. Wang, M. S. Mirmoosa, M. Nyman, N. Stefanou, N. Papanikolaou, V. Asadchy, and C. Rockstuhl, "Photonic time crystals assisted by quasi-bound states in the continuum," *Science Advances* **12**, eaed4055 (2026).

[P2] (*co-first authors) D. Globosits*, **P. Garg***, J. Hüpfl, A. C. Valero, T. Weiss, C. Rockstuhl, and S. Rotter, "Exceptional points, lasing, and coherent perfect absorption in floquet scattering systems," *Light: Science & Applications* **15**, 375 (2026).

[P3] **P. Garg**, M. Plum, and C. Rockstuhl, "Bound states in the continuum in multilayered time-varying metasurfaces," *npj Metamaterials, accepted*, `10.48550/arXiv.2607.06469` (2026).

[P4] (*co-first authors) X. Wang*, **P. Garg***, M. S. Mirmoosa, A. G. Lamprianidis, C. Rockstuhl, and V. Asadchy, "Expanding momentum bandgaps in photonic time crystals through resonances," *Nature Photonics* **19**, 149 (2025).

[P5] **P. Garg**, J. D. Fischbach, A. G. Lamprianidis, X. Wang, M. S. Mirmoosa, V. S. Asadchy, C. Rockstuhl, and T. J. Sturges, "Inverse-designed dispersive time-varying nanostructures," *Advanced Optical Materials* **13**, 2402444 (2025).

[P6] (*co-first authors) M. M. Asgari*, **P. Garg***, X. Wang*, M. S. Mirmoosa*, C. Rockstuhl, and V. Asadchy, "Theory and applications of photonic time crystals: a tutorial," *Advances in Optics and Photonics* **16**, 958 (2024).

[P7] **P. Garg**, A. G. Lamprianidis, S. Rahman, N. Stefanou, E. Almpanis, N. Papanikolaou, B. Verfürth, and C. Rockstuhl, "Two-step homogenization of spatiotemporal metasurfaces using an eigenmode-based approach," *Optical Materials Express* **14**, 549 (2024).

[P8] (*co-first authors) **P. Garg***, A. G. Lamprianidis*, D. Beutel, T. Karamanos, B. Verfürth, and C. Rockstuhl, "Modeling four-dimensional metamaterials: a T-matrix approach to describe time-varying metasurfaces," *Optics Express* **30**, Editor's Pick, 45832 (2022).

Research articles as contributing author

[P9] A. Demircan *et al.*, "Roadmap on 5D photonics for nano and beyond," *Nano futures, accepted*, 10.1088/2399-1984/ae8631 (2026).

[P10] J. D. Fischbach, F. Betz, L. Rebholz, **P. Garg**, K. Frizyuk, F. Binkowski, S. Burger, M. Hammerschmidt, and C. Rockstuhl, "Pole-expansion of the T-matrix based on a matrix-valued AAA-algorithm," *ACS Photonics* **13**, 5291 (2026).

[P11] Z. Li, H. Bahurmuz, M. H. Mostafa, M. S. Mirmoosa, **P. Garg**, C. Rockstuhl, X. Wang, and V. Asadchy, "Resonance-enhanced time reflection at photonic temporal interfaces," *arXiv preprint*, 10.48550/arXiv.2609.12332 (2026).

[P12] N. Asadova, K. Achouri, K. Arjas, B. Auguié, R. Aydin, A. Baron, D. Beutel, B. Bodermann, K. Boussaoud, S. Burger, M. Choi, K. M. Czajkowski, A. B. Evlyukhin, A. Fazel-Najafabadi, I. Fernandez-Corbaton, **P. Garg**, D. Globosits, U. Hohenester, H. Kim, S. Kim, P. Lalanne, E. C. Le Ru, J. Meyer, J. Mun, L. Pattelli, L. Pflug, C. Rockstuhl, J. Rho, S. Rotter, B. Stout, P. Törmä, J. O. Trigo, F. Tristram, N. L. Tsitsas, R. Vallée, K. Vynck, T. Weiss, P. Wiecha, T. Wriedt, V. Yannopapas, M. A. Yurkin, and G. P. Zouros, "T-matrix representation of optical scattering response: suggestion for a data format," *Journal of Quantitative Spectroscopy and Radiative Transfer* **333**, 109310 (2025).

[P13] N. Stefanou, I. Stefanou, E. Almpanis, N. Papanikolaou, **P. Garg**, and C. Rockstuhl, "Light scattering by a periodically time-modulated object of arbitrary shape: the extended boundary condition method," *Journal of the Optical Society of America B* **40**, 2842 (2023).

Conference & workshop contributions (only own presentations)

[C1] (invited talk) **P. Garg**, V. Asadchy, and C. Rockstuhl, "Photonic time crystals assisted by high-Q resonances," in META: the 16th international conference on metamaterials, photonic crystals and plasmonics, Ireland (2026).

[C2] (invited talk) **P. Garg**, X. Wang, M. S. Mirmoosa, A. G. Lamprianidis, V. Asadchy, and C. Rockstuhl, "Photonic time crystals assisted by structural resonances," in 7th URSI AP-RASC conference, Australia (2025).

[C3] **P. Garg**, C. Rockstuhl, and T. Sturges, "Inverse designed dispersive spatiotemporal metasurfaces," in Waves in time-varying media workshop, Spain, Winner of early career researcher prize (2025).

[C4] **P. Garg**, V. Asadchy, and C. Rockstuhl, "Photonic time crystals assisted by high-Q resonances," in Future challenges for nanophotonic scattering: workshop, Germany (2025).

[C5] **P. Garg**, T. Sturges, J. D. Fischbach, and C. Rockstuhl, "Inversely designed spatiotemporal metasurfaces to steer the spectral flow of light," in Metamaterials: the 18th international congress on artificial materials for novel wave phenomena, Greece (2024).

[C6] **P. Garg**, X. Wang, A. Lamprianidis, M. S. Mirmoosa, V. Asadchy, and C. Rockstuhl, "Enhancing the size of momentum bandgaps using resonant spatiotemporal metasurfaces," in Conference on lasers and electro-optics (CLEO), USA (2024).

[C7] **P. Garg**, A. G. Lamprianidis, and C. Rockstuhl, "Modeling four dimensional metamaterials," in Karlsruhe days of optics and photonics, Germany (2023).

[C8] **P. Garg**, A. G. Lamprianidis, and C. Rockstuhl, "Nanophotonic four dimensional metamaterials," in MPSP spring school, Germany (2023).

Contents

Publications **iii**
Research articles as lead author . . . iii
Research articles as contributing author . . . iv
Conference & workshop contributions (only own presentations) . . . iv

1. Introduction **1**

2. Classical electromagnetic theory for time-varying media **7**
2.1. Maxwell's Equations for time-varying media . . . 7
2.2. Eigenmodes of homogeneous time-varying media . . . 9
2.3. Source of time modulation . . . 10
2.3.1. Time modulation due to dynamic electron density . . . 11
2.3.2. Time modulation due to the fast optical Kerr effect . . . 12
2.3.3. Time modulation of non-dispersive media . . . 13
2.4. Structured time-varying media . . . 14
2.4.1. Time-varying spheres . . . 14
2.4.2. Time-varying metasurfaces . . . 19

3. Photonics of time-varying media: a literature overview **27**
3.1. Distinction between spatial and temporal inhomogeneities . . . 27
3.1.1. Spatial and temporal interfaces . . . 27
3.1.2. Photonic space crystals and photonic time crystals . . . 28
3.2. Experimental demonstration of time-varying metamaterials . . . 30
3.2.1. Observation of time refraction . . . 30
3.2.2. Observation of time reflection . . . 33
3.2.3. Observation of momentum bandgaps . . . 35
3.3. Current and future challenges . . . 36

4. Expanding momentum bandgaps in PTCs **39**
4.1. Physical concept . . . 40
4.2. Bandstructure calculation using the T-matrix method . . . 41
4.3. Momentum bandgaps in Mie resonant PTCs . . . 42
4.3.1. Momentum bandgaps for evanescent PWs . . . 42
4.3.2. Momentum bandgaps for propagating PWs . . . 46
4.4. Momentum bandgaps in qBIC resonant PTCs . . . 47
4.4.1. Kerr-induced time-varying permittivity . . . 48
4.4.2. Momentum bandgaps in multilayered sphere-based metasurfaces . . . 50
4.4.3. BICs in cylinder-based metasurfaces . . . 53

5. Scattering anomalies in PTCs **57**
5.1. S-matrix in a photon number flux-normalized basis . . . 58

5.2. Exceptional points, coherent perfect absorption, and lasing 61
5.2.1. Isolated time-varying spheres 61
5.2.2. Time-varying metasurfaces hosting SP-BICs 64
5.2.3. Time-varying cavities hosting FP-BICs 69
5.3. Nonreciprocity in multilayered metasurfaces hosting SP-BICs 74

6. Inverse-designed time-varying metamaterials 79
6.1. Inverse design framework 80
6.2. Radiative decay rate enhancement 82
6.2.1. Power calculation for oscillating dipoles 83
6.2.2. Anomalous Drexhage effect 84
6.3. Inverse-designed asymmetric light transmission 89

7. Conclusions 93
7.1. Summary 93
7.2. Outlook 94

Bibliography 97

A. Appendix 109
A.1. Definition of VSWs 109
A.2. Definition of unit vectors for PWs 109
A.3. Symmetry relation for VSWs for negative frequencies 109
A.4. Incident field coefficients in the VSW basis 110
A.5. Symmetry relation for translation coefficients for negative frequencies 110
A.6. Symmetry relation for the S-matrix blocks of a static substrate 112
A.7. Details of the convergence parameters used during simulations 112

Acknowledgements 115

Selbstständigkeitserklärung 117

1 | Introduction

Metamaterials refer to artificially structured media that are designed to tailor and control the propagation of light and its interaction with matter. In the 1960s, Veselago theorized that materials can have a negative refractive index if both their electric permittivity and magnetic permeability were simultaneously negative [1]. While the search for a naturally occurring negative refractive index material was never successful, Shelby et al. demonstrated in 2001 that a metamaterial composed of a lattice of split-ring resonators and metallic wires could exhibit an effective negative refractive index in the microwave regime [2]. Around the same time, Pendry argued that a negative refractive index would enable the phenomenon of perfect lensing [3]. These works set the stage for a surge of interest in the field of metamaterials, leading to the demonstration of exotic optical effects such as artificial magnetism [4], imaging beyond the diffraction limit [5], structure-induced strong optical activity [6], among many others. As the field developed, in 2006, the concept of electromagnetic cloaking was introduced [7, 8]. It was theoretically proposed that a system could be designed to be impenetrable to external electromagnetic fields. The experimental observation of such a cloaking phenomenon was reported in various publications [9–12].

With the advancement of nanofabrication technologies, many applications of metamaterials have become accessible at the near-infrared and visible frequencies [13]. Spatially structuring media at the nanoscale enables comprehensive control over how optical waves propagate in the three-dimensional (3D) space, allowing the amplitude, phase, and polarization of light to be tailored in the subwavelength regime. In this thesis, we refer to these spatially structured systems as *spatial metamaterials*. Many initial demonstrations of spatial metamaterials relied on metallic resonant elements. While the metallic structures allowed for the observation of extreme material parameters, such as negative permittivity and negative permeability, they suffered from high material losses. These losses limited the efficiency of the designed devices. The search for low-loss systems led to the use of dielectrics to create artificial structures. In fact, all-dielectric spatial metamaterials proved to be very compelling as they exhibited strong electric and magnetic response in the near-infrared and visible frequency regimes while possessing negligible material losses. For instance, metamaterial-inspired silicon nanophotonics in the near-infrared regime emerged as a major subfield thanks to the already existing silicon-based advanced fabrication capabilities [14]. Furthermore, in the visible regime, semiconductors such as titanium dioxide (TiO_2), gallium phosphide (GaP), and gallium nitride (GaN) are widely used [15].

A particularly important development in the research of spatial metamaterials was that of metasurfaces. Metasurfaces are formed by arranging their constituent building blocks (called meta-atoms) in the two-dimensional (2D) space [16]. Typically, the thickness of metasurfaces is of the order of the wavelength of light, thereby allowing the design of ultra-compact devices. Moreover, metasurfaces are readily fabricable using lithography and nanoprinting methods [17]. Much like their 3D counterparts, metasurfaces have emerged as promising platforms for achieving tailored optical responses. They have been used to demonstrate interesting

physical effects such as anomalous reflection and refraction [18], flat optical lensing [19], and phase and polarization manipulation [20], to name a few.

While the field of spatial metamaterials and metasurfaces is extremely developed by now, the ability to control light using structures with time-varying material parameters is comparatively in its nascent stage [21–23]. Time-varying metamaterials are media whose material properties depend explicitly on time. In fact, the time scale of the temporal modulation often compares with the oscillation period of light [24]. These metamaterials unlock additional degrees of freedom to control light propagation. They facilitate attaining tailored wave responses on demand in four dimensions (4D), i.e., three spatial dimensions and one temporal dimension [25]. The history of time-varying metamaterials dates back to the 1950s. Initially, Morgenthaler considered the physics of temporal interfaces where the permittivity of a bulk medium was changed abruptly in time [26]. He found that, analogous to a spatial interface, an initial plane wave gets divided into a forward-propagating and a backward-propagating plane wave. The forward-propagating wave is called the time-refracted wave, and the backward-propagating wave is called the time-reflected wave, in analogy to refracted and reflected waves from spatial interfaces [27]. Furthermore, the problem of light scattering from a time-varying slab was studied in [28]. Therein, the authors found that a slab made from a material with a time-varying permittivity supports the exponential growth of the scattered field as a function of time. As this research domain further developed, periodic arrangements of temporal interfaces were studied in [24, 29]. The resulting structures were called photonic time crystals (PTCs). These crystals exhibited bandgaps with respect to the momentum dimension. Such momentum bandgaps are dual to the frequency bandgaps that appear in conventional *spatial* photonic crystals [30].

On the experimental side, one of the major challenges in observing various exotic effects of temporal variation is the requirement of a strong modulation at an ultrafast time scale. In that context, epsilon-near-zero (ENZ) media have emerged as a viable platform to implement time-varying metamaterials [23]. In essence, the permittivity of an ENZ medium can be modulated by subjecting it to an intense pump pulse, which heats up its electrons, thereby changing their effective mass in a transient fashion [31]. Such a change has been observed at femtosecond time scales, with the modulation amplitudes ($\Delta\varepsilon/\varepsilon$ ratio) reaching more than 100%, when operated close to the ENZ condition. Another mechanism to induce temporal modulation in ENZ materials is that of ultrafast interband transitions. An intense pump pulse excites the electrons in the medium across the bandgap, inducing a time-varying electron density [32, 33]. Using the ENZ media, time-refraction at optical frequencies was demonstrated in [34–36]. Synthetically moving aperture due to a space-time temporal modulation was observed in [37]. Dynamically induced birefringence, dichroism, and chirality were shown in [38].

While the ENZ media are widely used in implementing ultrafast isolated temporal interfaces, there exist certain challenges. For instance, due to the slow relaxation time of the hot electrons, a time-periodic oscillation of the permittivity is difficult to achieve. Furthermore, due to the high intrinsic losses in the ENZ materials, there exists a risk of thermal damage as the pump intensities typically approach values of the order of a few TW/cm^2. These limitations have motivated the use of low-loss dielectric materials for implementing time-varying metamaterials. In particular, the fast optical Kerr effect (mediated by the third-order nonlinearity) can be exploited to attain a time-periodic permittivity modulation at hundreds of THz [39]. Laser-induced carrier generation is another pathway to implement time-varying permittivity profiles in dielectrics. For example, an ultrafast refractive-index modulation was observed in

silicon-based metasurfaces in [40]. Furthermore, frequency and momentum conversion were demonstrated in GaAs-based time-varying metasurfaces in [41, 42]. These studies highlight the potential of low-loss dielectric platforms for realizing rapid temporal modulation.

The experimental challenges associated with strong and fast modulation are less restrictive at lower frequencies, where temporal modulation can be implemented more readily. Consequently, several fundamental phenomena associated with time variation have been demonstrated in water-wave and microwave platforms. For instance, time-reflection was observed in the water-wave regime in [43]. Here, a time-boundary was created by applying a sudden jolt to a bath of water. Furthermore, in microwaves, time-reflection was observed due to a temporal interface formed by instantaneously changing the capacitance of a transmission line [44]. Such transmission lines were also used to observe momentum bandgaps in [45]. Moreover, a purely frequency upconverting metasurface was implemented in [46], using a microwave circuit with a time-varying capacitance.

Despite these developments, much of the research on time-varying metamaterials has focused on spatially homogeneous systems [21, 22]. Prior to this thesis, there had been a lack of rigorous theoretical works that described spatially structured time-varying metamaterials. An important advantage of using such systems is that the high-quality (high-Q) resonances arising from spatial structuring can be harnessed to enhance the effects of time variation [15, 47]. Physically, resonances confine light inside the photonic structures. Therefore, light experiences the effect of time modulation for a prolonged duration. Hence, strong effects are observed even when the temporal modulation amplitude is weak. Another important aspect of such systems is that various functionalities of purely spatial metamaterials can be combined with those of purely temporal metamaterials to give rise to exciting physical phenomena.

This thesis is a contribution to the research of resonant spatially structured time-varying metamaterials. Building upon the prior works involving the computational modeling of isolated time-varying meta-atoms [48] and static periodic structures [49], we design and study periodic time-varying metasurfaces. Specifically, we use the transition (T-) matrix and scattering (S-) matrix methods to numerically model the metasurfaces [48–52]. These methods have proven to be useful for studying spatial metamaterials. Here, we rigorously extend these methods to additionally incorporate temporal modulation. We remark that our theoretical framework can handle arbitrarily high modulation amplitudes and frequencies. Therefore, it is not limited to perturbative or adiabatic regimes of time modulation. Furthermore, beyond isolated metasurfaces, we have also implemented the stacking of multiple metasurfaces, enabling the study of more complex systems with additional degrees of freedom.

We apply our framework to exploit the high-Q Mie and quasi-bound states in the continuum resonances that the carefully designed metasurfaces may sustain to intensify the emerging scattering effects due to time modulation. We propose various scattering configurations in the infrared and visible frequency regimes that operate at perturbative modulation amplitudes. We study a wide range of phenomena such as momentum bandgaps, exceptional points, coherent perfect absorption, lasing, nonreciprocity, and inverse-design assisted frequency conversion in these metasurfaces. The ability to operate at low modulation amplitudes enhances the experimental feasibility and paves the way for future realizations of these phenomena at optical frequencies. Furthermore, this thesis represents an important step toward understanding and controlling the optical behavior of 3D spatial metamaterials under temporal modulation, opening a pathway to 4D spatiotemporal systems.

Structure of the thesis

This thesis consists of seven chapters. In *Chapter 2*, we discuss the classical electrodynamics of time-varying media using Maxwell's equations. We solve the wave equation for a homogeneous time-varying medium to compute its eigenmodes. Then, we provide the mathematical description of various sources of time modulation. These include time-varying electron density and Kerr-induced temporal modulation of the permittivity. In the second part of the chapter, we discuss the technical details of the computational tools used in this thesis (T- and S-matrix methods) to consider light scattering from time-varying spheres and metasurfaces. We provide a rigorous numerical formalism to implement these tools on a computer. We also describe the calculation of the physical observables such as scattering cross section for time-varying spheres, and reflectivity and transmissivity for time-varying metasurfaces. The theory developed in this chapter is utilized to explain various interesting physical effects in the subsequent chapters.

In *Chapter 3*, we provide an overview of the photonics of time-varying media. We begin by explaining how time-varying metamaterials differ from their spatial counterparts. In particular, we discuss the difference in light scattering from spatial and temporal inhomogeneities. Then, we review selected works that experimentally realized various unusual phenomena such as time refraction, time reflection, and the emergence of momentum bandgaps. Finally, we close the chapter by outlining the current and future challenges in the research field of temporal metamaterials.

In *Chapter 4*, we present the application of high-quality structural resonances to photonic time crystals. In particular, leveraging the Mie and quasi-bound states in the continuum (qBICs) of the meta-atoms, we show that noticeable momentum bandgaps could be achieved in the corresponding metasurface-based PTCs. Remarkably, such bandgaps are attained with a perturbative temporal modulation of the permittivity. We present the application of our approach to a wide class of geometries, i.e., metasurfaces made from homogeneous spheres, multilayered spheres, and homogeneous cylinders. This chapter is based on our works in [P1, P4].

In *Chapter 5*, we study unusual scattering phenomena such as the emergence of exceptional points (EPs), coherent perfect absorption (CPA), lasing, and nonreciprocity in various time-varying structures. We use a unified S-matrix framework to explain the formation of such scattering anomalies. In particular, we show the existence of EPs, CPA, and lasing in time-varying spheres, metasurfaces, and metasurface-based Fabry-Perot cavities. Furthermore, by breaking the time-reversal symmetry of the temporal modulation, we engineer strong nonreciprocity in multilayered metasurfaces. Harnessing nonreciprocity, we design the metasurface such that it supports one-way monochromatic light transmission. By exploiting the structural resonances of the considered scatterers, we attain the discussed scattering anomalies for perturbative temporal modulation of permittivity. This chapter is based on our works in [P2, P3].

In *Chapter 6*, we discuss the inverse design of time-varying structures such as spheres and metasurfaces. Using a differentiable T-matrix method, we build an inverse design framework. Therein, we treat the temporal profile of the periodic material modulation as the degree of freedom. We show the versatility of the framework using two key examples. First, we inverse-design the temporal modulation profile of a time-varying sphere such that a dipole placed in its vicinity exhibits the anomalous Drexhage effect. In particular, when placed close to the sphere, the dipole exhibits significant radiative decay rates for both radial and

tangential orientations. In a second example, we inverse design time-varying metasurfaces to enable one-way light transmission. The proposed device is made from a cascade of a time-varying metasurface and a narrowband frequency filter. By optimizing the metasurface for efficient frequency upconversion, we demonstrate that the cascaded system allows light to pass through in one direction while blocking it in the other direction. This chapter is based on our work in [P5].

In *Chapter 7*, we conclude the thesis with a brief summary of the main findings and an outlook on potential directions for future research.

2 | Classical electromagnetic theory for time-varying media

In this chapter, we describe the classical electromagnetic theory for time-varying media. In Sec. 2.1, we discuss Maxwell's equations together with the constitutive relations for dispersive time-varying systems. In particular, we use the material response functions that explicitly depend on time in the constitutive relations. The theoretical description of Sec. 2.1 is used to derive the eigenmodes of homogeneous time-varying media in Sec. 2.2. Then, in Sec. 2.3, we describe the sources of time modulation, such as dynamic electron density, and the fast optical Kerr effect. We provide the material response functions corresponding to these modulation mechanisms. We also give a brief mathematical description of non-dispersive time-varying media. Thereafter, we proceed in Sec. 2.4 to discuss the semi-analytical computational tools for modeling scattering from time-varying spheres and metasurfaces. In particular, we study the T- and S-matrix methods. We use the eigenmodes of the homogeneous time-varying media together with the appropriate interface conditions to develop a mathematical model for describing light scattering from these structured time-varying objects.

This chapter serves as an overview of the theoretical tools that are utilized in the subsequent parts of this thesis. Large portions of this chapter rely on the literature published prior to the current PhD research [P8, 48, 53]. In particular, the contents of Secs. 2.1–2.2 rely on [48], and parts of Secs. 2.3–2.4 rely on [P8, 48, 53]. We also use the open-access Python package `treams` to computationally implement some of the discussed numerical tools [49, 54].

2.1. Maxwell's Equations for time-varying media

Classical light propagation inside any medium is governed by Maxwell's equations. In the time domain, for a medium without source charges and currents, such equations are written as

$$\nabla \cdot \mathbf{D}(\mathbf{r}, t) = 0\,, \tag{2.1a}$$

$$\nabla \times \mathbf{E}(\mathbf{r}, t) = -\frac{\partial \mathbf{B}(\mathbf{r}, t)}{\partial t}\,, \tag{2.1b}$$

$$\nabla \cdot \mathbf{B}(\mathbf{r}, t) = 0\,, \tag{2.1c}$$

$$\nabla \times \mathbf{H}(\mathbf{r}, t) = \frac{\partial \mathbf{D}(\mathbf{r}, t)}{\partial t}\,. \tag{2.1d}$$

Maxwell's equations quantify light propagation in a medium together with the constitutive relations

$$\mathbf{D}(\mathbf{r}, t) = \varepsilon_0 \mathbf{E}(\mathbf{r}, t) + \mathbf{P}(\mathbf{r}, t)\,, \tag{2.2a}$$

$$\mathbf{B}(\mathbf{r}, t) = \mu_0 \mathbf{H}(\mathbf{r}, t)\,. \tag{2.2b}$$

Here, $\mathbf{E}(\mathbf{r},t)$ and $\mathbf{B}(\mathbf{r},t)$ are the electric and magnetic fields, respectively, $\mathbf{D}(\mathbf{r},t)$ is the electric displacement field, $\mathbf{H}(\mathbf{r},t)$ is the magnetizing field, and $\mathbf{P}(\mathbf{r},t)$ is the polarization density. Furthermore, ε_0 and μ_0 represent the electric permittivity and the magnetic permeability of vacuum, respectively. Note that, here, we have assumed non-magnetic media. For magnetic media, an additional magnetization density would need to be accounted for in Eq. (2.2b) [55].

In a linear, dispersive, time-varying, isotropic, and homogeneous medium, the polarization density is related to the electric field as [48]

$$\mathbf{P}(\mathbf{r},t) = \varepsilon_0 \int_{-\infty}^{\infty} R_\mathrm{e}(t,t-\tau)\,\mathbf{E}(\mathbf{r},\tau)\,\mathrm{d}\tau\,, \tag{2.3}$$

where $R_\mathrm{e}(t,t-\tau)$ is the real-valued causal response function of the medium. Specifically, the first argument t of $R_\mathrm{e}(.\,,.)$ represents the explicit time-dependence, and the second argument $t-\tau$ represents the non-instantaneous nature of the material response. Due to causality $R_\mathrm{e}(t,t-\tau)=0$ for $t-\tau<0$. Furthermore, for an instantaneous time-varying medium (i.e., non-dispersive), the response function simplifies to $R_\mathrm{e}(t,t-\tau)=\chi_\infty(t)\delta(t-\tau)$. Here, $\delta(t-\tau)$ is the Dirac delta distribution, and $\chi_\infty(t)$ is the linear time-dependent background susceptibility of the medium. Moreover, for a static medium, the response function becomes invariant with respect to its first argument.

Next, we Fourier transform Eq. (2.3) to obtain the relation between the polarization density and the electric field in the frequency domain as [48]

$$\tilde{\mathbf{P}}(\mathbf{r},\omega) = \varepsilon_0 \int_{-\infty}^{\infty} \tilde{R}_\mathrm{e}(\omega-\omega',\omega')\tilde{\mathbf{E}}(\mathbf{r},\omega')\,\mathrm{d}\omega'\,. \tag{2.4}$$

Here, $\tilde{\mathbf{P}}(\mathbf{r},\omega)$ and $\tilde{\mathbf{E}}(\mathbf{r},\omega)$ are the frequency-domain polarization density and electric field, respectively[1]. Furthermore, $\tilde{R}_\mathrm{e}(\omega-\omega',\omega')$ is the frequency-domain response function computed by a double Fourier transform of $R_\mathrm{e}(t,t-\tau)$, i.e., $\tilde{R}_\mathrm{e}(\omega-\omega',\omega') = \frac{1}{2\pi}\iint_{-\infty}^{\infty} R_\mathrm{e}(t,t-\tau)\,e^{i(\omega t-\omega'\tau)}\,\mathrm{d}t\,\mathrm{d}\tau$. For a non-dispersive medium, $\tilde{R}_\mathrm{e}(\omega-\omega',\omega')$ is invariant with respect to its second argument, and for a static medium it takes the form $\tilde{R}_\mathrm{e}(\omega-\omega',\omega')=\delta(\omega-\omega')\chi(\omega)$. Here, $\chi(\omega)$ is the susceptibility of the medium.

Next, using Eqs. (2.1), (2.2), and (2.4), we write Maxwell's equations for the time-varying medium in the frequency domain as [48]

$$\nabla\cdot\tilde{\mathbf{E}}(\mathbf{r},\omega) = -\int_{-\infty}^{\infty} \tilde{R}_\mathrm{e}(\omega-\omega',\omega')\nabla\cdot\tilde{\mathbf{E}}(\mathbf{r},\omega')\,\mathrm{d}\omega'\,, \tag{2.5a}$$

$$\nabla\cdot\tilde{\mathbf{H}}(\mathbf{r},\omega) = 0\,, \tag{2.5b}$$

$$\nabla\times\tilde{\mathbf{E}}(\mathbf{r},\omega) = i\omega\mu_0\tilde{\mathbf{H}}(\mathbf{r},\omega)\,, \tag{2.5c}$$

$$\nabla\times\tilde{\mathbf{H}}(\mathbf{r},\omega) = -i\omega\varepsilon_0\tilde{\mathbf{E}}(\mathbf{r},\omega) - i\omega\varepsilon_0\int_{-\infty}^{\infty} \tilde{R}_\mathrm{e}(\omega-\omega',\omega')\tilde{\mathbf{E}}(\mathbf{r},\omega')\,\mathrm{d}\omega'\,. \tag{2.5d}$$

[1]For performing the Fourier transform, we adopt the convention, $\tilde{F}(\omega)=\frac{1}{\sqrt{2\pi}}\int_{-\infty}^{\infty}F(t)e^{i\omega t}\,\mathrm{d}t$.

Here, $\tilde{\mathbf{H}}(\mathbf{r},\omega)$ is the frequency-domain magnetizing field. Finally, using Eq. (2.5), we can write the wave equation for the electric field in the time-varying medium as

$$\nabla \times \nabla \times \tilde{\mathbf{E}}(\mathbf{r},\omega) = k^2(\omega) \left[\tilde{\mathbf{E}}(\mathbf{r},\omega) + \int_{-\infty}^{\infty} \tilde{R}_{\mathrm{e}}(\omega-\omega',\omega') \tilde{\mathbf{E}}(\mathbf{r},\omega') \,\mathrm{d}\omega' \right], \tag{2.6}$$

where $k(\omega) = \omega/c_0$ with c_0 being the speed of light in a vacuum.

In the following, we utilize the presented formalism to compute the eigenmodes of homogeneous time-varying media.

2.2. Eigenmodes of homogeneous time-varying media

We solve the wave equation given by Eq. (2.6) to find the eigenmodes of homogeneous time-varying media. We assume that the properties of the medium vary with time in a periodic fashion, i.e., $R_{\mathrm{e}}(t, t-\tau)$ is periodic with respect to the variable t. Following [48], we use the method of separation of variables to find the eigenmodes. Specifically, we consider the ansatz

$$\tilde{\mathbf{E}}(\mathbf{r},\omega) = \int \mathcal{A}_\kappa \, \mathcal{H}_\kappa(\omega) \, \mathbf{F}_\kappa(\mathbf{r}) \,\mathrm{d}\kappa \,, \tag{2.7}$$

where $\mathcal{H}_\kappa(\omega)$ and $\mathbf{F}_\kappa(\mathbf{r})$ are the spectral and spatial parts of the eigenmodes, respectively, and $\mathcal{A}_\kappa$ is the complex amplitude. Substituting the ansatz in Eq. (2.6) and using the separation variable κ^2, we get the following decoupled equations [48]

$$\nabla \times \nabla \times \mathbf{F}_\kappa(\mathbf{r}) = \kappa^2 \mathbf{F}_\kappa(\mathbf{r}) \,, \tag{2.8a}$$

$$k^2(\omega) \left[\mathcal{H}_\kappa(\omega) + \int_{-\infty}^{\infty} \tilde{R}_{\mathrm{e}}(\omega-\omega',\omega') \mathcal{H}_\kappa(\omega') \,\mathrm{d}\omega' \right] = \kappa^2 \mathcal{H}_\kappa(\omega) \,. \tag{2.8b}$$

Here, Eq. (2.8a) is the usual Helmholtz equation for a spatially homogeneous medium. The functions $\mathbf{F}_\kappa(\mathbf{r})$ may, for instance, be chosen as a set of plane waves (PWs), vector cylindrical waves (VCWs), or vector spherical waves (VSWs). The specific choice of $\mathbf{F}_\kappa(\mathbf{r})$ becomes crucial when we consider the spatial interfaces; we discuss those implications in Sec. 2.4. Furthermore, Eq. (2.8b) arises purely due to the time modulation of the medium. In the following, we discuss the steps to compute $\mathcal{H}_\kappa(\omega)$.

To solve Eq. (2.8b) for $\mathcal{H}_\kappa(\omega)$ numerically, several simplifications have to be made. First, we truncate the considered frequency spectrum. The integral term in Eq. (2.8b) implies that the value of $\mathcal{H}_\kappa(\omega)$ depends on the corresponding values at infinitely many frequencies ω'. While Eq. (2.8b) is exact, it cannot be solved numerically without truncating the integral limits in a finite frequency window. For numerical accuracy, the frequency window can be chosen sufficiently large such that the resulting solution converges. Second, we use the fact that $R_{\mathrm{e}}(t, t-\tau)$ is a periodic function of time, i.e., $R_{\mathrm{e}}(t+j\tau_{\mathrm{m}}, t-\tau) = R_{\mathrm{e}}(t, t-\tau)$, with $j \in \mathbb{Z}$. In the frequency domain, such a periodicity implies $\tilde{R}_{\mathrm{e}}(\omega-\omega',\omega') = \sum_j \delta(\omega-\omega'-j\Omega)\bar{R}_{\mathrm{e}}(\omega-\omega',\omega')$, with $\Omega = 2\pi/\tau_{\mathrm{m}}$ being the modulation frequency. Using these two assumptions, Eq. (2.8b) simplifies to [48]

$$k^2(\omega_j)\left[\mathcal{H}_\kappa(\omega_j)+\sum_{n=0}^{J-1}\bar{R}_\mathrm{e}(\omega_j-\omega_n,\omega_n)\mathcal{H}_\kappa(\omega_n)\right]=\kappa^2\mathcal{H}_\kappa(\omega_j)\,, \tag{2.9}$$

with $\omega_j = \omega + (j + j_0)\Omega$. Physically, Eq. (2.9) signifies that the eigenmodes of periodic time-varying media consist of electric fields whose frequencies form a comb. Furthermore, the field at a frequency ω_j depends on the fields at all other frequencies of the comb. Here, j_0 is an appropriately chosen integer that fixes the index of the Floquet frequency ω in the comb, and J is the total number of frequencies in the comb. We choose J to be sufficiently large to obtain convergent solutions for the simulations in Chapters 4, 5, and 6. Next, for each frequency comb characterized by ω, we transform Eq. (2.9) to the matrix form as

$$\boldsymbol{\mathcal{K}}(\omega)\boldsymbol{\mathcal{H}}_\kappa(\omega)=\kappa^2(\omega)\boldsymbol{\mathcal{H}}_\kappa(\omega)\,,\text{with} \tag{2.10a}$$

$$\boldsymbol{\mathcal{K}}(\omega)=\mathbf{K}^2(\omega)\left[\mathbf{I}+\bar{\mathbf{R}}_\mathrm{e}(\omega)\right]\,, \tag{2.10b}$$

$$\mathbf{K}(\omega)=\mathrm{diag}[k_0,k_1,...,k_{J-1}]\,,\text{and} \tag{2.10c}$$

$$\boldsymbol{\mathcal{H}}_\kappa(\omega)=[\mathcal{H}_\kappa(\omega_0),\mathcal{H}_\kappa(\omega_1),...,\mathcal{H}_\kappa(\omega_{J-1})]^\mathrm{T}\,. \tag{2.10d}$$

Here, $\mathbf{I}$ is the identity matrix, and the j^{th}-row, n^{th}-column element of the matrix $\bar{\mathbf{R}}_\mathrm{e}$ is $\bar{R}_\mathrm{e}(\omega_j-\omega_n,\omega_n)$. The dimension of the matrices $\mathbf{K}$, $\bar{\mathbf{R}}_\mathrm{e}$, and $\boldsymbol{\mathcal{K}}$ is J. We deduce that the computational task of finding the spectral part of the eigenmodes reduces to evaluating the eigenvalues and the eigenvectors of the matrix $\boldsymbol{\mathcal{K}}$. Specifically, $\boldsymbol{\mathcal{K}}$ has the eigenvalues κ_i^2, and the corresponding eigenvectors $\boldsymbol{\mathcal{H}}_{\kappa_i}$ with $i \in [0, 1, .., J-1]$.

Finally, using Eqs. (2.7) and (2.10), we write the eigenmodes of the wave equation in a homogeneous time-varying medium as [48]

$$\tilde{\mathbf{E}}(\mathbf{r},\bar{\omega})=\int_0^\Omega\sum_{i,j=0}^{J-1}\mathcal{A}_{\kappa_i}\,\delta(\bar{\omega}-\omega_j)\mathcal{H}_{\kappa_i}(\omega_j)\,\mathbf{F}_{\kappa_i}(\mathbf{r})\,\mathrm{d}\omega\,. \tag{2.11}$$

These eigenmodes are used to solve the scattering problem from time-varying spheres and metasurfaces in Sec. 2.4. Note that, here, $\bar{\omega}$ denotes the frequency argument of the total field, whereas $\omega \in (0, \Omega)$ characterizes the individual frequency combs, with $\omega_j = \omega + (j + j_0)\Omega$.

In the following, we discuss various physical mechanisms that are widely used to induce temporal modulation in known materials.

2.3. Source of time modulation

So far, we have considered the explicit time-dependence of the response function as a mere mathematical feature appearing in the constitutive relations (see Eq. (2.3)). To experimentally realize such time-dependent response functions at optical frequencies, two distinct mechanisms have proven to be useful. One of them concerns the ultrafast interband transitions of electrons in the medium. An intense pump beam excites electrons across the bandgap, thereby dynamically modifying the carrier density associated with the relevant Drude-Lorentz oscillators [32, 33]. The second relies on the fast optical Kerr effect, where a

strong pump beam modulates the response of the medium in time due to the third-order Kerr nonlinearity [56–58]. Assuming weak probe fields, the constitutive relation for such a Kerr medium can be linearized to define an effective time-dependent response function. Here, we discuss the time-varying response functions for these two approaches. For completeness, we also provide the expression for the response function of a non-dispersive time-varying medium.

2.3.1. Time modulation due to dynamic electron density

For a multipole Drude-Lorentz medium, the total polarization density is $\mathbf{P}(\mathbf{r},t) = \mathbf{P}_\infty(\mathbf{r},t) + \sum_n \mathbf{P}_n(\mathbf{r},t)$. Here, $\mathbf{P}_\infty(\mathbf{r},t) = \varepsilon_0 \chi_{\infty,\mathrm{st}}\, \mathbf{E}(\mathbf{r},t)$ is the non-resonant (background) contribution to the total polarization density. We assume the background susceptibility to be constant in time in the present case. Furthermore, the n^{th} resonant contribution $\mathbf{P}_n(\mathbf{r},t)$ satisfies [48]

$$\left[\frac{\partial^2}{\partial t^2} + \gamma_n \frac{\partial}{\partial t} + \omega_{0n}^2\right] \mathbf{P}_n(\mathbf{r},t) = \frac{N_n(t) e^2}{m_\mathrm{e}} \mathbf{E}(\mathbf{r},t)\,, \tag{2.12}$$

where γ_n, ω_{0n}, and $N_n(t)$ are the damping parameter, resonance frequency, and time-periodic electron density of the n^{th} oscillator, respectively. Furthermore, e and m_e are the charge and effective mass of an electron, respectively. In general, a time-periodic $N_n(t)$ can be written as

$$N_n(t) = N_{n,\mathrm{st}} \left[1 + \frac{1}{2}\sum_{q=1}^{Q} (M_{q,n} e^{iq\Omega t} + \mathrm{c.c.})\right]\,, \tag{2.13}$$

where $N_{n,\mathrm{st}}$ is the electron density in the static case, $M_{q,n}$ are complex-valued modulation amplitudes, and c.c. represents the complex conjugate. The c.c. term ensures that $N_n(t)$ is real-valued for all times t. Due to the conservation of the total number of electrons, $N_n(t)$ must satisfy the sum rule

$$\sum_n N_n(t) = \sum_n N_{n,\mathrm{st}}\,. \tag{2.14}$$

Physically, a time-dependent $N_n(t)$ can be realized by utilizing the ultrafast interband transitions in the materials [31, 59]. An intense pump beam with a time-periodic intensity excites electrons across the bandgaps, consequently modulating N_n as a function of time. However, we acknowledge here that we assume an ultrafast excitation and relaxation of the electrons at optical frequencies. While the ultrafast excitation has been realized in experiments, the relaxation of such excited electrons at optical speeds has proven to be infeasible with currently known materials [34]. Furthermore, our model ignores the time-dependence of γ_n, which is inevitable as the electrons are redistributed across the oscillators. Nevertheless, the employed model allows for a relatively straightforward implementation of a dispersive time-dependent material response, while capturing the novel effects of temporal modulation. A related mechanism to induce time modulation is the utilization of hot-electron nonlinearities. In essence, a strong pump beam can heat up the electrons in a medium, thereby changing the effective mass m_e in a transient fashion (see Eq. (2.12)). We direct the interested reader to Ref. [60], which discusses more general Drude-Lorentz models for time-varying media. Finally, solving Eq. (2.12) in the frequency domain and using Eq. (2.4),

we get the following expression for the frequency-domain response function [48]

$$\tilde{R}_{\mathrm{e}}(\omega-\omega',\omega') = \chi_{\infty,\mathrm{st}}\delta(\omega-\omega') + \frac{1}{\sqrt{2\pi}}\sum_n \frac{e^2}{m_{\mathrm{e}}\varepsilon_0}\frac{\tilde{N}_n(\omega-\omega')}{(\omega_{0n}^2 - i\gamma_n\omega - \omega^2)}\,, \text{with} \tag{2.15a}$$

$$\tilde{N}_n(\omega-\omega') = \sqrt{2\pi}N_{n,\mathrm{st}}\Bigg\{\delta(\omega-\omega') + \frac{1}{2}\Bigg[\sum_{q=1}^{Q} M_{q,n}\delta(\omega-\omega'+q\Omega) + M_{q,n}^*\delta(\omega-\omega'-q\Omega)\Bigg]\Bigg\}\,. \tag{2.15b}$$

We use the dynamic electron density model developed here for the simulations in Chapter 6.

Next, we discuss the temporal modulation mechanism associated with the fast optical Kerr effect.

2.3.2. Time modulation due to the fast optical Kerr effect

The real-valued physical polarization density in a medium supporting third-order nonlinearities can be written as [P1, 57, 58, 61]

$$\mathbf{P}_{\mathrm{r}}(\mathbf{r},t) = \varepsilon_0\left[\int_{-\infty}^{\infty} R_{\mathrm{e}}^{(1)}(t-\tau)\,\mathbf{E}_{\mathrm{r}}(\mathbf{r},\tau)\mathrm{d}\tau + \chi^{(3)}E_{\mathrm{pump}}^2(\mathbf{r},t)\,\mathbf{E}_{\mathrm{r}}(\mathbf{r},t)\right]\,, \tag{2.16}$$

where $\mathbf{P}_{\mathrm{r}}(\mathbf{r},t)$ and $\mathbf{E}_{\mathrm{r}}(\mathbf{r},t)$ are defined such that $\mathbf{P}_{\mathrm{r}}(\mathbf{r},t) = \Re\left(\mathbf{P}(\mathbf{r},t)\right)$ and $\mathbf{E}_{\mathrm{r}}(\mathbf{r},t) = \Re\left(\mathbf{E}(\mathbf{r},t)\right)$. Furthermore, $R_{\mathrm{e}}^{(1)}(t-\tau)$ and $\chi^{(3)}$ are the linear response function and the third-order susceptibility of the medium, respectively. Note that we have assumed an instantaneous third-order nonlinear response of the material to the *electric field* (not intensity) with a response function $R_{\mathrm{e}}^{(3)}(t-\tau) = \chi^{(3)}\delta(t-\tau)$. Physically, such an instantaneous response is mediated by the virtual excitation and relaxation of electrons inside the medium [61]. Furthermore, $E_{\mathrm{pump}}(\mathbf{r},t)$ is the applied pump field *inside* the medium. We use $E_{\mathrm{pump}}(\mathbf{r},t) = E_{\mathrm{p}}(\mathbf{r})\cos(\omega_{\mathrm{p}}t+\phi(\mathbf{r}))$. Here, $E_{\mathrm{p}}(\mathbf{r})$ is the real-valued pump field amplitude, ω_{p} and $\phi(\mathbf{r})$ are the pump frequency and phase, respectively. Therefore, the polarization density takes the form

$$\mathbf{P}_{\mathrm{r}}(\mathbf{r},t) = \varepsilon_0\int_{-\infty}^{\infty} R_{\mathrm{e}}^{(1)}(t-\tau)\,\mathbf{E}_{\mathrm{r}}(\mathbf{r},\tau)\mathrm{d}\tau + \varepsilon_0\chi^{(3)}E_{\mathrm{p}}^2(\mathbf{r})\cos^2(\omega_{\mathrm{p}}t+\phi(\mathbf{r}))\,\mathbf{E}_{\mathrm{r}}(\mathbf{r},t) \tag{2.17}$$

$$= \varepsilon_0\int_{-\infty}^{\infty} R_{\mathrm{e}}^{(1)}(t-\tau)\,\mathbf{E}_{\mathrm{r}}(\mathbf{r},\tau)\mathrm{d}\tau + \varepsilon_0\frac{\chi^{(3)}}{2}E_{\mathrm{p}}^2(\mathbf{r})\left[1+\cos(2\omega_{\mathrm{p}}t+2\phi(\mathbf{r}))\right]\,\mathbf{E}_{\mathrm{r}}(\mathbf{r},t)\,. \tag{2.18}$$

For simplicity, we drop the spatial dependence of $E_{\mathrm{p}}(\mathbf{r})$ and $\phi(\mathbf{r})$, therefore,

$$\mathbf{P}_{\mathrm{r}}(\mathbf{r},t) = \varepsilon_0\int_{-\infty}^{\infty}\left\{R_{\mathrm{e}}^{(1)}(t-\tau) + \delta(t-\tau)\frac{\chi^{(3)}}{2}E_{\mathrm{p}}^2\left[1+\cos(2\omega_{\mathrm{p}}t+2\phi)\right]\right\}\,\mathbf{E}_{\mathrm{r}}(\mathbf{r},\tau)\mathrm{d}\tau\,. \tag{2.19}$$

Clearly, the strong pump approximation allows us to write a linearized dependence of the polarization density on the electric fields. Due to linearity, Eq. (2.19) can also be rewritten for the complex-valued polarization density and electric field as

$$\mathbf{P}(\mathbf{r},t) = \varepsilon_0\int_{-\infty}^{\infty}\left\{R_{\mathrm{e}}^{(1)}(t-\tau) + \delta(t-\tau)\frac{\chi^{(3)}}{2}E_{\mathrm{p}}^2\left[1+\cos(2\omega_{\mathrm{p}}t+2\phi)\right]\right\}\,\mathbf{E}(\mathbf{r},\tau)\mathrm{d}\tau\,. \tag{2.20}$$

We find that the fast optical Kerr effect gives rise to the following effective linear response function

$$R^{(1)}_{\text{eff}}(t, t-\tau) = R^{(1)}_{\text{e}}(t-\tau) \; + \delta(t-\tau)\frac{\chi^{(3)}}{2}E^2_{\text{p}}\left[1+\cos(2\omega_{\text{p}}t+2\phi)\right] . \tag{2.21}$$

Here, the second term depends explicitly on time. Next, we assume $R^{(1)}(t-\tau) = \chi_{\infty,\text{st}}\delta(t-\tau) + R^{(1)}_{\text{disp}}(t-\tau)$, where $R^{(1)}_{\text{disp}}(t-\tau)$ is the dispersive part of the linear response function. Therefore,

$$R^{(1)}_{\text{eff}}(t, t-\tau) = R^{(1)}_{\text{disp}}(t-\tau) \; + \delta(t-\tau)\chi_{\infty}(t)\,, \tag{2.22}$$

where we have defined a time-dependent background susceptibility as

$$\chi_{\infty}(t) = \chi_{\infty,\text{st}} + \frac{\chi^{(3)}E^2_{\text{p}}}{2}\left[1+\cos(\Omega t+2\phi)\right] , \tag{2.23}$$

with modulation frequency $\Omega = 2\omega_{\text{p}}$. Note that, in the present case, $R^{(1)}_{\text{disp}}(t-\tau)$ does not explicitly depend on time. We again use the multipole Drude-Lorentz model to account for dispersion. Specifically, we use Eq. (2.12) with static electron densities, i.e., $N_n = N_{n,\text{st}}$ to consider the $R^{(1)}_{\text{disp}}(t-\tau)$ term. Therefore, in the frequency domain, Eq. (2.21) can be written as

$$\begin{aligned}\tilde{R}^{(1)}_{\text{eff}}(\omega-\omega', \omega') = \delta(\omega-\omega')\sum_n \frac{e^2}{m_{\text{e}}\varepsilon_0}\frac{N_{n,\text{st}}}{\omega^2_{0n}-i\gamma_n\omega-\omega^2} \\ + \chi_{\infty,\text{st}}\Bigg\{\delta(\omega-\omega') \\ + \frac{\chi^{(3)}E^2_{\text{p}}}{2\chi_{\infty,\text{st}}}\left[\delta(\omega-\omega') + \frac{1}{2}\Big(e^{2i\phi}\delta(\omega-\omega'+\Omega) + e^{-2i\phi}\delta(\omega-\omega'-\Omega)\Big)\right]\Bigg\}.\end{aligned} \tag{2.24}$$

We use the Kerr-induced temporal modulation formalism developed here for the simulations in Chapter 4.

Next, we discuss the temporal modulation mechanism in a non-dispersive medium.

2.3.3. Time modulation of non-dispersive media

In a non-dispersive time-varying medium with $R_{\text{e}}(t, t-\tau) = \chi_{\infty}(t)\delta(t-\tau)$, we write the polarization density as

$$\mathbf{P}(\mathbf{r}, t) = \varepsilon_0 \int_{-\infty}^{\infty} \chi_{\infty}(t)\delta(t-\tau)\,\mathbf{E}(\mathbf{r}, \tau)\mathrm{d}\tau\,, \tag{2.25a}$$

$$= \varepsilon_0\,\chi_{\infty}(t)\,\mathbf{E}(\mathbf{r}, t)\,, \tag{2.25b}$$

where $\chi_{\infty}(t)$ is defined as

$$\chi_{\infty}(t) = \chi_{\infty,\text{st}}\left[1+\frac{1}{2}\sum_{q=1}^{Q}(M_q e^{iq\Omega t}+\text{c.c.})\right] . \tag{2.26}$$

In the frequency domain, the corresponding response function is written as

$$\tilde{R}_{\mathrm{e}}(\omega-\omega',\omega') = \chi_{\infty,\mathrm{st}}\Bigg\{\delta(\omega-\omega') + \frac{1}{2}\Bigg[\sum_{q=1}^{Q} M_q\,\delta(\omega-\omega'+q\Omega) + M_q^*\,\delta(\omega-\omega'-q\Omega)\Bigg]\Bigg\}. \quad (2.27)$$

The non-dispersive model is helpful in gaining insights into the effects that arise purely due to the time modulation [24]. We utilize such a model for the simulations in Chapter 5.

In this section, we have discussed various modulation mechanisms that can be utilized to induce time-varying material parameters in known materials. Next, we introduce the numerical models for studying complex time-varying scatterers. In particular, we discuss the T- and S-matrix frameworks for time-varying spheres and metasurfaces.

2.4. Structured time-varying media

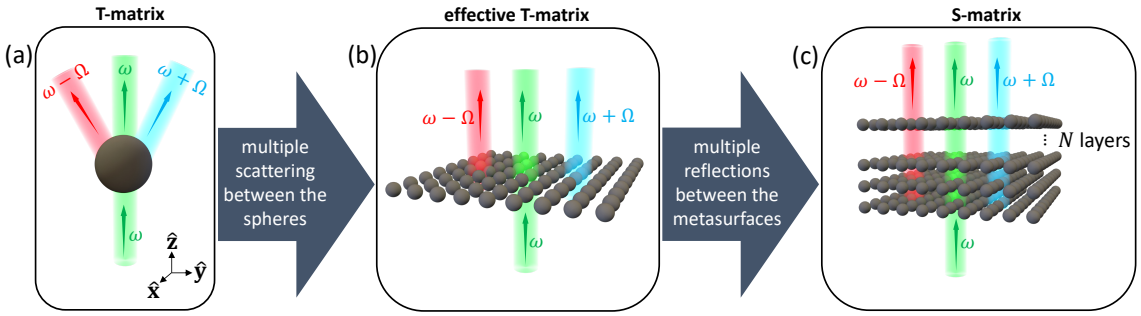


Figure 2.1.: **Various time-varying scattering objects.** (a) A time-varying sphere, (b) a metasurface made from a periodic arrangement of the time-varying spheres, and (c) a multilayered metasurface constructed by stacking N time-varying metasurface layers. This figure has been adapted from [P3]. © The authors, licensed under CC BY 4.0.

In this section, we discuss the theory to computationally model various time-varying scattering structures (see Fig. 2.1). In particular, we describe the T- and S-matrix methods [50, 62, 63]. We note that all the considered computational tools have been verified with the full-wave solver COMSOL Multiphysics for correctness in prior works [P8, 48, 53, 64]. Specifically, in Subsec. 2.4.1, we discuss isolated time-varying spheres. In Subsec. 2.4.2, we describe monolayer and multilayered time-varying metasurfaces.

2.4.1. Time-varying spheres

We begin with isolated time-varying spheres (Fig. 2.1(a)). As mentioned before, we use the T- and S-matrix methods to numerically model the scattering response of the spheres [48, 65].

T-matrix method

We expand the incident field $\mathbf{E}^{\mathrm{inc}}(\mathbf{r},t)$ and the scattered field $\mathbf{E}^{\mathrm{sca}}(\mathbf{r},t)$ for a time-varying sphere in a basis of VSWs for a specific frequency comb characterized by the frequency ω

as [48]

$$\mathbf{E}^{\text{inc}}(\mathbf{r},t) = \sum_j \tilde{\mathbf{E}}^{\text{inc}}(\mathbf{r},\omega_j)\mathrm{e}^{-i\omega_j t} = \sum_{jlms} A^{\text{inc}}_{jlms}\mathbf{F}^{(1)}_{lms}(k_j\mathbf{r})\mathrm{e}^{-i\omega_j t}, \tag{2.28a}$$

$$\mathbf{E}^{\text{sca}}(\mathbf{r},t) = \sum_j \tilde{\mathbf{E}}^{\text{sca}}(\mathbf{r},\omega_j)\mathrm{e}^{-i\omega_j t} = \sum_{jlms} A^{\text{sca}}_{jlms}\mathbf{F}^{(3)}_{lms}(k_j\mathbf{r})\mathrm{e}^{-i\omega_j t}, \tag{2.28b}$$

where $k_j = \omega_j/c_0$. Importantly, $k_j < 0$ for $\omega_j < 0$. $\mathbf{F}^{(1)}_{lms}(k_j\mathbf{r})$ and $\mathbf{F}^{(3)}_{lms}(k_j\mathbf{r})$ are regular and radiating VSWs, respectively[2]. Furthermore, $l \in \{1,2,..,l_{\max}\}$ is the multipolar order, $m \in \{-l,-l+1,..,l-1,l\}$ is the index quantifying the z-component of the angular momentum, and $s \in \{0,1\}$ is the polarization index of the VSWs. We use $s=0$ for TE and $s=1$ for TM polarization. Moreover, A^{inc}_{jlms} and A^{sca}_{jlms} are the incident and scattered field coefficients, respectively.

Next, we use Eq. (2.11) to expand the fields $\mathbf{E}^{\text{int}}(\mathbf{r},t)$ *inside* the sphere as [48]

$$\mathbf{E}^{\text{int}}(\mathbf{r},t) = \sum_j \tilde{\mathbf{E}}^{\text{int}}(\mathbf{r},\omega_j)\mathrm{e}^{-i\omega_j t} = \sum_{jlms}\left[\sum_i A^{\text{int}}_{ilms}H_{\kappa_i}(\omega_j)\mathbf{F}^{(1)}_{lms}(\kappa_i\mathbf{r})\right]\mathrm{e}^{-i\omega_j t}, \tag{2.29}$$

where A^{int}_{ilms} are the internal field coefficients. Note that we have used the regular VSWs $\mathbf{F}^{(1)}_{lms}(\kappa_i\mathbf{r})$ as a choice for $\mathbf{F}_{\kappa_i}(\mathbf{r})$ due to the spatial symmetry of the sphere.

To solve the scattering problem, we need to be able to find $\mathbf{A}^{\text{sca}}$ given $\mathbf{A}^{\text{inc}}$. Such a link between the incident and scattered field coefficients is provided by the T-matrix $\mathbf{T}_0(\omega)$ of the sphere [48], i.e.,

$$\mathbf{A}^{\text{sca}} = \mathbf{T}_0(\omega)\,\mathbf{A}^{\text{inc}}. \tag{2.30}$$

Here, $\mathbf{T}_0(\omega)$ is a polychromatic square matrix with the dimension $2Jl_{\max}(l_{\max}+2)$. The matrix $\mathbf{T}_0(\omega)$ is analytically computed by imposing the following interface conditions on the surface of the sphere [48]

$$\hat{\mathbf{r}}\times\Big[\mathbf{E}^{\text{int}}(\mathbf{r},t) - \mathbf{E}^{\text{sca}}(\mathbf{r},t) - \mathbf{E}^{\text{inc}}(\mathbf{r},t)\Big]\Big|_{r=\mathcal{R}} = 0, \tag{2.31a}$$

$$\hat{\mathbf{r}}\times\Big[\mathbf{H}^{\text{int}}(\mathbf{r},t) - \mathbf{H}^{\text{sca}}(\mathbf{r},t) - \mathbf{H}^{\text{inc}}(\mathbf{r},t)\Big]\Big|_{r=\mathcal{R}} = 0, \tag{2.31b}$$

where $\mathcal{R}$ is the radius of the sphere. Using the expression for the incident, scattered, and internal fields from Eqs. (2.28) and (2.29) in Eq. (2.31), and following the rigorous derivation in [48], we attain the expression of the T-matrix entries for the multipolar order l and polarization s as

$$\mathbf{T}_{0,ls}(\omega) = \mathbf{Y}^{21}_{ls}(\omega) + \mathbf{Y}^{22}_{ls}(\omega)\,, \text{ where} \tag{2.32a}$$

$$\mathbf{Y}_{ls}(\omega) = \begin{bmatrix} \bar{\boldsymbol{\mathcal{H}}}(\omega)\,\mathbf{Z}^{(1)}_{ls}(\omega) & -\mathring{\mathbf{Z}}^{(3)}_{ls}(\omega) \\ \mathbf{K}^{-1}(\omega)\,\bar{\boldsymbol{\mathcal{H}}}(\omega)\,\boldsymbol{\kappa}(\omega)\,\mathbf{Z}^{(1)}_{ls}(\omega) & -\mathring{\mathbf{Z}}^{(3)}_{ls}(\omega) \end{bmatrix}^{-1} \begin{bmatrix} \mathring{\mathbf{Z}}^{(1)}_{ls}(\omega) & \mathbf{0} \\ \mathbf{0} & \mathring{\mathbf{Z}}^{(1)}_{ls}(\omega) \end{bmatrix}, \tag{2.32b}$$

[2](see Appendix Sec. A.1 for the definition of the VSWs)

with the square matrices of dimension J defined as

$$\bar{\boldsymbol{\mathcal{H}}}(\omega) = \left[\boldsymbol{\mathcal{H}}_{\kappa_0}(\omega)\,,..\,,\,\boldsymbol{\mathcal{H}}_{\kappa_{J-1}}(\omega)\right], \tag{2.33a}$$

$$\boldsymbol{\kappa}(\omega) = \mathrm{diag}[\kappa_0(\omega)\,,..\,,\,\kappa_{J-1}(\omega)], \tag{2.33b}$$

$$\mathbf{Z}_{ls}^{(\iota)}(\omega) = \mathrm{diag}\Big[z_{ls}^{(\iota)}(\kappa_0(\omega)\mathcal{R})\,,..\,,\,z_{ls}^{(\iota)}(\kappa_{J-1}(\omega)\mathcal{R})\Big], \tag{2.33c}$$

$$\mathring{\mathbf{Z}}_{ls}^{(\iota)}(\omega) = \mathrm{diag}\Big[z_{ls}^{(\iota)}(k_0\mathcal{R})\,,..\,,\,z_{ls}^{(\iota)}(k_{J-1}\mathcal{R})\Big]. \tag{2.33d}$$

Here, $z_{l0}^{(\iota)}(x)$ denotes the spherical Bessel function of the first kind for $\iota = 1$, the spherical Hankel function of the first kind for $\iota = 3$, and the spherical Hankel function of the second kind for $\iota = 4$, each of order l. Moreover, $z_{l1}^{(\iota)}(x) = \frac{1}{x}\frac{\mathrm{d}}{\mathrm{d}x}[xz_{l0}^{(\iota)}(x)]$. Note that due to the spatial symmetry of the sphere, the matrices $\mathbf{T}_{0,ls}(\omega)$ and $\mathbf{Y}_{ls}(\omega)$ are invariant with respect to the index m. Furthermore, because of time-modulation, these matrices are off-diagonal with respect to the frequency index j. Importantly, to construct the full T-matrix $\mathbf{T}_0(\omega)$, the elements of $\mathbf{T}_{0,ls}(\omega)$ must be arranged for all the considered values of l, s, and m. We show the resulting structure of $\mathbf{T}_0(\omega)$ for the static and time-varying cases in Figs. 2.2(a)–(b). We utilize the T-matrix formalism discussed here for the simulations in Chapters 4, 5, and 6.

We remark here that although we focus on the T-matrix method for homogeneous time-varying spheres, it is also possible to analytically compute the T-matrix of multilayered spheres [53]. Furthermore, for arbitrarily shaped finite-sized time-varying scatterers, the extended boundary condition method (EBCM) can be used to compute their T-matrix [P13].

S-matrix method

Another widely used computational tool in scattering theory is the S-matrix [51, 63]. For spheres (and other finite-sized scatterers), the S-matrix links the coefficients of the incoming and outgoing fields expanded on the basis of VSWs $\mathbf{F}^{(4)}(k_j\mathbf{r})$ and $\mathbf{F}^{(3)}(k_j\mathbf{r})$, respectively. Here, $\mathbf{F}^{(4)}(k_j\mathbf{r})$ are the incoming VSWs (see Appendix Sec. A.1). Using the properties of VSWs, the S-matrix can be easily calculated from the T-matrix of a time-varying sphere as [63]

$$\mathbf{S}_0(\omega) = \mathbf{I} + 2\mathbf{T}_0(\omega)\,. \tag{2.34}$$

We utilize the S-matrices of time-varying spheres in Chapter 5.

Scattering of unit plane waves

Next, we discuss the steps to compute the scattering response of time-varying spheres to incident PWs. Consider an incident monochromatic unit PW of the form $\mathbf{E}^{\mathrm{inc}}(\mathbf{r},t) = e^{i(\mathbf{k}\cdot\mathbf{r}-\omega t)}\hat{\mathbf{e}}_{\mathrm{inc}}(\mathbf{k})$ to the sphere. Here, $\hat{\mathbf{e}}_{\mathrm{inc}}(\mathbf{k})$ is a unit vector (see Appendix Sec. A.2). To solve the scattering problem, first, the incident field coefficients A_{jlms}^{inc} are computed according to Eq. (2.28a) in the VSW basis. For positive incident frequencies, i.e., $\omega > 0$, we use the Python package `treams` to compute A_{jlms}^{inc}. For negative incident frequencies, i.e., $\omega < 0$, we use the symmetry relation (see Appendix Secs. A.3–A.4 for a detailed derivation)

$$A_{jlms}^{\mathrm{inc}}(\omega, -\mathbf{k}^*, \hat{\mathbf{e}}_{\mathrm{inc}}^*(\mathbf{k})) = (-1)^{l-m+\delta_{\alpha 1}} A_{jl(-m)s}^{\mathrm{inc}*}(-\omega, \mathbf{k}, \hat{\mathbf{e}}_{\mathrm{inc}}(\mathbf{k}))\,. \tag{2.35}$$

The relation implies that the incident field coefficients of the PW $e^{-i(\mathbf{k}^*\cdot\mathbf{r}+\omega t)}\hat{\mathbf{e}}_{\mathrm{inc}}^*(\mathbf{k})$ are linked to that of the PW $e^{i(\mathbf{k}\cdot\mathbf{r}-(-\omega)t)}\hat{\mathbf{e}}_{\mathrm{inc}}(\mathbf{k})$. Therefore, we can compute the incident

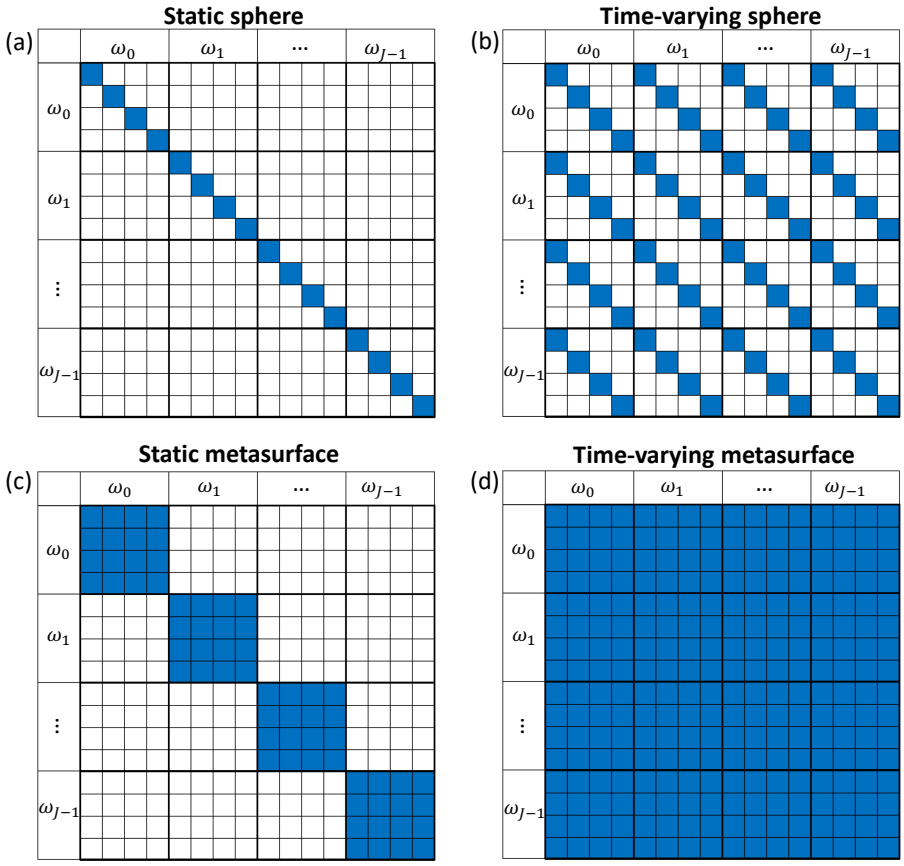


Figure 2.2.: **Polychromatic T-matrices.** The structure of the T-matrix of (a) a static sphere, (b) a time-varying sphere, (c) a static metasurface, and (d) a time-varying metasurface. Blue shading represents a non-zero entry while white shading indicates a zero entry. The T-matrices have a block form with respect to frequency ω_j. In the static case, each diagonal block represents the usual monochromatic T-matrix of the underlying structure. Furthermore, in such a case, the off-diagonal blocks' entries are zero, signifying a monochromatic response. By contrast, in the time-varying case, the off-diagonal entries can be non-zero due to time modulation-induced frequency coupling. This figure has been adapted with permission from [P8]. © Optica Publishing Group.

field coefficients for $\omega < 0$ from those of $\omega > 0$. Note that because the incident PW is monochromatic, $A^{\text{inc}}_{jlms} = 0 \; \forall \; j \neq -j_0$. Next, we use Eq. (2.30) to compute the corresponding scattered field coefficients A^{sca}_{jlms}. Finally, the resulting polychromatic scattered field can be computed using Eq. (2.28b).

Scattering cross section

Here, we discuss the computation of the scattering cross section of the time-varying sphere. Consider an incident PW of the form $\mathbf{E}^{\text{inc}}(\mathbf{r}, t) = U^{\text{inc}} e^{i(\mathbf{k}\cdot\mathbf{r} - \omega t)} \hat{\mathbf{e}}_{\text{inc}}(\mathbf{k})$ to the sphere. The corresponding scattered field is polychromatic and has the form given by Eq. (2.28b). The instantaneous Poynting vector for the scattered field is

$$\boldsymbol{\mathcal{S}}^{\text{sca}}(\mathbf{r}, t) = \mathbf{E}^{\text{sca}}_{\text{r}}(\mathbf{r}, t) \times \mathbf{H}^{\text{sca}}_{\text{r}}(\mathbf{r}, t)\,, \tag{2.36}$$

where $\mathbf{E}^{\text{sca}}_{\text{r}}(\mathbf{r}, t) = \Re\{\mathbf{E}^{\text{sca}}(\mathbf{r}, t)\}$ and $\mathbf{H}^{\text{sca}}_{\text{r}}(\mathbf{r}, t) = \Re\{\mathbf{H}^{\text{sca}}(\mathbf{r}, t)\}$. The time-averaged power flux passing through an imaginary sphere with area $A' = 4\pi R'^2$ in the far-field circumscribing the time-varying sphere is computed by integrating the Poynting vector $\boldsymbol{\mathcal{S}}^{\text{sca}}$ as

$$\langle \boldsymbol{\mathcal{S}}^{\text{sca}} \rangle = \lim_{R' \to \infty} \frac{1}{\tau_d} \int_{A'} \int_{\tau_{\text{d}}} \boldsymbol{\mathcal{S}}^{\text{sca}}(\mathbf{r}, t) \cdot \hat{\mathbf{n}} \, \mathrm{d}t \, \mathrm{d}A\,, \tag{2.37}$$

where τ_{d} is the integration time of a detector, and $\hat{\mathbf{n}} \, \mathrm{d}A$ is an element of the area vector. Using the expression of scattered fields in terms of VSWs (Eq. (2.28b)) and utilizing the asymptotic behavior of spherical Bessel functions, we get [65, 66]

$$\langle \boldsymbol{\mathcal{S}}^{\text{sca}} \rangle = \frac{1}{2Z_0} \sum_j \sum_{lms} \frac{1}{|k_j|^2} |A^{\text{sca}}_{jlms}|^2\,. \tag{2.38}$$

The scattering cross section σ_{sca} of the time-varying sphere is computed by dividing $\langle \boldsymbol{\mathcal{S}}^{\text{sca}} \rangle$ by the time-averaged power flux of the incident PW passing through the geometric cross section of the sphere (i.e., a circle with area πR^2 and area vector parallel to $\mathbf{k}$). Such incident power flux is

$$\langle \boldsymbol{\mathcal{S}}^{\text{inc}} \rangle = \frac{\pi R^2}{2Z_0} |U^{\text{inc}}|^2\,. \tag{2.39}$$

Therefore, σ_{sca} can be written as

$$\sigma_{\text{sca}} = \frac{\langle \boldsymbol{\mathcal{S}}^{\text{sca}} \rangle}{\langle \boldsymbol{\mathcal{S}}^{\text{inc}} \rangle} = \sum_j \sigma_{\text{sca},j} = \frac{1}{\pi R^2 |U^{\text{inc}}|^2} \sum_j \sum_{lms} \frac{1}{|k_j|^2} |A^{\text{sca}}_{jlms}|^2\,, \tag{2.40}$$

where $\sigma_{\text{sca},j}$ is the frequency-resolved scattering cross section of the sphere. Note that σ_{sca} can be written as an incoherent sum of $\sigma_{\text{sca},j}$ terms for $\omega \neq n\Omega/2$ ($n \in \mathbb{Z}$). When $\omega = n\Omega/2$, the interference between the positive and negative scattered frequencies introduces non-zero cross terms which have to be properly considered while computing $\langle \boldsymbol{\mathcal{S}}^{\text{sca}} \rangle$ (see Ref. [67] for more details). We utilize the scattering cross section computations in Chapters 4 and 6.

So far, we have focused on isolated time-varying meta-atoms. In what follows, we discuss the metasurfaces made from a periodic arrangement of these meta-atoms in 2D.

2.4.2. Time-varying metasurfaces

In this subsection, we discuss the T- and S-matrix methods for time-varying metasurfaces. We consider monolayer as well as multilayered metasurfaces.

T-matrix method

We first describe the T-matrix method for monolayer time-varying metasurfaces. The considered metasurface is made from an infinite periodic lattice of time-varying spheres in 2D (see Fig. 2.1(b)). For computationally modeling such a structure, multiple scattering between the spheres in the lattice has to be taken into account. Therefore, the lattice sums have to be rigorously considered to evaluate its effective T-matrix. Such an effective T-matrix $\mathbf{T}_{\text{eff}}(\omega, \mathbf{k}_{\parallel})$ is written as [P8, 54]

$$\mathbf{T}_{\text{eff}}(\omega, \mathbf{k}_{\parallel}) = \left(\mathbf{I} - \mathbf{T}_0(\omega) \sum_{\mathbf{R} \neq 0} \mathbf{C} \, \mathrm{e}^{i\mathbf{k}_{\parallel} \cdot \mathbf{R}} \right)^{-1} \mathbf{T}_0(\omega) \,, \tag{2.41}$$

where $\mathbf{k}_{\parallel}$ is the Bloch wavevector, and $\mathbf{R}$ is a lattice vector. Furthermore, the block-diagonal matrix $\mathbf{C}$ is given by

$$\mathbf{C} = \begin{bmatrix} \mathbf{c}(-k_0\mathbf{R}) & \mathbf{0} & \cdots & \mathbf{0} \\ \mathbf{0} & \mathbf{c}(-k_1\mathbf{R}) & \cdots & \mathbf{0} \\ \vdots & \vdots & \ddots & \vdots \\ \mathbf{0} & \mathbf{0} & \cdots & \mathbf{c}(-k_{J-1}\mathbf{R}) \end{bmatrix} . \tag{2.42}$$

Here, the sub-matrix $\mathbf{c}(-k_j\mathbf{R})$ contains the translation coefficients for VSWs at frequency ω_j (see Appendix Sec. A.5). Furthermore, $\mathbf{c}(-k_j\mathbf{R})$ satisfies the symmetry relation (see Appendix Sec. A.5 for a detailed derivation)

$$c^{\{lms\},\{l'm's'\}}(-k_j\mathbf{R}) = (-1)^{(l-l'+m'-m+\delta_{s1}-\delta_{s'1})} \left[c^{\{l(-m)s\},\{l'(-m')s'\}}(-(-k_j^*)\mathbf{R}) \right]^* . \tag{2.43}$$

For $k_j \in \mathbb{R}$, the symmetry relation allows us to compute $\mathbf{c}(-k_j\mathbf{R})$ for $k_j < 0$ from the corresponding values at $k_j > 0$. In combination with Eq. (2.43), the matrix $\mathbf{C}$ and the associated lattice sum in Eq. (2.41) can be directly computed using open-source codes written for static metamaterials. In this work, we use the Python package `treams` for such a computation [49]. We show the comparison of the structures of the resulting effective T-matrices of static and time-varying metasurfaces in Figs. 2.2(c)–(d). We utilize the effective T-matrix formalism in Chapter 4 for computing the bandstructures, and in Chapter 6 for the inverse design of the time-varying metasurfaces.

By definition, the effective T-matrix links the incident and scattered field coefficients of the metasurface as [P8, 54]

$$\mathbf{A}^{\text{sca}} = \mathbf{T}_{\text{eff}}(\omega, \mathbf{k}_{\parallel}) \, \mathbf{A}^{\text{inc}} \,, \tag{2.44}$$

where the coefficient vector $\mathbf{A}^{\text{inc}}$ is related to the corresponding incident field $\mathbf{E}^{\text{inc}}(\mathbf{r}, t)$ by the expansion given in Eq. (2.28a). However, the vector $\mathbf{A}^{\text{sca}}$ is related to the corresponding scattered field $\mathbf{E}^{\text{sca}}(\mathbf{r}, t)$ as [P8, 54]

$$\mathbf{E}^{\mathrm{sca}}(\mathbf{r},t)=\sum_{j}\left(\sum_{\mathbf{R}}\sum_{lms}A^{\mathrm{sca}}_{jlms}\mathbf{F}^{(3)}_{lms}(k_j(\mathbf{r}-\mathbf{R}))e^{i\mathbf{k}_{\parallel}\cdot\mathbf{R}}\right)e^{-i\omega_j t}. \tag{2.45}$$

Here, the sum over the lattice vectors $\mathbf{R}$ is necessary to take into account the contribution of each sphere in the lattice to the scattered field. To simplify the computation of the scattered field, we use the integral representation of VSWs in Eq. (2.45). Note that $\mathbf{E}^{\mathrm{sca}}(\mathbf{r},t)$ contains components with both positive and negative frequencies ω_j. Therefore, the sign of ω_j should be properly accounted for while evaluating $\mathbf{E}^{\mathrm{sca}}(\mathbf{r},t)$.

For $\omega_j > 0$, the integral representation of VSWs is given by [54]

$$\begin{aligned}
\mathbf{F}^{(3)}_{lm0}(k_j\mathbf{r}) &= \frac{1}{2\pi i^{l}}\int\frac{\mathrm{d}^2\mathbf{k}_{\parallel}}{k_j\Gamma_{\mathbf{k}_{\parallel}}}\,\mathbf{X}_{lm}(\hat{\mathbf{k}})e^{i\mathbf{k}\cdot\mathbf{r}},\\
\mathbf{F}^{(3)}_{lm1}(k_j\mathbf{r}) &= \frac{1}{2\pi i^{\,l-1}}\int\frac{\mathrm{d}^2\mathbf{k}_{\parallel}}{k_j\Gamma_{\mathbf{k}_{\parallel}}}\,\hat{\mathbf{k}}\times\mathbf{X}_{lm}(\hat{\mathbf{k}})e^{i\mathbf{k}\cdot\mathbf{r}}\,,\\
&\text{with } \mathbf{k}=\mathbf{k}_{\parallel}\pm\hat{\mathbf{z}}\Gamma_{\mathbf{k}_{\parallel}}\,,\quad \text{for } z\gtrless 0,\ \text{where } \Gamma_{\mathbf{k}_{\parallel}}=\sqrt{k_j^2-\mathbf{k}_{\parallel}^2}\,.
\end{aligned} \tag{2.46}$$

For $\omega_j < 0$, using the symmetry property of VSWs given by Eq. (A.4), the integral representation can be written as

$$\begin{aligned}
\mathbf{F}^{(3)}_{lm0}(k_j\mathbf{r}) &= \frac{(-1)^{l+m+\delta_{01}}}{2\pi(-i)^{l}}\int\frac{\mathrm{d}^2\mathbf{k}_{\parallel}}{(-k_j)\,\Gamma^{*}_{\mathbf{k}_{\parallel}}}\,\mathbf{X}^{*}_{l-m}(\hat{\mathbf{k}})\,e^{-i\mathbf{k}^{*}\cdot\mathbf{r}}\,,\\
\mathbf{F}^{(3)}_{lm1}(k_j\mathbf{r}) &= \frac{(-1)^{l+m+\delta_{11}}}{2\pi(-i)^{\,l-1}}\int\frac{\mathrm{d}^2\mathbf{k}_{\parallel}}{(-k_j)\,\Gamma^{*}_{\mathbf{k}_{\parallel}}}\,\hat{\mathbf{k}}^{*}\times\mathbf{X}^{*}_{l-m}(\hat{\mathbf{k}})\,e^{-i\mathbf{k}^{*}\cdot\mathbf{r}}\,,\\
&\text{with } \mathbf{k}=\mathbf{k}_{\parallel}\pm\hat{\mathbf{z}}\,\Gamma_{\mathbf{k}_{\parallel}},\quad \text{for } z\gtrless 0,\ \text{where } \Gamma_{\mathbf{k}_{\parallel}}=\sqrt{(-k_j)^2-\mathbf{k}_{\parallel}^2}\,.
\end{aligned} \tag{2.47}$$

Substituting Eq. (2.46) in Eq. (2.45) and simplifying using the Poisson's sum formula [68], we can write the scattered field for $\omega_j > 0$ as

$$\mathbf{E}^{\mathrm{sca}}(\mathbf{r},t)=\sum_{j}\sum_{\mathbf{g}\alpha d}U^{\mathrm{sca}}_{j\mathbf{g}\alpha d}\,e^{i(\mathbf{k}_{j\mathbf{g}\alpha d}\cdot\mathbf{r}-\omega_j t)}\,\hat{\mathbf{e}}_{\alpha}(\mathbf{k}_{j\mathbf{g}\alpha d})\,. \tag{2.48}$$

Here,

$$U^{\mathrm{sca}}_{j\mathbf{g}\alpha d} = \sum_{lms} \frac{2\pi\gamma_{lm} e^{im\phi_{\mathbf{k}_{j\mathbf{g}\alpha d}}}}{k_j A_{\mathrm{u}}\, i^{\,l+1}\Gamma_{\mathbf{k}_{j\mathbf{g}\alpha d}}} a^{\mathbf{k}_{j\mathbf{g}\alpha d}}_{jlms}\,, \tag{2.49a}$$

$$\mathbf{k}_{j\mathbf{g}\alpha d} = (\mathbf{k}_\parallel + \mathbf{g}) + \hat{\mathbf{z}}(-1)^{\delta_{d\downarrow}}\Gamma_{\mathbf{k}_{j\mathbf{g}\alpha d}}\,, \tag{2.49b}$$

$$\Gamma_{\mathbf{k}_{j\mathbf{g}\alpha d}} = \sqrt{k_j^2 - (\mathbf{k}_\parallel + \mathbf{g})^2}\,, \tag{2.49c}$$

$$a^{\mathbf{k}_{j\mathbf{g}\alpha d}}_{jlm0} = A^{\mathrm{sca}}_{jlm0} \frac{\partial}{\partial\theta} P_l^m(\cos\theta)\Big|_{\theta=\theta_{\mathbf{k}_{j\mathbf{g}\alpha d}}} + A^{\mathrm{sca}}_{jlm1} \frac{m}{\sin\theta} P_l^m(\cos\theta)\Big|_{\theta=\theta_{\mathbf{k}_{j\mathbf{g}\alpha d}}}\,, \tag{2.49d}$$

$$a^{\mathbf{k}_{j\mathbf{g}\alpha d}}_{jlm1} = A^{\mathrm{sca}}_{jlm0} \frac{m}{\sin\theta} P_l^m(\cos\theta)\Big|_{\theta=\theta_{\mathbf{k}_{j\mathbf{g}\alpha d}}} + A^{\mathrm{sca}}_{jlm1} \frac{\partial}{\partial\theta} P_l^m(\cos\theta)\Big|_{\theta=\theta_{\mathbf{k}_{j\mathbf{g}\alpha d}}}\,, \tag{2.49e}$$

$$\gamma_{lm} = i\sqrt{\frac{(l-m)!}{(l+m)!}\frac{(2l+1)}{4\pi l(l+1)}}\,, \tag{2.49f}$$

$$\theta_{\mathbf{k}_{j\mathbf{g}\alpha d}} = \arccos\left(\frac{k_{z;j\mathbf{g}\alpha d}}{k_j}\right)\,, \tag{2.49g}$$

$$\phi_{\mathbf{k}_{j\mathbf{g}\alpha d}} = \mathrm{arctan2}\left(\frac{k_{y;j\mathbf{g}\alpha d}}{k_{x;j\mathbf{g}\alpha d}}\right)\,, \tag{2.49h}$$

where A_{u} is the area of the unit cell of the metasurface.

Similarly, using Eqs. (2.47) in Eq. (2.45), the scattered field for $\omega_j < 0$ is written as

$$\mathbf{E}^{\mathrm{sca}}(\mathbf{r},t) = \sum_j \sum_{\mathbf{g}\alpha d} U^{\mathrm{sca}}_{j\mathbf{g}\alpha d}\, e^{-i(\mathbf{k}^*_{j\mathbf{g}\alpha d}\cdot\mathbf{r}+\omega_j t)}\, \hat{\mathbf{e}}^*_\alpha(\mathbf{k}_{j\mathbf{g}\alpha d})\,, \tag{2.50}$$

where

$$U^{\mathrm{sca}}_{j\mathbf{g}\alpha d} = \sum_{lms} \frac{(-1)^{l+m} 2\pi\gamma^*_{l-m} e^{im\phi^*_{\mathbf{k}_{j\mathbf{g}\alpha d}}}}{(-k_j)A_{\mathrm{u}}\,(-i)^{\,l+1}\Gamma^*_{\mathbf{k}_{j\mathbf{g}\alpha d}}} a^{\mathbf{k}_{j\mathbf{g}\alpha d}}_{jlms}\,, \tag{2.51a}$$

$$\mathbf{k}_{j\mathbf{g}\alpha d} = (-\mathbf{k}_\parallel + \mathbf{g}) + \hat{\mathbf{z}}(-1)^{\delta_{d\downarrow}}\Gamma_{\mathbf{k}_{j\mathbf{g}\alpha d}}\,, \tag{2.51b}$$

$$\Gamma_{\mathbf{k}_{j\mathbf{g}\alpha d}} = \sqrt{(-k_j)^2 - (-\mathbf{k}_\parallel + \mathbf{g})^2}\,, \tag{2.51c}$$

$$a^{\mathbf{k}_{j\mathbf{g}\alpha d}}_{jlm0} = A^{\mathrm{sca}}_{jlm0}\left[\frac{\partial}{\partial\theta} P_l^{-m}(\cos\theta)\Big|_{\theta=\theta_{\mathbf{k}_{j\mathbf{g}\alpha d}}}\right]^* - A^{\mathrm{sca}}_{jlm1}\left[\frac{m}{\sin\theta} P_l^{-m}(\cos\theta)\Big|_{\theta=\theta_{\mathbf{k}_{j\mathbf{g}\alpha d}}}\right]^*\,, \tag{2.51d}$$

$$a^{\mathbf{k}_{j\mathbf{g}\alpha d}}_{jlm1} = A^{\mathrm{sca}}_{jlm0}\left[\frac{m}{\sin\theta} P_l^{-m}(\cos\theta)\Big|_{\theta=\theta_{\mathbf{k}_{j\mathbf{g}\alpha d}}}\right]^* - A^{\mathrm{sca}}_{jlm1}\left[\frac{\partial}{\partial\theta} P_l^{-m}(\cos\theta)\Big|_{\theta=\theta_{\mathbf{k}_{j\mathbf{g}\alpha d}}}\right]^*\,, \tag{2.51e}$$

$$\theta_{\mathbf{k}_{j\mathbf{g}\alpha d}} = \arccos\left(\frac{k_{z;j\mathbf{g}\alpha d}}{-k_j}\right)\,, \tag{2.51f}$$

$$\phi_{\mathbf{k}_{j\mathbf{g}\alpha d}} = \mathrm{arctan2}\left(\frac{k_{y;j\mathbf{g}\alpha d}}{k_{x;j\mathbf{g}\alpha d}}\right)\,. \tag{2.51g}$$

S-matrix method

Next, we discuss the transformation of the effective T-matrix to the S-matrix. For metasurfaces, the S-matrix connects the incident field coefficients to the outgoing field coefficients

expanded in a PW basis. Note that the outgoing field $\mathbf{E}^{\text{out}}(\mathbf{r},t)$ satisfies $\mathbf{E}^{\text{out}}(\mathbf{r},t) = \mathbf{E}^{\text{sca}}(\mathbf{r},t) + \mathbf{E}^{\text{inc}}(\mathbf{r},t)$. We expand the incident fields $\mathbf{E}^{\text{inc}}(\mathbf{r},t)$ and outgoing fields $\mathbf{E}^{\text{out}}(\mathbf{r},t)$ in a basis of PWs as

$$\mathbf{E}^{\text{inc}}(\mathbf{r},t) = \sum_{\substack{j\mathbf{g}\alpha d \\ \text{s.t. } \omega_j>0}} U^{\text{inc}}_{j\mathbf{g}\alpha d} e^{i(\mathbf{k}_{j\mathbf{g}\alpha d}\cdot\mathbf{r}-\omega_j t)}\,\hat{\mathbf{e}}_\alpha(\mathbf{k}_{j\mathbf{g}\alpha d}) + \sum_{\substack{j\mathbf{g}\alpha d \\ \text{s.t. } \omega_j<0}} U^{\text{inc}}_{j\mathbf{g}\alpha d} e^{-i(\mathbf{k}^*_{j\mathbf{g}\alpha d}\cdot\mathbf{r}+\omega_j t)}\,\hat{\mathbf{e}}^*_\alpha(\mathbf{k}_{j\mathbf{g}\alpha d})\,, \tag{2.52a}$$

$$\mathbf{E}^{\text{out}}(\mathbf{r},t) = \sum_{\substack{j\mathbf{g}\alpha d \\ \text{s.t. } \omega_j>0}} U^{\text{out}}_{j\mathbf{g}\alpha d} e^{i(\mathbf{k}_{j\mathbf{g}\alpha d}\cdot\mathbf{r}-\omega_j t)}\,\hat{\mathbf{e}}_\alpha(\mathbf{k}_{j\mathbf{g}\alpha d}) + \sum_{\substack{j\mathbf{g}\alpha d \\ \text{s.t. } \omega_j<0}} U^{\text{out}}_{j\mathbf{g}\alpha d} e^{-i(\mathbf{k}^*_{j\mathbf{g}\alpha d}\cdot\mathbf{r}+\omega_j t)}\,\hat{\mathbf{e}}^*_\alpha(\mathbf{k}_{j\mathbf{g}\alpha d})\,, \tag{2.52b}$$

where

$$\mathbf{k}_{j\mathbf{g}\alpha d} = \begin{cases} \left(\mathbf{k}_\parallel + \mathbf{g}\right) + \hat{\mathbf{z}}\,(-1)^{\delta_{d\downarrow}}\,\Gamma_z, \quad \text{with } \Gamma_z = \sqrt{k_j^2 - \left(\mathbf{k}_\parallel + \mathbf{g}\right)^2}, \quad \text{if } \omega_j > 0, \\ \left(-\mathbf{k}_\parallel + \mathbf{g}\right) + \hat{\mathbf{z}}\,(-1)^{\delta_{d\downarrow}}\,\Gamma_z, \quad \text{with } \Gamma_z = \sqrt{(-k_j)^2 - \left(-\mathbf{k}_\parallel + \mathbf{g}\right)^2}, \quad \text{if } \omega_j < 0. \end{cases} \tag{2.52c}$$

The variable $d = \uparrow, \downarrow$ denotes the upward- and downward-propagating fields, respectively, while $\alpha = 0, 1$ corresponds to the TE- and TM-polarized PWs, respectively. In addition, $\mathbf{k}_{j\mathbf{g}\alpha d}$ represents a wavevector, $\mathbf{g}$ characterizes the diffraction order, and $\hat{\mathbf{e}}_\alpha$ is a unit vector (see Appendix Sec. A.2). Furthermore, $U^{\text{inc}}_{j\mathbf{g}\alpha d}$ and $U^{\text{out}}_{j\mathbf{g}\alpha d}$ denote the incident and outgoing field coefficients in the PW basis, respectively. In the above expansion, we retain G diffraction orders. Here, the branch cuts between $\omega_j > 0$ and $\omega_j < 0$ arise from the specific form of the scattered field produced by the metasurface in the PW basis (see Eqs. (2.48)–(2.51)). Note that the outgoing field coefficients satisfy the relation

$$U^{\text{out}}_{j\mathbf{g}\alpha d} = U^{\text{sca}}_{j\mathbf{g}\alpha d} + U^{\text{inc}}_{j\mathbf{g}\alpha d}\,. \tag{2.53}$$

Furthermore, the coefficients $\mathbf{U}^{\text{inc}}$ and $\mathbf{U}^{\text{out}}$ are connected by the S-matrix $\mathbf{S}$ as [P8, 69]

$$\begin{pmatrix} \mathbf{U}^{\text{out}}_\downarrow \\ \mathbf{U}^{\text{out}}_\uparrow \end{pmatrix} = \underbrace{\begin{pmatrix} \mathbf{S}_{\downarrow\uparrow} & \mathbf{S}_{\downarrow\downarrow} \\ \mathbf{S}_{\uparrow\uparrow} & \mathbf{S}_{\uparrow\downarrow} \end{pmatrix}}_{\mathbf{S}(\omega,\mathbf{k}_\parallel)} \begin{pmatrix} \mathbf{U}^{\text{inc}}_\uparrow \\ \mathbf{U}^{\text{inc}}_\downarrow \end{pmatrix}. \tag{2.54}$$

Here, $\mathbf{S}$ is a square matrix with the dimension $4JG$, and $\mathbf{S}_{dd'}$ denotes the block mapping the incident field coefficients $\mathbf{U}^{\text{inc}}_{d'}$ to the outgoing field coefficients $\mathbf{U}^{\text{out}}_{d}$. We choose the arrangement of the sub-blocks in the full S-matrix $\mathbf{S}$ according to Ref. [70].

In this work, we compute the S-matrix of a metasurface from its effective T-matrix. The required computational steps are shown in Fig. 2.3. In essence, we consider an incident unit PW to the metasurface according to Eq. (2.52a). Next, we compute the incident field coefficients $\mathbf{A}^{\text{inc}}$ for the PW using Eq. (2.28a) in the VSW basis. Then, the corresponding scattered field coefficients $\mathbf{A}^{\text{sca}}$ in the VSW basis are calculated using the effective T-matrix

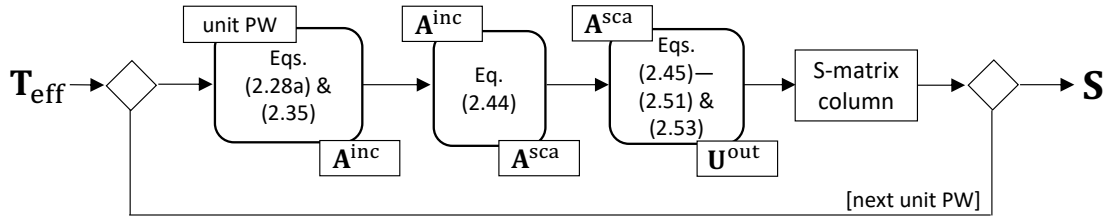


Figure 2.3.: **Computing the S-matrix of a time-varying metasurface.** The flow of the computational steps needed to evaluate the S-matrix of a time-varying metasurface from its effective T-matrix.

according to Eq. (2.44). Utilizing $\mathbf{A}^{\text{sca}}$, we compute the scattered field coefficients $\mathbf{U}^{\text{sca}}$ according to Eqs. (2.48)–(2.51). Finally, we use Eq. (2.53) to compute $\mathbf{U}^{\text{out}}$. This $\mathbf{U}^{\text{out}}$ vector constitutes a column of the S-matrix. The process is repeated by considering another unit PW to compute another column of the S-matrix.

S-matrix of multilayered metasurfaces

To compute the S-matrix of a stack of metasurfaces, multiple reflections between the metasurface layers have to be taken into account (see Fig. 2.1(c)). We numerically incorporate these multiple reflections using the S-matrix star product [71]. In particular, the S-matrix of the stack of N metasurfaces is expressed as

$$\mathbf{S}(\omega, \mathbf{k}_{\parallel}) = \mathbf{S}^{(0)} \star \mathbf{S}_{\text{prop},\mathbf{r}_0} \star \mathbf{S}^{(1)} \star \mathbf{S}_{\text{prop},\mathbf{r}_1} \star \mathbf{S}^{(2)} ... \star \mathbf{S}_{\text{prop},\mathbf{r}_{\text{N}-2}} \star \mathbf{S}^{(N-1)}\,, \tag{2.55}$$

where $\mathbf{S}^{(i)}$ is the S-matrix of the i^{th} metasurface, and $\mathbf{S}_{\text{prop},\mathbf{r}_{\text{i}}}$ is the S-matrix that takes into account the phase accumulation of the PWs while traveling between i^{th} and $(i+1)^{\text{th}}$ metasurfaces. Assuming that the $(i+1)^{\text{th}}$ metasurface is spatially located above the i^{th} metasurface, $\mathbf{S}_{\text{prop},\mathbf{r}_{\text{i}}}$ can be written as

$$S^{\{j\mathbf{g}\alpha d\},\{j'\mathbf{g}'\alpha' d'\}}_{\text{prop},\mathbf{r}_i}(\omega, \mathbf{k}_{\parallel}) = \begin{cases} \delta_{jj'}\delta_{dd'}\delta_{\alpha\alpha'}\delta_{\mathbf{g}\mathbf{g}'} e^{i(-1)^{\delta_{d\downarrow}}\mathbf{k}_{j\mathbf{g}\alpha d}\cdot\mathbf{r}_i}\,, \text{if } \omega_j > 0\,, \\ \\ \delta_{jj'}\delta_{dd'}\delta_{\alpha\alpha'}\delta_{\mathbf{g}\mathbf{g}'} e^{-i(-1)^{\delta_{d\downarrow}}\mathbf{k}^{*}_{j\mathbf{g}\alpha d}\cdot\mathbf{r}_i}\,, \text{if } \omega_j < 0\,, \end{cases} \tag{2.56}$$

where $\mathbf{r}_i$ is the spatial displacement vector drawn from the i^{th} to $(i+1)^{\text{th}}$ metasurface. We utilize the S-matrix formalism for studying the scattering anomalies in time-varying metasurfaces in Chapter 5.

Inclusion of a static substrate

The blocks of the S-matrix $\mathbf{S}^{\text{subs}}$ of a planar static substrate (slab) have a block diagonal form with respect to the frequency index j, i.e.,

$$\mathbf{S}^{\text{subs}}_{dd'}(\omega, \mathbf{k}_{\parallel}) = \begin{bmatrix} \mathbf{s}^{\text{subs}}_{dd'}(\omega_0, \mathbf{k}_{\parallel}) & \mathbf{0} & \cdots & \mathbf{0} \\ \mathbf{0} & \mathbf{s}^{\text{subs}}_{dd'}(\omega_1, \mathbf{k}_{\parallel}) & \cdots & \mathbf{0} \\ \vdots & \vdots & \ddots & \vdots \\ \mathbf{0} & \mathbf{0} & \cdots & \mathbf{s}^{\text{subs}}_{dd'}(\omega_{J-1}, \mathbf{k}_{\parallel}) \end{bmatrix}. \tag{2.57}$$

Here, $\mathbf{s}^{\text{subs}}_{dd'}(\omega_j, \mathbf{k}_{\parallel})$ are the usual monochromatic S-matrix blocks of the static substrate at frequency ω_j for the Bloch wavevector $\mathbf{k}_{\parallel}$. For $\omega_j > 0$, these blocks can be computed directly

using the Python package `treams`. For $\omega_j < 0$, we use the symmetry relation (see Appendix Sec. A.6)

$$\mathbf{s}^{\mathrm{subs}}_{dd'}(\omega_j, \mathbf{k}_\parallel) = \left[\mathbf{s}^{\mathrm{subs}}_{dd'}(-\omega_j, -\mathbf{k}_\parallel)\right]^* . \tag{2.58}$$

Using the relation, the S-matrix blocks $\mathbf{s}^{\mathrm{subs}}_{dd'}(\omega_j, \mathbf{k}_\parallel)$ for $\omega_j < 0$ can be computed from those for $\omega_j > 0$. Once the full S-matrix $\mathbf{S}^{\mathrm{subs}}$ of the substrate is known, Eq. (2.55) can be used to compute the S-matrix of composite structures involving time-varying metasurfaces on a substrate.

Reflectivity and transmissivity

Next, we discuss the computation of the reflectivity and transmissivity for time-varying metasurfaces. Consider a monochromatic upward-propagating incident PW to the metasurface. Using the Poynting vector, the space- and time-averaged intensity of the PW can be written as

$$I^{\mathrm{inc}} = \lim_{A'\to\infty} \frac{1}{A'} \frac{1}{\tau_{\mathrm{d}}} \int_{A'} \int_{\tau_{\mathrm{d}}} \boldsymbol{\mathcal{S}}^{\mathrm{inc}}(\mathbf{r}, t) \cdot \hat{\mathbf{z}} \, \mathrm{d}t \, \mathrm{d}A \,, \tag{2.59}$$

where the area A' is assumed to be in the $x-y$ plane spatially below the metasurface. Using the expression $\mathbf{E}^{\mathrm{inc}}(\mathbf{r}, t) = U^{\mathrm{inc}} e^{i(\mathbf{k}\cdot\mathbf{r}-\omega t)} \hat{\mathbf{e}}_{\mathrm{inc}}(\mathbf{k})$ for the electric field of the incident PW, we get

$$I^{\mathrm{inc}} = \frac{|U^{\mathrm{inc}}|^2}{2Z_0|k|} |\Re\{k_z\}| \,, \tag{2.60}$$

where Z_0 is the impedance of vacuum. The incident PW gives rise to the polychromatic outgoing field of the form given by Eq. (2.52b). Therefore, using Eq. (2.59), the space- and time-averaged intensities for the corresponding reflected and transmitted fields are written as

$$I^{\mathrm{ref}} = \sum_j I^{\mathrm{ref}}_j = \frac{1}{2Z_0} \sum_j \sum_{\mathbf{g}\alpha} \frac{1}{|k_j|} |U^{\mathrm{out}}_{j\mathbf{g}\alpha\downarrow}|^2 \, |\Re\{k_{z;j\mathbf{g}\alpha\downarrow}\}| \,, \tag{2.61a}$$

$$I^{\mathrm{tra}} = \sum_j I^{\mathrm{tra}}_j = \frac{1}{2Z_0} \sum_j \sum_{\mathbf{g}\alpha} \frac{1}{|k_j|} |U^{\mathrm{out}}_{j\mathbf{g}\alpha\uparrow}|^2 \, |\Re\{k_{z;j\mathbf{g}\alpha\uparrow}\}| \,, \tag{2.61b}$$

where the spatial integration for the reflected (transmitted) field is taken over an infinite planar area spatially below (above) the metasurface. Finally, we define the total reflectivity and transmissivity as

$$R = \frac{I^{\mathrm{ref}}}{I^{\mathrm{inc}}} = \sum_j R_j = \frac{\sum_j \sum_{\mathbf{g}\alpha} \frac{1}{|k_j|} |U^{\mathrm{out}}_{j\mathbf{g}\alpha\downarrow}|^2 \, |\Re\{k_{z;j\mathbf{g}\alpha\downarrow}\}|}{\frac{|U^{\mathrm{inc}}|^2}{|k|} |\Re\{k_z\}|} \,, \tag{2.62a}$$

$$T = \frac{I^{\mathrm{tra}}}{I^{\mathrm{inc}}} = \sum_j T_j = \frac{\sum_j \sum_{\mathbf{g}\alpha} \frac{1}{|k_j|} |U^{\mathrm{out}}_{j\mathbf{g}\alpha\uparrow}|^2 \, |\Re\{k_{z;j\mathbf{g}\alpha\uparrow}\}|}{\frac{|U^{\mathrm{inc}}|^2}{|k|} |\Re\{k_z\}|} \,, \tag{2.62b}$$

where R_j and T_j are the frequency-resolved reflectivities and transmissivities. The symbol R for reflectivity is not to be confused with the lattice vector $\mathbf{R}$. Note R and T can be written

as incoherent sums of R_j and T_j when $\omega \neq n\Omega/2$ ($n \in \mathbb{Z}$) for all $\mathbf{k}_\parallel$ values. For $\omega = n\Omega/2$, such a form holds only for $\mathbf{k}_\parallel \neq 0$. If $\omega = n\Omega/2$ and $\mathbf{k}_\parallel = 0$, the interference between the positive and negative frequencies leads to non-zero cross terms in the expressions of I^{ref} and I^{tra} (see Ref. [67] for more details). We utilize the discussed expressions of the reflectivity and transmissivity of the time-varying metasurfaces in Chapters 5 and 6.

Chapter summary

In this chapter, we have discussed the classical electromagnetic theory for time-varying media. We started by discussing Maxwell's equations and the relevant constitutive relations for linear, isotropic, homogeneous, and dispersive time-varying systems. Specifically, we derived the wave equation for such media. Next, using the technique of separation of variables, we solved the wave equation to obtain the corresponding eigenmodes. We also discussed various physical mechanisms that can be utilized to induce time-varying material properties. These include dynamic electron density and the fast optical Kerr effect. We provided the frequency-domain expressions of the corresponding material response functions.

In the second part of the chapter, we considered structured time-varying media. Specifically, we discussed the T- and S-matrix methods for time-varying spheres, monolayer metasurfaces, and multilayered metasurfaces. We provided a rigorous numerical formalism to implement these tools on a computer. We also discussed the computational steps for obtaining the physical observables such as the scattering cross section for the time-varying spheres, and reflectivity and transmissivity for time-varying metasurfaces.

This chapter sets the theoretical foundation for understanding various interesting physical phenomena arising from temporal modulation, which are discussed in the subsequent chapters.

3 | Photonics of time-varying media: a literature overview

In this chapter, we provide an overview of the photonics of time-varying media. We begin by highlighting the differences in wave scattering from spatial and temporal inhomogeneities (Sec. 3.1). We then review the recent advances in the field of time-varying metamaterials, highlighting the works dealing with the observation of time refraction, time reflection, and momentum bandgaps (Sec. 3.2). Finally, we conclude by examining the present challenges and outlining future directions in this rapidly evolving area of research (Sec. 3.3).

We remark that this chapter relies entirely on the works published in the literature prior to this thesis.

3.1. Distinction between spatial and temporal inhomogeneities

In this section, we compare how light interacts with spatial and temporal inhomogeneities. To begin with, we consider the difference between light scattering from spatial interfaces and temporal interfaces. Next, we extend the discussion to a comparison between a periodic arrangement of such interfaces, i.e., photonic space crystals and photonic time crystals. The discussion in this part is mostly done on phenomenological grounds with the purpose of developing an intuitive understanding of the underlying physics. Furthermore, for simplicity, we ignore the effects of material dispersion.

3.1.1. Spatial and temporal interfaces

The most basic configuration for light scattering is that of an interface. We begin with the interaction of light with a spatial interface (see Fig. 3.1(a)). Here, the permittivity of a medium abruptly changes at $z = z_{\text{int}}$ from ε_1 to ε_2. Furthermore, the medium is spatially uniform in the $x-$ and $y-$directions, and does not depend on time. For simplicity, we consider a monochromatic, $x-$polarized incident PW of the form $\mathbf{E}^{\text{inc}}(z,t) = U^{\text{inc}} e^{i(k_z^{\text{inc}} z - \omega_{\text{inc}} t)} \hat{\mathbf{x}}$ propagating along the $+z$ direction. It is well known that at a spatial interface, an incident PW splits into a reflected and a refracted PW [55]. The electric field corresponding to the reflected PW has the form $\mathbf{E}^{\text{ref}}(z,t) = U^{\text{ref}} e^{i(k_z^{\text{ref}} z - \omega_{\text{ref}} t)} \hat{\mathbf{x}}$, and that for the refracted PW has the form $\mathbf{E}^{\text{tra}}(z,t) = U^{\text{tra}} e^{i(k_z^{\text{tra}} z - \omega_{\text{tra}} t)} \hat{\mathbf{x}}$. Because the medium is invariant in time, the frequency of the PWs remains conserved as the light is scattered from the interface, i.e., $\omega_{\text{ref}} = \omega_{\text{tra}} = \omega_{\text{inc}}$. However, since the medium is spatially inhomogeneous, the wavevector of the PWs is not conserved. In particular, $k_z^{\text{ref}} = -k_z^{\text{inc}}$, and $k_z^{\text{tra}} = \sqrt{\frac{\varepsilon_2}{\varepsilon_1}} k_z^{\text{inc}}$ [55]. Clearly, the reflected PW, i.e., $\mathbf{E}^{\text{ref}}(z,t) = U^{\text{ref}} e^{i\left(-k_z^{\text{inc}} z - \omega_{\text{inc}} t\right)} \hat{\mathbf{x}}$ travels along the $-z$ direction, which is opposite to the propagation direction of the incident PW. On the other hand, the refracted PW, i.e., $\mathbf{E}^{\text{tra}}(z,t) = U^{\text{tra}} e^{i\left(\sqrt{\frac{\varepsilon_2}{\varepsilon_1}} k_z^{\text{inc}} z - \omega_{\text{inc}} t\right)} \hat{\mathbf{x}}$ travels along the $+z$ direction, which is the same as the propagation direction of the incident PW.

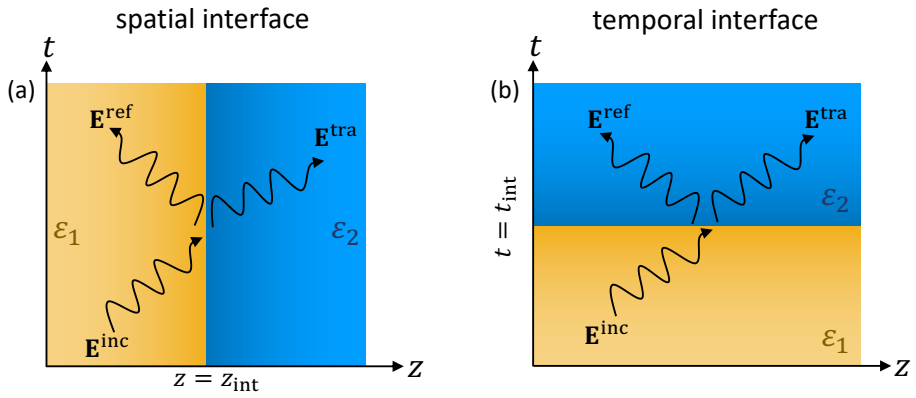


Figure 3.1.: **A conceptual illustration of light scattering at spatial and temporal interfaces.** (a) A spatial interface. Here, an incident PW splits into a reflected and a refracted PW. During the scattering process, the frequency of the PWs is conserved, while the wavevector can change. (b) A temporal interface. Here, an incident PW gives rise to a backward-propagating time-reflected PW and a forward-propagating time-refracted PW. During the scattering process, the wavevector of the PWs is conserved, while the frequency can change. Note that due to causality, the time-reflected PW travels backward in space (and not in time).

Dual to the spatial interface, a temporal interface refers to a configuration where the permittivity of a medium changes abruptly in time. As shown in Fig. 3.1(b), we investigate a medium whose permittivity changes from ε_1 to ε_2 at time $t = t_{\mathrm{int}}$. Notably, the medium is spatially invariant in all three dimensions. For simplicity, we consider a $+z-$propagating incident PW of the same form as before, which is present in the medium for $t < t_{\mathrm{int}}$. Upon scattering from the temporal interface, the incident PW again splits into a reflected and a refracted PW [21, 26]. However, due to the spatial homogeneity, the wavevector of the PWs cannot change during such a scattering event, i.e., $k_z^{\mathrm{ref}} = k_z^{\mathrm{tra}} = k_z^{\mathrm{inc}}$. On the other hand, since the system is time-varying, the frequency of the PWs can change. To arrive at the expression of the allowed frequencies in the medium for $t > t_{\mathrm{int}}$, we use the relation $\varepsilon_1\omega_{\mathrm{inc}}^2/c_0^2 = \varepsilon_2\omega_2^2/c_0^2$. Such a relation follows from the invariance of the wavevector before and after the interface. Consequently, the scattered PWs can possess the frequencies $\omega_2 = \pm\sqrt{\frac{\varepsilon_1}{\varepsilon_2}}\omega_{\mathrm{inc}}$. We define $\omega_{\mathrm{ref}} = -\sqrt{\frac{\varepsilon_1}{\varepsilon_2}}\omega_{\mathrm{inc}}$, and $\omega_{\mathrm{tra}} = +\sqrt{\frac{\varepsilon_1}{\varepsilon_2}}\omega_{\mathrm{inc}}$. Clearly, the negative-frequency PW, i.e., $\mathbf{E}^{\mathrm{ref}}(z,t) = U^{\mathrm{ref}}e^{i\left(k_z^{\mathrm{inc}}z+\sqrt{\frac{\varepsilon_1}{\varepsilon_2}}\omega_{\mathrm{inc}}t\right)}\hat{\mathbf{x}}$, travels in the spatial direction opposite to the incident PW; hence it is termed a time-reflected wave. Here, although the wavevector remains directed along $+z$, the negative frequency reverses the direction of the phase velocity of the PW, so that the time-reflected PW propagates along $-z$. On the other hand, the positive-frequency PW, i.e., $\mathbf{E}^{\mathrm{tra}}(z,t) = U^{\mathrm{tra}}e^{i\left(k_z^{\mathrm{inc}}z-\sqrt{\frac{\varepsilon_1}{\varepsilon_2}}\omega_{\mathrm{inc}}t\right)}\hat{\mathbf{x}}$ travels in the same spatial direction as the incident PW ($+z$ direction); therefore, it is termed a time-refracted wave.

3.1.2. Photonic space crystals and photonic time crystals

In the previous subsection, we discussed individual spatial and temporal interfaces. An interesting configuration is attained by considering a periodic arrangement of these interfaces.

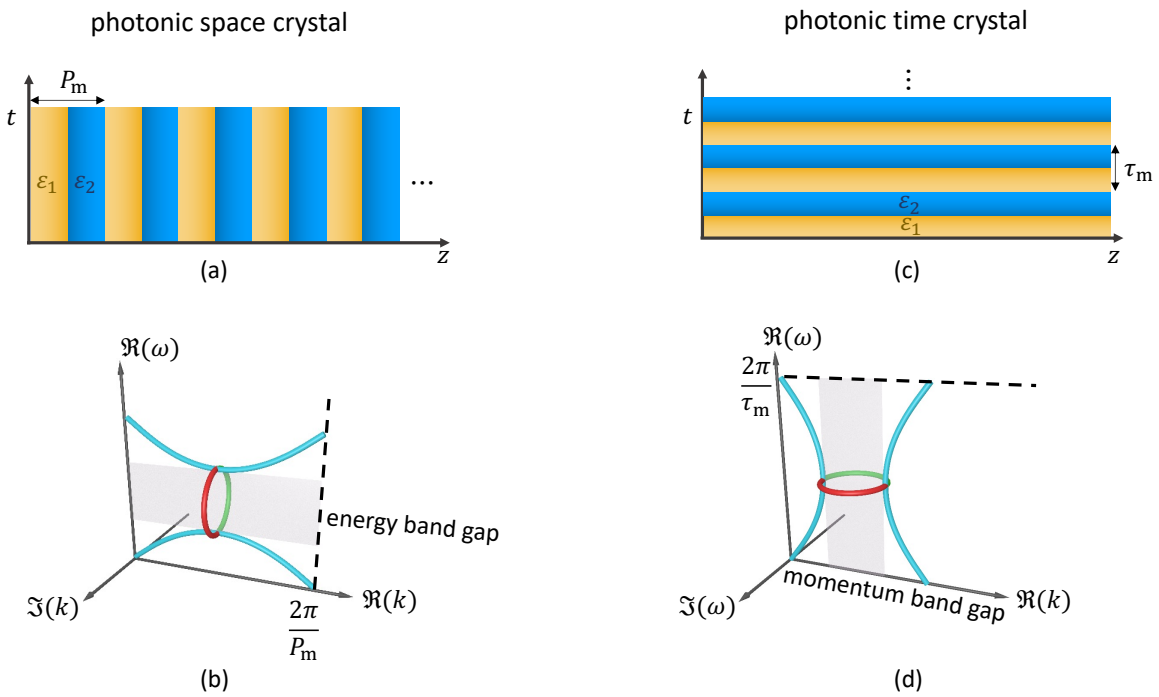


Figure 3.2.: **Photonic space crystals and photonic time crystals.** (a) A photonic space crystal (PSC) formed by alternating the permittivity of a medium between ε_1 and ε_2 with the period P_m along the spatial coordinate z. (b) The energy (frequency) bandgap supported by the PSC. Inside such a gap, eigenmodes with complex wavenumber k exist, corresponding to spatially evanescent modes. Specifically, the modes with $\Im(k) > 0$ decay along the $+z$, and those with $\Im(k) < 0$ decay along the $-z$ direction. (c) A photonic time crystal (PTC) formed by alternating the permittivity of a medium between ε_1 and ε_2 with the period τ_m as a function of time. (d) The momentum (wavenumber) bandgap supported by the PTC. Inside such a gap, eigenmodes with complex frequency ω exist. The mode with $\Im(\omega) > 0$ exponentially grows, while that with $\Im(\omega) < 0$ exponentially decays with time. Note that the sizes of the spatial and temporal Brillouin zones (BZ) are $2\pi/P_m$ and $2\pi/\tau_m$, respectively. This figure has been adapted with permission from [P6]. © Optica Publishing Group.

The system obtained by a periodic arrangement of spatial interfaces is known as a photonic space crystal (PSC) [30, 72, 73]. Note that, for a long time, such structures were simply referred to as photonic crystals [30]. However, to distinguish spatially periodic structures from their temporal counterparts, we will explicitly refer to them as photonic space crystals. On the other hand, the system formed by a periodic arrangement of temporal interfaces is called a photonic time crystal (PTC) [22, 74].

In Fig. 3.2(a), we show a PSC. Here, the permittivity of the medium alternates between ε_1 and ε_2 as a function of z with the period P_m. Applying the Bloch theorem, the bandstructure of the PSC is obtained by folding the bandstructure of the underlying spatially homogeneous medium along the wavenumber axis (see Fig. 3.2(b)) [30]. At the crossing of the folded bands in $\omega - k$ space, energy (frequency) bandgaps are opened. Within these gaps, the wavenumber k becomes complex, resulting in spatially evanescent modes. Assuming the PW convention $e^{i(kz-\omega t)}$ for the modal fields, the modes with $\Im(k) > 0$ decay along the $+z$ direction, and those with $\Im(k) < 0$ decay along the $-z$ direction. The key physical consequence of the complex wavenumber is that PSCs do not support propagating modes within the energy bandgap.

In the dual case, by a periodic repetition of the temporal interfaces, PTCs are formed (see Fig. 3.2(c)). Here, the permittivity of the medium alternates between ε_1 and ε_2 as a function of time t with the period τ_m. Applying the Floquet theorem, the bandstructure of the PTC can be obtained by folding the bandstructure of the underlying static medium along the frequency axis (see Fig. 3.2(d)) [24]. At the crossing of the folded bands in the $\omega - k$ space, momentum (wavenumber) bandgaps are opened. These gaps possess eigenmodes with complex frequencies. In the assumed time convention, the modes with $\Im(\omega) > 0$ have exponentially growing, while those with $\Im(\omega) < 0$ have exponentially decaying field amplitudes as a function of time. Since the PTCs do not conserve energy (they do not constitute a passive system as work is permanently done to change the permittivity), the exponentially growing modes inside the momentum bandgaps can also be excited. Physically, once the PTCs are tuned to the momentum bandgap configuration, an incident PW can excite modes with both $\Im(\omega) > 0$ and $\Im(\omega) < 0$. Due to their amplifying nature, the modes with $\Im(\omega) > 0$ dominate the total output response. Therefore, the system is driven into a temporal instability, and an exponentially growing output field is obtained as a function of time. The energy of this exponentially growing field comes at the expense of a depleting pump, which acts as the source of time modulation in the PTCs [24].

So far, we have focused on the theoretical aspects of time-varying media to explain the underlying physics. In the following, we discuss several works that demonstrated various unique time-modulation-induced phenomena in experiments.

3.2. Experimental demonstration of time-varying metamaterials

In this section, we review selected works that experimentally demonstrated various exotic phenomena in time-varying metamaterials. In particular, we discuss the observation of time refraction, time reflection, and momentum bandgaps.

3.2.1. Observation of time refraction

Time refraction has been discussed in various works in the literature [27, 34–36, 75]. In particular, the authors in Ref. [34] observed time refraction experimentally using indium tin

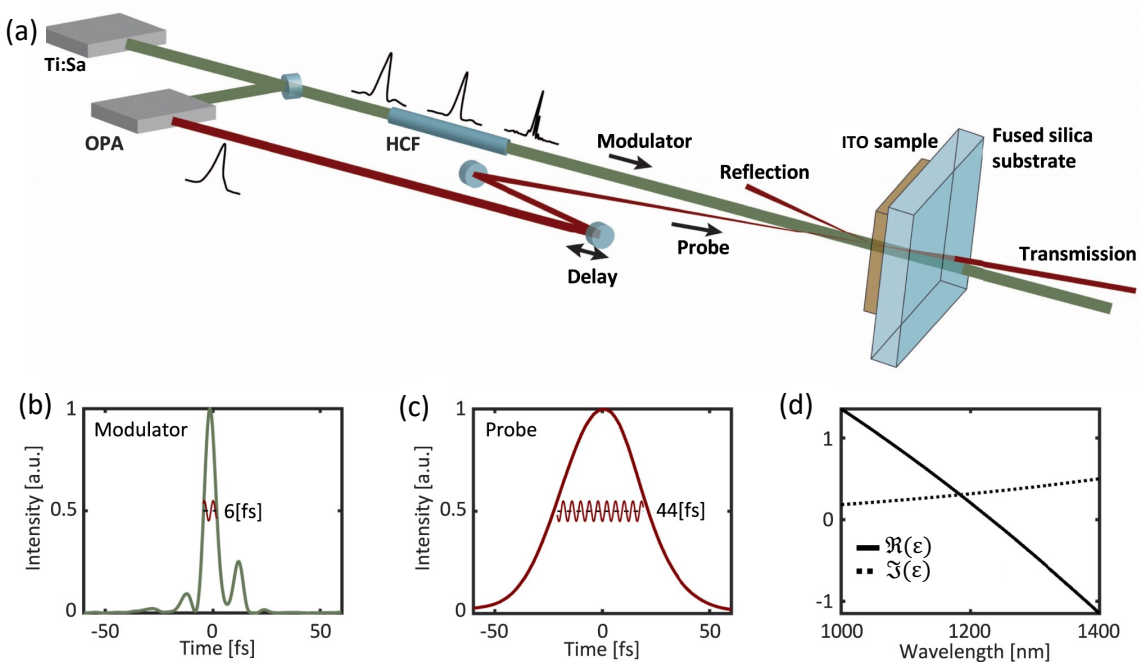


Figure 3.3.: **A modulator-probe setup to observe time refraction**. (a) The Ti:Sa laser produces an 800 nm 30 fs pulse which goes through an HCF. The HCF compresses the pulse to 6 fs. This compressed pulse modulates the refractive index of the ITO sample. A part of the pulse from the Ti:Sa laser is directed to an OPA, which downconverts it to a 1225 nm central wavelength. This downconverted pulse is used as the probe which experiences the time-varying refractive index. (b), (c) The intensity of the modulator and probe pulses as a function of time, respectively. (d) The real and imaginary parts of the permittivity of unmodulated ITO as a function of wavelength. We note that the ENZ point of ITO occurs near 1225 nm, which is also the central wavelength of the probe. This figure has been adapted from [34]. © The authors, licensed under CC BY 4.0.

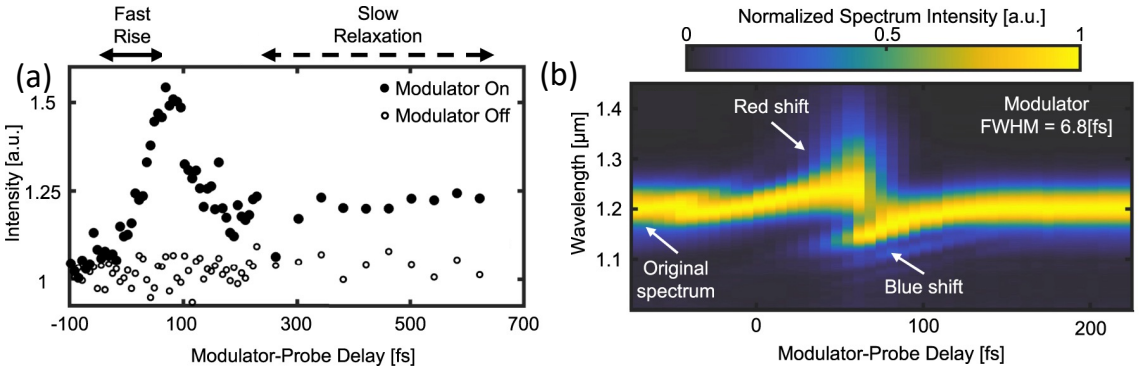


Figure 3.4.: **Observable effects due to time refraction**. (a) The intensity of the spatially transmitted probe field from the ITO sample as a function of modulator-probe delay. Here, as the modulator is turned on, the transmitted intensity undergoes a time-dependent change. Initially, due to a fast rise of the refractive index of ITO, the transmitted intensity increases. Then, as the refractive index relaxes back, the transmitted intensity also relaxes to its original value. (b) The normalized intensity spectrum of the spatially transmitted probe field as a function of wavelength and modulator-probe delay. Initially, the probe undergoes a red shift due to a rise in the refractive index of ITO. Thereafter, the probe experiences a blue shift due to a fall in the refractive index. Finally, the probe's spectrum approaches the initial configuration as the refractive index relaxes back to its original value. This figure has been adapted from [34]. © The authors, licensed under CC BY 4.0.

oxide (ITO) at near-infrared frequencies. The following discussion is based entirely on the results originally reported in that work.

The experimental setup used to observe time refraction is shown in Fig. 3.3(a). It consists of a modulator-probe type configuration. Here, a titanium sapphire (Ti:Sa) laser emits a 30 fs pulse at a central wavelength of 800 nm, which is compressed down to a 6 fs pulse using an argon-filled hollow-core fiber (HCF) (see Fig. 3.3(b)). The compressed pulse modulates the permittivity (and hence the refractive index) of the ITO sample, onto which it is directed. The power density of the modulating pulse is 2 TW/cm^2. A part of the pulse emitted by the Ti:Sa laser is fed to an optical parametric amplifier (OPA) which downconverts the pulse to a central wavelength of 1225 nm. This downconverted pulse acts as the probe. It has a temporal width of 44 fs. The power density of the probe pulse is five orders of magnitude lower as compared to the modulating pulse (see Fig. 3.3(c)). Moreover, the single cycle of the probe pulse is merely 4.1 fs long. Clearly, the modulator changes the refractive index of ITO at a time scale comparable to a single cycle of the probe (see Fig. 3.3(b)). Notably, the central wavelength of the probe is taken at the ENZ point of ITO to enhance the relative refractive index change $\Delta n/n$ (see Fig. 3.3(d)). At that wavelength, the modulator-induced refractive index change of ITO is $\Delta n \sim 0.5$.

In the experiment, the intensity of the spatially transmitted probe is measured. Such an intensity carries the signature of the time-varying refractive index of the ITO sample. We show the transmitted intensity as a function of modulator-probe delay in Fig. 3.4(a). We observe that when the modulator is turned on, the intensity experiences a fast rise. Such a behavior comes from the fast increase of the refractive index of ITO. Thereafter, the intensity relaxes back slowly toward its initial value. Such a relaxation process is attributed to the slow relaxation of the ITO refractive index to its original value. Physically, the modulator drives the free electrons of ITO to higher energies within the conduction band, increasing its

refractive index. Thereafter, these electrons relax back to their initial energies. However, the relaxation process is much slower than the excitation process. Therefore, the refractive index relaxes back slowly.

Next, we show the normalized intensity spectrum of the transmitted probe as a function of wavelength and modulator-probe delay (see Fig. 3.4(b)). We observe that first, the transmitted spectrum undergoes a red shift and then it experiences a blue shift. Finally, it relaxes back to the initial spectral configuration. Such a behavior is expected, as initially the refractive index of ITO experiences an increase, and hence, energy is drawn from the probe, causing a red shift. Thereafter, because the refractive index decreases during the relaxation process, the probe gains energy and experiences a blue shift. For a sufficiently long modulator-probe delay, the probe returns to its original spectral configuration, as the refractive index has completely relaxed back to its initial value. Note that the observed red and blue shifts are the direct consequences of the frequency conversion caused by time refraction (see Subsec. 3.1.1).

We remark here that there are more works that have observed time refraction experimentally. For example, in Ref. [35], a similar experimental setup was used but with Cadmium Oxide (CdO) at mid-infrared frequencies. On the other hand, the authors in Ref. [36] showed a broadband frequency translation of a probe pulse at near-infrared frequencies using an ITO film, which was attributable to time refraction. Furthermore, time refraction was also observed at elastic and acoustic frequencies in Ref. [76] and Ref. [77], respectively.

3.2.2. Observation of time reflection

At a temporal interface, light can also undergo time reflection. However, observing time reflection has proven to be a comparatively difficult task at optical frequencies. Similar to spatial reflection, the strength of the time-reflected signal is proportional to the modulation amplitude of the refractive index [21]. Furthermore, it requires refractive index changes at sub-cycle time scales. Since achieving strong refractive-index modulation at optical frequencies is highly challenging, the resulting time-reflected signals are typically very weak and difficult to detect.

Nevertheless, in Ref. [44], the authors used a transmission line (TL) to demonstrate time reflection at microwave frequencies. The used experimental setup is shown in Figs. 3.5(a)–(b). It consists of an array of capacitors arranged along with individual switches for each capacitor (see Fig. 3.5(c) for the circuit diagram). As the switches are closed at time $t = t_{\text{int}}$, the effective impedance of the TL instantaneously decreases, creating a temporal interface (see Fig. 3.5(d)). Such a temporal interface gives rise to a time-reflected signal.

To observe time reflection, the voltage $V_1(t)$ in the input port of the TL is measured as a function of time (see Fig. 3.5(e)). Here, up to time $t \approx 60$ ns, we observe the initial input voltage. Then, as the switches in the TL are closed at $t = t_{\text{int}} \approx 60$ ns, after about 3 ns, a backward-propagating signal is measured as it enters the input port. This signal is the time-reflected signal. After approximately 140 ns, another signal enters the input port, corresponding to the time-refracted signal. After propagating to the end of the TL, this signal is spatially reflected at the mismatched termination. Here, we note that during time reflection, the signal is time-reversed (i.e., $t \to -t$). Therefore, the receiver at the input port registers the features of the reflected signal in a reversed order as compared to how it was originally sent. Conversely, during spatial reflection, the signal undergoes a parity inversion

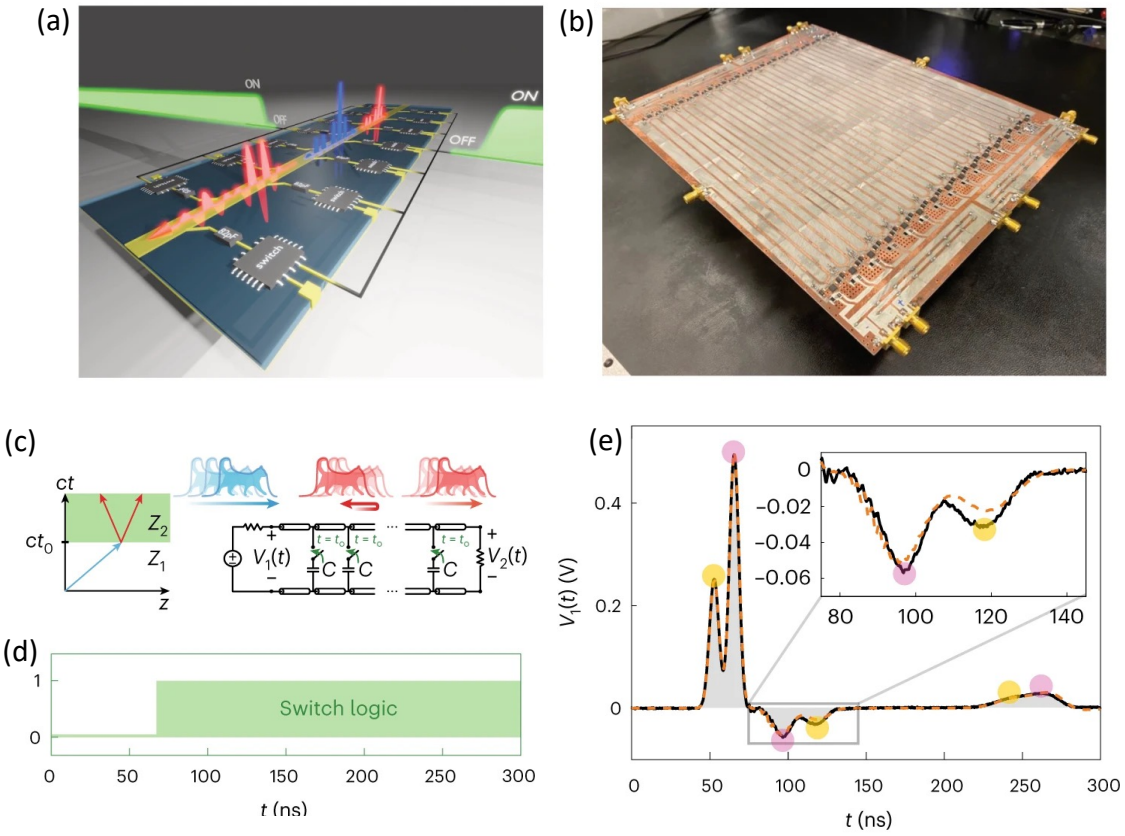


Figure 3.5.: **Time reflection at microwave frequencies**. (a) A transmission line (TL) formed by an array of capacitors to perform the time reflection experiment. (b) Photograph of the fabricated TL. (c) The circuit diagram of the TL. We note that each capacitor arm consists of a switch. (d) The switch logic used in the experiment. At $t = t_{\text{int}} \approx 60$ ns, all the switches are closed, which decreases the effective impedance of the TL instantaneously. (e) The measured voltage $V_1(t)$ as a function of time in the input port. Up to time $t \approx 60$ ns, the initial input signal appears. Then, after about 3 ns of closing the switches, the time-reflected signal arrives at the input port. Finally, after $t = 140$ ns, the time-refracted signal, after being spatially reflected at the TL termination, also arrives at the input port. Note that the inset in (c) shows the change of the impedance from Z_1 to Z_2 as the switches are closed. This figure has been adapted from [44], with permission from Springer Nature.

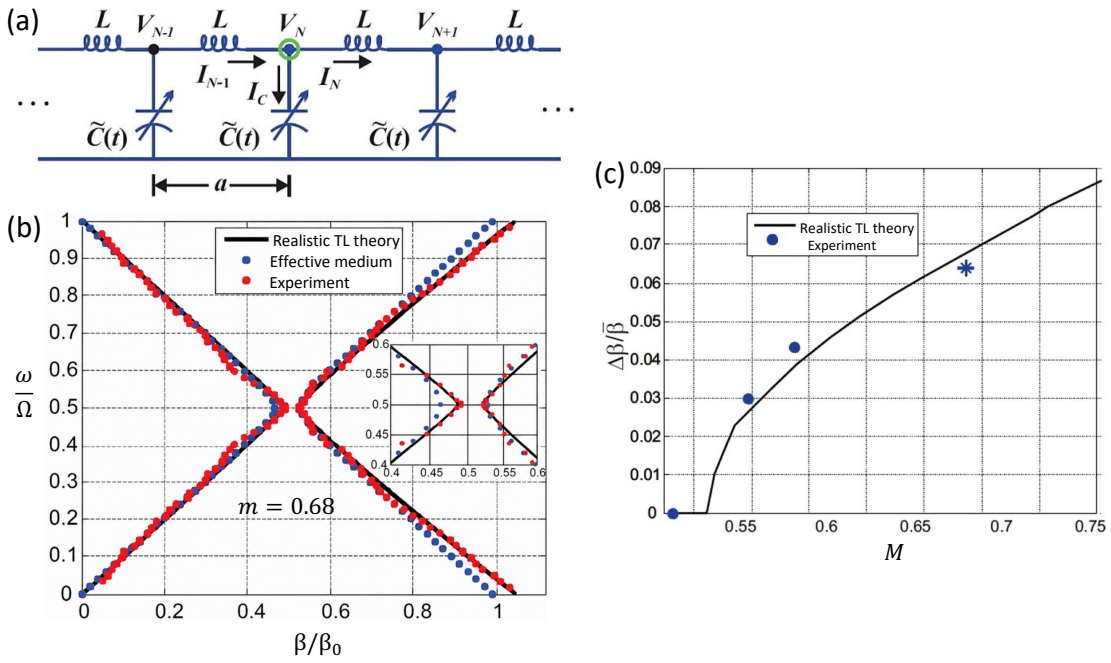


Figure 3.6.: **Observation of the momentum bandgap**. (a) A transmission line (TL) made from an array of LC circuits. Here, the capacitance $\tilde{C}(t)$ is a periodic function of time with modulation frequency Ω and amplitude M. In the effective medium limit, the TL mimics a homogeneous system that has a time-periodic permittivity. (b) The bandstructure of the TL measured experimentally (red dots), calculated using effective medium theory (blue dots), and calculated using the realistic TL theory (black curves). We clearly observe the existence of a momentum bandgap. (c) The variation of the gap-midgap ratio $\Delta\beta/\bar{\beta}$ as a function of the modulation amplitude M. There exists a threshold M due to the resistive losses to open a bandgap. Furthermore, beyond the threshold, $\Delta\beta/\bar{\beta}$ increases with M. Note that β_0 is a normalization constant that depends on the system parameters. Adapted from [45], with the permission of AIP Publishing.

(i.e., $z \to -z$). Therefore, the features of the reflected signal are observed in the same order as they were initially sent.

We remark here that the research on observing time reflection is rapidly growing. Apart from the microwave platform discussed here, time reflection was also observed in the water wave and elastic wave regimes in Ref. [43] and Ref. [76], respectively. At optical frequencies, a recent preprint has shown such an effect using CdO [33]. On the theoretical front, the authors in Ref. [78] showed that structural resonances of a dielectric sphere array can be used to strongly enhance the time-reflected field. Furthermore, the authors in Ref. [79] showed that time reflection can be enhanced by temporally modulating the permittivity of a spatial interface near its critical angle.

3.2.3. Observation of momentum bandgaps

Similar to time reflection and time refraction, momentum bandgaps have also been experimentally observed. In Ref. [45], the authors used a TL to mimic a PTC configuration and illustrated that such a system supports momentum bandgaps at microwave frequencies.

The circuit diagram of the TL is shown in Fig. 3.6(a). It consists of an array of LC circuits. Furthermore, by means of varactors, a time-varying capacitance $\tilde{C}(t)$ is realized in the TL. The varactors are fed with identical external voltage $V_\Omega(t)$. Specifically, the external voltage is such that $\tilde{C}(t)$ is a periodic function of time with the modulation frequency Ω and amplitude M. The distance between the time-varying capacitors is a. Furthermore, the nodal signal voltage in the circuit has a traveling wave form given by $v_N(t) = v(t)e^{i\beta Na}$. In the effective medium limit, i.e., $\beta a/2 \ll 1$, the TL mimics a homogeneous medium with a time-periodic permittivity.

Next, using the output voltage of the TL, the experimental bandstructure was extracted (see red dots in Fig. 3.6(b)). We find that, expectedly, the TL supports a momentum bandgap. This measured bandstructure is also compared with the realistic TL theory (black curves in Fig. 3.6(b)), and effective medium theory (blue dots in Fig. 3.6(b)). We observe an excellent agreement of the measured bandstructure with these theoretical predictions.

An important property of the momentum bandgaps is that their size increases with the modulation amplitude M. This property was experimentally verified using the TL setup. The variation of the gap-midgap ratio $\Delta\beta/\bar{\beta}$ is shown as a function of M in Fig. 3.6(c). Expectedly, it is observed that $\Delta\beta/\bar{\beta}$ increases with M (blue dots). Furthermore, it can also be seen that there exists a threshold M for opening a bandgap. Such a threshold M exists as a sufficiently large modulation is needed to overcome the resistive losses in the TL circuit. These experimental results also match well with the theoretical prediction provided by the realistic TL theory (black curve).

Another notable work that showed the observation of momentum bandgaps using TL is Ref. [80]. Furthermore, the characteristic time-modulation-induced parametric amplification was shown at microwave frequencies using an LC circuit-based metasurface in Ref. [81], and at optical frequencies using the Kerr effect in ITO in Ref. [56].

We remark here that the momentum bandgaps at frequencies higher than the microwave frequencies have yet to be observed. The observation of such gaps requires a strong periodic modulation of the material properties. Fulfilling such a strong modulation amplitude requirement at higher frequencies (such as in the optical regime) is very challenging [82]. Nevertheless, solutions such as using structural resonances [83] and spatial dispersion [84] have been proposed to relax this strong modulation amplitude requirement.

3.3. Current and future challenges

While many physical phenomena related to the photonics of time-varying media have been theoretically investigated and experimentally realized, there exists a plethora of challenges that need to be overcome for the further growth of this research domain. They are summarized in the following and serve, at least partially, as a motivation for the thesis.

High modulation strength and frequency requirement: It has been demonstrated that to observe many exotic phenomena in time-varying metamaterials, a strong modulation amplitude of the material properties is required together with a high modulation frequency. Fulfilling these two requirements at optical frequencies is challenging with the current state of the art [82, 85]. For instance, while the ENZ materials can show large step-like changes of the refractive index ($\Delta n/n > 100\%$), due to the slow relaxation times of their conduction band electrons, it is not possible to sustain a time-periodic oscillation in them [31]. Moreover, in dielectrics, using the fast optical Kerr effect can induce periodic refractive index changes

at optical frequencies. However, the attainable modulation amplitude remains rather low ($\Delta n/n \leq 1\%$) due to the weak third-order nonlinearities [39, 86]. Therefore, it becomes very important to find materials or tailored systems that can be utilized to induce strong changes in the refractive index at ultrafast rates reaching hundreds of THz.

Combining spatial and temporal periodicities: Time-varying metamaterials promise to control light in four dimensions (4D), i.e., three spatial dimensions and one temporal dimension [25]. However, a large part of the recent work has focused on spatially homogeneous time-varying systems [21]. Therefore, there is an urgent need to study configurations formed by combining the spatial and temporal periodicities [29, 37, 87–90]. Examples involve structures made from finite-sized time-varying meta-atoms [41, 83, 84, 91–93], those with a traveling-wave type modulation [89, 94–97], and those having a space-time moving aperture [37]. Admittedly, studying a spatiotemporal structure is a challenging task both theoretically and experimentally. On the theoretical front, such a structure introduces a higher degree of complexity in the constitutive relations. On the other hand, in experiments, spatially structuring a material reduces its thermal damage threshold considerably [98, 99]. Therefore, creating large refractive index changes using strong optical pumps becomes difficult. Nevertheless, using structural resonances allows for observing pronounced effects of time modulation despite weak amplitudes [83, 92]. Such a concept has been borrowed from the field of resonant nanophotonics [15]. A careful application of other well-known concepts to time-varying metamaterials may bring truly 4D geometries within reach.

Distinguishing conventional nonlinear optics from time-varying optics: It has been well established that realizing time-varying material properties at optical frequencies requires harnessing the nonlinearities of the materials [31, 57, 59, 100]. This raises a natural question of how time-varying optics is different from conventional nonlinear optics. At the level of observable effects, there are similarities. For example, both the time-varying metamaterials and conventional nonlinear systems show parametric amplification, frequency conversion, and nonreciprocity. At the same time, the physical mechanisms of these effects in temporal metamaterials differs from those in conventional nonlinear devices. For instance, for parametric amplification, the phase-matching condition is satisfied in time rather than in space in the temporal metamaterials [57, 101]. Furthermore, owing to the modes with conserved k, time-varying metamaterials exhibit momentum bandgaps [24]. The existence of such bandgaps has not been reported in conventional nonlinear devices. These similarities and distinctions hint at the need for comprehensive studies that clearly separate the conventional nonlinear effects from the time modulation-induced effects. Such studies will serve as guidelines while identifying research gaps to study novel optical phenomena.

Arbitrarily shaped 3D meta-atoms: To fully harness the capabilities of metamaterials, being able to study arbitrarily shaped meta-atoms is crucial. In the static domain, there exists a plethora of full-wave simulation tools to numerically model such complex meta-atoms [64, 102, 103]. However, these tools are not well-optimized for the time-varying case. Therefore, it becomes computationally very expensive to obtain the scattering response of 3D time-varying meta-atoms. There have been very few studies that attempted to solve this issue. For example, the extended boundary condition method (EBCM) was developed for arbitrarily shaped 3D time-varying objects [P13]; quasi-normal mode (QNM) theories were developed to obtain the response of time-varying meta-atoms from the QNMs of their static counterparts [104–107]; perturbative Born theory was used in [108]; finite-difference time-domain (FDTD) techniques were utilized in [101]. While these theoretical studies represent important first steps in efficiently modeling complex temporal meta-atoms, more effort is needed in this

direction. Having access to meta-atoms with diverse shapes will allow us to explore exciting physical phenomena such as time-varying chirality [109, 110], as well as to engineer their multipolar optical response [111].

Chapter summary

In this chapter, we provided a literature overview of the photonics of time-varying media. We started by comparing the scattering of light from spatial and temporal interfaces. Thereafter, we discussed the physics of photonic space crystals and photonic time crystals. We found that the former host energy (frequency) bandgaps, while the latter host momentum (wavenumber) bandgaps. Next, we discussed the experimental observation of time refraction, time reflection, and photonic time crystals based on various published works. Finally, we closed the chapter by outlining the current challenges and future opportunities in the field of time-varying metamaterials.

4 | Expanding momentum bandgaps in PTCs

Photonic time crystals (PTCs) are formed by periodically modulating the material properties (such as the permittivity) of the underlying media as a function of time [22]. PTCs exhibit momentum bandgaps as their hallmark feature [24]. Inside such gaps, eigenmodes with complex frequency ω exist. In the time convention $e^{-i\omega t}$, the modes with $\Im(\omega) > 0$ lead to the amplification of the input light fields as a function of time (see Subsec. 3.1.2).

PTCs have been recently demonstrated at microwave frequencies due to the availability of fast variable electronic and radio frequency (RF) components [45, 80, 81]. However, experimentally realizing PTCs at optical frequencies is a major challenge [82]. Attaining the required temporal modulation is extremely demanding as PTCs require permittivity variation at twice the oscillation frequency of light. Furthermore, a strong modulation, with relative permittivity change approaching 100%, is simultaneously needed when considering homogeneous PTCs. Using hot-electron nonlinearities, ENZ materials can support such a strong modulation. However, due to the slow relaxation time of the heated electrons, it is not possible to sustain a *periodic* time-variation in such media at hundreds of THz [34, 59]. On the other hand, the fast optical Kerr effect can induce a periodic temporal modulation of the permittivity at optical frequencies [56]. However, the relatively small third-order nonlinear susceptibility, $\chi^{(3)}$, of most known materials limits the achievable relative permittivity change to below 1% at realistic pump intensities [39, 57, 61]. In theory, the pump intensities can be increased to attain stronger modulation, but obtaining noticeable PTC features requires intensities on the order of TW/cm^2. Such high intensities are typically above the thermal damage threshold of the Kerr media [82, 112].

To overcome the aforementioned challenges in realizing PTCs, we turn to the nanophotonic toolbox. We harness structural resonances to enhance light-matter interactions in PTCs. Specifically, we consider metasurface-based PTCs that are formed by periodically arranging spatially structured meta-atoms made from a time-varying material in a 2D lattice. The constituent meta-atoms are designed to support high-Q resonances thanks to the spatial structuring. Exploiting the resonant confinement of light, we observe noticeable momentum bandgaps in the considered structures even for weak permittivity modulation. The corresponding modulation can in principle be realized in platforms based on low-loss dielectrics, utilizing the optical Kerr effect.

This chapter is structured as follows: in Sec. 4.1, we introduce the general physical concept of using resonances to expand the momentum bandgaps while maintaining a weak temporal modulation. In Sec. 4.2, we outline the numerical steps needed to compute the bandstructures of time-varying metasurfaces using their T-matrices. In Sec. 4.3, we describe the utilization of the Mie resonances of the meta-atoms to achieve noticeable bandgaps at weak permittivity modulation. We demonstrate the emergence of bandgaps for both evanescent and propagating PWs. Finally, in Sec. 4.4, we explore the exploitation of the quasi-bound states in the continuum (qBICs) of the meta-atoms to attain such bandgaps at even weaker modulation.

The content of this chapter is based on our works in [P1, P4].

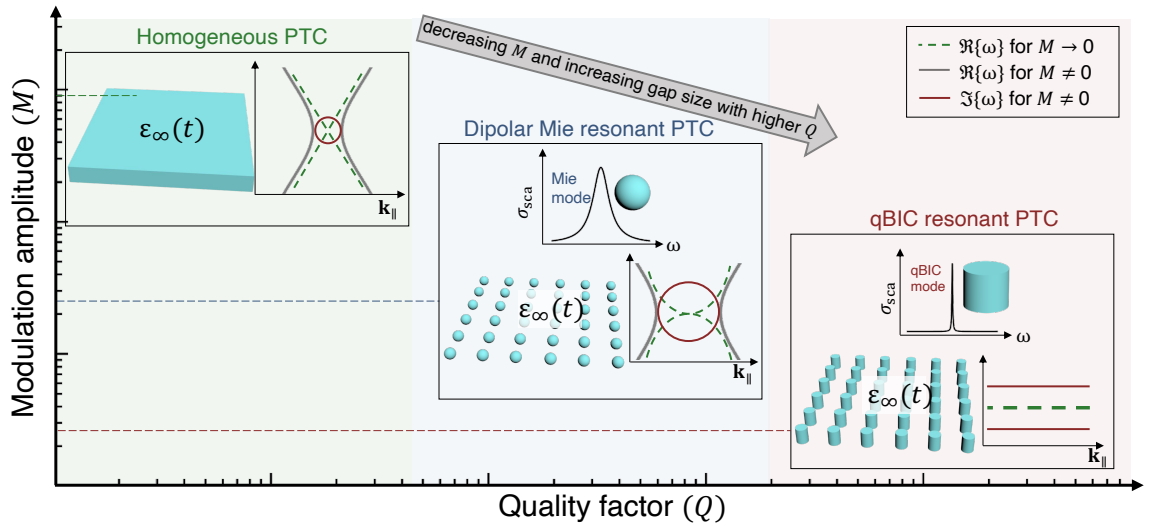


Figure 4.1.: **A conceptual illustration.** The variation of the modulation amplitude (M) to open momentum bandgaps in various PTC implementations with the Q-factor (Q) of the resonances of the underlying static media. As Q increases, the required M to open a bandgap reduces. Here, we show a spatially homogeneous PTC (left column), a metasurface-based PTC made from Mie resonant meta-atoms (central column), and another metasurface-based PTC made from qBIC-supporting meta-atoms (right column). The resonances of the static meta-atoms are depicted by plotting their scattering cross sections σ_{sca} as a function of the frequency ω. Furthermore, the bandstructures of the PTCs in both the temporal empty lattice approximation (i.e., $\Omega \neq 0$, $M \to 0$) and the time-varying cases (i.e., $\Omega \neq 0$, $M \neq 0$) are provided. This figure has been adapted with permission from [P1]. © The authors, licensed under CC BY 4.0.

4.1. Physical concept

We illustrate the physical concept of expanding momentum bandgaps using resonances in Fig. 4.1. For simplicity, we ignore the effects of material dispersion. Therefore, the background permittivity of the underlying media can be written as $\varepsilon_\infty(t) = 1 + \chi_{\infty,\text{st}}[1 + M\cos(\Omega t)]$ (see Eq. (2.26)). For a spatially homogeneous medium, in the static case, the dispersion relation is a straight line. The periodic time modulation of the background permittivity, in a temporal empty lattice approximation (i.e., $\Omega \neq 0$, $M \to 0$), causes a folding of the bandstructure along the frequency axis. Specifically, at $\Re(\omega)/\Omega = 0.5$, the modes of the original and the folded bands form a crossing. When the modulation amplitude becomes finite (i.e., $M \neq 0$), these crossed bands interact with each other, forming a momentum bandgap. However, because the bands of the static medium are linear, the interacting modes remain confined to a very narrow momentum range. Therefore, the size of the resulting momentum bandgap is extremely small even for substantial modulation amplitudes (i.e., $M \sim 100\%$).

To enhance the size of the bandgap, the medium can be spatially structured, and the resonances of the resulting system can be exploited. A prototypical example of such a resonance is that of a dipolar Mie resonance. It occurs when a multipole moment inside a spatially finite scatterer is resonantly excited. Arranging such a resonant Mie scatterer in a lattice, the bands of the resulting static metasurface experience a strong curvature due to the resonant modulation of the otherwise linear dispersion. Switching on the time

modulation with the modulation frequency approximately twice the Mie resonance frequency, the dispersion relation folds around this curved band. In this case, the modes interact over a much larger momentum range to form a bandgap than in the homogeneous PTC (see Fig. 4.1). Consequently, a larger momentum bandgap is obtained. Furthermore, the required modulation amplitude is also lowered. Such a behavior arises because the high Q-factor of the Mie resonance extends the duration for which light interacts with time-varying matter, leading to strong effects of temporal modulation despite low M.

While the dipolar Mie resonance assists in enhancing the gap size as compared to the homogeneous PTCs, the concept of resonantly enhanced momentum bandgaps can be pushed to extremes by using even higher-Q resonances. A particularly interesting nanophotonic resonance is a qBIC. Such a resonance, in an ideal case, can possess diverging Q-factors (i.e., $Q \to \infty$) and therefore can drive the enhancement of light-matter interactions to its limits. We use the 3D finite meta-atoms that possess such qBICs in the static case. Upon placing them in the metasurface lattice, an extremely flat photonic band emerges (see Fig. 4.1). Now, choosing the modulation frequency at twice the frequency of the flat band, a wide momentum bandgap is obtained at vanishingly small M that covers the entire BZ. Using this understanding of exploiting the resonances of structured media, one can pave the way for realistic PTCs at perturbative modulation amplitudes.

In the following section, we discuss the computational method to evaluate the bandstructures of time-varying metasurfaces using their T-matrices.

4.2. Bandstructure calculation using the T-matrix method

As this chapter relies on the demonstration of noticeable momentum bandgaps, here, we outline the steps to numerically compute the bandstructures of time-varying metasurfaces. We obtain the bandstructures using the effective T-matrix of the metasurface (see Eq. (2.41)). For calculating the spectral and momentum location of an eigenmode, we require a non-zero scattered field in the absence of an incident excitation, i.e., $\mathbf{A}_{\text{sca}} \neq 0$ for $\mathbf{A}_{\text{inc}} = 0$ [113]. Using Eqs. (2.41) and (2.44), we find that such a requirement is fulfilled if the following holds

$$\underbrace{\left|\mathbf{I} - \mathbf{T}_0(\omega) \sum_{\mathbf{R}\neq 0} \mathbf{C} \mathrm{e}^{i\mathbf{k}_\parallel \cdot \mathbf{R}}\right|}_{\left|\mathbf{\Psi}\left(\omega, \mathbf{k}_\parallel\right)\right|} = 0\,. \tag{4.1}$$

Therefore, those (ω, $\mathbf{k}_\parallel$) pairs that satisfy Eq. (4.1) characterize the spectral and momentum location of an eigenmode in the parameter space. Here, due to the radiative and material losses of the metasurface as well as the gain/loss induced by the time modulation, Eq. (4.1) is satisfied for complex-valued ω. Furthermore, the condition in Eq. (4.1) is numerically equivalent to minimizing the lowest singular value S_{min} of the matrix $\mathbf{\Psi}\left(\omega, \mathbf{k}_\parallel\right)$. We find that minimizing S_{min} performs numerically better than minimizing the determinant directly (see Supplementary Sec. 9 in [P4]). Therefore, in Sec. 4.3, we illustrate the bandstructures of the metasurfaces by computing the color plots of S_{min} as a function of ω and $\mathbf{k}_\parallel$.

By contrast, for plotting the bandstructures in Sec. 4.4, we adopt a slightly different strategy. By applying the adaptive Antoulas–Anderson (AAA) algorithm, for a fixed in-plane

wavevector $\mathbf{k}_\parallel$, we first construct a rational approximation $r_{\mathbf{k}_\parallel}(\omega)$ given by

$$r_{\mathbf{k}_\parallel}(\omega) \approx f(\omega, \mathbf{k}_\parallel) = \frac{1}{\left|\mathbf{\Psi}(\omega, \mathbf{k}_\parallel)\right|}, \tag{4.2}$$

using a sufficiently large set of sampled values of $\left|\mathbf{\Psi}(\omega, \mathbf{k}_\parallel)\right|$. The eigenmode frequencies are then obtained by locating the poles of $r_{\mathbf{k}_\parallel}(\omega)$, yielding the combinations of ω and $\mathbf{k}_\parallel$ that satisfy Eq. (4.1). Finally, the bandstructures are depicted as scatter plots of the resulting (ω, $\mathbf{k}_\parallel$) pairs. We direct the interested reader to [114] for the details of the application of the AAA algorithm to T-matrix-based frameworks.

In the following, we show the resonance-assisted enhancement of the momentum bandgap sizes in the Mie and qBIC resonant PTCs. We begin with the Mie resonant PTCs.

4.3. Momentum bandgaps in Mie resonant PTCs

In this section, we discuss how the Mie resonances of the meta-atoms allow us to reduce the required modulation amplitudes to observe noticeable momentum bandgaps in time-varying metasurfaces. We consider a metasurface made from a square lattice of time-varying dielectric spheres (see Fig. 4.2(a)). For simplicity, hereafter we consider the metasurface to be subwavelength in the parameter range of interest. Furthermore, initially, we ignore material dispersion. Therefore, the background permittivity of the material from which the spheres are made reads $\varepsilon_\infty(t) = 1 + \chi_{\infty,\mathrm{st}}[1 + M\cos(\Omega t)]$ (see Eq. (2.26)). Since the metasurface has a 2D spatial periodicity in the xy-plane with period Λ, and a temporal periodicity with period $2\pi/\Omega$, it represents a (2+1)D spatiotemporal crystal. In this section, the radius $\mathcal{R}$ of the spheres is fixed to 210.6 nm, and the lattice period Λ is set to $3\mathcal{R}$. Here, $\mathcal{R}$ is chosen precisely such that the momentum bandgaps in the resonant case occur at near-infrared frequencies. Furthermore, the static background susceptibility is chosen as $\chi_{\infty,\mathrm{st}} = 10.68$, corresponding to silicon, which is nearly lossless and dispersionless in the considered near-infrared frequency regime [115]. In the following, we show the emergence of noticeable momentum bandgaps for both the evanescent and propagating PWs using such time-varying metasurfaces.

4.3.1. Momentum bandgaps for evanescent PWs

In this subsection, we optimize the time-varying metasurfaces to support momentum bandgaps for evanescent PWs. To begin with, we show the bandstructure of the metasurface under static conditions in Fig. 4.2(b). Note that we provide the convergence parameters such as $l_{\max}$, j_0 , and J for all the simulations in this thesis in Appendix Sec. A.7. We observe the existence of flat bands in the bandstructure due to the Mie resonances of the spheres. For comparison, we show the scattering cross section[1] σ_{sca} of an isolated sphere under static conditions as a function of the frequency ω in Fig. 4.2(c). From Fig. 4.2(c), we observe the occurrence of a magnetic dipolar (MD) and an electric dipolar resonance (ED) that explains the existence of the flat bands in Fig. 4.2(b). Physically, due to these resonances, light is

[1]Here, and in the following, we compute the scattering cross section σ_{sca} of a static meta-atom using its T-matrix $\mathbf{T}$ as $\sigma_{\mathrm{sca}} = \frac{2}{(k\mathcal{R})^2}\|\mathbf{T}\|_{\mathrm{HS}}^2$. Here, $\|.\|_{\mathrm{HS}}$ represents the Hilbert-Schmidt norm. For non-spherical objects, by definition, such an expression evaluates the rotationally averaged scattering cross section (see Eq. (43) in [116]).

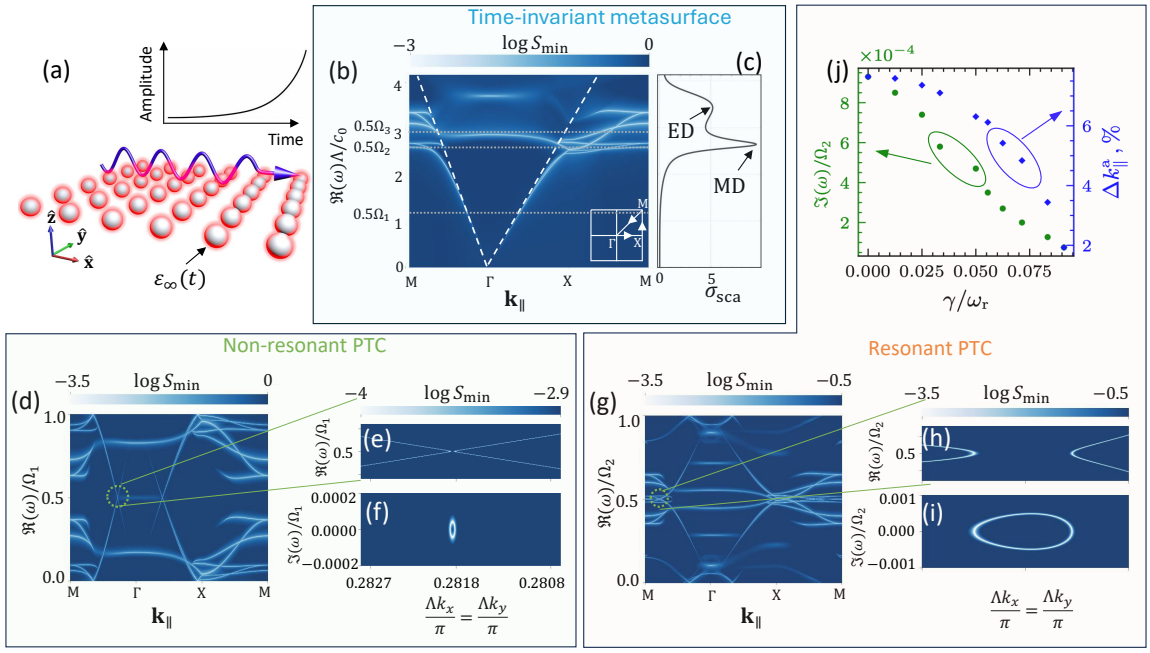


Figure 4.2.: **A Mie resonant PTC for evanescent waves.** (a) A time-varying metasurface made from a square lattice of dielectric spheres. Here, the background permittivity of each sphere is $\varepsilon_\infty(t) = 1 + \chi_{\infty,\mathrm{st}}[1 + M\cos(\Omega t)]$. (b) The bandstructure of the metasurface in (a) for the static case. (c) The scattering cross section $\sigma_{\rm sca}$ of an isolated static sphere as a function of frequency ω. Here, MD represents the magnetic dipolar, and ED represents the electric dipolar resonance of the sphere. (d) The bandstructure of the time-varying metasurface with $M = 0.01$ and $\Omega = \Omega_1 = 2\pi \times 183$ THz. We observe the crossing of the linear bands of the static metasurface. (e) The zoomed bandstructure in the green-highlighted region in (d). We note the existence of a tiny momentum bandgap with size $\Delta k_\parallel = 0.0183\%$. (f) The imaginary part of the frequency $\Im(\omega)$ inside the bandgap for a fixed $\Re(\omega) = \Omega_1/2$. (g) Same as (d) but with $\Omega = \Omega_2 = 2\pi \times 392$ THz. (h), (i) The real and imaginary parts of the frequency ω in the green-highlighted region of (g), respectively. Here, we observe the existence of a comparatively large momentum bandgap with $\Delta k_\parallel = 6.59\%$ despite the same modulation amplitude of $M = 0.01$. (j) The imaginary part of the frequency $\Im(\omega)$ at the center of the bandgap in (i) and the relative amplification bandwidth $\Delta k_\parallel^{\rm a}$ as a function of the damping parameter γ. Note that Γ, X, and M denote the high-symmetry points of the first BZ of the square lattice. Furthermore, the white dashed lines in (b) are the light lines. This figure has been adapted from [P4]. © The authors, licensed under CC BY-ND 4.0.

strongly confined inside the spheres. Such a confinement reduces the radiative coupling between the neighboring spheres in the metasurface, leading to a reduced spatial dispersion of the resulting eigenmodes. Such reduced spatial dispersion manifests itself as flat bands in the bandstructure of the metasurface. As will be shown below, exploiting these flat bands dramatically reduces the modulation amplitude M for attaining noticeable momentum bandgaps. Note that the bandstructure shown hereafter accommodates the eigenmodes for both TE- and TM-polarized PWs. However, in this section, we optimize the metasurfaces for the TE-polarized PWs.

Next, we plot the bandstructures of the time-varying metasurfaces. We start by choosing the modulation frequency to be Ω_1 (see Fig. 4.2(b)). Here, since $\omega = \Omega_1/2 = 2\pi \times 91.5$ THz is far away from the flat bands, this configuration corresponds to a scenario of modulating a non-resonant metasurface. Moreover, we observe that the dispersion around $\omega = \Omega_1/2$ is linear (see Fig. 4.2(b)). This is because the metasurface is spatially homogenizable near and below $\omega = \Omega_1/2$ [117, P7]. Therefore, a time-varying metasurface with the modulation frequency Ω_1 mimics the properties of a conventional (space-uniform) PTC.

In Fig. 4.2(d), we show the bandstructure of this non-resonant metasurface. We choose $M = 0.01$, which is close to the maximum attainable modulation amplitude value in silicon before thermal damage occurs [112, 118]. We observe the folding of the bandstructure as obtained in the static case. Such folding is expected as the metasurface possesses a discrete time-translational symmetry with the period $2\pi/\Omega_1$. Therefore, the Floquet-Bloch theorem requires that the bandstructure of the metasurface should also be periodic in the reciprocal space with the periodicity Ω_1 (see Sec. 3.1.2)[24, 30]. Furthermore, we observe that the bandstructure is mirror symmetric about $\omega = \Omega_1/2$. This behavior can be understood as follows. In the static case, the bandstructure is symmetric about $\omega = 0$. This symmetry follows from the complex-conjugation symmetry of the time-invariant Maxwell equations: for every mode with frequency ω, there exists a corresponding complex-conjugate mode at frequency $-\omega^*$. Therefore, when the bands are translated along the ω-dimension upon time modulation with the periodicity Ω_1, a mirror-symmetric bandstructure about $\omega = \Omega_1/2$ is obtained. Furthermore, the folding of the bandstructure forms several band crossings in the M$-\Gamma-$X region. At these crossings, the contributing bands are phase-matched in space as well as in time. Such a phase-matching allows for their strong interaction, leading to the opening of momentum bandgaps (see the Supplementary Sec. 3 in [83]).

We show a momentum bandgap in the M$-\Gamma$ region in Fig. 4.2(e). The resulting gap size is very narrow, i.e., $\Delta k_\parallel = 0.0183\%$. We use $\Delta k_\parallel = 2|k_\parallel^{(2)} - k_\parallel^{(1)}|/|k_\parallel^{(2)} + k_\parallel^{(1)}|$, where $k_\parallel^{(1)}$ and $k_\parallel^{(2)}$ are the $k_\parallel$ values at the edges of the bandgap. We also plot the imaginary part of the frequency $\Im(\omega)$ for a fixed $\Re(\omega) = \Omega_1/2$ in Fig. 4.2(f). Inside the bandgap, we find that eigenmodes with both positive and negative imaginary parts of the frequency exist [21, 119]. Therefore, when an incident PW couples to the bandgap modes, its propagation can be described by the linear superposition of these eigenmodes. Due to the existence of the modes with positive imaginary parts, such an incident PW gets exponentially amplified as a function of time (see inset Fig. 4.2(a)). Furthermore, we note that $\Im(\omega)$ is maximal at the center of the bandgap, implying a maximal amplification rate there (see Fig. 4.2(f)). We emphasize that the modes with $\Im(\omega) < 0$ correspond to exponentially decaying solutions as a function of time. Therefore, they eventually die out for time $t \gg 1/|\Im(\omega)|$. Furthermore, since the bandgap lies below the light lines (see Fig. 4.2(b)), only evanescent incident PWs couple to its modes.

Importantly, due to its very narrow size, utilizing the bandgap for amplification requires very fine-tuning of the in-plane wavevector $\mathbf{k}_\parallel$ of the incident fields. Such a requirement renders the bandgap impractical to use. On the other hand, attempts to increase the bandgap size with increasing M require a very high pump intensity (on the order of a few TW/cm^2) [82]. Due to material losses, such high pump intensities typically lead to the thermal damage of the underlying system. To circumvent these issues, we exploit the flat bands of the static metasurfaces in the following.

In sharp contrast to the previous case, when half of the modulation frequency is near the MD resonance frequency of the spheres (see the horizontal line at $\omega = \Omega_2/2 = 2\pi \times 196$ THz in Fig. 4.2(b)), the bandgap significantly expands in the time-varying case. Because $\Omega_2/2$ coincides with the spectral position of a flat band, the corresponding configuration can be considered as resonant. The bandstructure for such a resonant metasurface is demonstrated in Fig. 4.2(g). Here, we use the same modulation amplitude as before, i.e., $M = 0.01$. Again, we observe the folding of the bandstructure of the static case with the periodicity Ω_2. As mentioned before, due to the interaction of the bands at $\omega = \Omega_2/2$, we expect a momentum bandgap at that frequency. Therefore, in Fig. 4.2(h), we show the bandstructure in the highlighted region of Fig. 4.2(g). The corresponding imaginary part of the frequency $\Im(\omega)$ for a fixed $\Re(\omega) = \Omega_2/2$ is shown in Fig. 4.2(i). Clearly, from Figs. 4.2(h)-(i), we observe the presence of a noticeable momentum bandgap. Numerically, the size of the bandgap is $\Delta k_\parallel = 6.59\%$. Remarkably, the MD resonance of the spheres with the Q-factor $Q \approx 6$ leads to the widening of the bandgap by a factor of about 350 as compared to the non-resonant case, due to the enhanced light-matter interactions.

It is essential to note from Fig. 4.2(g) that the obtained momentum bandgap is not complete since there exist band modes for $\Re(\omega) \neq \Omega_2/2$ within the $\mathbf{k}_\parallel$ range of the bandgap. However, such an incompleteness does not pose an issue in amplifying the incident PWs. This is because the exponentially growing modes at $\Re(\omega) = \Omega_2/2$ inside the gap stay dominant as compared to the modes at other frequencies for the $\mathbf{k}_\parallel$ values within the gap. We also observe from Fig. 4.2(i) that $\Im(\omega)$ inside the bandgap is almost independent of $\mathbf{k}_\parallel$. This implies that all the incident waves that couple to the modes inside the bandgap with different values of $\mathbf{k}_\parallel$ get exponentially amplified in time at almost similar rates. Furthermore, as before, the bandgap lies below the light lines (see Fig. 4.2(b)). Therefore, only evanescent PWs can be amplified using it. Moreover, the comparison of Figs. 4.2(f) and (i) reveals that the structural resonances not only increase the bandgap size, but the amplification rate also gets enhanced. This enhancement is evident from the fact that $\Im(\omega)$ is an order of magnitude larger in the resonant case. Such a behavior arises because the fields corresponding to the bandgap modes in the resonant case are strongly localized inside the spheres. Such a localization facilitates a stronger interaction of light with time-varying matter, leading to a higher $\Im(\omega)$. On the other hand, for bandgap modes in the non-resonant case, such a preferential localization of the modal fields inside the spheres does not exist.

Next, we consider the effects of the material losses by modeling the material of the spheres using a single-pole Drude-Lorentz model with the damping factor γ and the resonance frequency ω_r (see Eq. (2.12)). We assume the electron density of the material of the spheres to be $N(t) = N_\mathrm{st}[1 + M\cos(\Omega t)]$. Here, the used Drude-Lorentz parameters correspond to those of silicon in the relevant spectral domain [115]. Note that the single-pole Drude-Lorentz model does not follow the sum rule in Eq. (2.14). Furthermore, to quantify the range of $\mathbf{k}_\parallel$ vectors that get amplified, instead of the bandgap size, we use relative amplification

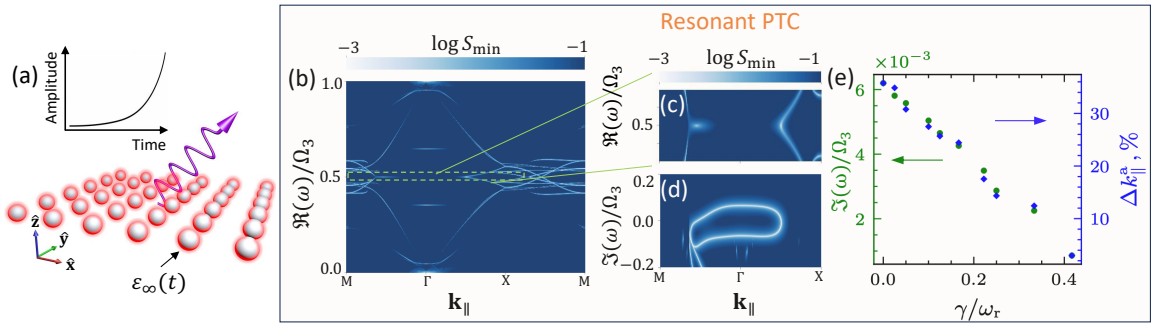


Figure 4.3.: **A Mie resonant PTC for propagating waves.** (a) A time-varying metasurface made from a square lattice of dielectric spheres. (b) The bandstructure of the time-varying metasurface with $M = 0.06$ and $\Omega = \Omega_3 = 2\pi \times 428$ THz. We observe the crossing of flat bands of the static metasurface in the radiative zone (i.e., near the $\Gamma-$point). (c) The zoomed bandstructure in the green-highlighted region in (b), exhibiting a noticeable momentum bandgap. (d) The imaginary part of the frequency $\Im(\omega)$ inside the bandgap for a fixed $\Re(\omega) = \Omega_3/2$. (e) The imaginary part of the frequency $\Im(\omega)$ at the center of the bandgap in (d) and the amplification bandwidth $\Delta k_\parallel^a$ as a function of the damping parameter γ. Note that the frequency $\Omega_3/2$ was indicated in Fig. 4.2(b). This figure has been adapted from [P4]. © The authors, licensed under CC BY-ND 4.0.

bandwidth $\Delta k_\parallel^a$. We define $\Delta k_\parallel^a = 2|k_\parallel^{a2} - k_\parallel^{a1}|/|k_\parallel^{a2} + k_\parallel^{a1}|$. Here, $k_\parallel^{a1}$ and $k_\parallel^{a2}$ correspond to those values of $k_\parallel$ for a bandgap where $\Im(\omega) = 0$.

We plot the relative amplification bandwidth $\Delta k_\parallel^a$ and the imaginary part of the frequency $\Im(\omega)$ at the center of the bandgap of the resonant case as a function of γ in Fig. 4.2(j). Here, we observe that as γ increases, $\Im(\omega)$ becomes less positive. Furthermore, with increasing γ, $\Delta k_\parallel^a$ also decreases. Such a behavior is expected, as increasing γ implies increasing material losses that counteract the amplification provided by the time-varying medium. Therefore, $\Im(\omega)$ becomes less positive, implying a lower amplification rate of the fields. Furthermore, increasing γ moves the contour of the imaginary part of the frequency vertically downwards in the $\Im(\omega) - \mathbf{k}_\parallel$ space, leading to smaller amplification bandwidths. However, despite the losses, up to $\gamma \approx 0.05\omega_r$, the relative amplification bandwidth $\Delta k_\parallel^a$ stays more than 6% while maintaining a positive $\Im(\omega)$ (see Fig. 4.2(j)). For $\gamma \approx 0.05\omega_r$ the imaginary part of the permittivity is 0.028 at the frequency $\Omega_2/2$. Such a value of the imaginary part of the permittivity is orders of magnitude larger than that of silicon at the considered frequency [115]. Therefore, we conclude that the reported bandgap enhancement survives even in the presence of material losses.

In the following, we discuss the emergence of the momentum bandgaps in Mie resonant metasurfaces for propagating PWs.

4.3.2. Momentum bandgaps for propagating PWs

So far, we have discussed how the resonances of the metasurfaces pave the way for a power-efficient device that supports noticeable momentum bandgaps for low modulation amplitudes. However, the previously discussed bandgaps occurred below the light line. Therefore, only evanescent incident PWs can couple to such bandgaps. As a next step, we design the metasurfaces such that they support a noticeable momentum bandgap above the light lines, i.e., for propagating PWs.

From Fig. 4.2(b), for the static metasurface, we observe the existence of a flat band above the light lines near the frequency $\omega = \Omega_3/2 = 2\pi \times 214$ THz around the $\Gamma-$point. Because this band is located above the light lines, its constituent modes possess a non-zero radiative decay rate. Next, we turn on the time modulation to study the emerging momentum bandgaps. We choose the modulation frequency to be Ω_3. Furthermore, the modulation amplitude is taken as $M = 0.06$. Note that we could have chosen an even lower value of M, but that comes at the expense of a reduced bandgap size. The corresponding bandstructure of the time-varying metasurface is shown in Fig. 4.3(b). Again, we observe the folding of the bandstructure of Fig. 4.2(b) in Fig. 4.3(b) with the periodicity of Ω_3 along the frequency dimension. We expect the existence of a momentum bandgap at $\omega = \Omega_3/2$. Therefore, we plot the bandstructure in the highlighted region of Fig. 4.3(b) in Fig. 4.3(c). Furthermore, the imaginary part of the frequency $\Im(\omega)$ is shown in Fig. 4.3(d). Clearly, we observe a noticeable momentum bandgap at $\omega = \Omega_3/2$ in Figs. 4.3(c)–(d). Remarkably, despite the small modulation amplitude, the momentum bandgap is very large and spans over a wide range of incident angles: up to 54° in the incidence plane parallel to $\Gamma-$M and 33° parallel to $\Gamma-$X. Note that these angles are determined by the $\mathbf{k}_\parallel$ values at the edges of the bandgap. Because the bandgap appears in the region above the light lines, the modes inside it can couple to free-space modes, facilitating their amplification. Furthermore, due to the almost constant $\Im(\omega)$ inside the bandgap (see Fig. 4.3(d)), the waves that couple to its eigenmodes get amplified at almost similar rates irrespective of the value of $\mathbf{k}_\parallel$. We note that the plot of $\Im(\omega)$ is not symmetric about $\Im(\omega) = 0$ due to the finite radiative losses of the eigenmodes above the light lines.

Finally, Fig. 4.3(e) shows the effects of material losses on the momentum bandgap. Again, we observe that increasing γ leads to less positive $\Im(\omega)$ and a lower $\Delta k_\parallel^{\mathrm{a}}$. However, $\Im(\omega)$ stays positive for $\gamma < 0.45\omega_{\mathrm{r}}$. For such a value of γ, the imaginary part of the permittivity is 0.3, which is many orders of magnitude larger than the corresponding value for silicon at $\Omega_3/2$ [115]. Therefore, we conclude that the bandgap enhancement survives in the presence of realistic losses even for this example.

In this section, we considered the exploitation of the Mie resonances of the meta-atoms to attain noticeable momentum bandgaps at small modulation amplitudes. In the following, we explore the utilization of the qBIC resonances of the meta-atoms to reduce the required modulation amplitudes even further for attaining such bandgaps.

4.4. Momentum bandgaps in qBIC resonant PTCs

Bound states in the continuum are a special class of nanophotonic resonances. By definition, they reside in the radiation continuum of a scattering structure while exhibiting infinite Q-factors [120]. There are several physical mechanisms that can lead to the creation of a BIC. For instance, symmetry-protected BICs (SP-BICs) arise from the spatial symmetries of the scatterer. Specifically, the symmetry of the corresponding BIC eigenmode is incompatible with that of the available radiation channels, thereby preventing the mode from coupling to the radiative continuum. BICs can also arise from the accidental cancellation of radiative leakage from an eigenmode, resulting from destructive interference between the available contributions to the radiation channels of the scatterer. Such BICs typically appear for an optimized set of geometry parameters of the scatterer and are termed accidental BICs (or geometric BICs). Finally, in theory, extreme material parameters such as zero ($\varepsilon \to 0$) or

diverging permittivity ($\varepsilon \to \infty$) also give rise to BICs. These BICs are termed material-induced BICs. We guide the interested reader to [47] for a more elaborate discussion on several BIC-forming mechanisms.

By reciprocity, a resonance that does not radiate can not be excited by an incident excitation in the far field. Therefore, true BICs with infinite Q-factors are seldom used in photonics. However, slightly detuning the scattering system from the true BIC condition gives rise to qBICs. Such qBICs possess ultra-high but *finite* Q-factors. Therefore, they can couple to incident excitations in the far field while intensifying light-matter interactions. Such high-Q resonances have revolutionized many areas of photonics. These include ultrasensitive sensing [121], low-threshold nanolasing [122], and nonlinear light generation [123], among many others [124].

Despite the widespread adoption of qBICs in many research domains, their application to time-varying systems has remained extremely limited [41, 125]. To the best of the author's knowledge, prior to this thesis, the physics of qBICs was never combined with that of PTCs. In this section, to address this research gap and to exploit the opportunities, we study metasurface-based PTCs that exploit these high-Q resonances. In particular, we focus on the qBICs hosted by meta-atoms (see Fig. 4.1). Essentially, placing such resonant meta-atoms in a metasurface lattice and turning on their time-modulation allows us to obtain noticeable momentum bandgaps at perturbative modulation amplitudes. We find that, in terms of required pump intensities, such qBIC-assisted PTCs perform even better than the Mie-resonant PTCs described earlier.

This section is structured as follows: in Subsec. 4.4.1, we briefly describe the physical model to account for the Kerr-induced time-varying permittivity. Then, in Subsec. 4.4.2, we consider the material-induced qBICs in multilayered spheres that exploit the vanishing permittivity of some of the layers of the spheres. We study how the Q-factor impacts the threshold modulation amplitude to open a momentum bandgap. We also discuss the effect of material losses on the threshold modulation amplitude. Then, we proceed in Subsec. 4.4.3 to exploit the geometric qBICs of isolated dielectric cylinders made from germanium. Using realistic material parameters, we consider metasurfaces made from such resonant cylinders. We optimize the metasurface such that noticeable momentum bandgaps are attained at pump intensities an order of magnitude below those required for the Mie resonant PTCs.

We remark that we compute the T-matrices of the isolated time-varying multilayered spheres using the theory developed by Dr. Aristeidis Lamprianidis [53]. The computational implementation of that theoretical framework was mainly carried out by Leander Zimmer in collaboration with the author. Furthermore, we use the dynamic extended boundary condition method (EBCM) to compute the T-matrices of isolated time-varying cylinders [P13]. The theoretical and computational development of the dynamic EBCM code was done in the groups of Prof. Nikolaos Stefanou and Dr. Nikolaos Papanikolaou.

4.4.1. Kerr-induced time-varying permittivity

In the following subsections, we use the optical Kerr effect as the source of time modulation (see Subsec. 2.3.2 for more details). Specifically, we assume that the considered meta-atoms are made from a material whose time-varying background permittivity is given by $\varepsilon_\infty(t) = \varepsilon_{\infty,\mathrm{st}}\,\{1 + M[\,1 + \cos(\Omega t)\,]\}$. Here, $\varepsilon_{\infty,\mathrm{st}} = 1 + \chi_{\infty,\mathrm{st}}$ is the background permittivity of the corresponding static medium, M is the modulation amplitude, and Ω is the modulation frequency. Furthermore, $M = \frac{\chi^{(3)} E_\mathrm{p}^2}{2\varepsilon_{\infty,\mathrm{st}}}$, and $\Omega = 2\omega_\mathrm{p}$.

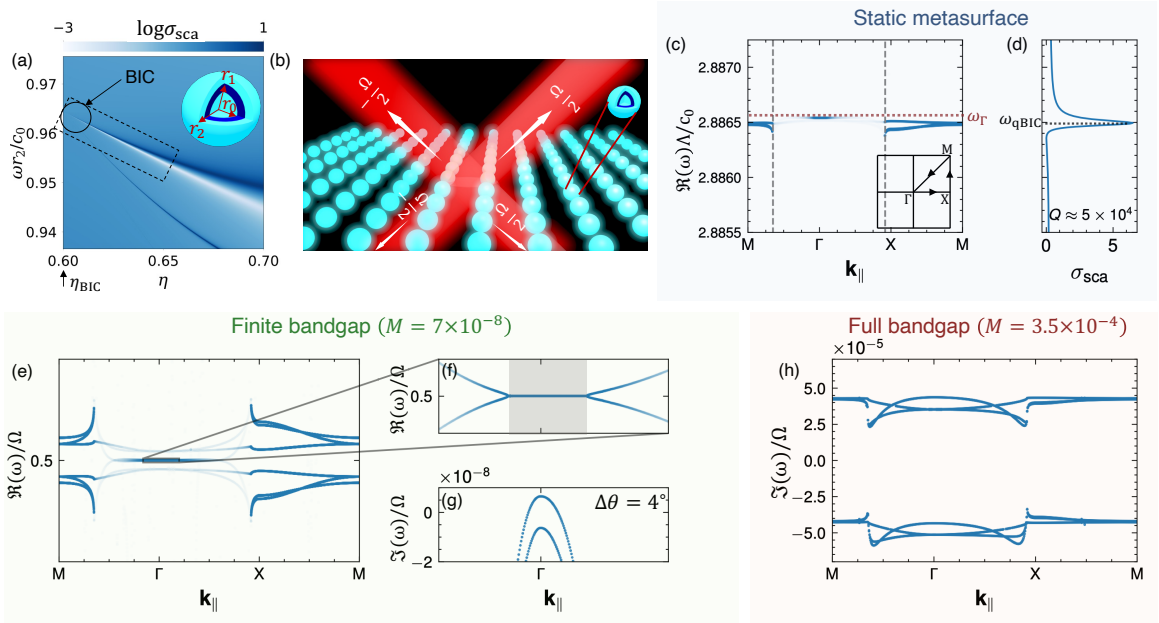


Figure 4.4.: **A qBIC resonant PTC based on a multilayered sphere metasurface.** (a) The scattering cross section σ_{sca} of the isolated static multilayered sphere as a function of the frequency ω and the geometry parameter η. Here, $\eta = r_1/r_2$. (b) An illustration of the time-varying metasurface made from a square lattice of the multilayered spheres. (c) The bandstructure of the metasurface in (b) under static conditions. (d) The scattering cross section σ_{sca} of the isolated static multilayered sphere as a function of the frequency ω. The sphere supports a qBIC at $\omega = \omega_{\text{qBIC}}$ with the quality factor $Q \approx 5 \times 10^4$. (e) The bandstructure of the time-varying metasurface with $M = 7 \times 10^{-8}$ and $\Omega = 2\omega'_\Gamma = 2\pi \times 459.4$ THz. (f) The zoomed bandstructure in the gray-highlighted region in (e). We note the existence of a noticeable momentum bandgap with the incident angle range $\Delta\theta = 4°$. (g) The imaginary part of the frequency $\Im(\omega)$ inside the bandgap for a fixed $\Re(\omega) = \Omega/2$. The symmetry of the displayed modes is compatible with TM-polarized PWs. (h) The imaginary part of the frequency inside the full bandgap supported by the metasurface with $M = 3.5 \times 10^{-4}$ and $\Omega = 2\pi \times 459.3$ THz. We observe that there exist modes with $\Im(\omega) > 0$ for all $\mathbf{k}_\parallel$ values on the edges of the IBZ. Note that the gray dashed lines in (c) are the light lines. This figure has been adapted from [P1]. © The authors, licensed under CC BY 4.0.

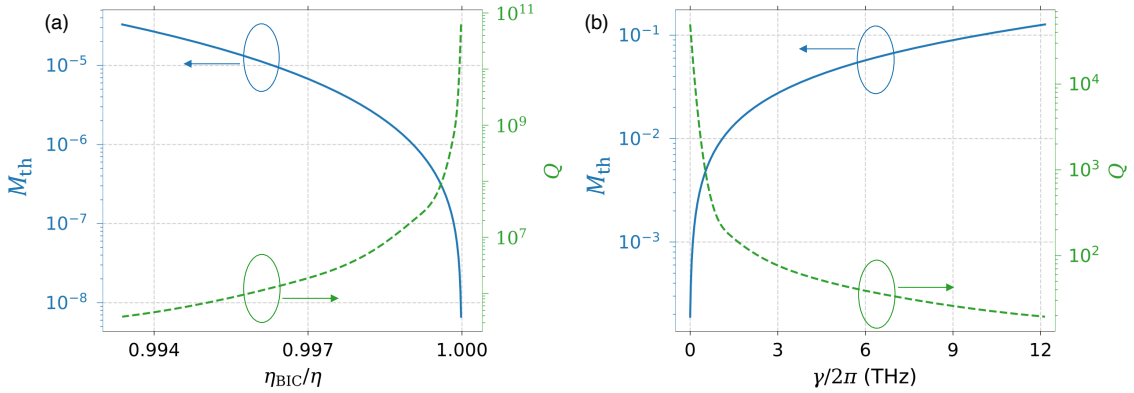


Figure 4.5.: **Impact of the Q-factor on the modulation amplitude.** The threshold modulation amplitude M_{th} to open a full momentum bandgap in the multilayered sphere-based metasurface as a function of the geometry parameter η (blue curve in (a)) and the damping parameter γ (blue curve in (b)). The Q-factor Q of the underlying qBIC of the static multilayered sphere as a function of η (green curve in (a)) and γ (green curve in (b)). This figure has been adapted from [P1]. © The authors, licensed under CC BY 4.0.

In the following, using this time-varying background permittivity model, we discuss qBIC-assisted momentum bandgap enhancement in metasurfaces made from multilayered spheres and cylinders.

4.4.2. Momentum bandgaps in multilayered sphere-based metasurfaces

We begin by analyzing a static multilayered sphere. The considered sphere has three layers (see the inset in Fig. 4.4(a)). The innermost and the outermost layers are made from aluminum zinc oxide (AZO), while the middle layer is made from silicon dioxide (SiO_2). We model the dispersive part of the permittivity of the AZO layers using the Drude-Lorentz model (see the $R_{\mathrm{disp}}(t-\tau)$ term in Eq. (2.22)). Here, we use the corresponding Drude-Lorentz parameters from [126]. Furthermore, the SiO_2 layer is assumed to be non-dispersive. Its permittivity is fixed at $\varepsilon_{\infty,\mathrm{st}} = 2.15$. We denote the radii of the innermost, middle, and the outermost layers by r_0, r_1, and r_2, respectively. We use $r_0 = 120$ nm, $r_1 = \eta r_2$, and $r_2 = 200$ nm, where η is a variable. For a theoretical demonstration, initially we ignore the material losses in AZO by setting the damping parameter γ to zero. We plot the scattering cross section σ_{sca} as a function of the frequency ω and the geometry parameter η of the resulting lossless static sphere in Fig. 4.4(a). Here, we observe the existence of the scattering zeros (bright features) and poles (dark features) of the sphere. In fact, in the highlighted region (see the dotted box), we find that these poles and zeros approach each other in the parameter space, eventually coalescing at $\eta = \eta_{\mathrm{BIC}} \approx 0.6$. Such a coalescence is the hallmark feature of a BIC. The BIC appears at a frequency where the permittivity of the AZO layers is exactly zero. We remark that these material-induced compact BICs were first introduced in [127, 128]. In the following, we study how such BICs affect the bandstructures of the metasurfaces.

We consider a metasurface made from a square lattice of the multilayered spheres (see Fig. 4.4(b)). We use a lattice period of $\Lambda = 3r_2$. Furthermore, we choose $\eta = 1.018\eta_{\mathrm{BIC}} =$

0.611 so that the spheres support a qBIC. Here, the used η is slightly detuned from η_{BIC}, as a true BIC does not couple to far-field incident excitation, as mentioned before. Nevertheless, the resulting qBIC supports an extremely high Q-factor, i.e., $Q \approx 5 \times 10^4$. Next, we plot the bandstructure of the corresponding static metasurfaces in Fig. 4.4(c). We observe the emergence of extremely flat bands due to the qBICs of the spheres. For comparison, we show the scattering cross section of an isolated sphere in Fig. 4.4(d). From Fig. 4.4(d), we find that the sphere supports a high-Q qBIC at $\omega = \omega_{\text{qBIC}}$, which explains the emergence of the flat bands in Fig. 4.4(c). The shown qBIC has an electric dipolar character. Furthermore, due to the spatial symmetry of the sphere, the qBIC is three-fold degenerate. Upon placing the sphere in the metasurface lattice, such a degeneracy is lifted. Hence, there exist three distinct flat bands in Fig. 4.4(c). The transparency of these bands is directly proportional to the radiative losses of the underlying modes. We further note that the flat band frequency at the $\Gamma-$point is $\omega_\Gamma = \omega_{\text{qBIC}}$.

Next, we consider the time-varying case. We assume the background permittivity of the AZO layers to be time-varying. The SiO_2 layer is assumed to be static. We choose $\Omega = 2\omega'_\Gamma$. Here, ω'_Γ is slightly different from ω_Γ. This is because the pump wave offsets the background permittivity by an amount $M\varepsilon_\infty$. Such an offset DC-shifts the flat band frequency ω_Γ to ω'_Γ. Numerically, $\Omega = 2\pi \times 459.4$ THz. Furthermore, we consider an extremely small value of M, i.e., $M = 7 \times 10^{-8}$. The bandstructure of the corresponding time-varying metasurface is shown in Fig. 4.4(e). As expected, the bandstructure folds about $\omega = \Omega/2$. Moreover, due to the flatness of the static bands, we observe a large area in the parameter space where the original and the time-modulation-induced bands overlap (see the gray box). In this overlap region, we expect to see a momentum bandgap. Therefore, we plot the zoomed bandstructure in the region of interest in Fig. 4.4(f). We observe the existence of a noticeable momentum bandgap despite a perturbative M. Hereafter, we use the incident angle range $\Delta\theta$ corresponding to the bandgap to quantify the gap size. In the present case $\Delta\theta = 4°$. The resulting bandgap is noticeable, as such gap sizes are not achieved in homogeneous PTCs even with $M \sim 1$ (see Subsec. 4.3.1). The intensified light-matter interactions, due to the extremely high-Q qBIC, facilitate the opening of this gap in the metasurface. We also show the imaginary part of the frequency inside the bandgap for a fixed $\Re(\omega) = \Omega/2$ in Fig. 4.4(g). Expectedly, we observe modes with both positive and negative imaginary parts of the frequency ω inside the bandgap. The symmetry of the displayed modes is compatible with TM-polarized PWs.

The qBIC-assisted PTCs can also support full momentum bandgaps. To demonstrate such a behavior, we increase the modulation amplitude to $M = 3.5 \times 10^{-4}$. Importantly, increasing M changes the DC-shift of the flat band frequency, leading to a slightly different ω'_Γ. Therefore, the modulation frequency is modified to $\Omega = 2\omega'_\Gamma = 2\pi \times 459.3$ THz. All other parameters of the metasurface are unchanged. In this configuration, we show the imaginary part of the frequency inside the bandgap in Fig. 4.4(h). We observe that $\Im(\omega) > 0$ for all possible values of $\mathbf{k}_\parallel$ on the edges of the irreducible BZ (IBZ), leading to the demonstration of a full bandgap. Note that, here, and in the following examples with full bandgaps, we numerically verified that $\Im(\omega) > 0$ inside the entire IBZ.

Next, we study the impact of the Q-factor on the threshold modulation amplitude M_{th} to open a bandgap. For a fair comparison, we always require a full bandgap. In Fig. 4.5(a), we plot M_{th} as a function of the geometry parameter η (see the blue curve). We find that as η approaches η_{BIC}, the required modulation amplitude to open a full bandgap asymptotically goes to zero. Such a behavior is expected because as $\eta \to \eta_{\text{BIC}}$, the Q-factor of the underlying

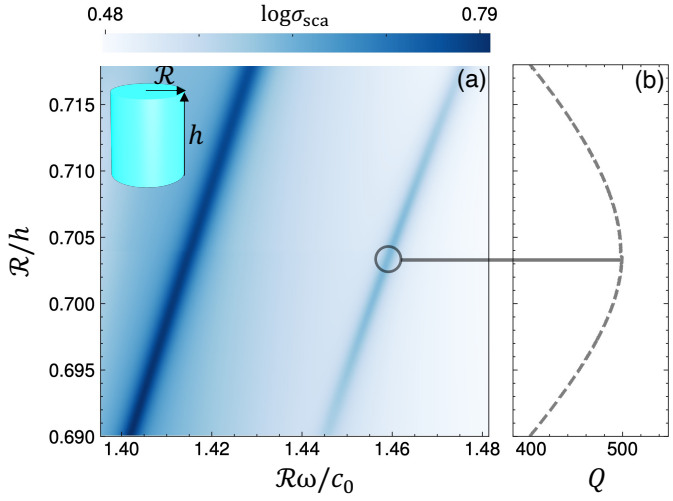


Figure 4.6.: **The qBICs of isolated static cylinders.** (a) The rotationally averaged scattering cross section σ_{sca} of the isolated static cylinder as a function of its aspect ratio $\mathcal{R}/h$ and the frequency ω. We observe the emergence of two modal branches. In particular, the modes on the right branch are qBICs. (b) The Q-factors Q of the modes on the right branch in (a) as a function of the aspect ratio. Note that we fix the radius of the cylinder as $\mathcal{R} = 1.03 \times 10^3$ nm and vary its height h to change the aspect ratio. The highest-Q qBIC with $Q \approx 500$ is marked by a circle in (a). This figure has been adapted from [P1]. © The authors, licensed under CC BY 4.0.

resonance diverges (see the green curve). These diverging-Q resonances push the light-matter interactions to extremes by reducing the radiative losses in an otherwise lossless system, leading to full bandgaps despite perturbative modulation amplitudes.

So far, for a theoretical demonstration, we ignored the material losses of AZO. Next, we show the impact of these losses on M_{th}. We plot M_{th} as a function of the damping parameter γ in Fig. 4.5(b) (see the blue curve). We observe that M_{th} increases with increasing γ. Such a behavior is expected as the material losses in the system decrease the Q-factors of the qBICs (see the green curve). Therefore, a higher M_{th} is needed to open a full bandgap. Physically, M_{th} increases because a larger time-modulation-induced gain is required to compensate for the intrinsic losses. In fact, the experimentally reported value of γ for AZO in its ENZ regime is $\gamma \approx 2\pi \times 12$ THz [126]. The corresponding M_{th} to open full bandgaps is $M_{\text{th}} = 0.13$.

We remark here that in the lossless case, qBIC-assisted PTCs made from ENZ spheres assist in decreasing M_{th}. However, assuming realistic losses, the required modulation amplitude values are rather high. In the literature, metamaterial-based approaches have been proposed to realize effective ENZ response with minimal material losses [129]. Such an approach could be beneficial to attain full momentum bandgaps in practice at smaller modulation amplitudes. Another challenge with the present design is that a multilayered sphere-based metasurface is relatively difficult to fabricate. Keeping these issues in mind, in the following, we propose a more practical design of the metasurface-assisted PTCs. In particular, we study the qBICs of dielectric cylinders and show that noticeable momentum bandgaps can be attained in the corresponding time-varying metasurfaces with realistic pump intensities.

4.4.3. BICs in cylinder-based metasurfaces

We begin with an isolated static germanium (Ge) cylinder supporting a high-Q qBIC (see the inset in Fig. 4.6(a)). Here, we consider the realistic material parameters of Ge from the outset. In particular, we account for the material losses using the Drude-Lorentz model (see the $R_{\text{disp}}(t-\tau)$ term in Eq. (2.22)). The corresponding Drude-Lorentz parameters are retrieved from the complex permittivity data in [130]. To understand the qBIC formation mechanism of such a cylinder, we show its rotationally averaged scattering cross section σ_{sca} as a function of its aspect ratio $\mathcal{R}/h$ and the frequency ω (see Fig. 4.6(a)). Here, h represents the height of the cylinder. We observe that there exist two resonance branches in the considered parameter range. These branches represent hybrid modes formed by the interaction of the cylinder's Mie-type modes with the azimuthal index $m = 0$ and principal (radial) index $n = 1$, and neighboring Mie-type modes with indices $m = 0$ and $n = 2$ [131]. In particular, the far-field profiles of the hybrid modes in the right branch result from the destructive interference of the far fields of the parent modes. Consequently, these modes exhibit relatively high-Q factors. In fact, a detailed analysis reveals that such modes are accidental qBICs formed by the Friedrich-Wintgen mechanism (see Ref. [131] for details). The symmetry of these qBICs is compatible with that of the TE-polarized PWs.

We show the Q-factors of the qBIC modes on the right branch in Fig. 4.6(b). We observe that in the considered parameter range, the isolated cylinder hosts resonances with Q-factors exceeding 400. In the following, we fix the aspect ratio of the cylinder to the optimal value of $\mathcal{R}/h \approx 0.703$ for which the Q-factor of the corresponding qBIC is $Q \approx 500$. Note that such a value of Q is considerably lower than that for the multilayered sphere because realistic material losses in the cylinders are taken into account. Nevertheless, as demonstrated below, $Q \approx 500$ is sufficiently high to substantially reduce the modulation amplitude required to achieve noticeable momentum bandgaps compared with homogeneous and Mie-resonant PTCs.

Next, we place the resulting resonant cylinder in a square lattice to form a metasurface (see Fig. 4.7(a)). We use $\mathcal{R} = 1.03 \times 10^3$ nm, and the lattice period $\Lambda = 3.2\mathcal{R}$. First, we consider the static case. We plot the bandstructure of the corresponding metasurface in Fig. 4.7(b). We observe the existence of a flat band due to the qBIC of the cylinder. We denote the flat band frequencies at the $\Gamma-$ and $\text{X}-$ points by ω_Γ and ω_X, respectively. Furthermore, to explain the emergence of the flat band, we plot the rotationally averaged scattering cross section σ_{sca} of the cylinder in Fig. 4.7(c). Here, we observe the existence of the aforementioned qBIC with $Q \approx 500$, which gives rise to the flat band.

Next, we turn on the time modulation. We choose the modulation amplitude to be $M = 10^{-4}$. Our analysis reveals that this value of M corresponds to a pump intensity of 0.7 GW/cm^2 [P1]. First, we show the existence of a noticeable momentum bandgap near the $\Gamma-$point. Therefore, we choose the modulation frequency as $\Omega = 2\omega'_\Gamma$. Here, ω'_Γ is the DC-shifted flat band frequency at the $\Gamma-$point. Numerically, $\Omega = 2\omega'_\Gamma = 2\pi \times 136$ THz. The bandstructure of the corresponding time-varying metasurface is shown in Fig. 4.7(d). We observe a noticeable momentum bandgap near the $\Gamma-$point with the incident angle range of $\Delta\theta = 4^\circ$. We also show the imaginary part of the frequency $\Im(\omega)$ inside the bandgap for a fixed $\Re(\omega) = \Omega/2$. Again, we find that there exist modes with both the positive and negative imaginary parts of the frequency. The symmetry of the displayed modes is compatible with the TE-polarized PWs.

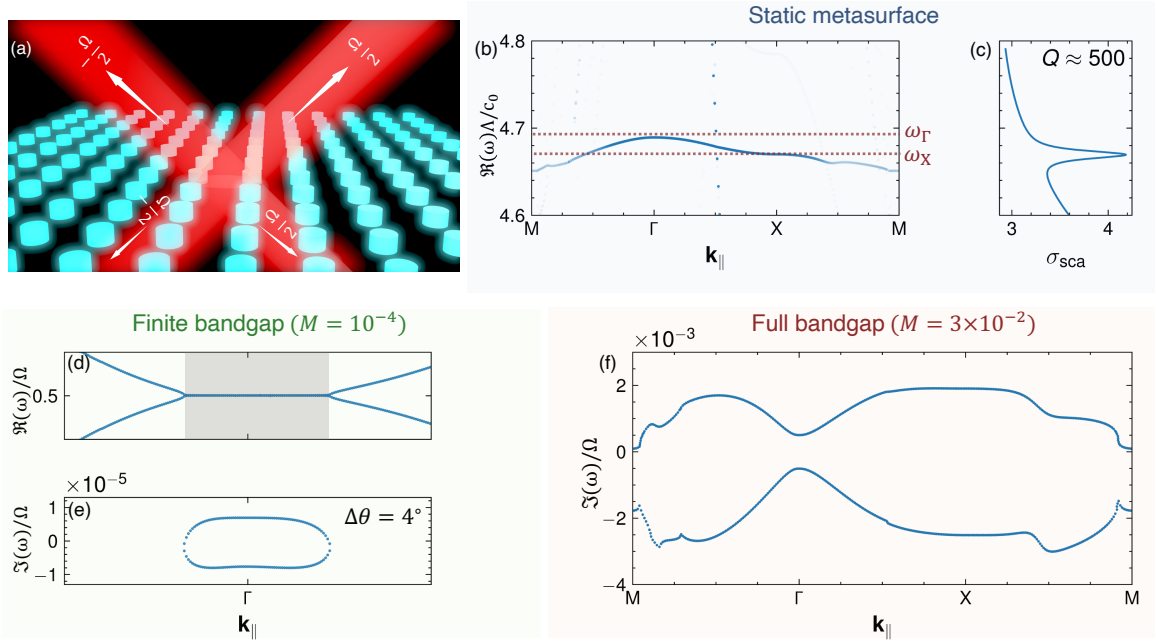


Figure 4.7.: **A qBIC resonant PTC based on a cylinder metasurface.** (a) An illustration of the time-varying metasurface made from a square lattice of cylinders. (b) The bandstructure of the metasurface in (a) under static conditions. (c) The rotationally averaged scattering cross section σ_{sca} of the isolated static cylinder as a function of the frequency ω. The cylinder supports a qBIC with the quality factor $Q \approx 500$. (d) The bandstructure of the time-varying metasurface with $M = 10^{-4}$ and $\Omega = 2\omega'_\Gamma = 2\pi \times 136$ THz. We observe the existence of a noticeable momentum bandgap with the incident angle range $\Delta\theta = 4°$ near the $\Gamma-$point. (e) The imaginary part of the frequency $\Im(\omega)$ inside the bandgap for a fixed $\Re(\omega) = \Omega/2$. We find that there exist modes with both the positive and negative imaginary parts of the frequency. Furthermore, the symmetry of the displayed modes is compatible with the TE-polarized PWs. (f) The imaginary part of the frequency inside a full bandgap supported by the metasurface with $M = 3 \times 10^{-2}$ and $\Omega = 2\omega'_X = 2\pi \times 134$ THz. We observe that there exist modes with $\Im(\omega) > 0$ for all $\mathbf{k}_\parallel$ values at the edges of the IBZ. Here, ω_Γ and ω_X are the original, and ω'_Γ and ω'_X are the DC-shifted flat band frequencies. This figure has been adapted from [P1]. © The authors, licensed under CC BY 4.0.

We emphasize that the cylinder-based metasurface requires much lower modulation amplitudes to open noticeable momentum bandgaps as compared to both the Mie-resonant and homogeneous PTCs (see Sec. 4.3). In fact, we found that, for similar material parameters, the qBIC-resonant PTCs require an order of magnitude lower M than the dipolar Mie-resonant PTCs to open bandgaps of similar size. Furthermore, we note that the laser-induced damage threshold intensity of Ge is approximately 100 GW/cm^2 under multi-shot pump pulses [132]. Spatial structuring lowers this intensity by an order of magnitude, i.e., to approximately 10 GW/cm^2 [98, 99]. Therefore, we conclude that our design operating at 0.7 GW/cm^2 is well implementable using the Kerr-induced time-varying permittivity mechanism. Furthermore, we have explicitly confirmed that the utilized qBICs of the cylinders are robust against thermo-optic and thermal expansion effects.

Finally, we demonstrate that similar to the previous example, the cylinder-based metasurface can also host full bandgaps. To do so, we increase the modulation amplitude to $M = 3 \times 10^{-2}$, and fix the modulation frequency to $\Omega = 2\omega'_{\mathrm{X}}$. Our simulations show that for this choice of Ω, the required M to open a full bandgap is minimized. Numerically, $\Omega = 2\omega'_{\mathrm{X}} = 2\pi \times 134$ THz. We keep all the other parameters unchanged. We plot the imaginary part of the frequency $\Im(\omega)$ as a function of the in-plane wavevector $\mathbf{k}_{\|}$ in Fig. 4.7(f). Here, we observe that $\Im(\omega) > 0$ for all the $\mathbf{k}_{\|}$ values at the edges of the IBZ, leading to the demonstration of a full bandgap. We remark that the pump intensity corresponding to the used modulation amplitude in this case is 210 GW/cm^2. Such a value is about 20 times higher than the damage threshold of structured Ge under the multi-shot pump pulses. However, under a single-shot pulse, it has been demonstrated that the damage threshold of structured Ge could be considerably increased [133]. Therefore, a careful optimization of the repetition rate of the pump pulse could bring full momentum bandgaps within reach of future experiments.

Chapter summary

In this chapter, we presented the application of high-Q resonances to open noticeable momentum bandgaps in metasurface-based PTCs. Using Mie resonant spherical meta-atoms, we found that the size of the momentum bandgaps can be expanded for both the evanescent and propagating PWs despite small modulation amplitudes as compared to homogeneous PTCs. We also confirmed the robustness of the obtained bandgaps against material losses. Next, we utilized even higher-Q qBICs of multilayered spherical and cylindrical meta-atoms. Specifically, using the multilayered sphere-based metasurfaces, we showed that, in theory, the required modulation amplitude to open a momentum bandgap approaches zero as the spheres are tuned to support diverging-Q resonances. Finally, using cylinder-based metasurfaces, we proposed a more practical design of the resonant PTCs. We demonstrated that the required values of the modulation amplitudes to open noticeable bandgaps are well within reach using the Kerr-induced time-varying permittivity. We believe that our results will pave the way for the first experimental realization of the PTCs at optical frequencies.

In the next chapter, building on our understanding of resonant PTCs, we study the physics of scattering anomalies such as exceptional points, coherent perfect absorption, lasing, and nonreciprocity in time-varying metasurfaces. Leveraging the qBICs, all these effects are observed at perturbative modulation amplitudes.

5 | Scattering anomalies in PTCs

Scattering anomalies refer to unconventional scattering phenomena in engineered photonic structures [51]. In recent years, there has been a growing interest in studying unusual phenomena such as the emergence of exceptional points, coherent perfect absorption, coherent amplification (lasing), and nonreciprocity in metamaterials [51, 134]. In the following, we provide a short introduction to these physical effects.

Exceptional points: Exceptional points (EPs) refer to those special points in the parameter space where two or more eigenvalues of the S-matrix of a scattering structure coalesce. Crucially, the corresponding eigenvectors must also become parallel to form the EPs. Therefore, the space spanned by the eigenvectors reduces, and the S-matrix becomes defective [51]. Furthermore, near EPs, the eigenvalues are extremely sensitive to the perturbation of the system parameters. Therefore, EP-supporting structures are promising for sensing applications [135]. In photonics, parity-time ($\mathcal{PT}$) symmetric structures have been extensively considered for studying the physics of EPs. The permittivity of such structures satisfies the relation $\varepsilon(\mathbf{r}) = \varepsilon^*(-\mathbf{r})$, which corresponds to a spatially arranged gain-loss material distribution [136]. Analogously, systems with a time-varying permittivity form a gain-loss type configuration with respect to the temporal dimension. Roughly speaking, for non-dispersive systems, when the permittivity of a medium decreases, the electromagnetic fields gain energy from the system. Conversely, when the permittivity increases, the fields lose energy to the system. Due to this gain-loss mechanism, time-varying media also support EPs [137].

Coherent perfect absorption: Coherent perfect absorption (CPA) occurs when an incoming light field optimally structured in its degrees of freedom in space and time is injected into a structure such that no outgoing field is produced. Such a cancellation of the outgoing field results from destructive interference between the contributions to each outgoing channel. In terms of the S-matrix, a CPA state corresponds to the field of an eigenvector with a vanishing eigenvalue [138]. CPA allows for the engineering of perfect absorbers for specific incoming fields. Because time-varying systems do not conserve energy, they can be designed to exhibit CPA [137].

Coherent amplification (lasing): As the time-reversed version of CPA, coherent amplification (lasing) occurs when a finite outgoing field is generated from an active system for a vanishing incoming field. A scattering system achieves such a regime when its radiative and material losses are exactly compensated by a gain-inducing mechanism. In terms of the S-matrix, a lasing state occurs when one of its eigenvalues reaches infinity at a real frequency. Furthermore, the spatiotemporal field pattern of the lasing state is given by the field profile of the corresponding eigenvector. Because time-varying systems do not conserve energy, they can also be driven into such a lasing regime [137].

Nonreciprocity: Nonreciprocity implies that the field generated by a source at an observation mode differs from that obtained when the source and the observation modes are interchanged [134]. Nonreciprocity has been extensively studied in the literature to enable directional effects such as one-way light transmission [139], one-way amplification [140], asymmetric heat emission [141], among many others [134]. In linear systems, nonreciprocity can be attained

by breaking their time-reversal symmetry [134]. Therefore, linear time-varying metamaterials form viable candidates to study nonreciprocal light propagation. In essence, the time-reversal symmetry can be broken by assuming a time-asymmetric permittivity modulation. Such an asymmetric modulation implies that $\varepsilon(t)$ is such that there exists no time t_0 for which $\varepsilon(-t+t_0) = \varepsilon(t+t_0)$ [134].

In this chapter, we study the anomalous scattering phenomena of EPs, CPA, lasing, and nonreciprocity in time-varying metamaterials. We harness the resonances of the underlying structures to realize these phenomena at extremely small modulation amplitudes. In particular, in Sec. 5.1, we discuss the transformation of the S-matrix to a photon number flux-normalized basis, and the emerging symmetry-based constraints. Then, in Sec. 5.2, utilizing such constraints, we reveal the existence of EPs, CPA, and lasing in time-varying spheres, metasurfaces, and Fabry-Perot cavities. Finally, in Sec. 5.3, by breaking the time-reversal symmetry using a traveling-wave-type permittivity modulation in multilayered metasurfaces, we uncover nonreciprocal light propagation. We remark that for simplicity, we ignore material dispersion in this chapter. Therefore, we account for the temporal modulation of the underlying media using a dispersionless time-periodic background permittivity $\varepsilon_\infty(t)$ (see Subsec. 2.3.3).

This chapter is based on our works in [P2, P3]. We acknowledge a close collaboration with Dr. David Globosits from the group of Prof. Stefan Rotter at the TU Wien, who laid the foundation for studying EPs, CPA, lasing, and nonreciprocity using S-matrices. The author extended these concepts to complex scattering objects such as time-varying spheres and metasurfaces, as presented here.

5.1. S-matrix in a photon number flux-normalized basis

The S-matrices of time-periodic structures satisfy certain important relations when expressed in photon number flux-normalized bases. In the following, we discuss these bases and the corresponding relations for time-varying spheres and metasurfaces. We also provide a physical interpretation of the eigenvalues of the S-matrices in such bases.

Time-varying spheres

First, we consider a sphere made from a time-varying medium (see Fig. 2.1(a)). For a given set of scattered field coefficients $\mathbf{A}^{\mathrm{sca}}$, the time-averaged scattered power flux $\langle \boldsymbol{\mathcal{S}}_j^{\mathrm{sca}} \rangle$ at the frequency ω_j in the far field of the sphere is given by (see Eq. (2.38))

$$\langle \boldsymbol{\mathcal{S}}_j^{\mathrm{sca}} \rangle = \sum_{lms} \frac{1}{2Z_0} \frac{c_0^2}{|\omega_j|^2} |A_{jlms}^{\mathrm{sca}}|^2 \,. \tag{5.1}$$

Therefore, the photon number flux ϕ_j corresponding to $\langle \boldsymbol{\mathcal{S}}_j^{\mathrm{sca}} \rangle$ can be written as

$$\phi_j = \frac{\langle \boldsymbol{\mathcal{S}}^{\mathrm{sca}} \rangle}{\hbar |\omega_j|} = \sum_{lms} \frac{c_0^2 \left| A_{jlms}^{\mathrm{sca}} \right|^2}{2Z_0 \hbar |\omega_j|^3} \,, \tag{5.2}$$

where $\hbar$ is the reduced Planck's constant. Using the expression of ϕ_j, we find that the scattered field coefficients $\tilde{\mathbf{A}}^{\mathrm{sca}}$ in a photon number flux-normalized basis can be obtained by

the transformation

$$\tilde{A}^{\mathrm{sca}}_{jlms} = \sqrt{\frac{c_0^2}{2Z_0\hbar|\omega_j|^3}}\, A^{\mathrm{sca}}_{jlms}\,. \tag{5.3}$$

Similarly, for the incident field coefficients $\tilde{\mathbf{A}}^{\mathrm{inc}}$, we can write

$$\tilde{A}^{\mathrm{inc}}_{j'l'm's'} = \sqrt{\frac{c_0^2}{2Z_0\hbar|\omega_{j'}|^3}} A^{\mathrm{inc}}_{j'l'm's'}\,. \tag{5.4}$$

The T-matrix $\tilde{\mathbf{T}}_0(\omega)$ of the sphere in a photon number flux-normalized basis satisfies $\tilde{\mathbf{A}}^{\mathrm{sca}} = \tilde{\mathbf{T}}_0(\omega)\,\tilde{\mathbf{A}}^{\mathrm{inc}}$ (see Eq. (2.30)). Using Eqs. (5.3)–(5.4), the elements of $\tilde{\mathbf{T}}_0(\omega)$ can be calculated from those of $\mathbf{T}_0(\omega)$ by the transformation

$$\tilde{T}_0^{\{jlms\},\{j'l'm's'\}} = \sqrt{\left|\frac{\omega_{j'}}{\omega_j}\right|^3} T_0^{\{jlms\},\{j'l'm's'\}}. \tag{5.5}$$

Finally, the S-matrix $\tilde{\mathbf{S}}_0(\omega)$ of the time-varying sphere in a photon number flux-normalized basis can be calculated from $\tilde{\mathbf{T}}_0(\omega)$ as (see Eq. (2.34))

$$\tilde{\mathbf{S}}_0(\omega) = \mathbf{I} + 2\tilde{\mathbf{T}}_0(\omega)\,. \tag{5.6}$$

For time-periodic modulation profiles of $\varepsilon_\infty(t)$, the matrix $\tilde{\mathbf{S}}_0(\omega)$ satisfies the pseudounitarity condition [142]

$$\tilde{\mathbf{S}}_0^\dagger \mathbf{V} \tilde{\mathbf{S}}_0 = \mathbf{V}\,. \tag{5.7}$$

Furthermore, for time-reversal symmetric modulation profiles of $\varepsilon_\infty(t)$, i.e., reciprocal configurations, $\tilde{\mathbf{S}}_0(\omega)$ satisfies the reciprocity condition [143]

$$\mathbf{V}\tilde{\mathbf{S}}_0^{\mathrm{T}}\mathbf{V} = \tilde{\mathbf{S}}_0\,. \tag{5.8}$$

Here, $\mathbf{V}$ is a diagonal matrix with entries ± 1 depending on the sign of ω_j. Specifically, the elements of $\mathbf{V}$ are given as $V^{\{jlms\},\{j'l'm's'\}} = \delta_{jj'}\delta_{ll'}\delta_{mm'}\delta_{ss'}\frac{\omega_j}{|\omega_j|}$. Note that the pseudounitarity condition of the S-matrix can be derived by considering the generalized Poynting theorem for time-varying systems (see [142] for details). Furthermore, the reciprocity condition can be derived by invoking the generalized Lorentz reciprocity theorem for time-varying media (see [134] and [143] for details).

Time-varying metasurfaces

Next, we consider time-varying metasurfaces (see Fig. 2.1(b)–(c)). The far-field intensity flux I_j^{out} carried by the outgoing fields of the metasurface at the frequency ω_j is given by (see Eq. (2.61))

$$I_j^{\mathrm{out}} = \sum_{\mathbf{g}\alpha d} \frac{c_0}{2Z_0} \frac{|k^{\mathrm{p}}_{z;j\mathbf{g}\alpha d}|}{|\omega_j|} |U^{\mathrm{out,p}}_{j\mathbf{g}\alpha d}|^2\,. \tag{5.9}$$

Here, $U^{\mathrm{out,p}}_{j\mathbf{g}\alpha d}$ refer to the field coefficients corresponding to the propagating outgoing waves (with $\Re\{k_{z;j\mathbf{g}\alpha d}\} = k^{\mathrm{p}}_{z;j\mathbf{g}\alpha d} \neq 0$). The contribution of the evanescent waves (with $\Re\{k_{z;j\mathbf{g}\alpha d}\} =$

0) to I_j^{out} is zero as they do not carry any intensity flux. The photon number flux ϕ_j corresponding to I_j^{out} is given by

$$\phi_j = \frac{I_j^{\text{out}}}{\hbar|\omega_j|} = \sum_{\mathbf{g}\alpha d} \frac{c_0}{2Z_0} \frac{|k^{\text{p}}_{z;j\mathbf{g}\alpha d}|}{\hbar|\omega_j|^2} |U^{\text{out,p}}_{j\mathbf{g}\alpha d}|^2 \,. \tag{5.10}$$

From the expression of ϕ_j, we find that the outgoing field coefficients $\tilde{\mathbf{U}}^{\text{out,p}}$ in a photon number flux-normalized basis can be obtained by the transformation

$$\tilde{U}^{\text{out,p}}_{j\mathbf{g}\alpha d} = \sqrt{\frac{c_0|k^{\text{p}}_{z;j\mathbf{g}\alpha d}|}{2Z_0\hbar|\omega_j|^2}} U^{\text{out,p}}_{j\mathbf{g}\alpha d} \,. \tag{5.11}$$

Similarly, for the incident field coefficients $\tilde{\mathbf{U}}^{\text{inc,p}}$, we can write

$$\tilde{U}^{\text{inc,p}}_{j'\mathbf{g}'\alpha' d'} = \sqrt{\frac{c_0|k^{\text{p}}_{z;j'\mathbf{g}'\alpha' d'}|}{2Z_0\hbar|\omega'_j|^2}} U^{\text{inc,p}}_{j'\mathbf{g}'\alpha' d'} \,. \tag{5.12}$$

The S-matrix $\tilde{\mathbf{S}}_{\text{pp}}(\omega, \mathbf{k}_\parallel)$ of the metasurface in a photon number flux-normalized basis satisfies $\tilde{\mathbf{U}}^{\text{out,p}} = \tilde{\mathbf{S}}_{\text{pp}}(\omega, \mathbf{k}_\parallel)\, \tilde{\mathbf{U}}^{\text{inc,p}}$ (see Eq. (2.54)). Note that for metasurfaces, the incoming fields are the incident fields. From Eqs. (5.11)–(5.12), we find that the elements of $\tilde{\mathbf{S}}_{\text{pp}}(\omega, \mathbf{k}_\parallel)$ can be calculated from those of $\mathbf{S}_{\text{pp}}(\omega, \mathbf{k}_\parallel)$ using the transformation

$$\tilde{S}^{\{j\mathbf{g}\alpha d\},\{j'\mathbf{g}'\alpha' d'\}}_{\text{pp}} = \left|\frac{\omega_{j'}}{\omega_j}\right| \sqrt{\left|\frac{k^{\text{p}}_{z;j\mathbf{g}\alpha d}}{k^{\text{p}}_{z;j'\mathbf{g}'\alpha' d'}}\right|} S^{\{j\mathbf{g}\alpha d\},\{j'\mathbf{g}'\alpha' d'\}}_{\text{pp}} \,. \tag{5.13}$$

Note that the matrix $\mathbf{S}_{\text{pp}}(\omega, \mathbf{k}_\parallel)$ is a reduced version of the full S-matrix $\mathbf{S}(\omega, \mathbf{k}_\parallel)$ given in Eq. (2.54). By definition, $\mathbf{S}_{\text{pp}}(\omega, \mathbf{k}_\parallel)$ only accounts for the propagating incident and outgoing PWs. Physically, such a reduced S-matrix corresponds to the case when the sources and the detectors are kept in the far field of the metasurface.

Similar to the sphere, for time-periodic modulation profiles of $\varepsilon_\infty(t)$, the matrix $\tilde{\mathbf{S}}_{\text{pp}}(\omega, \mathbf{k}_\parallel)$ satisfies the pseudounitarity condition [142]

$$\tilde{\mathbf{S}}^\dagger_{\text{pp}} \mathbf{V} \tilde{\mathbf{S}}_{\text{pp}} = \mathbf{V} \,. \tag{5.14}$$

Furthermore, for time-reversal symmetric modulation profiles of $\varepsilon_\infty(t)$, $\tilde{\mathbf{S}}_{\text{pp}}(\omega, \mathbf{k}_\parallel)$ satisfies the reciprocity condition [134, 143]

$$\mathbf{V} \tilde{\mathbf{S}}^{\text{T}}_{\text{pp}} \mathbf{V} = \tilde{\mathbf{S}}_{\text{pp}} \,. \tag{5.15}$$

Here, the elements of $\mathbf{V}$ are given by $V^{\{j\mathbf{g}\alpha d\},\{j'\mathbf{g}'\alpha' d'\}} = \delta_{jj'}\delta_{\mathbf{g}\mathbf{g}'}\delta_{\alpha\alpha'}\delta_{dd'}\frac{\omega_j}{|\omega_j|}$.

Physical interpretation of the eigenvalues

The pseudounitarity condition (see Eqs. (5.7) and (5.14)) implies that the eigenvalues of the corresponding S-matrix appear as inverse conjugate pairs, i.e., $\left(\lambda, \frac{1}{\lambda^*}\right)$ [142, 144]. To physically interpret these eigenvalues, we start by assuming that $\tilde{\mathbf{x}}$ is an eigenvector of

the S-matrix $\tilde{\mathbf{s}}$ of an arbitrary time-varying scatterer. Here, $\tilde{\mathbf{s}}$ is expressed in a photon number flux-normalized basis. Because $\tilde{\mathbf{x}}$ is an eigenvector, it satisfies $\tilde{\mathbf{s}}\tilde{\mathbf{x}} = \lambda\tilde{\mathbf{x}}$. However, by definition, an incoming state $\tilde{\mathbf{u}}^{\text{in}}$ is mapped to the outgoing state $\tilde{\mathbf{u}}^{\text{out}}$ by the S-matrix as $\tilde{\mathbf{u}}^{\text{out}} = \tilde{\mathbf{s}}\tilde{\mathbf{u}}^{\text{in}}$ (see Eq. (2.54)). Therefore, if $\tilde{\mathbf{u}}^{\text{in}} = \tilde{\mathbf{x}}$ is an incoming state to the scatterer, the corresponding outgoing state is $\tilde{\mathbf{u}}^{\text{out}} = \lambda\tilde{\mathbf{x}}$. In particular, if $|\lambda| \to 0$, $\tilde{\mathbf{u}}^{\text{out}} \to 0$. Therefore, for a finite incoming field, we get a negligible outgoing field. Physically, the incoming field gets absorbed by the scatterer, signifying CPA. Conversely, if $|\lambda| \to \infty$, $\tilde{\mathbf{u}}^{\text{out}} \to \infty$. Therefore, for a finite incoming field, we get a diverging outgoing field. Furthermore, in the limit when the incoming field becomes arbitrarily small, a finite outgoing field can still be obtained due to a diverging $|\lambda|$, signifying lasing.

We further note that because $\tilde{\mathbf{u}}^{\text{in}} = \tilde{\mathbf{x}}$ is expressed in a photon number flux-normalized basis, $\tilde{\mathbf{x}}^\dagger\tilde{\mathbf{x}}$ represents the incoming photon number flux. For the corresponding outgoing state $\tilde{\mathbf{u}}^{\text{out}} = \lambda\tilde{\mathbf{x}}$, the photon number flux is $|\lambda|^2\tilde{\mathbf{x}}^\dagger\tilde{\mathbf{x}}$. Therefore, if $|\lambda| = 1$, the system conserves the photon number flux. On the other hand, if $|\lambda| \neq 1$, the flux conservation does not hold.

In the following, we always express the S-matrices of the time-varying spheres and metasurfaces in a photon number flux-normalized basis. We utilize the discussed pseudounitarity and reciprocity relations to explain various emerging features from such complex scatterers.

5.2. Exceptional points, coherent perfect absorption, and lasing

In this section, we focus on the emergence of EPs, CPA, and lasing for a wide class of time-varying structures. We consider isolated time-varying spheres, time-varying metasurfaces hosting symmetry-protected BICs (SP-BICs), and time-varying cavities hosting Fabry-Perot BICs (FP-BICs).

5.2.1. Isolated time-varying spheres

We begin with an isolated time-varying sphere (see Fig. 5.1(a)). We assume the background permittivity of the material of the sphere to be of the form $\varepsilon_\infty(t) = 1 + \chi_{\infty,\text{st}}[1 + M\cos(\Omega t)]$ (see Subsec. 2.3.3). We use $\chi_{\infty,\text{st}} = 11.67$ here and in the following subsection. Furthermore, we set the modulation frequency to $\Omega = 2\pi \times 151$ THz, and the radius of the sphere to $\mathcal{R} = 568$ nm.

First, we plot the complex eigenvalues λ of the S-matrix $\tilde{\mathbf{S}}_0(\omega)$ of the sphere as a function of the modulation amplitude M for various values of the frequency ω (see Figs. 5.1(b)–(d)). Specifically, we use $\omega = 0.47\Omega$, $\omega = 0.5\Omega$, and $\omega = 0.53\Omega$. For all three cases, we find that as the modulation is turned on, i.e., $M \gtrsim 0$, all the eigenvalues of $\tilde{\mathbf{S}}_0(\omega)$ reside on the unit circle. As M is increased, in all three cases, several pairs of the eigenvalues approach each other on the unit circles and eventually coalesce, forming EPs. Due to the spatial symmetry of the sphere in 3D, three such eigenvalue pairs form EPs in each case. We have explicitly verified that the corresponding eigenvectors also become parallel at the EPs.

As M is further increased, the eigenvalue pairs leave the unit circles. Specifically, for $\omega = 0.5\Omega$, three eigenvalues approach zero, while their partner eigenvalues approach infinity (not shown). We note that due to the pseudounitarity of $\tilde{\mathbf{S}}_0(\omega)$, its eigenvalues appear as inverse-conjugate pairs, i.e., $\{\lambda, 1/\lambda^*\}$. Therefore, if one of the eigenvalues approaches zero ($|\lambda| \to 0$), its partner eigenvalue has to approach infinity ($1/|\lambda^*| \to \infty$). A zero eigenvalue corresponds to a CPA point, while an infinite eigenvalue corresponds to a lasing point (see Sec. 5.1). We find that the CPA and lasing eigenvalues primarily arise due to the

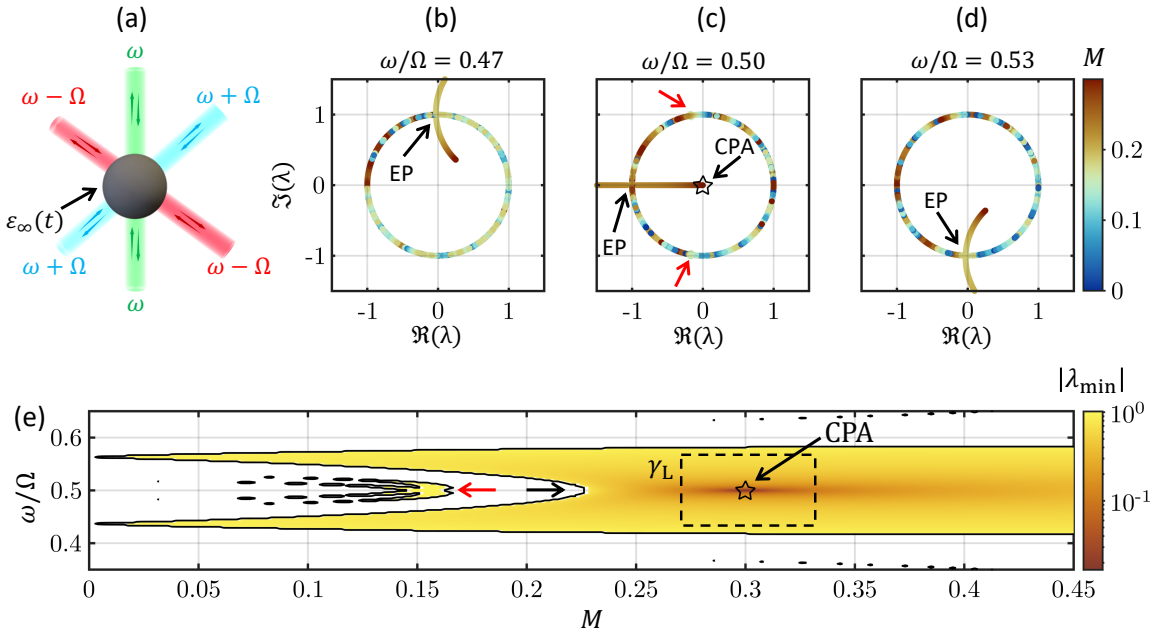


Figure 5.1.: **EPs, CPA, and lasing in time-varying spheres.** (a) A sphere made from a time-varying material with the background permittivity $\varepsilon_\infty(t) = 1 + \chi_{\infty,\mathrm{st}}[1 + M\cos(\Omega t)]$. (b),(c), and (d) The complex eigenvalues of the S-matrix of the time-varying sphere as a function of the modulation amplitude M for the frequencies $\omega = 0.47\Omega$, $\omega = 0.5\Omega$, and $\omega = 0.53\Omega$, respectively. In all three cases, for $M \gtrsim 0$, the eigenvalues reside on the unit circle. As M is increased, some of the eigenvalues coalesce, forming EPs. Upon further increasing M, the eigenvalues leave the unit circle. Specifically, for $\omega = 0.5\Omega$, some of the eigenvalues approach zero, marking a CPA point (enclosed by the star symbol). Furthermore, the partner eigenvalues simultaneously approach infinity, signifying lasing (not shown). (e) The absolute value of the minimal eigenvalue λ_{min} of the S-matrix as a function of ω and M. As before, we observe that near $\omega = 0.5\Omega$, upon increasing M, $|\lambda_{\mathrm{min}}|$ departs from the unity condition, forming EPs (black curve). Furthermore, the CPA point at $M = 0.3$ for which $|\lambda_{\mathrm{min}}| \to 0$ is clearly visible (enclosed by the star symbol). Note that the red arrows in (c) and (e) mark the EPs that are formed due to the higher-order scattered frequencies, i.e., for $j < -j_0 - 1$ and $j > -j_0$. This figure has been adapted from [P2]. © The authors, licensed under CC BY 4.0.

magnetic dipolar part of the S-matrix $\tilde{\mathbf{S}}_0(\omega)$ of the sphere. Moreover, the corresponding eigenvectors have a dominant contribution from the lowest-order scattered frequencies, i.e., $j \in \{-j_0 - 1, -j_0\}$ (see Sec. 2.2). Importantly, before the EP, since the eigenvalues are unimodular (i.e., $|\lambda| = 1$), the time-varying sphere conserves the photon number flux. On the other hand, beyond the EP, since $|\lambda| \neq 1$, this conservation is broken. Therefore, the EP marks a transition of the system from a regime in which the eigenstates conserve the photon number flux to a regime in which the eigenstates break this conservation. Furthermore, we note the existence of additional EPs (red arrows) at certain modulation amplitudes in Fig. 5.1(c). These EPs are primarily formed due to the higher-order scattered frequencies, i.e., for $j < -j_0 - 1$ and $j > -j_0$. Upon increasing M, the eigenvalues corresponding to these EPs leave the unit circle, but rather than going to zero (or infinity), they recombine on the unit circle in the considered M range.

In Figs. 5.1(b) and (d), we note that beyond the EPs, while the eigenvalues leave the unit circles, none of them reach the extreme values of zero and infinity. Such a behavior is expected, as only for $\omega = 0.5\Omega$, the parametric amplification condition is satisfied in the systems with a sinusoidal temporal modulation (see Eq. (15) in [57]). Therefore, for $\omega \neq 0.5\Omega$, it is not possible to realize CPA and lasing points. Nevertheless, with more complicated temporal permittivity modulation, such as the traveling-wave-type modulation, CPA and lasing can be achieved even for $\omega \neq 0.5\Omega$ [145].

To study the influence of the frequency ω and the modulation amplitude M further, we plot the absolute value of the minimal eigenvalue λ_{min} of the S-matrix of the sphere as a function of ω and M (see Fig. 5.1(e)). By minimal, we refer to the eigenvalue with the smallest absolute value. Here, we observe that when the system is detuned sufficiently far from the $\omega = 0.5\Omega$ condition, $|\lambda_{\text{min}}|$ is unity, and no EPs appear (white region). By contrast, near $\omega = 0.5\Omega$ at finite M, we observe the onset of non-unity $|\lambda_{\text{min}}|$, signifying EPs (black curve). Upon further increasing M, as expected, $|\lambda_{\text{min}}|$ departs from the unity condition, entering the non-conservative regime. In fact, at $\omega = 0.5\Omega$ and $M = 0.3$, we observe that $|\lambda_{\text{min}}|$ becomes negligible, indicating a CPA point there (enclosed by the star symbol). Furthermore, the partner eigenvalue $|\lambda_{\text{max}}|$ approaches infinity for the same M and ω, indicating the simultaneous existence of a lasing point (not shown). Here, $\lambda_{\text{max}} = 1/\lambda^*_{\text{min}}$ is the eigenvalue with the largest absolute value. We emphasize that beyond the CPA/lasing point, upon further increasing M, $|\lambda_{\text{min}}|$ becomes finite again. This behavior arises because the modulation-induced gain shifts the zeros/poles of the S-matrix away from the real-frequency axis into the complex-frequency plane. Consequently, when considering only real frequencies, as here, the zeros/poles are no longer captured, resulting in a finite $|\lambda_{\text{min}}|$ and $|\lambda_{\text{max}}|$.

In Fig. 5.1(e), we note that due to a finite numerical precision of M, while $|\lambda_{\text{min}}|$ becomes extremely small at the CPA point, i.e., $|\lambda_{\text{min}}| = 2 \times 10^{-4}$, it does not exactly become zero. To unambiguously prove that in the vicinity of such an eigenvalue, there exists a true CPA point, we compute the winding number, $\text{wind}\{\tilde{\mathbf{S}}(\omega)\}$, along a closed loop γ_{L}. Here, γ_{L} is parameterized by $0 \leq \phi_{\text{L}} < 2\pi$ in the parameter space (see Fig. 5.1(e)). The winding number is zero if the loop does not enclose a vanishing or diverging eigenvalue. However, if the loop encloses a CPA/lasing point, we expect the winding number to be $\pm 2n_{\text{deg}}$ [146, 147]. Here, n_{deg} is the number of CPA/lasing points enclosed in the loop. For polychromatic

pseudounitary S-matrices, the winding number is given by [143]

$$\text{wind}\{\tilde{\mathbf{S}}_0(\omega)\} \quad = \quad \frac{1}{2\pi i}\int_0^{2\pi} \mathrm{d}\phi_\mathrm{L}\,\mathrm{Tr}\left(\mathbf{V}\tilde{\mathbf{S}}_0^\dagger(\omega)\mathbf{V}\frac{\mathrm{d}\tilde{\mathbf{S}}_0(\omega)}{\mathrm{d}\phi_\mathrm{L}}\right). \tag{5.16}$$

We numerically verify that $\text{wind}\{\tilde{\mathbf{S}}_0(\omega)\} = 6 - 3.5\times10^{-4}$ in the present case, as expected, due to the threefold degeneracy ($n_\mathrm{deg} = 3$) of each eigenvalue of the time-varying sphere.

Next, we investigate the far-field intensity profiles of the CPA and lasing eigenstates. We operate at $\omega = 0.5\Omega$, and $M = 0.3$. We plot the space-integrated incoming and outgoing intensities $I_\mathrm{in}(t)$ and $I_\mathrm{out}(t)$ for the CPA and lasing states as a function of time in Fig. 5.2. For numerical convenience, we spatially integrate the intensities over the surface of an imaginary sphere with radius $\mathcal{R}_\mathrm{far} = 1000c_0\tau_\mathrm{m}$, such that $\mathcal{R}_\mathrm{far} \gg \mathcal{R}$. Specifically, in Figs. 5.2(a)–(b), we plot the incoming and outgoing intensities of the CPA state. The corresponding eigenvalue is very small, i.e., $|\lambda_\mathrm{min}| = 2\times10^{-4}$. We find that the outgoing intensity $I_\mathrm{out}(t)$ of the CPA state is many orders of magnitude smaller than the corresponding incoming intensity $I_\mathrm{in}(t)$. Such a behavior confirms that upon interaction with the time-varying sphere, most of the incoming photons are absorbed. Physically, the outgoing field is such that it experiences a strong destructive interference in the far field of the sphere. Therefore, there is a near-perfect cancellation of the outgoing radiation, leading to CPA.

Similarly, the incoming and outgoing intensities for the lasing state are shown in Figs. 5.2(c)–(d). The corresponding eigenvalue is very large, i.e., $|\lambda_\mathrm{max}| = 1/|\lambda_\mathrm{min}| = 5\times10^3$. We find that the outgoing intensity $I_\mathrm{out}(t)$ is many orders of magnitude larger than the incoming intensity $I_\mathrm{in}(t)$, signifying extreme amplification. Physically, a diverging eigenvalue arises due to the existence of an S-matrix pole in the parameter space. Such a pole appears at real frequencies when the radiative and material losses of the system are exactly compensated by time-modulation-induced gain. Therefore, while operating near a pole, an arbitrarily small incoming field gives rise to a finite outgoing field. Hence, the system supports extreme amplification of the incoming field, as observed here.

We further highlight that the incoming CPA and the outgoing lasing intensity profiles are the time-reversed versions of each other due to reciprocity (see Figs. 5.2(a) and (d)). Since the sinusoidal temporal modulation preserves the time-reversal symmetry, the considered system is reciprocal. Therefore, the configuration attained by time-reversing the CPA behavior is also supported by the system. However, time-reversed CPA behavior implies that a system generates a finite outgoing field for an arbitrarily small incoming field. Such outgoing field generation from an arbitrarily small incoming field corresponds to lasing, explaining the correlation of the intensity profiles of the lasing and CPA states.

In the following subsection, we discuss the physics of EP, CPA, and lasing points in even more complex scattering structures, i.e., resonant time-varying metasurfaces.

5.2.2. Time-varying metasurfaces hosting SP-BICs

So far, we have demonstrated that time-varying spheres host EP, CPA, and lasing points. In this subsection, we extend the discussion of such scattering anomalies to time-varying metasurfaces. Specifically, we show that by exploiting the high-Q qBIC resonances of the metasurfaces, the required modulation amplitudes for obtaining the scattering anomalies can be considerably reduced.

We study a metasurface that is made from a square lattice of spheres (see Fig. 5.3(a)). Initially, we explore the static case. We optimize the geometric parameters of the metasurface

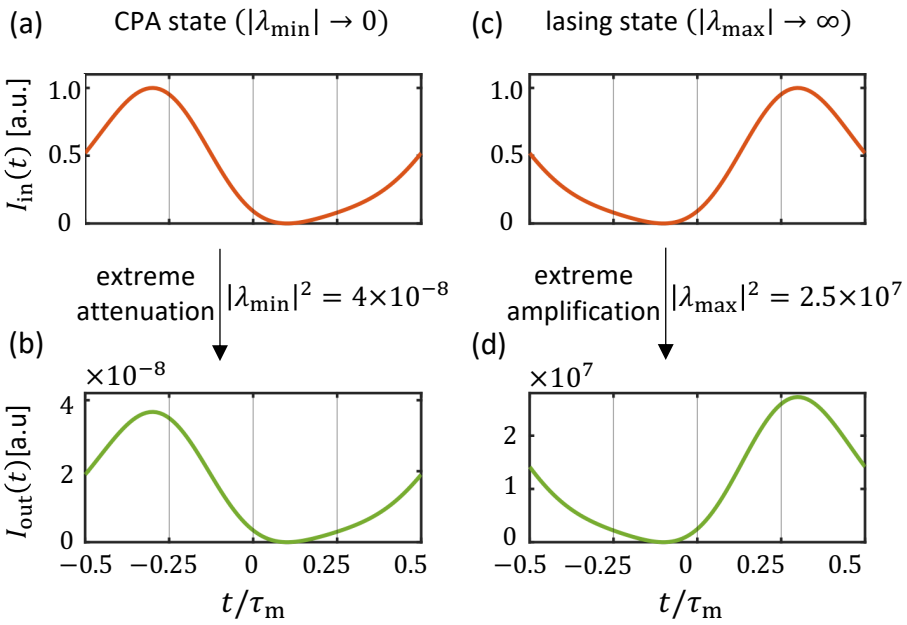


Figure 5.2.: **Outgoing and incoming intensities for the CPA and lasing states of the sphere.** (a) The space-integrated incoming intensity $I_{\text{in}}(t)$ as a function of time t for the CPA state. Here, the eigenvalue corresponding to the CPA state is $|\lambda_{\min}| = 2 \times 10^{-4}$. (b) The resulting outgoing intensity $I_{\text{out}}(t)$ when the incoming CPA state is injected into the system. We observe that the outgoing intensity is many orders of magnitude smaller than the incoming intensity. Hence, most of the incoming field gets absorbed by the time-varying system. (c) The space-integrated incoming intensity $I_{\text{in}}(t)$ as a function of time t for the lasing state. The eigenvalue corresponding to such a state is $|\lambda_{\max}| = 5 \times 10^{3}$. (d) The resulting outgoing intensity $I_{\text{out}}(t)$ when the incoming lasing state is injected into the system. Here, we observe that the outgoing intensity is many orders of magnitude larger than the incoming intensity. Therefore, extreme amplification of the incoming field takes place, signifying lasing. Note that the spatial integration of the intensities is done over an imaginary sphere of radius $\mathcal{R}_{\text{far}} = 1000 c_0 \tau_{\text{m}}$, such that $\mathcal{R}_{\text{far}} \gg \mathcal{R}$. Further note that the intensity corresponding to the outgoing lasing state is the time-reversed version of the incoming CPA state, due to the reciprocity of the system. This figure has been adapted from [P2]. © The authors, licensed under CC BY 4.0.

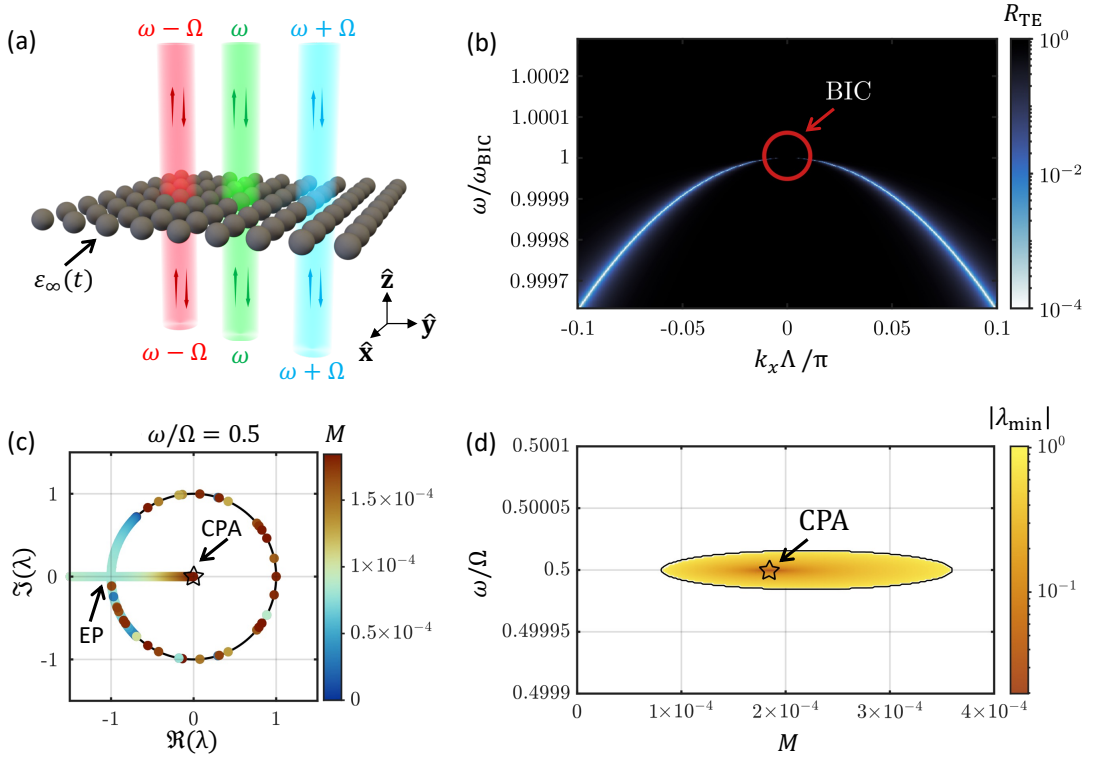


Figure 5.3.: **EPs, CPA, and lasing in time-varying metasurfaces.** (a) A time-varying metasurface made from a square lattice of spheres. Here, the material of each sphere has the background permittivity $\varepsilon_\infty(t) = 1 + \chi_{\infty,\mathrm{st}}[1 + M\cos(\Omega t)]$. (b) The reflectivity R_{TE} of the metasurface as a function of ω and k_x for the TE-polarized incident PWs. Here, we observe the existence of a resonance branch. As $\omega \to \omega_{\mathrm{BIC}}$ and $k_x \to 0$, the linewidth of the resonances on the branch narrows, eventually disappearing at $\omega = \omega_{\mathrm{BIC}}$ and $k_x = 0$. The resulting infinite-Q resonance at the Γ-point is an SP-BIC. (c) The complex eigenvalues of the S-matrix of the time-varying metasurface as a function of the modulation amplitude M at the frequency $\omega = 0.5\Omega$. Here, for $M \gtrsim 0$, the eigenvalues reside on a unit circle. As M is increased, two of the eigenvalues coalesce, forming an EP. Upon further increasing M, the eigenvalues leave the unit circle. One of the eigenvalues approaches zero, marking a CPA point (enclosed by the star symbol). On the other hand, the partner eigenvalue simultaneously approaches infinity, marking a lasing point (not shown). (d) The absolute value of the minimal eigenvalue λ_{min} of the S-matrix as a function of ω and M. As before, we observe that near $\omega = 0.5\Omega$, upon increasing M, $|\lambda_{\mathrm{min}}|$ departs from the unity condition, forming EPs (black curve). Furthermore, the CPA point at $M = 1.84 \times 10^{-4}$ for which $|\lambda_{\mathrm{min}}| \to 0$ is clearly visible (enclosed by the star symbol). Due to the resonant nature of the metasurface, the EP, CPA, and lasing points are observed at extremely small modulation amplitudes. For simplicity, we use $k_y = 0$ in all the simulations. Furthermore, in (c)–(d), we assume $k_x = 0.05\pi/\Lambda$ for which the metasurface supports a qBIC at $\omega = \omega_{\mathrm{qBIC}}$. This figure has been adapted from [P2]. © The authors, licensed under CC BY 4.0.

such that it supports an SP-BIC at the Γ-point, i.e., for $k_x = k_y = 0$. The radius of the spheres forming the metasurface is $\mathcal{R} = 225$ nm, and the lattice period is $\Lambda = 3\mathcal{R}$. Furthermore, the metasurface is subwavelength, and its response is predominantly dipolar. To numerically demonstrate the existence of the SP-BIC, using Eq. (2.62a), we plot the reflectivity R_{TE} of the metasurface as a function of k_x for TE-polarized incident PWs in Fig. 5.3(b). Here, for simplicity, we assume $k_y = 0$. We observe the existence of a resonance branch in the $\omega - k_x$ space. Furthermore, as $\omega \to \omega_{\mathrm{BIC}}$ and $k_x \to 0$, the linewidth of the resonances on the branch progressively becomes sharper, eventually vanishing at $\omega = \omega_{\mathrm{BIC}}$ and $k_x = 0$. This linewidth disappearance is a hallmark feature of a BIC. Such a resonance is termed SP-BIC because the symmetry of the corresponding eigenmode is not compatible with any of the available radiation channels of the metasurface at the Γ-point. By breaking the mirror symmetry of the lattice in the $x - y$ plane or by choosing an operating point slightly away from the Γ-point, we can excite high-Q qBICs. In the following, employing the latter approach by choosing $k_x \neq 0$, we exploit the qBICs of the metasurface.

For the simulations in the time-varying case, we use $k_x = 0.05\pi/\Lambda$, and correspondingly $\omega_{\mathrm{qBIC}} = 0.99991\omega_{\mathrm{BIC}}$. The symmetry of the resulting qBIC is compatible with TE-polarized PWs. Moreover, we choose the value of ω_{qBIC} so precisely due to the extremely narrow frequency region spanned by the resonance branch in Fig. 5.3(b). Furthermore, we use $\Omega = 2\omega_{\mathrm{qBIC}}$ ($= 2\pi \times 387$ THz). This choice implies that the lowest-order scattered frequencies are such that $\omega_{-j_0-1} = -\omega_{\mathrm{qBIC}}$ and $\omega_{-j_0} = \omega_{\mathrm{qBIC}}$. Notably, the metasurface is resonant at both frequencies. Therefore, despite time modulation, the field of the resulting eigenmode remains highly confined inside the metasurface. Such a confinement assists in considerably reducing the required modulation amplitude to observe the scattering anomalies, as shown in the following.

To reveal the existence of EP, CPA, and lasing points, we plot the complex eigenvalues of the S-matrix $\tilde{\mathbf{S}}(\omega, \mathbf{k}_\parallel)$ of the metasurface as a function of the modulation amplitude M (see Fig. 5.3(c)). Here, as for the sphere, we observe that as the modulation is turned on (i.e., $M \gtrsim 0$), all the eigenvalues of the S-matrix reside on a unit circle. As M is increased, two of the eigenvalues approach each other and eventually coalesce, forming an EP. We explicitly confirmed that the corresponding eigenvectors also become parallel at the EP. Upon further increasing M, leaving the unit circle, one of the eigenvalues approaches zero (i.e., $|\lambda| \to 0$), forming a CPA point. On the other hand, its partner eigenvalue approaches infinity (i.e., $|\lambda| \to \infty$), forming a lasing point. As before, such a correlated behavior of the eigenvalues arises because the eigenvalues of the pseudounitary S-matrix $\tilde{\mathbf{S}}(\omega, \mathbf{k}_\parallel)$ form inverse-conjugate pairs. Interestingly, we note that the EP, CPA, and lasing points arise at extremely small modulation amplitudes. The EP is formed at $M = 8.16 \times 10^{-5}$, and the CPA/lasing point is formed at $M = 1.84 \times 10^{-4}$. In theory, by moving closer to the BIC in the parameter space, i.e., $\omega \to \omega_{\mathrm{BIC}}$ and $k_x \to 0$, the required M for attaining the scattering anomalies can be made arbitrarily small. However, in realistic systems, losses induced due to material dispersion and fabrication imperfections always enforce a lower bound on M. Nevertheless, resonant metasurfaces with qBICs remain a useful platform to attain these unusual scattering features at relatively low modulation amplitudes.

To highlight the scattering anomalies more clearly, we plot the absolute value of the minimal eigenvalue of the S-matrix $\tilde{\mathbf{S}}(\omega, \mathbf{k}_\parallel)$ as a function of ω and M (see Fig. 5.4(d)). As before, we observe that when ω is sufficiently detuned from $\omega = 0.5\Omega$, the minimal eigenvalue is unimodular, i.e., $|\lambda_{\mathrm{min}}| = 1$ (white region). For ω values near 0.5Ω at finite M, we observe the departure of $|\lambda_{\mathrm{min}}|$ from unity, marking EPs (black curve). As M is further increased, at

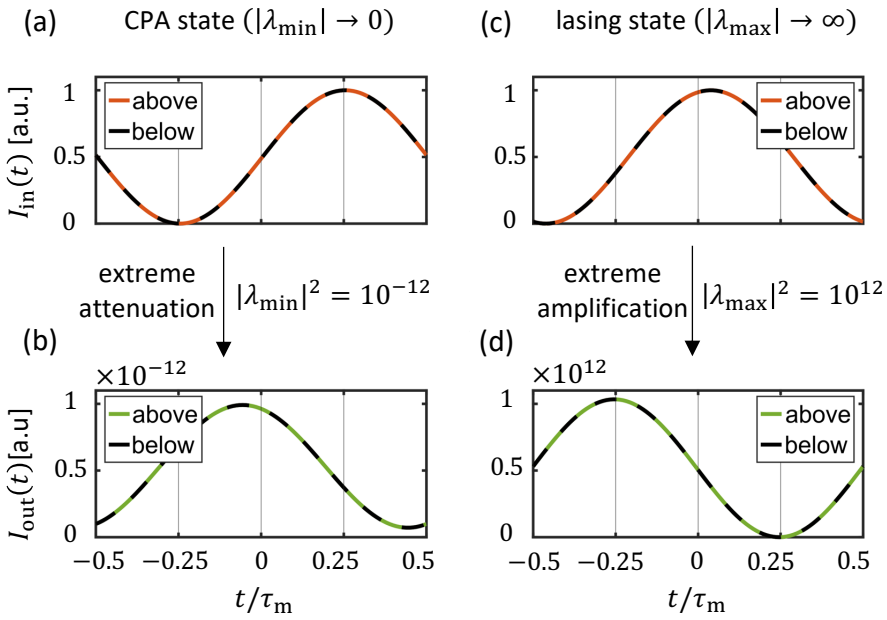


Figure 5.4.: **Outgoing and incoming intensities for the CPA and lasing states of the metasurface.** (a) The space-integrated incoming intensity $I_{\text{in}}(t)$ as a function of time t for the CPA state. Here, the eigenvalue corresponding to the CPA state is $|\lambda_{\min}| = 10^{-6}$. (b) The resulting outgoing intensity $I_{\text{out}}(t)$ when the incoming CPA state is injected into the system. Here, we observe that the outgoing intensity is many orders of magnitude smaller than the incoming intensity. Hence, most of the incoming field gets absorbed by the time-varying metasurface. (c) The space-integrated incoming intensity $I_{\text{in}}(t)$ as a function of time t for the lasing state. The eigenvalue corresponding to such a state is $|\lambda_{\max}| = 10^{6}$. (d) The resulting outgoing intensity $I_{\text{out}}(t)$ when the incoming lasing state is injected into the system. We observe that the outgoing intensity is many orders of magnitude larger than the incoming intensity. Therefore, extreme amplification of the incoming field takes place, signifying lasing. Note that the spatial integration of the intensities is done over infinite $x-y$ planes at $z = 1000\tau_{\text{m}}c_0$ (i.e., above the metasurface), and $z = -1000\tau_{\text{m}}c_0$ (i.e., below the metasurface). Further note that the intensity corresponding to the outgoing lasing state is the time-reversed version of the incoming CPA state, due to the reciprocity of the system. This figure has been adapted from [P2]. © The authors, licensed under CC BY 4.0.

$\omega = 0.5\Omega$ and $M = 1.84 \times 10^{-4}$, we observe a point where $|\lambda_{\min}|$ becomes extremely small, marking the CPA point (enclosed by the star symbol). At the same values of ω and M, the partner eigenvalue $\lambda_{\max}$ diverges, marking the lasing point (not shown). The winding number corresponding to such a CPA/lasing point is $\text{wind}\{\tilde{\mathbf{S}}(\omega, \mathbf{k}_{\|})\} = 2 - 10^{-4}$, as expected due to the TE-polarized qBIC of the metasurface (see Eq. (5.16)). Furthermore, as mentioned before, lasing occurs when the radiative loss (material loss is neglected in this chapter) of an eigenmode is exactly compensated by the time-modulation-induced gain. Here, since the eigenmode of the time-varying metasurface is formed by the hybridization of the qBIC modes at the frequencies ω_{qBIC} and $-\omega_{\text{qBIC}}$, it has an extremely small radiative loss. Consequently, only a small time-modulation-induced gain is needed to balance such loss. This explains the emergence of the lasing (and CPA) point at a perturbative M.

Next, we plot the far-field space-integrated incoming and outgoing intensities $I_{\text{in}}(t)$ and $I_{\text{out}}(t)$ as a function of time for the CPA and lasing states (see Fig. 5.4). We operate at $\omega = 0.5\Omega$ and $M = 1.84 \times 10^{-4}$. We show the corresponding intensities both below and above the metasurface plane. Specifically, we perform the spatial integration of the fields over infinite $x - y$ planes at $z = 1000 c_0 \tau_{\text{m}}$ (i.e., above the metasurface), and $z = -1000 c_0 \tau_{\text{m}}$ (i.e., below the metasurface). In Figs. 5.4(a)–(b), we consider the CPA state. The eigenvalue corresponding to such a state is extremely small, i.e., $|\lambda_{\min}| = 10^{-6}$. Consequently, we observe that for a finite incoming light field, a vanishingly small outgoing field is obtained, signifying CPA. Note that the incoming field consists of PWs that approach the metasurface from both above and below. This specific configuration of the incoming field is needed to facilitate the destructive interference of the resulting outgoing field.

Similarly, we consider the lasing state in Figs. 5.4(c)–(d). The eigenvalue corresponding to such a state is extremely large, i.e., $|\lambda_{\max}| = 1/|\lambda_{\min}| = 10^6$. Therefore, as expected, we find that a finite incoming field gives rise to a diverging outgoing field, indicating lasing. Furthermore, because the field amplification occurs at a perturbative modulation amplitude, our design is an example of a low-threshold metasurface-based laser [122]. Moreover, as before, due to reciprocity, we observe that the incoming CPA state (Fig. 5.4(a)) is the time-reversed version of the outgoing lasing state (Fig. 5.4(d)).

To summarize the discussion so far, we have studied the applications of the constraints imposed by pseudounitarity and reciprocity on the S-matrices of time-varying spheres and (monolayer) metasurfaces. We showed the existence of EP, CPA, and lasing points in these complex scattering structures. Specifically, for monolayer time-varying metasurfaces, we exploited qBICs to lower the required modulation amplitudes to attain the scattering anomalies.

In the remainder of this chapter, we investigate multilayered time-varying metasurfaces. First, using the example of Fabry-Perot cavities formed by stacking two identical metasurfaces, we show that the EP, CPA, and lasing points can be made polarization-insensitive. Second, by breaking the time-reversal symmetry of the temporal modulation, we engineer a strong nonreciprocal response in multilayered metasurfaces.

5.2.3. Time-varying cavities hosting FP-BICs

As emphasized earlier, metasurfaces represent powerful optical platforms that allow us to engineer light-matter interactions on demand. So far, in this thesis, we have seen that monolayer metasurfaces can support a range of interesting physical phenomena, including sizable momentum bandgaps and scattering anomalies. Upon careful optimization of their

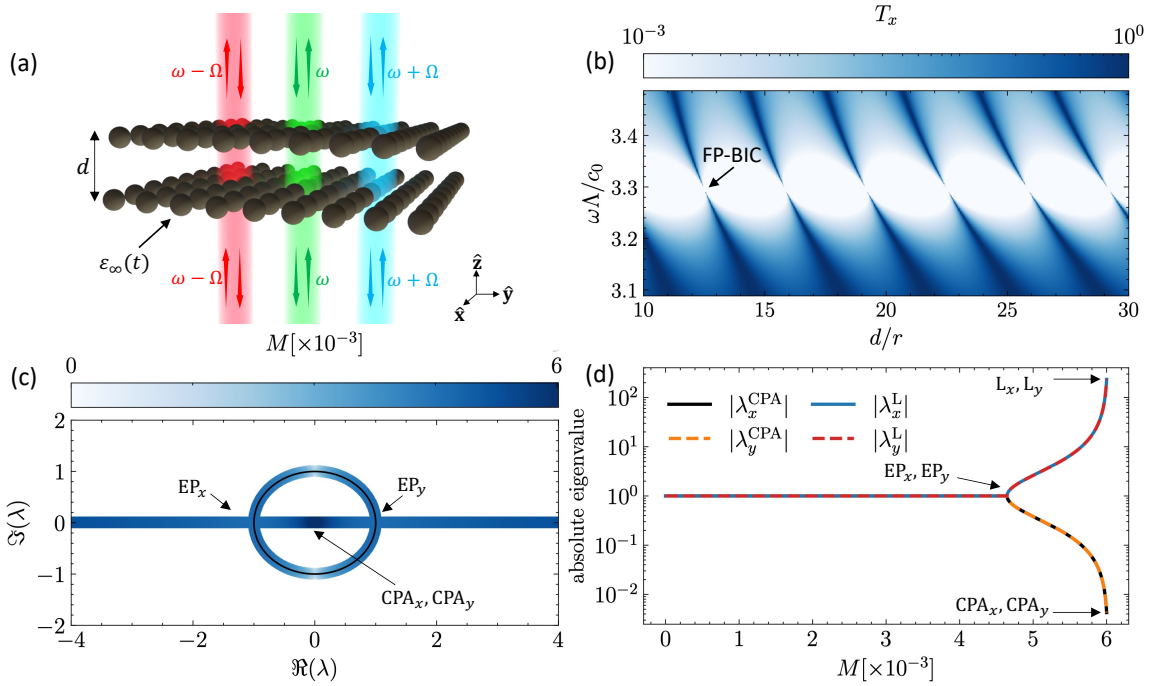


Figure 5.5.: **EPs, CPA, and lasing in time-varying FP cavities.** (a) A time-varying FP cavity made by stacking two identical metasurfaces. Each metasurface is made from a square lattice of spheres. The material of each sphere has the background permittivity $\varepsilon_\infty(t) = 1 + \chi_{\infty,\mathrm{st}}[1 + M\cos(\Omega t)]$. (b) The transmissivity T_x of the cavity as a function of frequency ω and the interlayer distance d for x-polarized normally incident PWs, under static conditions. We observe the existence of a series of FP-BICs. They are formed at a frequency where the individual layers are perfectly reflecting. (c) The complex eigenvalues of the S-matrix $\tilde{\mathbf{S}}_{\mathrm{pp}}(\omega, \mathbf{k}_\parallel)$ of the time-varying FP cavity as a function of the modulation amplitude M at the frequency $\omega = \omega_{\mathrm{qBIC}}$. Here, for $M \gtrsim 0$, all the eigenvalues reside on a unit circle. As M is increased, two of the eigenvalues corresponding to the x-polarized modes coalesce, forming EP$_x$. Upon further increasing M, these eigenvalues leave the unit circle. One of the eigenvalues approaches 0^-, marking the CPA$_x$ point. Conversely, the partner eigenvalue simultaneously approaches $-\infty$, marking L$_x$ (not shown). We observe a similar behavior for the y-polarized modes. The corresponding points for such modes are EP$_y$, CPA$_y$, and L$_y$. (d) The absolute values of the eigenvalues shown in (c) as a function of the modulation amplitude M. Here, EP, CPA, and lasing points for both the polarizations are clearly visible. In particular, the EPs appear near $M = 4.64 \times 10^{-3}$, and the CPA/lasing points appear near $M = 6 \times 10^{-3}$. This figure has been adapted from [P3]. © The authors, licensed under CC BY 4.0.

parameters, these single-layer structures can also enable strong nonlocal optical responses, engineered dispersion relations, and precise radiation control [16]. However, despite their versatility, the number of degrees of freedom in such metasurfaces is limited. In fact, the key knobs in monolayer metasurfaces are unit-cell geometry, lattice symmetry, and thickness. Consequently, devices requiring the simultaneous manipulation of various properties such as the resonance linewidths, polarization control, and radiation characteristics suffer major trade-offs due to limited design freedom [148].

Multilayered metasurfaces offer viable solutions to these limitations. By stacking metasurfaces on top of each other, additional design parameters can be accessed. These include distance, lateral displacement, and twist angle between the layers. For instance, varying the interlayer distance enables the manipulation of both the near- and far-field coupling between the layers. The former leads to mode hybridization, causing significant bandstructure modification [148]. The latter leads to the emergence of cavity resonances such as the Fabry-Perot BICs (FP-BICs) [149, 150]. On the other hand, lateral displacement allows breaking the in-plane mirror symmetries. Such symmetry breaking, for instance, can convert an SP-BIC into a qBIC, allowing comprehensive control over the resonance Q-factor [150]. Finally, the twist angle can be used to break the lateral mirror symmetry, enabling bi-anisotropic effects such as chirality without requiring complicated meta-atom shapes [151, 152]. Because these parameters can be varied even after nanofabrication, they also enable reconfigurability, allowing the same constituent metasurfaces to be used for different applications [148]. Finally, turning on the time modulation in multilayered metasurfaces increases the degrees of freedom even further, as each layer can possess a distinct modulation amplitude, frequency, and phase. The resulting structures provide a platform for combining the unique effects of temporal modulation with the enhanced functionalities enabled by multilayered systems [P3].

In this subsection, we focus on the simplest multilayered structure, i.e., a bilayer formed by stacking two identical metasurfaces. The parameters of the resulting metasurface-based cavity can be optimized to support FP-BICs [47]. In general, the formation of an FP-BIC requires two identical, perfectly reflecting mirrors. When the mirror separation is such that a cavity mode satisfies the Fabry–Perot phase-matching condition, an FP-BIC is formed [149, 150, 153]. Here, we employ perfectly reflecting metasurfaces as the constituent nanophotonic mirrors for the cavity. Furthermore, by turning on the time modulation in the resulting FP cavity, we show the emergence of polarization-insensitive scattering anomalies at perturbative modulation amplitudes.

The considered FP cavity is shown in Fig. 5.5(a). It is formed by stacking two identical metasurfaces. Here, each metasurface is made from a square lattice of dielectric spheres. We assume the background permittivity of the spheres in the metasurfaces to be a periodic function of time, i.e., $\varepsilon_\infty(t) = 1 + \chi_{\infty,\mathrm{st}}[1 + M\cos(\Omega t)]$. We choose the radius of the spheres as $\mathcal{R} = 800$ nm, and the lattice period is set to $\Lambda = 3.5\mathcal{R}$. We use Eq. (2.55) to compute the full S-matrix $\mathbf{S}(\omega, \mathbf{k}_\parallel)$ of the cavity. Once $\mathbf{S}(\omega, \mathbf{k}_\parallel)$ is computed, we transform it to the reduced matrix $\tilde{\mathbf{S}}_{\mathrm{pp}}(\omega, \mathbf{k}_\parallel)$ using Eq. (5.13).

The geometric parameters of the cavity are chosen such that it supports FP-BICs under static conditions. To illustrate this, we plot the transmissivity T_x of the cavity as a function of the frequency ω and the interlayer distance d for x-polarized normally incident PWs in Fig. 5.5(b). We observe the existence of a series of resonances with vanishing linewidths. These resonances are FP-BICs. We highlight that such BICs are formed at a frequency where the reflectivity of the individual metasurfaces is unity. Furthermore, we observe the

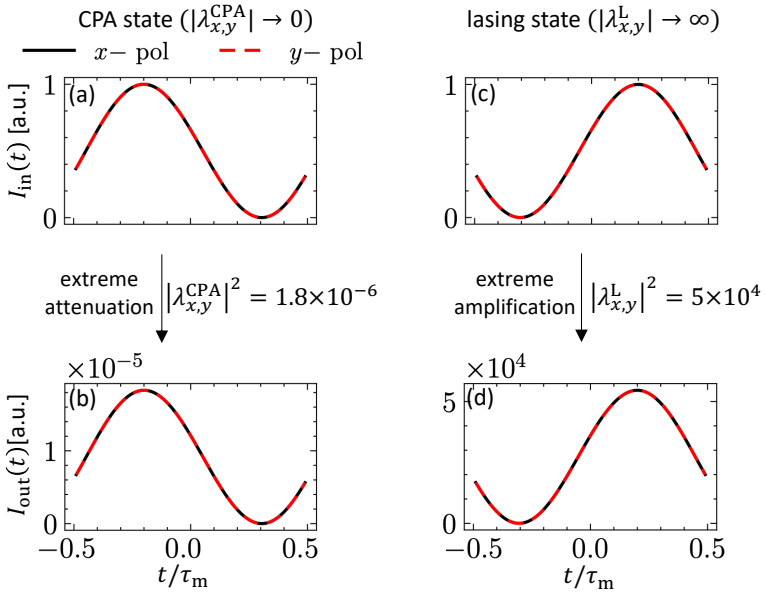


Figure 5.6.: **Outgoing and incoming intensities for CPA and lasing states of the FP cavity.** (a) The space-integrated incoming intensities $I_{\text{in}}(t)$ as a function of time t for the CPA states for both the x- and the y-polarizations. Here, the eigenvalues corresponding to the CPA states are $|\lambda_x^{\text{CPA}}| = |\lambda_y^{\text{CPA}}| = 4.3 \times 10^{-3}$. (b) The resulting outgoing intensities $I_{\text{out}}(t)$ when the incoming CPA states are injected into the system. We observe that the outgoing intensities are many orders of magnitude smaller than the incoming intensities. Hence, most of the incoming field gets absorbed by the time-varying FP cavity. (c) The space-integrated incoming intensities $I_{\text{in}}(t)$ as a function of time t for the lasing states. The eigenvalues corresponding to such states are $|\lambda_x^{\text{L}}| = |\lambda_y^{\text{L}}| = 2.33 \times 10^2$. (d) The resulting outgoing intensities $I_{\text{out}}(t)$ when the incoming lasing states are injected into the system. We find that the outgoing intensities are many orders of magnitude larger than the incoming intensities. Therefore, extreme amplification of the incoming fields takes place, signifying lasing. Note that the spatial integration of the intensities is done over infinite $x-y$ planes at $z = 1000\tau_{\text{m}}c_0$ (i.e., above the metasurface). We observe similar trends for the far-field intensities below the metasurface (not shown). Further note that the intensity corresponding to the outgoing lasing state is the time-reversed version of the incoming CPA state, due to the reciprocity of the time-varying FP cavity. This figure has been adapted from [P3]. © The authors, licensed under CC BY 4.0.

restoration of these BICs at specific distances d due to the fulfillment of the FP phase-matching condition. Such a condition implies that the modal field of the cavity is such that it experiences constructive interference inside the cavity at every round trip [149]. Furthermore, since the cavity preserves the C_4 symmetry in the $x-y$ plane, its scattering response is polarization-insensitive at normal incidence. Therefore, the FP-BICs are also obtained in the transmission spectrum for the y-polarized normally incident PWs (not shown). In the following, we slightly detune the system parameters from the true BIC condition. Specifically, we use $d = 12.78\mathcal{R}$, which corresponds to a qBIC at $\omega_{\text{qBIC}} = 3.266c_0/\Lambda$.

In the time-varying case, we again utilize the resonant modulation scheme. We use $\omega = \omega_{\text{qBIC}}$, and $\Omega = 2\omega_{\text{qBIC}}$. Therefore, the lowest-order scattered frequencies are on resonance, i.e., $\omega_{-j_0-1} = -\omega_{\text{qBIC}}$, and $\omega_{-j_0} = \omega_{\text{qBIC}}$. Notably, even in the time-varying case, the C_4 symmetry of the cavity is preserved. Therefore, the scattering anomalies induced by temporal modulation are polarization-insensitive at normal incidence.

To illustrate the existence of the EP, CPA, and lasing points, we plot the complex eigenvalues λ of the S-matrix $\tilde{\mathbf{S}}_{\mathrm{pp}}(\omega, \mathbf{k}_{\parallel})$ of the time-varying FP cavity as a function of the modulation amplitude M (see Fig. 5.5(c)). As before, for $M \gtrsim 0$, we find that all the eigenvalues lie on the unit circle. As M is increased, a pair of eigenvalues approach each other on the left part of the unit circle, eventually merging at an EP. We confirmed that the corresponding eigenvectors are also parallel at the EP. Furthermore, the eigenvectors are x-polarized. Therefore, we denote the EP by EP_x. Similarly, on the right part of the unit circle, we find another pair of eigenvalues that merge and form another EP. Here, the contributing eigenvectors are y-polarized. Therefore, the EP is denoted by EP_y. As M is increased further, the EP-forming eigenvalues leave the unit circle. For the x-polarized modes, one of the eigenvalues approaches 0^-, while its partner eigenvalue approaches $-\infty$, marking CPA (denoted by CPA_x) and lasing (denoted by L_x) points, respectively. A similar behavior is observed for the y-polarized modes, where one of the eigenvalues approaches 0^+, and the partner eigenvalue approaches $+\infty$, marking CPA_y and L_y points, respectively. We highlight that these polarization-insensitive scattering anomalies are obtained at perturbative modulation amplitudes, i.e., for $M \ll 1$, due to the resonant light trapping facilitated by the qBICs.

To illustrate the EP, CPA, and lasing points more clearly, we plot the absolute eigenvalues $\left\{|\lambda_x^{\mathrm{CPA}}|, |\lambda_x^{\mathrm{L}}|\right\}$ for CPA_x and L_x points, and $\left\{|\lambda_y^{\mathrm{CPA}}|, |\lambda_y^{\mathrm{L}}|\right\}$ for CPA_y and L_y points, as a function of M (see Fig. 5.5(d)). As expected, we find that for low M, all eigenvalues are unimodular. As M is increased, they depart from such a unity condition, marking the exceptional points EP_x and EP_y. As M is further increased, $|\lambda_x^{\mathrm{CPA}}|$ and $|\lambda_y^{\mathrm{CPA}}|$ approach zero, marking CPA_x and CPA_y points. Conversely, $|\lambda_x^{\mathrm{L}}|$ and $|\lambda_y^{\mathrm{L}}|$ approach infinity, marking L_x and L_y points. Specifically, the EPs appear near $M = 4.64 \times 10^{-3}$, and the CPA/lasing points appear near $M = 6 \times 10^{-3}$.

Next, we show the far-field intensity profiles corresponding to the CPA and lasing states in Fig. 5.6. We evaluate the far fields at $z = 1000 c_0 \tau_{\mathrm{m}}$ for both x- and y- polarizations. Specifically, in Figs. 5.6(a)–(b), we consider the CPA states. In Fig. 5.6(a), the incoming intensity $I_{\mathrm{in}}(t)$ is plotted as a function of time for both polarizations. The corresponding eigenvalues are very small, i.e., $|\lambda_x^{\mathrm{CPA}}| = |\lambda_y^{\mathrm{CPA}}| = 4.3 \times 10^{-3}$ at $M = 6 \times 10^{-3}$. Consequently, we observe a strong attenuation of the outgoing intensity $I_{\mathrm{out}}(t)$, signifying CPA.

Similarly, we consider the lasing states for both polarizations in Figs. 5.6(c)–(d). The corresponding eigenvalues are significantly large, i.e., $|\lambda_x^{\mathrm{L}}| = |\lambda_y^{\mathrm{L}}| = 2.33 \times 10^2$. Therefore, we observe that $I_{\mathrm{out}}(t)$ is orders of magnitude higher than $I_{\mathrm{in}}(t)$, signifying lasing. Furthermore, as before, we find that the incoming CPA state is the time-reversed version of the outgoing lasing state, thanks to the reciprocity of the time-varying FP cavity.

To summarize, in this subsection, we studied the scattering anomalies in bilayer time-varying cavities (i.e., FP cavities). We assumed identical temporal permittivity modulation in both the layers. In the following, we consider even more complicated structures by stacking more than two metasurfaces. Furthermore, by assuming a phase difference in the time-varying permittivities of the layers, we study nonreciprocal scattering systems. Employing the high-Q resonances of the multilayered metasurfaces, we attain one-way transmission of light at perturbative modulation amplitudes in these nonreciprocal systems.

5.3. Nonreciprocity in multilayered metasurfaces hosting SP-BICs

Time-varying optical platforms are viable candidates for enabling nonreciprocal light propagation [89, 134]. Physically, breaking time-reversal symmetry in a linear, lossless scattering system is required for realizing nonreciprocity [134]. For instance, an otherwise homogeneous medium, with a traveling-wave-type modulation of the background permittivity, i.e., $\varepsilon_\infty(z,t) = 1 + \chi_{\infty,\mathrm{st}}[1 + M\cos(\Omega t + Kz)]$ can exhibit nonreciprocal behavior [134]. Here, K is the modulation wavenumber. In the following, we engineer a nonreciprocal response in spatially discrete systems by breaking their time-reversal symmetry. In particular, we consider multilayered time-varying metasurfaces (see Fig. 5.7(a)).

The investigated metasurface is made by stacking four identical layers. The radius of the spheres in each layer is $\mathcal{R} = 800$ nm, the lattice period is $\Lambda = 2.5\mathcal{R}$, and the separation between the adjacent layers is $d = 10\mathcal{R}$. These geometric parameters are chosen such that the resulting multilayered metasurface is subwavelength and supports an SP-BIC under static conditions. Using Eq. (2.62), we plot the transmissivity T_{TE} of the metasurface as a function of the frequency ω and the x-component k_x of the in-plane wavevector in Fig. 5.7(b). For simplicity, we use $k_y = 0$ in this subsection. We observe the existence of a resonance with a vanishing linewidth at $k_x = 0$. Such a resonance is an SP-BIC. It is formed because the symmetry of the metasurface eigenmode at $k_x = 0$ is incompatible with the available radiation channels. In the time-varying case, we slightly detune the system from the true BIC condition to obtain a qBIC. Specifically, we use $k_x = 0.0179\pi/\Lambda$, for which the metasurface supports a qBIC at $\omega = \omega_{\mathrm{qBIC}} = 2.49c_0/\Lambda$. Furthermore, as before, we choose $\Omega = 2\omega_{\mathrm{qBIC}}$.

To emulate a traveling-wave-type modulation using the considered spatially discrete multilayered metasurface, we assume the background permittivity of the spheres in the n^{th} layer to be $\varepsilon_{\infty,n}(t) = 1 + \chi_{\infty,\mathrm{st}}[1 + M\cos(\Omega t + Kz_n)]$. Here, z_n denotes the z-coordinate of the n^{th} layer. Furthermore, $\phi_n = Kz_n$ represents a discrete phase profile that effectively replaces the continuous phase profile Kz associated with traveling wave modulation in spatially homogeneous media. We find that choosing $\phi_n = 2.85n\pi/4$ gives rise to a significant nonreciprocal response in the parameter range of interest, as shown in the following.

First, we plot the absolute value of the maximal eigenvalue $\lambda_{\max}$ of the S-matrix $\tilde{\mathbf{S}}_{\mathrm{pp}}(\omega, \mathbf{k}_\parallel)$ of the metasurface as a function of the modulation amplitude M in Fig. 5.7(c). Here, we operate at $\omega = \omega_{\mathrm{qBIC}}$, such that $\omega_{-j_0-1} = -\omega_{\mathrm{qBIC}}$, and $\omega_{-j_0} = \omega_{\mathrm{qBIC}}$. We observe the existence of a pole of $|\lambda_{\max}|$ (and hence that of $\tilde{\mathbf{S}}_{\mathrm{pp}}(\omega, \mathbf{k}_\parallel)$) at $M = 1.319 \times 10^{-4}$. Similar to the earlier example, such a pole appears at an M for which the time-modulation-induced gain exactly balances the radiative loss of the underlying eigenmode of the metasurface. Because the eigenmode is primarily formed by a qBIC of the metasurface, it has low radiative loss. Thus, we attain the pole for $M \ll 1$. The nonreciprocity of the metasurface is enhanced for the operating points in the vicinity of the pole. We quantify nonreciprocity using the parameter η_{r}, such that $\eta_{\mathrm{r}} = \|\mathbf{V}\tilde{\mathbf{S}}_{\mathrm{pp}}^{\mathrm{T}}\mathbf{V} - \tilde{\mathbf{S}}_{\mathrm{pp}}\|_{\mathrm{F}}$. Here, $\|.\|_{\mathrm{F}}$ represents the Frobenius norm. A non-zero value of η_{r} implies $\mathbf{V}\tilde{\mathbf{S}}_{\mathrm{pp}}^{\mathrm{T}}\mathbf{V} \neq \tilde{\mathbf{S}}_{\mathrm{pp}}$, and therefore broken reciprocity (see Eq. (5.15)). We plot η_{r} as a function of the frequency ω and the modulation amplitude M in Fig. 5.7(d). We find that when the modulation is turned on, i.e., $M \gtrsim 0$, $\eta_{\mathrm{r}} \approx 0$. As M increases, specifically near $M = 1.319 \times 10^{-4}$ and $\omega = \omega_{\mathrm{qBIC}}$, we observe $\eta_{\mathrm{r}} \neq 0$, signifying a strong nonreciprocal response there.

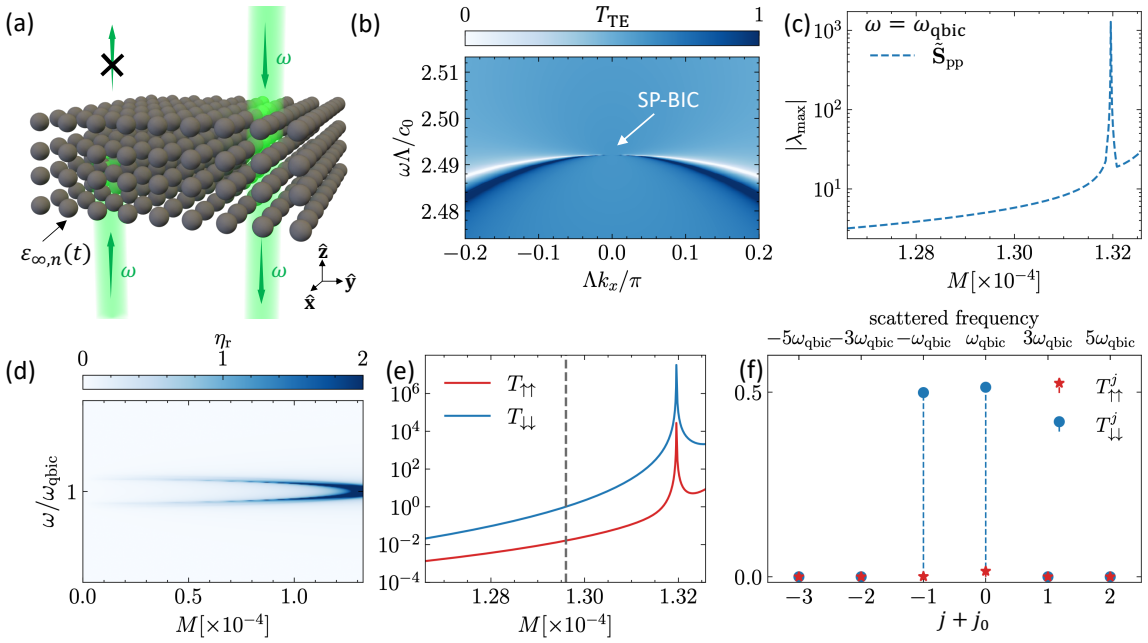


Figure 5.7.: **Nonreciprocity in time-varying multilayered metasurfaces.** (a) A time-varying multilayered metasurface formed by stacking four layers. Here, each layer is made from a square lattice of time-varying spheres. The spheres in the n^{th} layer have the background permittivity $\varepsilon_{\infty,n}(t) = 1 + \chi_{\infty,\text{st}}[1 + M\cos(\Omega t + \phi_n)]$. (b) The transmissivity T_{TE} of the metasurface as a function of the frequency ω and the x-component k_x of the in-plane wavevector for TE-polarized PWs, under static conditions. The metasurface exhibits an SP-BIC at $k_x = 0$. Furthermore, at $k_x = 0.0179\pi/\Lambda$, the qBIC frequency is $\omega = \omega_{\text{qBIC}} = 2.49c_0/\Lambda$. (c) The absolute value of the maximal eigenvalue $\lambda_{\max}$ of the S-matrix $\tilde{\mathbf{S}}_{\text{pp}}(\omega, \mathbf{k}_{\parallel})$ of the metasurface as a function of M at $\omega = \omega_{\text{qBIC}}$. We observe that at $M = 1.319 \times 10^{-4}$, $|\lambda_{\max}|$ diverges, indicating a pole of the S-matrix there. (d) The nonreciprocity parameter η_{r} as a function of ω and M. We find that near $\omega = \omega_{\text{qBIC}}$ and $M = 1.319 \times 10^{-4}$, $\eta_{\text{r}} \neq 0$, signifying a strong nonreciprocal response of the metasurface. (e) The total upward and downward transmissivities $T_{\uparrow\uparrow}$ and $T_{\downarrow\downarrow}$ of the metasurface as a function of M at $\omega = \omega_{\text{qBIC}}$. We observe a strong dissymmetry between $T_{\uparrow\uparrow}$ and $T_{\downarrow\downarrow}$, thanks to the nonreciprocity of the metasurface. In fact, at $M = 1.319 \times 10^{-4}$, both the transmissivities diverge due to the existence of a pole of the S-matrix at that M. (f) The harmonic-resolved transmissivity contributions $T^j_{\uparrow\uparrow}$ and $T^j_{\downarrow\downarrow}$ at $M = 1.296 \times 10^{-4}$ and $\omega = \omega_{\text{qBIC}}$. Here, we observe that for the upward-propagating incident PW, the harmonic-resolved ($T^j_{\uparrow\uparrow}$) as well as the total ($T_{\uparrow\uparrow}$) transmissivities are negligible. On the other hand, for the downward-propagating incident PW, light is dominantly transmitted to the frequencies $\pm\omega_{\text{qBIC}}$. In particular, $T_{\uparrow\uparrow} = 0.016$ while $T_{\downarrow\downarrow} = 1.01$. Therefore, the metasurface exhibits a strong one-way transmission response. Here, for simplicity, we assume $k_y = 0$ in all simulations. Furthermore, in the time-varying case, we use $\Omega = 2\omega_{\text{qBIC}}$. This figure has been adapted from [P3]. © The authors, licensed under CC BY 4.0.

Nonreciprocity induces directional bias in a photonic system [134]. Mathematically, $\mathbf{V}\tilde{\mathbf{S}}_{\mathrm{pp}}^{\mathrm{T}}\mathbf{V} \neq \tilde{\mathbf{S}}_{\mathrm{pp}}$ implies $|\tilde{\mathbf{S}}_{\mathrm{pp},\uparrow\uparrow}^{\mathrm{T}}| \neq |\tilde{\mathbf{S}}_{\mathrm{pp},\downarrow\downarrow}|$ (see Eq. (2.54)). In the present case, such a condition leads to an asymmetric transmission response of the metasurface, depending on the direction of propagation of the incident PW. To demonstrate the asymmetry, we plot the upward and downward transmissivities $T_{\uparrow\uparrow}$ and $T_{\downarrow\downarrow}$ of the multilayered metasurface as a function of M in Fig. 5.7(e). Hereafter, we use TE-polarized incident PWs with $\omega = \omega_{\mathrm{qBIC}}$, and $k_x = 0.0179\pi/\Lambda$. We observe a strong dissymmetry between $T_{\uparrow\uparrow}$ and $T_{\downarrow\downarrow}$ of about two orders of magnitude, thanks to nonreciprocity. In particular, at $M = 1.319 \times 10^{-4}$, we note that both the transmissivities diverge. Such a divergence is a direct consequence of the presence of a pole of the S-matrix of the metasurface at that M.

The parameters of the multilayered metasurface can be chosen such that it supports one-way monochromatic light transmission. In the following, we operate at $M = 1.296 \times 10^{-4}$ (see the gray-dotted line in Fig. 5.7(e)). We show the harmonic-resolved transmissivity contributions $T_{\uparrow\uparrow}^{j}$ and $T_{\downarrow\downarrow}^{j}$ in Fig. 5.7(f). Note that these transmissivity contributions are defined such that $T_{\uparrow\uparrow} = \sum_j T_{\uparrow\uparrow}^{j}$, and $T_{\downarrow\downarrow} = \sum_j T_{\downarrow\downarrow}^{j}$ (see Eq. (2.62)). We observe that when light is incident from the bottom, the corresponding harmonic-resolved transmissivity contributions $T_{\uparrow\uparrow}^{j}$ are negligible. In fact, the total upward transmissivity is $T_{\uparrow\uparrow} = 0.016$. On the other hand, when light is incident from the top, the field is dominantly transmitted to the frequencies $\pm\omega_{\mathrm{qBIC}}$. As such, the total downward transmissivity is $T_{\downarrow\downarrow} = 1.01$. Therefore, we conclude that the multilayered metasurface exhibits nonreciprocity-driven one-way light transmission. In fact, the downward transmitted field contains photons only at the energy $\hbar\omega_{\mathrm{qBIC}}$, which is the same as the energy of the incident photons. Hence, the proposed nonreciprocal system is suitable for monochromatic operation, despite time modulation.

Chapter summary

In this chapter, we studied unusual scattering phenomena such as the emergence of EPs, CPA, lasing, and nonreciprocity in a wide class of time-varying metamaterials. We used a unified S-matrix framework to numerically model the scattering response of complex time-varying scatterers. We found that expressing the S-matrix in a photon number flux-normalized basis imposes certain crucial constraints on its elements. For time-periodic systems, the S-matrix is pseudounitary. We showed that pseudounitarity has profound consequences on the scattering properties of the underlying objects. For instance, it imposes the requirement that the eigenvalues of the S-matrix appear as inverse-conjugate pairs, i.e., $\{\lambda, 1/\lambda^*\}$. This condition leads to a correlated behavior of the eigenvalues in the parameter space. When the temporal modulation amplitude is tuned to a specific optimal value, the eigenvalues and the associated eigenvectors coalesce, forming EPs. Upon further increasing the modulation amplitude, the eigenvalues can also approach extreme values such as zero and infinity, signifying CPA and lasing, respectively. We demonstrated such scattering anomalies in time-varying spheres, metasurfaces, and FP cavities. Similar to the previous chapter, by exploiting the structural resonances of the scatterers, we attained the discussed exotic effects at perturbative modulation amplitudes.

The S-matrix of the time-varying systems also satisfies a reciprocity condition for time-reversal symmetric profiles of the permittivity. Breaking this time-reversal symmetry gives rise to nonreciprocal wave propagation. We illustrated such a phenomenon in time-varying

multilayered metasurfaces. By emulating a traveling-wave-type modulation in such metasurfaces, we realized one-way monochromatic light transmission.

In the next chapter, we explore the concept of photonic inverse design in the context of time-varying metamaterials. Using a differentiable T-matrix-based framework, we design a time-varying sphere that exhibits the anomalous Drexhage effect. Furthermore, we illustrate asymmetric transmission of light using an inverse-designed monolayer time-varying metasurface.

6 | Inverse-designed time-varying metamaterials

One of the major challenges with spatial metamaterials is that their properties are typically fixed upon fabrication. Owing to the tunability of temporal modulation, time-varying metamaterials offer a viable route toward reconfigurability. In principle, by changing the temporal profile of the material modulation, various optical functionalities can be realized in the same structure [154]. Of course, other approaches exist for tuning the optical response post fabrication, including utilizing mechanical tuning, phase-change materials, and electro-optic and thermo-optic effects [155]. Nevertheless, time-varying metamaterials have proven to be particularly versatile in this context [21].

This reconfigurability, however, comes at the cost of an expanded design space. Temporal modulation of material properties introduces additional degrees of freedom for controlling the optical response of photonic structures. While these additional degrees of freedom provide a vast design space for tailoring optical functionalities, they also make the identification of optimal designs increasingly challenging. This prompts us to employ photonic inverse design for engineering the optical responses on demand. Inverse design is a well-established approach in nanophotonics for identifying system parameters that yield a predefined optical functionality [156]. Generally, the parameters of a photonic structure are iteratively optimized such that the resulting device fulfills the design goal. To perform such optimizations efficiently, gradients can be computed either using adjoint methods implemented alongside conventional electromagnetic solvers or by applying automatic differentiation to fully differentiable simulation frameworks. Both approaches enable gradient-based optimization with many design parameters [157].

Prior to this thesis, photonic inverse design had already been exploited to manipulate the properties of time-varying metamaterials. For instance, optical pulse shaping was performed for their enhanced interaction with temporally periodic media in [158], unidirectional scattering was realized in disordered PTCs in [159], topological state design in PTCs was performed in [160], nonreciprocal light propagation in spatiotemporally modulated structures was proposed in [161], and the spectral properties of a dispersionless time-varying sphere were manipulated in [154]. Despite these advances, there has been a lack of studies that apply the inverse design techniques to dispersive non-adiabatically modulated time-varying metamaterials. In this chapter, to address this research gap and to exploit the opportunities, we inverse design such metamaterials.

To appropriately utilize the tools of photonic inverse design, the scattering problem at hand has to be efficiently solved. Here, we develop the differentiable T-matrix method to account for scattering from time-varying metamaterials. In particular, we consider time-varying spheres and metasurfaces. We assume the electron density of the underlying media of these structures to be a periodic function of time (see Subsec. 2.3.1). Using a gradient-based optimization technique in combination with automatic differentiation, we identify optimal temporal profiles of the electron density to reach predefined functionalities (described in

Sec. 6.1). We demonstrate the application of our approach with two key examples. First, we design the time-varying electron density of an isolated sphere such that it exhibits an anomalous Drexhage effect (described in Sec. 6.2). Second, we design the electron density of a time-varying metasurface such that it supports efficient frequency upconversion. By cascading the metasurface with a narrowband frequency filter, we realize asymmetric transmission of light (described in Sec. 6.3).

This chapter is based on our work in [P5]. We acknowledge a close collaboration with Dr. Thomas Sturges in this work.

6.1. Inverse design framework

In this section, we describe the proposed inverse design framework (see Fig. 6.1), which relies on gradient-based optimization [157]. We model the considered time-varying spheres and metasurfaces using the T-matrix formalism (see Sec. 2.4). Our implementation is written in Python. We adapted and reimplemented the components of our Python code required for the present calculations using JAX-compatible operations, thereby making the relevant T-matrix computations differentiable. The resulting implementation uses automatic differentiation through the `jax.grad` utility to evaluate the gradients required for the optimization [162]. We use the software package `nlopt` to perform the gradient-based optimization [163].

Having built the differentiable T-matrix-based computational model, we perform the optimization. We assume the electron density $N(t)$ of the underlying media of the spheres and metasurfaces to be a periodic function of time. Using a single-pole Drude model, we expand $N(t)$ in a Fourier series as (Subsec. 2.3.1)

$$N(t) = N_{\mathrm{st}} \left[1 + \frac{1}{2} \sum_{q=1}^{Q} (M_q e^{iq\Omega t} + \mathrm{c.c.}) \right] , \tag{6.1}$$

where the electron density is non-negative and real at all times t. Furthermore, for brevity, we define a vector $\mathbf{M}$ that contains all the Fourier coefficients M_q. We formulate the inverse design problem such that it reduces to minimizing or maximizing an objective function $f_{\mathrm{obj}}(\mathbf{M})$. Note that the modulation frequency Ω is defined *a priori* and does not enter the optimization procedure.

To perform the minimization/maximization of $f_{\mathrm{obj}}(\mathbf{M})$, we utilize the gradient information (see Fig. 6.1). During this procedure, the gradients of $f_{\mathrm{obj}}(\mathbf{M})$ are computed with respect to all $M_q \in \mathbf{M}$. Here, reverse-mode automatic differentiation enables us to obtain the gradients of $f_{\mathrm{obj}}(\mathbf{M})$ with respect to all M_q in a single backward pass through the simulation [164]. Using these gradients, we iteratively update $\mathbf{M}$ until an extremum of $f_{\mathrm{obj}}(\mathbf{M})$ is reached. In essence, the optimization delivers an optimal coefficient vector $\mathbf{M} = \mathbf{M}_{\mathrm{opt}}$ which, in turn, corresponds to an optimal electron density $N(t)$ (see Fig. 6.1). Finally, using such an electron density, we perform a forward computation to verify that the target functionality has been reached.

We highlight that, in principle, there are many different approaches to perform inverse design of the considered structures. Global optimization techniques such as Bayesian [165] and particle swarm [166] optimization constitute powerful tools for optimizing complicated objective functions. However, they scale poorly with the number of design variables. Deep learning approaches are also possible [167, 168]. However, the computational cost of generating

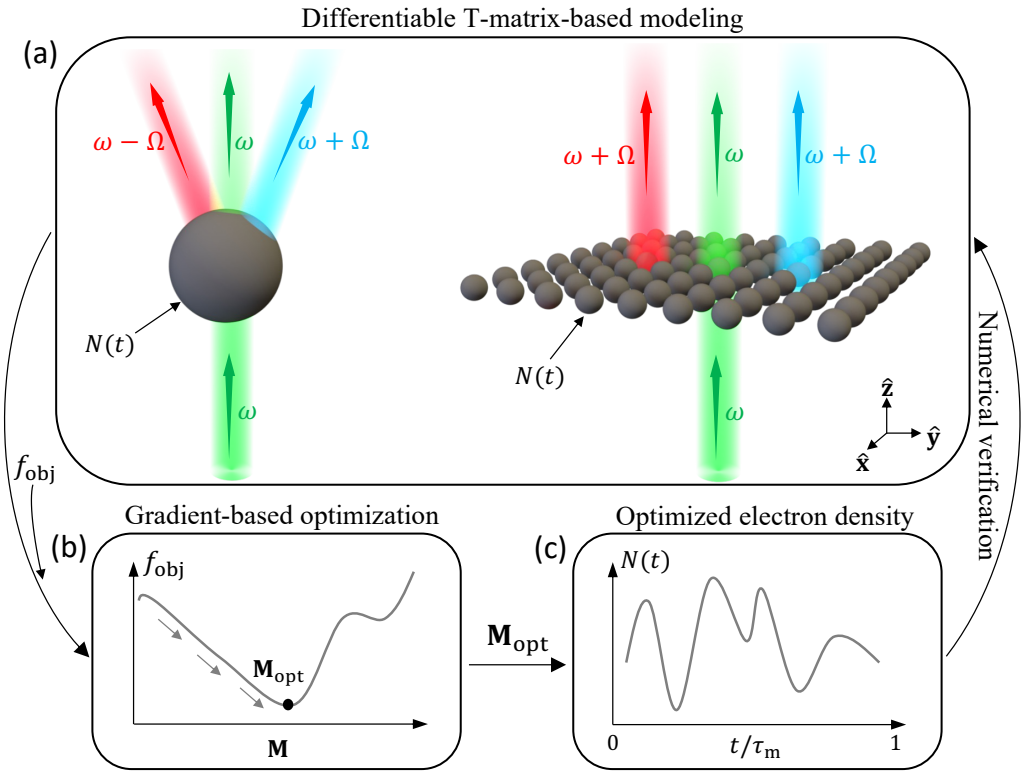


Figure 6.1.: **Inverse design framework.** We model the considered time-varying structures, i.e., spheres and metasurfaces, using a differentiable T-matrix-based framework. We assume the electron density $N(t)$ of the underlying media of these structures to be a periodic function of time. The Fourier coefficients of $N(t)$ are contained in a vector $\mathbf{M}$. These coefficients serve as the design variables. Depending on the target functionality, we define an objective function $f_{\text{obj}}(\mathbf{M})$. Using the gradient-based optimization technique, we minimize/maximize $f_{\text{obj}}(\mathbf{M})$. Such an optimization delivers the optimal coefficient vector $\mathbf{M} = \mathbf{M}_{\text{opt}}$. The vector $\mathbf{M}_{\text{opt}}$ corresponds to an optimal electron density $N(t)$. In the last step, we use this $N(t)$ to verify that the target functionality has been reached. This figure has been adapted from [P5]. © The authors, licensed under CC BY 4.0.

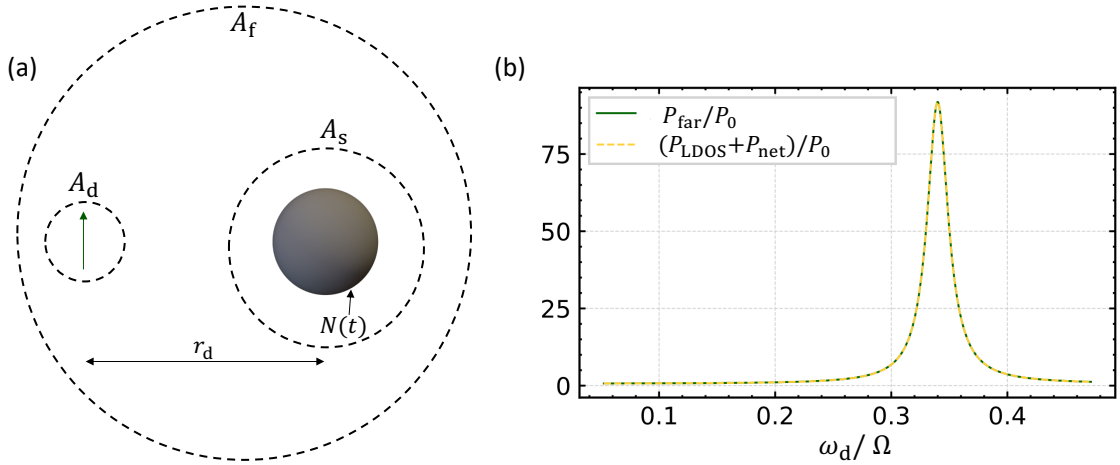


Figure 6.2.: **Power balance for the sphere-dipole system** (a) A system consisting of a dipole placed near a time-varying sphere at a distance r_d . The electron density $N(t)$ of the sphere is a periodic function of time with the modulation frequency Ω. (b) The power fluxes as a function of the dipole emission frequency ω_d for the system shown in (a). Here, P_{far}, P_{LDOS}, and P_{net} are the power fluxes crossing the areas A_f, A_d, and A_s, respectively. Furthermore, P_0 is the power flux emitted by the dipole in the absence of the sphere. This figure has been adapted from [P5]. © The authors, licensed under CC BY 4.0.

training datasets is very high, making such techniques undesirable when only a few individual optimizations are needed. In addition, the network may not faithfully represent the underlying physics. For these reasons, here we use automatic differentiation with a local gradient-based optimization algorithm [164]. Such an algorithm is independent of the number of design variables, and is, therefore, highly scalable. While there is no guarantee of reaching a global optimum, many locally optimal solutions often reach satisfactory target performance.

In the following, we apply the proposed inverse design framework to engineer the scattering properties of a time-varying sphere and a metasurface. We begin with the example of a time-varying sphere.

6.2. Radiative decay rate enhancement

The spontaneous radiative decay rates of excited atoms can be significantly modified by placing them in the vicinity of nanostructures [66, 169, 170]. For instance, in 1986, Yablonovitch proposed that placing an excited atom in a 3D photonic crystal with a frequency bandgap can completely suppress its spontaneous emission [72]. Classically, an excited atom can be modeled using an oscillating point electric dipole [171]. In recent years, there has been a growing interest in studying the modification of radiative decay rates of such dipoles in the vicinity of time-varying media [74, 172–174]. Importantly, because time-varying structures constitute electromagnetically open systems, they can provide optical gain and loss, modifying the decay rates of the dipoles significantly.

Here, we consider an electric dipole placed in the vicinity of a time-varying sphere (see Fig. 6.2(a)). The electron density $N(t)$ of the underlying medium of the sphere is a periodic function of time. Furthermore, the distance between the dipole and the sphere is r_d. Following

[175], we define the radiative decay rate enhancement $\gamma_{\text{rad}}/\gamma_0$ of the dipole in the vicinity of such a gain-loss sphere as

$$\frac{\gamma_{\text{rad}}}{\gamma_0} = \frac{P_{\text{far}}}{P_0}\,, \tag{6.2}$$

where γ_0 is the decay rate of the dipole in the absence of the sphere, and P_0 is the corresponding far-field power flux emitted by the dipole. Furthermore, P_{far} is the far-field power flux crossing an imaginary closed surface A_{f} enclosing both the dipole and the time-varying sphere (see Fig. 6.2(a)). We highlight that due to the power flux conservation, P_{far} satisfies [175]

$$P_{\text{far}} = P_{\text{LDOS}} + P_{\text{net}}\,, \tag{6.3}$$

where P_{LDOS} is the power flux crossing an imaginary surface A_{d} enclosing only the dipole, and $P_{\text{net}} = P_{\text{gain}} - P_{\text{loss}}$ is the power flux crossing an imaginary surface A_{s} enclosing only the time-varying sphere. Note that P_{gain} and P_{loss} represent the optical gain and loss, respectively, provided to the system by the time-varying sphere (see Fig. 6.2(a)). In the following, we provide the expressions to compute these powers using the T-matrix method.

6.2.1. Power calculation for oscillating dipoles

A z-oriented oscillating point electric dipole placed at a spatial location $\mathbf{r}_{\text{d}}$, emitting a monochromatic field at the frequency ω_{d}, corresponds to a current density distribution $\mathbf{J}_{\text{d}}(\mathbf{r},t) = -i\omega_{\text{d}}\mathbf{p}_0\delta(\mathbf{r}-\mathbf{r}_{\text{d}})e^{-i\omega_{\text{d}}t}$. Here, $\mathbf{p}_0 = p_0\hat{\mathbf{z}}$ is the dipole moment. The electric field emitted by the dipole has the spatial profile of the lowest-order z-oriented radiating transverse magnetic VSW. Such a field can be written as $\mathbf{E}^{\text{dip}}(\mathbf{r},t) = E_0\,\mathbf{F}^{(3)}_{l=1,m=0,s=1}(k_{\text{d}}(\mathbf{r}-\mathbf{r}_{\text{d}}))\,e^{-i\omega_{\text{d}}t}$, where $k_{\text{d}} = \omega_{\text{d}}/c_0$, and E_0 is the field amplitude. The dipole moment corresponding to $\mathbf{E}^{\text{dip}}(\mathbf{r},t)$ is $p_0 = \sqrt{6\pi}\frac{\varepsilon_0 c_0^3}{\omega_{\text{d}}^3}E_0$ [53]. Next, $\mathbf{E}^{\text{dip}}(\mathbf{r},t)$ can be expanded in terms of regular and radiating VSWs as (see Eq. (2.28))

$$\mathbf{E}^{\text{dip}}(\mathbf{r},t) = \sum_{jlms} d^{(1)}_{jlms}\mathbf{F}^{(1)}_{lms}(k_j\mathbf{r})\mathrm{e}^{-i\omega_j t}\,,\ \text{for}\ \ r < r_{\text{d}}\,, \tag{6.4a}$$

$$\mathbf{E}^{\text{dip}}(\mathbf{r},t) = \sum_{jlms} d^{(3)}_{jlms}\mathbf{F}^{(3)}_{lms}(k_j\mathbf{r})\mathrm{e}^{-i\omega_j t}\,,\ \text{for}\ r > r_{\text{d}}\,, \tag{6.4b}$$

where $\omega_{-j_0} = \omega_{\text{d}}$. Furthermore, since $\mathbf{E}^{\text{dip}}(\mathbf{r},t)$ is monochromatic, $d^{(1)/(3)}_{jlms} = 0\,\forall\, j \neq -j_0$. Moreover, because the spatial location $\mathbf{r}_{\text{d}}$ does not necessarily coincide with the origin of the coordinate system, $d^{(3)}_{jlms}$ can be non-zero for $l \neq 1$. Note that the dipole field is singular at the source position, i.e., $\mathbf{r} = \mathbf{r}_{\text{d}}$. Such a singularity cannot be represented by a finite number of regular VSWs, while a finite radiating-VSW expansion can represent it only when the expansion center is $\mathbf{r} = \mathbf{r}_{\text{d}}$ [66]. Next, we discuss the computation of P_{far}, P_{LDOS}, and P_{net} utilizing these field expansions.

To compute P_{far}, we integrate the time-averaged Poynting vector corresponding to the total field of the sphere-dipole system over the area A_{f} (see Fig. 6.2(a)). Note that the total field is given by the sum of the dipole field and the field scattered by the sphere, i.e., $\mathbf{E}^{\text{tot}}(\mathbf{r},t) = \mathbf{E}^{\text{dip}}(\mathbf{r},t) + \mathbf{E}^{\text{sca}}(\mathbf{r},t)$. In general, $\mathbf{E}^{\text{tot}}(\mathbf{r},t)$ is polychromatic, such that,

$\mathbf{E}^{\mathrm{tot}}(\mathbf{r},t) = \sum_j \mathbf{E}_j^{\mathrm{tot}}(\mathbf{r}) e^{-i(\omega_\mathrm{d}+(j+j_0)\Omega)t}$ (see Sec. 2.2). Performing the Poynting vector integration according to Eq. (2.37), we get

$$P_{\mathrm{far}} = \langle \boldsymbol{\mathcal{S}}^{\mathrm{far}} \rangle = \frac{1}{2Z_0} \sum_{jlms} \frac{1}{|k_j|^2} |A_{jlms}^{\mathrm{sca}} + d_{jlms}^{(3)}|^2 \,. \tag{6.5}$$

Next, to calculate the power flux P_{LDOS} crossing a surface that encloses only the dipole, one would typically integrate the time-averaged Poynting vector of the total field over A_d (see Fig. 6.2(a)). However, here we employ an alternative formulation for calculating P_{LDOS}, which is more convenient from a numerical standpoint. First, we compute the *instantaneous* power flux $P_{\mathrm{LDOS}}(t)$ crossing A_d as [172, 173, 176]

$$P_{\mathrm{LDOS}}(t) = -\frac{1}{2}\mathrm{Re}\left\{ \int_{V_\mathrm{d}} \left[\mathbf{J}_\mathrm{d}^*(\mathbf{r},t) \cdot \mathbf{E}^{\mathrm{tot}}(\mathbf{r},t) + \mathbf{J}_\mathrm{d}(\mathbf{r},t) \cdot \mathbf{E}^{\mathrm{tot}}(\mathbf{r},t) \right] \mathrm{d}V \right\} , \tag{6.6}$$

where V_d is the volume enclosed by the area A_d. Next, substituting the expressions for $\mathbf{J}_\mathrm{d}(\mathbf{r},t)$ and $\mathbf{E}^{\mathrm{tot}}(\mathbf{r},t)$, and performing the time-average, we get the power flux P_{LDOS} crossing the area A_d as [172]

$$P_{\mathrm{LDOS}} = \langle P_{\mathrm{LDOS}}(t) \rangle = \frac{\omega_\mathrm{d}}{2}\mathrm{Im}\left\{ \mathbf{p}_0 \cdot \mathbf{E}_{-j_0}^{\mathrm{tot}}(\mathbf{r}_\mathrm{d}) \right\} . \tag{6.7}$$

Here, the contributions due to $\mathbf{E}_{j\neq -j_0}^{\mathrm{tot}}$ cancel out due to time-averaging, as they are highly oscillatory. Note that the time-average is taken under the assumption that $\omega_\mathrm{d} \neq \frac{n\Omega}{2}$ with $n \in \mathbb{Z}$. Such an assumption is made to avoid the effects due to the time-modulation-induced parametric instability of the system.

Finally, to compute the power flux P_{net}, we integrate the time-averaged Poynting vector corresponding to the total field over the area A_s. Following Eq. (D.21b) in [66], for polychromatic fields, such an integration yields

$$P_{\mathrm{net}} = \langle \boldsymbol{\mathcal{S}}^{\mathrm{net}} \rangle = \frac{1}{2Z_0} \sum_{jlms} \frac{1}{|k_j|^2} \left(|A_{jlms}^{\mathrm{sca}}|^2 + \mathrm{Re}\left\{ A_{jlms}^{\mathrm{sca}}\, d_{jlms}^{(1)*} \right\} \right) . \tag{6.8}$$

Having discussed the calculation methods for various power fluxes, we numerically verify the conservation relation, $P_{\mathrm{far}} = P_{\mathrm{LDOS}} + P_{\mathrm{net}}$ (see Eq. (6.3)). For the test case, we use the configuration shown in Fig. 6.2(a). Here, we assume the electron density of the sphere to be $N(t) = N_{\mathrm{st}}[1 + 0.8\cos(\Omega t)]$ with $\Omega = 0.17 c_0/\mathcal{R}$. Furthermore, the radius of the sphere is $\mathcal{R} = 10$ nm, and the sphere-dipole distance is $r_\mathrm{d} = 15$ nm. Moreover, hereafter, we use gold as the underlying medium of the sphere with its Drude parameters retrieved from [177]. We plot the power fluxes P_{far} (green curve), and $P_{\mathrm{LDOS}} + P_{\mathrm{net}}$ (yellow curve) as a function of the dipole emission frequency ω_d in Fig. 6.2(b). We observe a perfect overlap of the two curves, verifying the conservation law.

In the following subsection, using the expressions for various power fluxes, we explore an anomalous Drexhage effect.

6.2.2. Anomalous Drexhage effect

In his seminal work in 1970, K. H. Drexhage showed that the radiative decay rate of a dipole near a perfect mirror depends on its relative orientation with respect to the mirror.

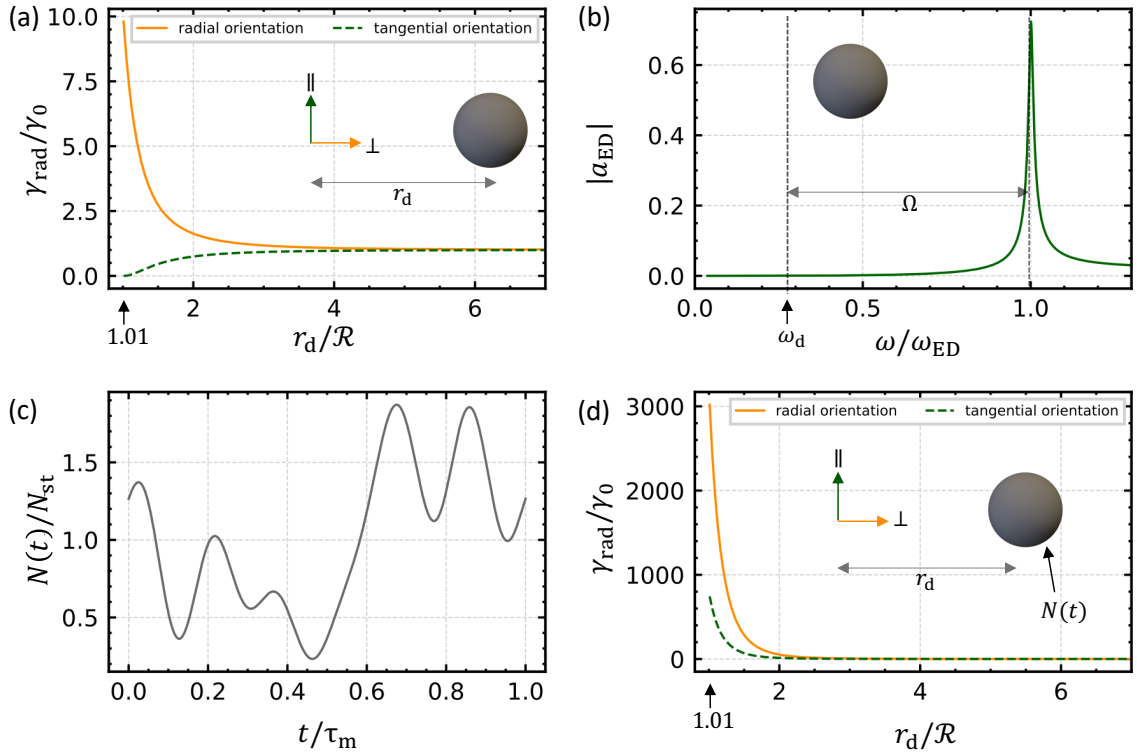


Figure 6.3.: **Anomalous Drexhage effect.** (a) The radiative decay rate enhancement $\gamma_{\mathrm{rad}}/\gamma_0$ as a function of the sphere-dipole distance r_{d} for a dipole placed in the vicinity of a static sphere. We find that for different orientations of the dipole (radial and tangential), the radiative decay rates are dissimilar due to the Drexhage effect. (b) The absolute value of the electric dipolar Mie coefficient of the static sphere as a function of the frequency ω. Here, the characteristic plasmonic resonance of the sphere is clearly visible at $\omega = \omega_{\mathrm{ED}}$. (c) The optimized electron density $N(t)$ for maximizing γ_{rad} for the tangential orientation of the dipole at $r_{\mathrm{d}}/\mathcal{R} \approx 1$. (d) Same as (a) but for the time-varying sphere with the electron density in (c). Here, we observe that γ_{rad} is significant for both the radial and tangential orientations of the dipole, leading to the demonstration of an anomalous Drexhage effect. This figure has been adapted from [P5]. © The authors, licensed under CC BY 4.0.

We observe a similar effect when the dipole is kept near a static sphere. We assume the radius of the sphere to be $\mathcal{R} = 10$ nm. Furthermore, we fix the dipole emission frequency at $\omega_\mathrm{d} = 0.072c_0/\mathcal{R}$, and its field amplitude at $E_0 = 1$ V/m. We plot the radiative decay rate enhancement $\gamma_\mathrm{rad}/\gamma_0$ as a function of the sphere-dipole distance r_d in Fig. 6.3(a). We observe that for the two different orientations of the dipole with respect to the sphere, i.e., radial ($\perp$) and tangential ($\parallel$) orientations, the radiative decay rate is different. In particular, for the radial orientation, in the regime $r_\mathrm{d}/\mathcal{R} \approx 1$, the radiative decay rate is significant, i.e., $\gamma_\mathrm{rad} \gg \gamma_0$. By contrast, for the tangential orientation, in the same regime, the radiative decay rate is negligible, i.e., $\gamma_\mathrm{rad} \ll \gamma_0$. Additionally, for $r_\mathrm{d}/\mathcal{R} \gg 1$, the radiative decay rates for both orientations saturate to γ_0.

To physically explain the orientation-dependent behavior of the radiative decay rate, we recall that γ_rad depends on the far-field power flux P_far (see Eq. (6.2)). Furthermore, P_far is computed for the total field $\mathbf{E}^\mathrm{tot}(\mathbf{r}, t) = \mathbf{E}^\mathrm{dip}(\mathbf{r}, t) + \mathbf{E}^\mathrm{sca}(\mathbf{r}, t)$ of the sphere-dipole system (see Eq. (6.5)). Therefore, the interference of the dipole field and the field scattered by the sphere dictates the radiative decay rate. In the present case, for $r_\mathrm{d}/\mathcal{R} \approx 1$, the total field gets enhanced due to constructive interference for the radial orientation of the dipole, leading to a significant γ_rad. On the other hand, for the tangential orientation, the total field gets canceled due to destructive interference, leading to a negligible γ_rad. Additionally, because $\mathbf{E}^\mathrm{sca}(\mathbf{r}, t)$ drops rapidly as r_d is increased [178], the interference effects become negligible for $r_\mathrm{d}/\mathcal{R} \gg 1$. Therefore, for both orientations of the dipole, γ_rad saturates to γ_0, when $r_\mathrm{d}/\mathcal{R} \gg 1$.

Next, we consider an anomalous Drexhage effect. It refers to a configuration in which the radiative decay rates are similar for both radially and tangentially oriented dipoles. We call such a behavior anomalous as it is in striking contrast to the conventional Drexhage effect studied from multiple perspectives [179, 180]. Our goal is to engineer the electron density profile $N(t)$ of the time-varying sphere such that it supports an anomalous Drexhage effect (see Eq. (6.1)). Specifically, we design $N(t)$ such that even for the tangential orientation of the dipole, γ_rad is significant when $r_\mathrm{d}/\mathcal{R} \approx 1$. From Eq. (6.2), we find that such a behavior can be achieved by maximizing the corresponding power flux P_far.

In the optimization, we fix $r_\mathrm{d}/\mathcal{R} = 1.01$ (see Fig. 6.3(a)). Furthermore, to identify the appropriate modulation frequency Ω, we plot the absolute value of the electric dipolar Mie coefficient a_ED of the static sphere as a function of the frequency ω in Fig. 6.3(b) [181]. Here, we observe the existence of the characteristic plasmonic resonance of the gold sphere at $\omega = \omega_\mathrm{ED}$. We choose the modulation frequency such that $\Omega = \omega_\mathrm{ED} - \omega_\mathrm{d}$. This choice is made because in the time-varying case, the first upconverted frequency $\omega_\mathrm{d} + \Omega$ coincides with the plasmonic resonance frequency ω_ED of the sphere. The plasmonic resonance can assist in enhancing P_far for an appropriately optimized time-varying electron density $N(t)$. Finally, we set the objective function to be minimized as $f_\mathrm{obj}(\mathbf{M}) = WP_0/P_\mathrm{far}(\mathbf{M}) + (1 - W)p(\mathbf{M})$. Here, $p(\mathbf{M})$ is a penalty function that penalizes the optimizer if it goes toward those values of $\mathbf{M}$ for which $N(t) \leq 0$ for any $t \in [0, \tau_\mathrm{m}]$. We define $p(\mathbf{M}) = \sum_{q=1}^{Q}[\max(|M_q|, \alpha) - \alpha]$. Here, if $|M_q| \leq \alpha$, $p_q = 0$, else $p_q > 0$. Effectively, the penalty function enforces an upper bound $\alpha > 0$ on every $|M_q|$. Moreover, $0 < W < 1$ is an appropriately chosen weight term. Here, we use $\alpha = 0.1$ and $W = 0.99$.

Having performed the optimization, we show the resulting electron density $N(t)$ in Fig. 6.3(c). Furthermore, in Fig. 6.3(d), we plot $\gamma_\mathrm{rad}/\gamma_0$ for both the radial and the tangential orientations of the dipole as a function of r_d for the corresponding time-varying case. We observe that for both orientations of the dipole, γ_rad is significant at $r_\mathrm{d}/\mathcal{R} \approx 1$, leading to

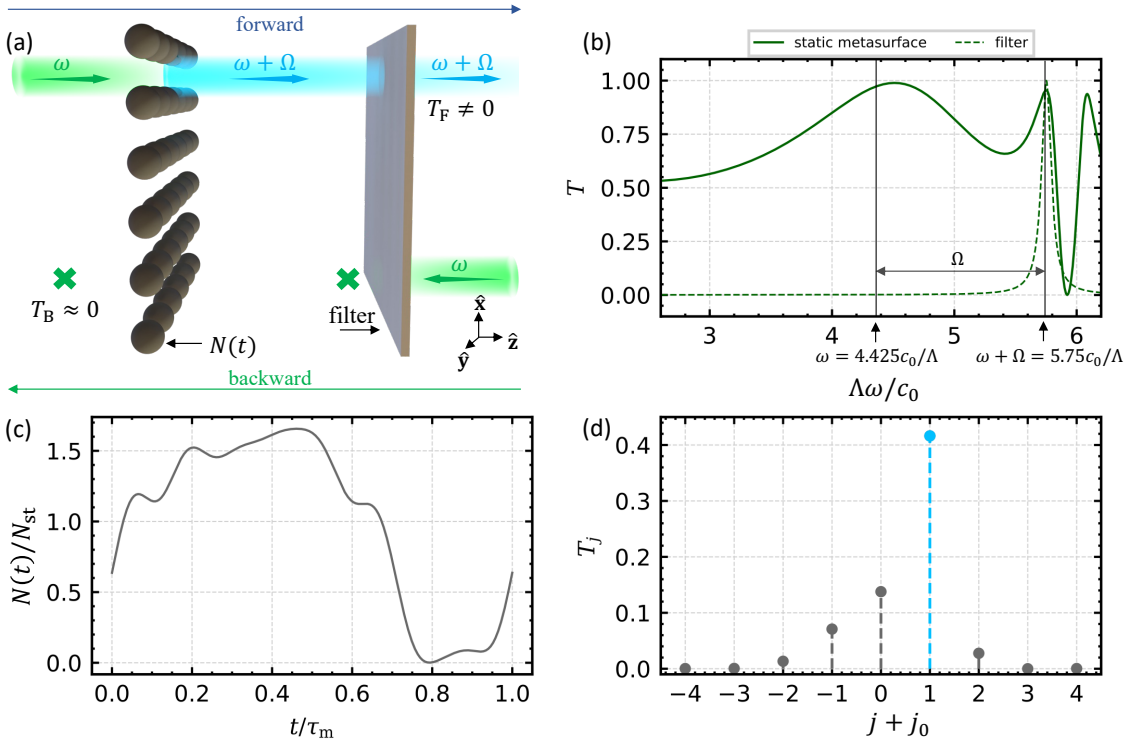


Figure 6.4.: **Inverse design of an asymmetric light-transmission device.** (a) A conceptual illustration of asymmetric light transmission from a cascaded system formed by a time-varying metasurface and a narrowband frequency filter. Here, T_{F} is the total forward, and T_{B} is the total backward transmissivity of the system. We note that the system supports a non-zero forward transmissivity, i.e., $T_{\mathrm{F}} \neq 0$. However, the total backward transmissivity is negligible, i.e., $T_{\mathrm{B}} \approx 0$. (b) The transmissivities of the metasurface under static conditions (solid curve) and the filter (dotted curve) as a function of the frequency ω. (c) The inverse-designed time-varying electron density profile of the underlying material of the metasurface for efficient frequency upconversion. (d) The corresponding harmonic-resolved transmissivity contributions T_j of the metasurface as a function of j for an incident PW at the frequency $\omega_{-j_0} = \omega = 4.425c_0/\Lambda$. Here, we observe a preferential transmission of light to the frequency $\omega_{-j_0+1} = \omega + \Omega = 5.75c_0/\Lambda$. We use x-polarized normally incident PWs for all the simulations. This figure has been adapted from [P5]. © The authors, licensed under CC BY 4.0.

the demonstration of an anomalous Drexhage effect. The optimized $N(t)$ is such that it facilitates the resonant enhancement of the field contribution $\mathbf{E}^{\mathrm{tot}}_{-j_0+1}(\mathbf{r})$ in the far field at the first upconverted frequency $\omega_{-j_0+1} = \omega_{\mathrm{d}} + \Omega$ for the tangential orientation. Such an enhancement, in turn, enhances P_{far} and γ_{rad} for the tangential orientation of the dipole. Note that even for the radial orientation, γ_{rad} is 300 times higher as compared to the static case. Such a behavior also arises due to the resonant enhancement of $\mathbf{E}^{\mathrm{tot}}_{-j_0+1}(\mathbf{r})$ for the radial orientation.

To summarize this subsection, we applied our inverse design framework to demonstrate an anomalous Drexhage effect in isolated time-varying spheres. In the following, we show the versatility of the framework by applying it to engineer the optical response of time-varying metasurfaces. By cascading an inverse-designed time-varying metasurface with a narrowband frequency filter, we realize asymmetric light transmission.

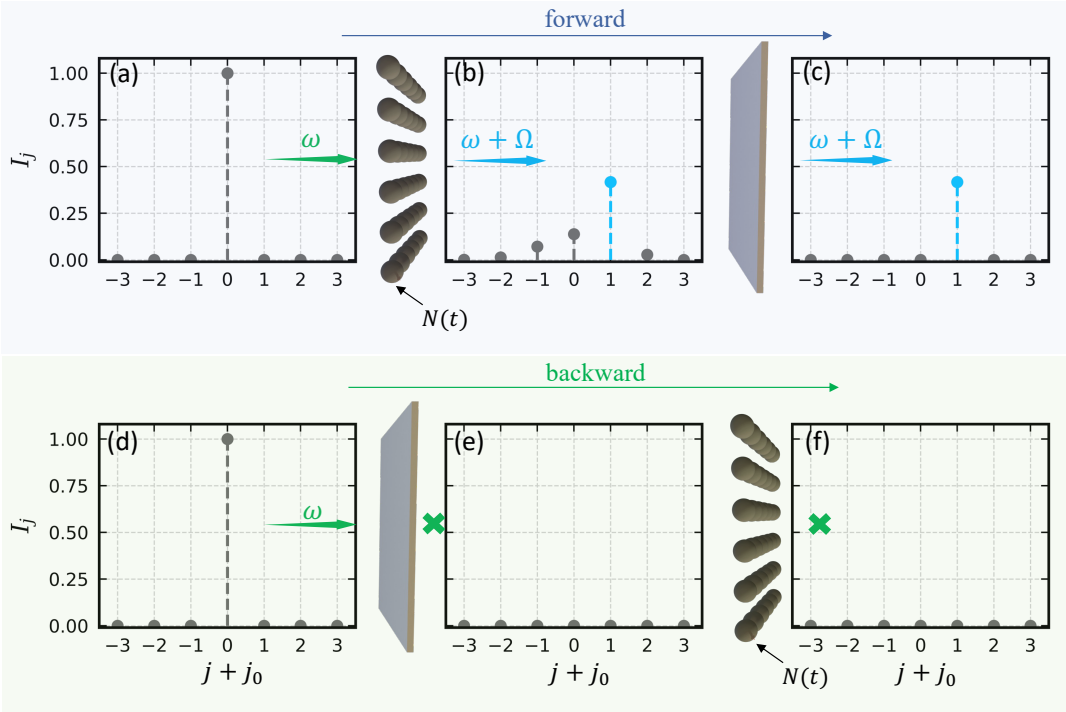


Figure 6.5.: **Demonstration of asymmetric light transmission.** The harmonic-resolved intensities I_j as a function of j for the forward propagation (top panel) and for the backward propagation (bottom panel) of light through the metasurface-filter cascade. From (a)–(c), we find that in the forward case, a non-zero transmitted field is obtained behind the filter. Conversely, from (d)–(f), we observe that in the backward case, a negligible transmitted field is obtained behind the metasurface. In particular, the total forward transmissivity is $T_\mathrm{F} = 0.41562$, and the total backward transmissivity is $T_\mathrm{B} = 0.00097$. Note that the time-varying metasurface preferentially upconverts the frequency ω to $\omega + \Omega$. Furthermore, the narrowband frequency filter only transmits the fields at the frequency $\omega + \Omega$.

6.3. Inverse-designed asymmetric light transmission

Frequency conversion is one of the most intriguing physical phenomena associated with time-varying media. As already shown in Chapters 4 and 5, exploiting time-modulation-assisted strong coupling of scattered frequencies, exotic phenomena such as momentum bandgaps, EPs, CPA, lasing, and nonreciprocity can be realized. However, those applications primarily relied on the parametric interaction of the frequencies symmetrically located at $+\Omega/2$ and $-\Omega/2$. Here, exploiting inverse design, we demonstrate that an asymmetric frequency coupling can also enable interesting physical effects. In particular, we design a metasurface-based device that supports asymmetric light transmission. This device allows light to pass through in one direction, while blocking it in the opposite direction [182–184].

The proposed asymmetric transmission device with ideal operation is depicted in Fig. 6.4(a). It is formed by cascading a time-varying metasurface with a narrowband frequency filter. When a PW at frequency ω is incident from the left side (forward propagation), it first encounters the metasurface. The metasurface upconverts the frequency of the incident PW to $\omega + \Omega$. Our design goal is to render this upconversion efficient. As the PW propagates further, it encounters a narrowband frequency filter that only allows light at the frequency $\omega + \Omega$ to pass through, blocking all other frequencies. Therefore, behind the filter, we obtain a non-zero forward transmissivity, i.e., $T_{\mathrm{F}} \neq 0$. Conversely, when a PW at the same frequency ω is incident from the right side (backward propagation), it encounters the filter first. Because the filter does not allow any further propagation of the PW, the final backward transmissivity is negligible, i.e., $T_{\mathrm{B}} \approx 0$.

The critical component of the asymmetric transmission device is the time-varying metasurface that can efficiently upconvert the frequency of incident PWs. We assume that the metasurface is made from a square lattice of spheres. The radius of the spheres is $\mathcal{R} = 150$ nm, and the lattice period is $\Lambda = 2.6\mathcal{R}$. These parameters are chosen such that the metasurface is subwavelength in the spectral range of interest. First, we consider the metasurface under static conditions. We show its transmissivity T as a function of the frequency ω in Fig. 6.4(b). Note that hereafter we use x-polarized normally incident PWs. We observe the existence of various resonances in the transmission spectrum of the static metasurface (solid curve). These are the Mie resonances of the metasurface. For the time-varying case, we choose $\omega = 4.425c_0/\Lambda$, and $\Omega = 1.325c_0/\Lambda$. Such a choice is made so that $\omega_{-j_0} = \omega$ and $\omega_{-j_0+1} = \omega + \Omega$ lie at the Mie resonances of the metasurface for an enhanced upconversion (see vertical lines in Fig. 6.4(b)).

We recall that the total transmissivity of the time-varying metasurface is given as $T = \sum_j T_j$, where T_j are the harmonic-resolved transmissivity contributions (see Eq. (2.62b)). In the present case, to render upconversion efficient, we aim to maximize T_{-j_0+1}. Therefore, we choose the objective function to be maximized as $f_{\mathrm{obj}}(\mathbf{M}) = WT_{-j_0+1}(\mathbf{M}) - (1-W)p(\mathbf{M})$. Here, the penalty function $p(\mathbf{M})$ retains the same form as before. However, since $f_{\mathrm{obj}}(\mathbf{M})$ is now maximized, the penalty term is assigned a negative weight. Furthermore, we use $\alpha = 0.055$ and $W = 0.84$.

The resulting optimized electron density $N(t)$ is shown in Fig. 6.4(c). Note that the $N(t)$ profile is such that it breaks the time-reversal symmetry, rendering the metasurface nonreciprocal. We also plot the corresponding harmonic-resolved transmissivity contributions T_j of the metasurface in Fig. 6.4(d). Here, we find that the optimized metasurface preferentially transmits light to the frequency ω_{-j_0+1} (with $T_{-j_0+1} = 0.42$). An analysis of the Fourier coefficients M_q reveals that the contribution of M_1 is the most significant to $N(t)$

(see Eq. (6.1)). Together with the resonant enhancement provided by the Mie resonance at ω_{-j_0+1}, the corresponding metasurface supports a significant transmissivity contribution T_{-j_0+1}. We highlight that the total transmission efficiency of the metasurface is about 66%. Approximately 15% of the incident energy is lost to reflection and about 19% to material losses.

Next, we cascade the upconverting metasurface with a narrowband frequency filter. The filter is designed using two parallel mirrors, each having a reflectivity of $R = 0.95$. Each mirror can be built using, for example, planar Bragg stacks [30]. We assume the gap between the mirrors is filled with a vacuum and has a width of 213 nm. The transmission spectrum of the filter is depicted by the dashed curve in Fig. 6.4(b). We observe that the filter exhibits high transmissivity only at $\omega_{-j_0+1} = 5.75c_0/\Lambda$. On the other hand, the transmissivity at other frequencies, including at $\omega_{-j_0} = 4.425c_0/\Lambda$, is negligible.

Finally, Fig. 6.5 illustrates the flow of light through the designed metasurface-filter cascade. The top panel shows the forward light propagation. Here, we plot the time-averaged intensities I_j defined according to Eq. (2.60) and Eq. (2.61b). In particular, we start with a monochromatic incident PW at the frequency $\omega_{-j_0} = \omega$. The corresponding harmonic-resolved intensity I_j is shown in Fig. 6.5(a). Clearly, only I_{-j_0} is non-zero. As the PW interacts with the time-varying metasurface, a preferential transmission to the frequency $\omega_{-j_0+1} = \omega + \Omega$ takes place, signified by $I_{-j_0+1} = 0.42$ (see Fig. 6.5(b)). Note that the quantities T_j and I_j are identical for the metasurface, as the time-averaged intensity corresponding to the incident PW is unity. Finally, as this light interacts with the narrowband filter, only the frequency ω_{-j_0+1} is transmitted, leading to a final forward transmissivity of $T_\mathrm{F} = 0.41562$. Conversely, the backward flow of light is depicted in the lower panel of Fig. 6.5. Here, we start with the same incident field as before at the frequency ω_{-j_0} (Fig. 6.5(d)). Because the incident field first interacts with the filter whose transmissivity is negligible at ω_{-j_0}, almost no light passes through. Therefore, the corresponding intensities in Figs. 6.5(e)–(f) are negligible. In fact, the total backward transmissivity is $T_\mathrm{B} = 0.00097$. A strong contrast between T_F and T_B clearly demonstrates that our inverse-designed cascaded device supports asymmetric light transmission.

Chapter summary

In this chapter, we utilized photonic inverse design to engineer the optical response of time-varying spheres and metasurfaces. We assumed the electron density of the underlying media of the structures to be a periodic function of time. Using the differentiable T-matrix method, we built an inverse design framework. Therein, we considered the Fourier coefficients of the temporal profile of the electron density as the design variables. Using a gradient-based optimization technique, our framework finds optimal Fourier coefficients to achieve predefined optical functionalities.

We applied the inverse design framework to two specific scattering problems. First, we considered a dipole placed near a time-varying sphere. We showed that the electron density of the material of the sphere can be engineered such that the sphere-dipole system exhibits an anomalous Drexhage effect. In such a case, the radiative decay rate of the dipole is significant for both radial and tangential orientations when the dipole is placed close to the sphere. Together with the electric dipolar resonance of the sphere, the optimized electron density facilitates such an anomalous behavior. Second, we inverse-designed time-varying

metasurfaces to build a device that exhibits asymmetric light propagation. The proposed device consists of a cascade of a time-varying metasurface and a narrowband frequency filter. The electron density of the underlying medium of the metasurface is optimized such that the metasurface preferentially upconverts the frequency of the incident PW from ω to $\omega + \Omega$. Then, such an upconverted PW encounters the filter that perfectly transmits fields only at $\omega + \Omega$, leading to significant total forward transmissivity. In the opposite direction, the same incident PW at frequency ω is completely blocked by the filter, leading to negligible total backward transmissivity.

We highlight that the inverse design framework is general and can be applied to engineer a wide range of optical phenomena in the considered structures. Furthermore, it can be easily adapted to various other time-varying scattering objects. From this perspective, our approach unlocks the opportunities to engineer novel reconfigurable photonic devices.

7 | Conclusions

In this thesis, we studied the interaction of light with resonant time-varying metamaterials. Exploiting the T- and S-matrix methods, we developed a computational framework that can account for the light scattering from complex time-varying objects. We applied the framework to engineer various optical functionalities in time-varying spheres, monolayer metasurfaces, and multilayered metasurfaces. We provide a summary of the main findings of this thesis in Sec. 7.1. Our results also hold significant potential for further research. We provide an outlook for the thesis in Sec. 7.2.

7.1. Summary

After an introduction, we discussed the classical electromagnetic theory for time-varying media in Chapter 2. We started by considering Maxwell's equations together with the appropriate constitutive relations. Utilizing the material response functions with an explicit time dependence, we derived the eigenmodes of spatially uniform time-varying media. Exploiting these eigenmodes, we solved the scattering problem for a time-varying sphere. In particular, we provided the analytical expressions to compute the T- and S-matrices of the sphere. We then extended the framework to time-varying metasurfaces formed by periodic arrangements of time-varying meta-atoms in 2D and derived the corresponding analytical expressions for their T- and S-matrices. Finally, using the S-matrix star product, we further extended the framework to incorporate multilayered time-varying metasurfaces. The discussed numerical tools have been verified with the full-wave solver COMSOL.

To motivate the work presented in this thesis, we provided an overview of the existing literature on time-varying optics in Chapter 3. We began by discussing the differences between light scattering from spatial and temporal inhomogeneities. In particular, we compared spatial and temporal interfaces, as well as photonic space crystals and photonic time crystals. We then reviewed selected experimental works demonstrating novel time-modulation-induced phenomena, including time refraction, time reflection, and the emergence of momentum bandgaps. Finally, we outlined the current challenges and future opportunities in the field of temporal metamaterials.

We discussed the first application of our proposed computational framework in Chapter 4. The observation of momentum bandgaps in spatially uniform time-varying media requires large permittivity modulation amplitudes, which are challenging to achieve at optical frequencies. We relaxed this large modulation amplitude requirement by exploiting the high-quality resonances supported by time-varying metasurfaces. First, we explored Mie resonant metasurfaces made from a periodic arrangement of homogeneous spheres. We showed that such structures can be designed to host noticeable momentum bandgaps at extremely small modulation amplitudes. Such a behavior arises thanks to the resonant light confinement in the metasurfaces. Next, to lower the required modulation amplitudes even further, we considered qBIC resonant time-varying metasurfaces. In particular, we studied two types of metasurfaces made from a periodic arrangement of identical scatterers. In

one kind of metasurface, these scatterers were multilayered spheres, and in another kind of metasurface, these scatterers were small cylinders. Using the lossless multilayered-sphere-based metasurface, we demonstrated that the threshold modulation amplitude to open a momentum bandgap asymptotically approaches zero as the quality factor of the qBIC diverges. Losses, naturally, cause a degradation of this effect. On the other hand, using the cylinder-based metasurface, we proposed a more practical qBIC resonant geometry for obtaining the momentum bandgaps. We showed that despite the material losses, these cylinder-based metasurfaces exhibit noticeable bandgaps at modulation amplitudes an order of magnitude below their Mie resonant counterparts. We highlight that all the bandstructures in this chapter were computed using the T-matrix method.

Moreover, carefully engineered time-varying metamaterials exhibit unconventional scattering phenomena. In Chapter 5, we demonstrated the emergence of scattering anomalies such as exceptional points (EPs), coherent perfect absorption (CPA), lasing, and nonreciprocal light propagation in various time-varying structures. We employed the symmetry-enforced constraints on the S-matrices of these structures to explain the origin of the unusual scattering effects. First, we demonstrated EPs, CPA, and lasing in time-varying spheres, metasurfaces, and Fabry-Perot cavities. We found that exploiting high-quality qBIC resonances enables the observation of these effects at extremely small modulation amplitudes. Next, we showed the emergence of resonance-assisted nonreciprocity in multilayered time-varying metasurfaces. By engineering the modulation phase of the metasurface layers, we emulated a traveling-wave-type permittivity modulation. The resulting metasurface breaks the time-reversal symmetry, giving rise to a strong nonreciprocal response. Harnessing nonreciprocity, we realized one-way monochromatic light transmission in such metasurfaces.

The temporal modulation of the material properties unlocks additional degrees of freedom for tailoring light-matter interactions. Photonic inverse design provides an efficient way to exploit these additional degrees of freedom and achieve target optical responses. In Chapter 6, we proposed a differentiable T-matrix-based inverse design framework for engineering the scattering properties of time-varying metamaterials. We treated the Fourier coefficients of the time-varying electron density profile of the underlying material as the design variables. For given objective functions, we performed gradient-based optimizations to obtain predefined optical functionalities. We applied the inverse design framework to both time-varying spheres and metasurfaces. In particular, we realized an anomalous Drexhage effect in time-varying spheres. Here, a dipole placed near a sphere exhibits similar radiative decay rates for two orthogonal orientations. Next, by optimizing the time-varying metasurface to support enhanced frequency upconversion, we realized asymmetric transmission of light.

7.2. Outlook

In the following, we want to outline the different research directions that can be explored based on the results of this thesis. One of the major puzzles in the field of time-varying metamaterials is the proper understanding of the sources of time modulation. In our work, we assumed the fast optical Kerr effect and dynamic electron density as the time-modulation-inducing mechanisms. While we were able to capture many exotic functionalities enabled by the temporal modulation, our mathematical model to consider these sources was rather phenomenological. Therefore, a more involved study that rigorously accounts for the modulating pump field will be a valuable addition to bring the theoretical description

of temporal metamaterials much closer to reality. Such a study will also help to clearly distinguish conventional nonlinear optics from time-varying optics.

A further development of our work could be the consideration of arbitrarily shaped meta-atoms. In this thesis, we focused on spherical and cylindrical meta-atoms to demonstrate various physical effects. However, introducing more complex meta-atom geometries can open new avenues for studying effects such as time-varying chirality and for engineering the underlying multipolar interactions. As our T- and S-matrix frameworks for time-varying metasurfaces do not depend on the shapes of the meta-atoms, they can directly incorporate arbitrarily shaped meta-atoms.

Other interesting avenues for expanding the design space of time-varying metasurfaces include the consideration of aperiodic lattices and unit cells comprising multiple time-varying particles. Such extensions have already been explored for static metasurfaces. Building on these developments, the tools proposed in this thesis can be used to guide the computational implementation of more advanced time-varying structures.

Bibliography

[1] V. G. Veselago, "The electrodynamics of substances with simultaneously negative values of ε and μ," *Physics-Uspekhi* **10**, 509 (1968).

[2] R. A. Shelby, D. R. Smith, and S. Schultz, "Experimental verification of a negative index of refraction," *Science* **292**, 77 (2001).

[3] J. B. Pendry, "Negative refraction makes a perfect lens," *Physical Review Letters* **85**, 3966 (2000).

[4] D. R. Smith, W. J. Padilla, D. C. Vier, S. C. Nemat-Nasser, and S. Schultz, "Composite medium with simultaneously negative permeability and permittivity," *Physical Review Letters* **84**, 4184 (2000).

[5] A. Grbic and G. V. Eleftheriades, "Overcoming the diffraction limit with a planar left-handed transmission-line lens," *Physical Review Letters* **92**, 117403 (2004).

[6] J. K. Gansel, M. Thiel, M. S. Rill, M. Decker, K. Bade, V. Saile, G. von Freymann, S. Linden, and M. Wegener, "Gold helix photonic metamaterial as broadband circular polarizer," *Science* **325**, 1513 (2009).

[7] J. B. Pendry, D. Schurig, and D. R. Smith, "Controlling electromagnetic fields," *Science* **312**, 1780 (2006).

[8] U. Leonhardt, "Optical conformal mapping," *Science* **312**, 1777 (2006).

[9] D. Schurig, J. J. Mock, B. J. Justice, S. A. Cummer, J. B. Pendry, A. F. Starr, and D. R. Smith, "Metamaterial electromagnetic cloak at microwave frequencies," *Science* **314**, 977 (2006).

[10] B. Zhang, Y. Luo, X. Liu, and G. Barbastathis, "Macroscopic invisibility cloak for visible light," *Physical Review Letters* **106**, 033901 (2011).

[11] J. Valentine, J. Li, T. Zentgraf, G. Bartal, and X. Zhang, "An optical cloak made of dielectrics," *Nature Materials* **8**, 568 (2009).

[12] T. Ergin, N. Stenger, P. Brenner, J. B. Pendry, and M. Wegener, "Three-dimensional invisibility cloak at optical wavelengths," *Science* **328**, 337 (2010).

[13] Y. Yang, Y. Jeon, Z. Dong, J. K. W. Yang, M. Haddadi Moghaddam, D.-S. Kim, D. K. Oh, J. Lee, M. Hentschel, H. Giessen, D. Kang, G. Kim, T. Tanaka, Y. Zhao, J. Bürger, S. A. Maier, H. Ren, W. Jung, M. Choi, G. Bae, H. Chen, S. Jeon, J. Kim, E. Lee, H. Kang, Y. Park, D. Du Nguyen, I. Kim, P. Cencillo-Abad, D. Chanda, X. Jing, N. Liu, I. V. Martynenko, T. Liedl, Y. Kwak, J.-M. Nam, S.-M. Park, T. W. Odom, H.-E. Lee, R. M. Kim, K. T. Nam, H. Kwon, H.-H. Jeong, P. Fischer, J. Yoon, S.-H. Kim, S. Shim, D. Lee, L. A. Pérez, X. Qi, A. Mihi, H. Keum, M. Shim, S. Kim, H. Jang, Y. S. Jung, C. Rossner, T. A. König, A. Fery, Z. Li, K. Aydin, C. A. Mirkin, J. Seong, N. Jeon, Z. Xu, T. Gu, J. Hu, H. Kwon, H. Jung, H. Alijani, I. Aharonovich, J. Kim, and J. Rho, "Nanofabrication for nanophotonics," *ACS Nano* **19**, 12491 (2025).

[14] I. Staude and J. Schilling, "Metamaterial-inspired silicon nanophotonics," *Nature Photonics* **11**, 274 (2017).

[15] A. I. Kuznetsov, A. E. Miroshnichenko, M. L. Brongersma, Y. S. Kivshar, and B. Luk'yanchuk, "Optically resonant dielectric nanostructures," *Science* **354**, aag2472 (2016).

[16] A. V. Kildishev, A. Boltasseva, and V. M. Shalaev, "Planar photonics with metasurfaces," *Science* **339**, 1232009 (2013).

[17] S. M. Kamali, E. Arbabi, A. Arbabi, and A. Faraon, "A review of dielectric optical metasurfaces for wavefront control," *Nanophotonics* **7**, 1041 (2018).

[18] N. Yu, P. Genevet, M. A. Kats, F. Aieta, J.-P. Tetienne, F. Capasso, and Z. Gaburro, "Light propagation with phase discontinuities: generalized laws of reflection and refraction," *Science* **334**, 333 (2011).

[19] M. Khorasaninejad and F. Capasso, "Metalenses: versatile multifunctional photonic components," *Science* **358**, eaam8100 (2017).

[20] A. Arbabi, Y. Horie, M. Bagheri, and A. Faraon, "Dielectric metasurfaces for complete control of phase and polarization with subwavelength spatial resolution and high transmission," *Nature Nanotechnology* **10**, 937 (2015).

[21] E. Galiffi, R. Tirole, S. Yin, H. Li, S. Vezzoli, P. Huidobro, M. Silveirinha, R. Sapienza, A. Alú, and J. Pendry, "Photonics of time-varying media," *Advanced Photonics* **4**, 014002 (2022).

[22] E. Lustig, O. Segal, S. Saha, C. Fruhling, V. M. Shalaev, A. Boltasseva, and M. Segev, "Photonic time-crystals - fundamental concepts [invited]," *Optics Express* **31**, 9165 (2023).

[23] S. Saha, O. Segal, C. Fruhling, E. Lustig, M. Segev, A. Boltasseva, and V. M. Shalaev, "Photonic time crystals: a materials perspective," *Optics Express* **31**, 8267 (2023).

[24] J. R. Zurita-Sánchez, P. Halevi, and J. C. Cervantes-González, "Reflection and transmission of a wave incident on a slab with a time-periodic dielectric function $\varepsilon(t)$," *Physical Review A* **79**, 053821 (2009).

[25] N. Engheta, "Four-dimensional optics using time-varying metamaterials," *Science* **379**, 1190 (2023).

[26] F. Morgenthaler, "Velocity modulation of electromagnetic waves," *IRE Transactions on Microwave Theory and Techniques* **6**, 167 (1958).

[27] J. T. Mendonça and P. K. Shukla, "Time refraction and time reflection: two basic concepts," *Physica Scripta* **65**, 160 (2002).

[28] D. Holberg and K. Kunz, "Parametric properties of fields in a slab of time-varying permittivity," *IEEE Transactions on Antennas and Propagation* **14**, 183 (1966).

[29] F. Biancalana, A. Amann, and E. P. O'Reilly, "Gap solitons in spatiotemporal photonic crystals," *Physical Review A* **77**, 011801(R) (2008).

[30] J. D. Joannopoulos, S. G. Johnson, J. N. Winn, and R. D. Meade, *Photonic crystals: molding the flow of light*, 2nd (Princeton University Press, USA, 2008).

[31] M. Z. Alam, I. D. Leon, and R. W. Boyd, "Large optical nonlinearity of indium tin oxide in its epsilon-near-zero region," *Science* **352**, 795 (2016).

[32] O. Segal, N. Konforty, O. Schiller, M. J. Tolchin, T. Yasniger, S. Saha, R. W. Spangler, J.-P. Maria, Y. Plotnik, and M. Segev, "Before the cycle is over: subcycle time refraction at optical frequencies," *Physical Review Research* **8**, L022054 (2026).

[33] O. Segal, N. Konforty, O. Schiller, M. J. Tolchin, T. Yasniger, M. Birk, A. Palatnik, S. Saha, P. Sidorenko, J.-P. Maria, Y. Plotnik, and M. Segev, "About time: observation of time-reflection at optical frequencies," *arXiv preprint*, `10.48550/arXiv.2605.15632` (2026).

[34] E. Lustig *et al.*, "Time-refraction optics with single cycle modulation," *Nanophotonics* **12**, 2221 (2023).

[35] O. Segal, N. Konforty, O. Schiller, M. J. Tolchin, T. Yasniger, S. Saha, R. W. Spangler, J.-P. Maria, Y. Plotnik, and M. Segev, "Before the cycle is over: subcycle time refraction at optical frequencies," *Physical Review Research* **8**, L022054 (2026).

[36] Y. Zhou, M. Z. Alam, M. Karimi, J. Upham, O. Reshef, C. Liu, A. E. Willner, and R. W. Boyd, "Broadband frequency translation through time refraction in an epsilon-near-zero material," *Nature Communications* **11**, 2180 (2020).

[37] A. C. Harwood, S. Vezzoli, T. V. Raziman, C. Hooper, R. Tirole, F. Wu, S. A. Maier, J. B. Pendry, S. A. R. Horsley, and R. Sapienza, "Space-time optical diffraction from synthetic motion," *Nature Communications* **16**, 5147 (2025).

[38] W. Jaffray, S. Stengel, A. Boltasseva, V. M. Shalaev, M. A. Vincenti, D. de Ceglia, M. Scalora, C. Rizza, and M. Ferrera, "All-optical polarization control in time-varying low-index films via plasma symmetry breaking," *Nature Photonics* **20**, 628 (2026).

[39] N. K. Hon, R. Soref, and B. Jalali, "The third-order nonlinear optical coefficients of si, ge, and $Si_{1-x}Ge_x$ in the midwave and longwave infrared," *Journal of Applied Physics* **110**, 011301 (2011).

[40] F. Bijloo, K. Murzyn, F. van Emmerik, A. J. den Boef, P. M. Kraus, and A. F. Koenderink, "Near-unity all-optical modulation of third-harmonic generation with a fano-resonant dielectric metasurface," *Nano Letters* **24**, 12942 (2024).

[41] N. Karl, P. P. Vabishchevich, M. R. Shcherbakov, S. Liu, M. B. Sinclair, G. Shvets, and I. Brener, "Frequency conversion in a time-variant dielectric metasurface," *Nano Letters* **20**, 7052 (2020).

[42] D. A. Shilkin, S. T. Ha, R. Paniagua-Domínguez, and A. I. Kuznetsov, "Ultrafast modulation of a nonlocal semiconductor metasurface under spatially selective optical pumping," *Nano Letters* **24**, 14229 (2024).

[43] V. Bacot, M. Labousse, A. Eddi, M. Fink, and E. Fort, "Time reversal and holography with spacetime transformations," *Nature Physics* **12**, 972 (2016).

[44] H. Moussa, G. Xu, S. Yin, E. Galiffi, Y. Radi, and A. Alú, "Observation of temporal reflection and broadband frequency translation at photonic time interfaces," *Nature Physics* **19**, 863 (2023).

[45] J. R. Reyes-Ayona and P. Halevi, "Observation of genuine wave vector (k or β) gap in a dynamic transmission line and temporal photonic crystals," *Applied Physics Letters* **107**, 074101 (2015).

[46] Z. Wu and A. Grbic, "Serrodyne frequency translation using time-modulated metasurfaces," *IEEE Transactions on Antennas and Propagation* **68**, 1599 (2020).

[47] C. W. Hsu, B. Zhen, A. D. Stone, J. D. Joannopoulos, and M. Soljačić, "Bound states in the continuum," *Nature Reviews Materials* **1**, 16048 (2016).

[48] G. Ptitcyn, A. Lamprianidis, T. Karamanos, V. Asadchy, R. Alaee, M. Müller, M. Albooyeh, M. S. Mirmoosa, S. Fan, S. Tretyakov, and C. Rockstuhl, "Floquet–mie theory for time-varying dispersive spheres," *Laser & Photonics Reviews* **17**, 2100683 (2023).

[49] D. Beutel, I. Fernandez-Corbaton, and C. Rockstuhl, "Treams – a T-matrix-based scattering code for nanophotonics," *Computer Physics Communications* **297**, 109076 (2024).

[50] P. Waterman, "Matrix formulation of electromagnetic scattering," *Proceedings of the IEEE* **53**, 805 (1965).

[51] A. Krasnok, D. Baranov, H. Li, M.-A. Miri, F. Monticone, and A. Alú, "Anomalies in light scattering," *Advances in Optics & Photonics* **11**, 892 (2019).

[52] N. Stefanou, V. Yannopapas, and A. Modinos, "Multem 2: a new version of the program for transmission and band-structure calculations of photonic crystals," *Computer Physics Communications* **132**, 189 (2000).

[53] A. G. Lamprianidis, "Phd thesis: generalized transition matrix methods for the analysis of linear nanophotonic systems," *Karlsruher Institut für Technologie (KIT)* (2023).

[54] D. Beutel, A. Groner, C. Rockstuhl, and I. Fernandez-Corbaton, "Efficient simulation of biperiodic, layered structures based on the T-matrix method," *Journal of Optical Society of America B* **38**, 1782 (2021).

[55] D. J. Griffiths, *Introduction to electrodynamics*, 4th ed. (Cambridge University Press, 2017).

[56] E. Galiffi, A. C. Harwood, S. Vezzoli, R. Tirole, A. Alù, and R. Sapienza, "Optical coherent perfect absorption and amplification in a time-varying medium," *Nature Photonics* **20**, 163 (2026).

[57] J. B. Khurgin, "Photonic time crystals and parametric amplification: similarity and distinction," *ACS Photonics* **11**, 2150 (2024).

[58] Y. Xiao, "Phd thesis: propagation of optical pulses in dynamic media: a time transformation method," *University of Rochester* (2014).

[59] W. Jaffray, S. Stengel, F. Biancalana, C. B. Fruhling, M. Ozlu, M. Scalora, A. Boltasseva, V. M. Shalaev, and M. Ferrera, "Spatio-spectral optical fission in time-varying subwavelength layers," *Nature Photonics* **19**, 558 (2025).

[60] B. Dixon, C. M. Hooper, I. R. Hooper, and S. A. R. Horsley, "Scattering in time-varying drude-lorentz models," *Journal of Optics* **28**, 035101 (2026).

[61] J. B. Khurgin, M. Clerici, and N. Kinsey, "Fast and slow nonlinearities in epsilon-near-zero materials," *Laser & Photonics Reviews* **15**, 2000291 (2021).

[62] G. Mie, "Beiträge zur optik trüber medien, speziell kolloidaler metallösungen," *Annalen der Physik* **330**, 377 (1908).

[63] P. Waterman, "T-matrix methods in acoustic scattering," *Journal of Acoustic Society of America* **125**, 42 (2009).

[64] COMSOL, *Comsol Multiphysics*, https://www.comsol.com/comsol-multiphysics.

[65] I. Stefanou, P. A. Pantazopoulos, and N. Stefanou, "Light scattering by a spherical particle with a time-periodic refractive index," *Journal of the Optical Society of America B* **38**, 407 (2021).

[66] E. Stamatopoulou, "Phd thesis: strong light–matter interactions in extreme plasmonic and mie-resonant systems," English, *Syddansk Universitet. Det Tekniske Fakultet, SDU, Denmark*, https://doi.org/10.21996/z9nq-c258 (2023).

[67] E. Hendry, C. M. Hooper, W. P. Wardley, and S. A. R. Horsley, "Effects due to generation of negative frequencies during temporal diffraction," *arXiv preprint*, 10.48550/arXiv.2507.03491 (2025).

[68] D. T. Beutel, "Phd thesis: a holistic framework for electromagnetic scattering simulations based on the T-matrix method," *Karlsruher Institut für Technologie (KIT)* (2024).

[69] E. Panagiotidis, E. Almpanis, N. Papanikolaou, and N. Stefanou, "Optical transitions and nonreciprocity in spatio-temporally periodic layers of spherical particles," *Advanced Optical Materials* **11**, 2202812 (2023).

[70] A. Novitsky, D. Lyakhov, D. Michels, A. A. Pavlov, A. S. Shalin, and D. V. Novitsky, "Unambiguous scattering matrix for non-Hermitian systems," *Physical Review A* **101**, 043834 (2020).

[71] R. C. Rumpf, "Improved formulation of scattering matrices for semi-analytical methods that is consistent with convention," *Progress In Electromagnetics Research B* **35**, 241 (2011).

[72] E. Yablonovitch, "Inhibited spontaneous emission in solid-state physics and electronics," *Physical Review Letters* **58**, 2059 (1987).

[73] S. John, "Strong localization of photons in certain disordered dielectric superlattices," *Physical Review Letters* **58**, 2486 (1987).

[74] M. Lyubarov, Y. Lumer, A. Dikopoltsev, E. Lustig, Y. Sharabi, and M. Segev, "Amplified emission and lasing in photonic time crystals," *Science* **377**, 425 (2022).

[75] J. T. Mendonça, "Time refraction and spacetime optics," *Symmetry* **16**, 1548 (2024).

[76] S. Wang, N. Shao, H. Chen, J. Chen, H. Qian, Q. Wu, H. Duan, A. Alú, and G. Huang, "Experimental realization of temporal refraction and reflection in elastic beams," *Nature Communications* **16**, 9520 (2025).

[77] B. L. Kim, C. Chong, and C. Daraio, "Temporal refraction in an acoustic phononic lattice," *Physical Review Letters* **133**, 077201 (2024).

[78] S. Rawat, S. Mukherjee, and G. Shvets, "Generation and enhancement of persistent nanoscale magnetization in all-dielectric metasurfaces by optically injected and localized free carriers," *Advanced Science*, e76635 (2026).

[79] L. Bar-Hillel, A. Dikopoltsev, A. Kam, Y. Sharabi, O. Segal, E. Lustig, and M. Segev, "Time refraction and time reflection above critical angle for total internal reflection," *Physical Review Letters* **132**, 263802 (2024).

[80] B. Huang, Z. Zhu, G. Yu, and Z. Gao, "Observation of full momentum bandgap in photonic time crystals," *arXiv preprint*, 10.48550/arXiv.2604.17408 (2026).

[81] X. Wang, M. S. Mirmoosa, V. S. Asadchy, C. Rockstuhl, S. Fan, and S. A. Tretyakov, "Metasurface-based realization of photonic time crystals," *Science Advances* **9**, eadg7541 (2023).

[82] Z. Hayran, J. B. Khurgin, and F. Monticone, "$\hbar\omega$ versus $\hbar k$: dispersion and energy constraints on time-varying photonic materials and time crystals," *Optical Materials Express* **12**, 3904 (2022).

[83] V. Asadchy, A. Lamprianidis, G. Ptitcyn, M. Albooyeh, Rituraj, T. Karamanos, R. Alaee, S. Tretyakov, C. Rockstuhl, and S. Fan, "Parametric mie resonances and directional amplification in time-modulated scatterers," *Physical Review Applied* **18**, 054065 (2022).

[84] M. Salehi, M. Ciabattoni, and F. Monticone, "Nonlocal photonic time crystals: infinite momentum bandgaps with minimal modulation speed and strength," *arXiv preprint*, `doi.org/10.48550/arXiv.2604.13444` (2026).

[85] J. B. Khurgin, "Energy and power requirements for alteration of the refractive index," *Laser & Photonics Reviews* **18**, 2300836 (2024).

[86] B. Borchers, C. Brée, S. Birkholz, A. Demircan, and G. Steinmeyer, "Saturation of the all-optical kerr effect in solids," *Optics Letters* **37**, 1541 (2012).

[87] Y. Sharabi, A. Dikopoltsev, E. Lustig, Y. Lumer, and M. Segev, "Spatiotemporal photonic crystals," *Optica* **9**, 585 (2022).

[88] X. Wen, X. Zhu, H. W. Wu, and J. Li, "Realizing spatiotemporal effective media for acoustic metamaterials," *Physical Review B* **104**, L060304 (2021).

[89] D. L. Sounas and A. Alù, "Non-reciprocal photonics based on time modulation," *Nature Photonics* **11**, 774 (2017).

[90] C. Caloz, Z.-L. Deck-Léger, A. Bahrami, O. C. Vicente, and Z. Li, "Generalized space-time engineered modulation (gstem) metamaterials: a global and extended perspective," *IEEE Antennas and Propagation Magazine* **65**, 50 (2023).

[91] T. Guo, J. Sueiro, G. M. Andolina, A. Levchuk, S. Ponzoni, R. Grasset, D. Monthe, I. Aupiais, D. Daineka, J. Briatico, T. V. de Oliveira, A. Ponomaryov, A. Arshad, A. Karimbana-Kandy, G. L. Prajapati, I. Ilyakov, J.-C. Deinert, S. F. Maehrlein, L. Perfetti, M. Schirò, and Y. Laplace, "Plasmonic metamaterial time crystal," *Nature* **656**, 343 (2026).

[92] M. Blanco de Paz, J. R. Deop-Ruano, D. M. Solís, and A. Manjavacas, "Lattice resonances in periodic arrays of time-modulated scatterers," *Laser & Photonics Reviews*, e03171 (2026).

[93] S. A. Mann, D. L. Sounas, and A. Alú, "A generalized kirchhoff's law of thermal radiation for floquet media," *arXiv preprint*, `10.48550/arXiv.2607.24985` (2026).

[94] X. Wang, V. Asadchy, S. Fan, and S. Tretyakov, "Space–time metasurfaces for power combining of waves," *ACS Photonics* **8**, 3034 (2021).

[95] X. Guo, Y. Ding, Y. Duan, and X. Ni, "Nonreciprocal metasurface with space–time phase modulation," *Light: Science & Applications* **8**, 123 (2019).

[96] P. Huidobro, M. Silveirinha, E. Galiffi, and J. Pendry, "Homogenization theory of space-time metamaterials," *Physical Review Applied* **16**, 014044 (2021).

[97] F. R. Prudêncio and M. G. Silveirinha, "Synthetic axion response with space-time crystals," *Physical Review Applied* **19**, 024031 (2023).

[98] C. Kern, M. Zürch, J. Petschulat, T. Pertsch, B. Kley, T. Käsebier, U. Hübner, and C. Spielmann, "Comparison of femtosecond laser-induced damage on unstructured vs. nano-structured au-targets," *Applied Physics A* **104**, 15 (2011).

[99] G. Grinblat, Y. Li, M. P. Nielsen, R. F. Oulton, and S. A. Maier, "Efficient third harmonic generation and nonlinear subwavelength imaging at a higher-order anapole mode in a single germanium nanodisk," *ACS Nano* **11**, 953 (2017).

[100] F. Bijloo, M. Ogienko, A. J. den Boef, P. M. Kraus, and A. F. Koenderink, "All-optical nonlinear real and fourier-space shaping with all-dielectric fano resonant metasurfaces," *ACS Nano* **20**, 4845 (2026).

[101] J. Baxter, A. Pérez-Casanova, L. Cortes-Herrera, A. Calà Lesina, I. De Leon, and L. Ramunno, "Dynamic nanophotonics in epsilon-near-zero conductive oxide films and metasurfaces: a quantitative, nonlinear, computational model," *Advanced Photonics Research* **4**, 2200280 (2023).

[102] JCM, *JCM suite: The simulation tool for nano-optics*, `https://jcmwave.com/`.

[103] M. Fruhnert, I. Fernandez-Corbaton, V. Yannopapas, and C. Rockstuhl, "Computing the T-matrix of a scattering object with multiple plane wave illuminations," *Beilstein Journal Nanotechnology* **8**, 614 (2017).

[104] A. Canós Valero, S. Gladyshev, D. Globosits, S. Rotter, E. A. Muljarov, and T. Weiss, "Revealing the resonant physics of open photonic time crystals," *Laser & Photonics Reviews*, e71318 (2026).

[105] C. M. Hooper, I. R. Hooper, and S. A. R. Horsley, "Quasinormal modes in dispersive photonic time crystals," *Physical Review A* **113**, 043526 (2026).

[106] B. Vial and R. V. Craster, "Quasinormal modes of floquet media slabs," *Physical Review B* **112**, 214201 (2025).

[107] Y. Sun, S. Fan, and G. Hu, "Quasinormal mode basis for open floquet photonic systems," *Physical Review Letters* **136**, 206903 (2026).

[108] D. Galanis, E. Almpanis, N. Papanikolaou, and N. Stefanou, "Perturbative born theory for light scattering by time-modulated scatterers," *Physical Review A* **113**, 053508 (2026).

[109] S. Koufidis, T. Koutserimpas, F. Monticone, and M. Mccall, "Electromagnetic wave propagation in time-periodic chiral media," *Optical Materials Express* **14**, 3006 (2024).

[110] I. Fernandez-Corbaton, "Helicity and duality symmetry in light matter interactions: theory and applications," *arXiv preprint*, `10.48550/arXiv.1407.4432` (2015).

[111] S. Bahmani, A. B. Evlyukhin, E. Hassan, and A. C. Lesina, "Topology optimization of optical nanoantennas with desired multipoles," *Optics Express* **33**, 19418 (2025).

[112] B. Cowan, "Optical damage threshold of silicon for ultrafast infrared pulses," *AIP Conference Proceedings* **877**, 837 (2006).

[113] A. Rahimzadegan, T. Karamanos, R. Alaee, A. Lamprianidis, D. Beutel, R. Boyd, and C. Rockstuhl, "A comprehensive multipolar theory for periodic metasurfaces," *Advanced Optical Materials* **10**, 2102059 (2022).

[114] J. D. Fischbach, F. Betz, N. Asadova, P. Tassan, D. Urbonas, T. Stöferle, R. F. Mahrt, S. Burger, C. Rockstuhl, F. Binkowski, and T. J. Sturges, "A Framework to Compute Resonances Arising from Multiple Scattering," *Advanced Theory & Simulations* **8**, 2400989 (2025).

[115] O. Vetterl, F. Finger, R. Carius, P. Hapke, L. Houben, O. Kluth, A. Lambertz, A. Mück, B. Rech, and H. Wagner, "Intrinsic microcrystalline silicon: a new material for photovoltaics," *Solar Energy Materials and Solar Cells* **62**, 97 (2000).

[116] M. I. Mishchenko, L. D. Travis, and D. W. Mackowski, "T-matrix computations of light scattering by nonspherical particles: a review," *Journal of Quantitative Spectroscopy and Radiative Transfer* **55**, 535 (1996).

[117] R. Venkitakrishnan, T. Höß, T. Repän, F. Z. Goffi, M. Plum, and C. Rockstuhl, "Lower limits for the homogenization of periodic metamaterials made from electric dipolar scatterers," *Physical Review B* **103**, 195425 (2021).

[118] M. N. Polyanskiy, I. V. Pogorelsky, M. Babzien, K. L. Vodopyanov, and M. A. Palmer, "Nonlinear refraction and absorption properties of optical materials for high-peak-power long-wave-infrared lasers," *Optical Materials Express* **14**, 696 (2024).

[119] E. Lustig, Y. Sharabi, and M. Segev, "Topological aspects of photonic time crystals," *Optica* **5**, 1390 (2018).

[120] K. Koshelev, S. Lepeshov, M. Liu, A. Bogdanov, and Y. Kivshar, "Asymmetric metasurfaces with high-Q resonances governed by bound states in the continuum," *Physical Review Letters* **121**, 193903 (2018).

[121] D. K. Thapa and S. Biswas, "Leveraging bound states in the continuum for advanced ultra-sensitive sensing technologies," *Materials Horizons* **12**, 5096 (2025).

[122] Y. Ren, P. Li, Z. Liu, Z. Chen, Y.-L. Chen, C. Peng, and J. Liu, "Low-threshold nanolasers based on miniaturized bound states in the continuum," *Science Advances* **8**, eade8817 (2022).

[123] P. Vabishchevich and Y. Kivshar, "Nonlinear photonics with metasurfaces," *Photonics Research* **11**, B50 (2023).

[124] M. Kang, T. Liu, C. T. Chan, and M. Xiao, "Applications of bound states in the continuum in photonics," *Nature Reviews Physics* **5**, 659 (2023).

[125] Z. Hayran and F. Monticone, "Capturing broadband light in a compact bound state in the continuum," *ACS Photonics* **8**, 813 (2021).

[126] L. Caspani, R. P. M. Kaipurath, M. Clerici, M. Ferrera, T. Roger, J. Kim, N. Kinsey, M. Pietrzyk, A. Di Falco, V. M. Shalaev, A. Boltasseva, and D. Faccio, "Enhanced nonlinear refractive index in ϵ-near-zero materials," *Physical Review Letters* **116**, 233901 (2016).

[127] F. Monticone and A. Alù, "Embedded photonic eigenvalues in 3d nanostructures," *Physical Review Letters* **112**, 213903 (2014).

[128] M. G. Silveirinha, "Trapping light in open plasmonic nanostructures," *Physical Review A* **89**, 023813 (2014).

[129] P. Kelly, W. Zhang, M. Liu, and L. Kuznetsova, "Engineering the structural, plasmonic, and optical properties of multilayered aluminum-doped zinc oxide metamaterial grown by pulsed laser deposition," *Applied Optics* **58**, 5681 (2019).

[130] T. Amotchkina, M. Trubetskov, D. Hahner, and V. Pervak, "Characterization of e-beam evaporated ge, ybf3, zns, and laf3 thin films for laser-oriented coatings," *Applied Optics* **59**, A40 (2020).

[131] M. V. Rybin, K. L. Koshelev, Z. F. Sadrieva, K. B. Samusev, A. A. Bogdanov, M. F. Limonov, and Y. S. Kivshar, "High-Q supercavity modes in subwavelength dielectric resonators," *Physical Review Letters* **119**, 243901 (2017).

[132] R. Malik, B. Mills, J. H. V. Price, M. Petrovich, Z. Moktadir, Z. Li, and H. N. Rutt, "Determination of the mid-ir femtosecond surface-damage threshold of germanium," *Applied Physics A* **113**, 127 (2013).

[133] D. R. Austin, K. R. P. Kafka, Y. H. Lai, Z. Wang, C. I. Blaga, and E. A. Chowdhury, "Femtosecond laser damage of germanium from near- to mid-infrared wavelengths," *Optics Letters* **43**, 3702 (2018).

[134] V. S. Asadchy, M. S. Mirmoosa, A. Díaz-Rubio, S. Fan, and S. A. Tretyakov, "Tutorial on electromagnetic nonreciprocity and its origins," *Proceedings of the IEEE* **108**, 1684 (2020).

[135] M.-A. Miri and A. Alù, "Exceptional points in optics and photonics," *Science* **363**, eaar7709 (2019).

[136] L. Feng, R. El-Ganainy, and L. Ge, "Non-hermitian photonics based on parity–time symmetry," *Nature Photonics* **11**, 752 (2017).

[137] T. T. Koutserimpas and R. Fleury, "Electromagnetic fields in a time-varying medium: exceptional points and operator symmetries," *IEEE Transactions on Antennas and Propagation* **68**, 6717 (2020).

[138] Y. D. Chong, L. Ge, H. Cao, and A. D. Stone, "Coherent perfect absorbers: time-reversed lasers," *Physical Review Letters* **105**, 053901 (2010).

[139] A. B. Khanikaev, S. H. Mousavi, G. Shvets, and Y. S. Kivshar, "One-way extraordinary optical transmission and nonreciprocal spoof plasmons," *Physical Review Letters* **105**, 126804 (2010).

[140] G. Lin, S. Zhang, Y. Hu, Y. Niu, J. Gong, and S. Gong, "Nonreciprocal amplification with four-level hot atoms," *Physical Review Letters* **123**, 033902 (2019).

[141] Z. Zhang and L. Zhu, "Nonreciprocal thermal photonics for energy conversion and radiative heat transfer," *Physical Review Applied* **18**, 027001 (2022).

[142] D. Globosits, J. Hüpfl, and S. Rotter, "Pseudounitary floquet scattering matrix for wave-front shaping in time-periodic photonic media," *Physical Review A* **110**, 053515 (2024).

[143] D. Globosits, "Phd thesis: the floquet scattering matrix in photonics: a tool for wave control in periodically time-varying systems," *Technische Universität Wien* (2026).

[144] A. Mostafazadeh, "Pseudounitary operators and pseudounitary quantum dynamics," *Journal of Mathematical Physics* **45**, 932 (2004).

[145] E. Galiffi, P. A. Huidobro, and J. B. Pendry, "Broadband nonreciprocal amplification in luminal metamaterials," *Physical Review Letters* **123**, 206101 (2019).

[146] Z. Sakotic, P. Stankovic, V. Bengin, A. Krasnok, A. Alú, and N. Jankovic, "Non-Hermitian control of topological scattering singularities emerging from bound states in the continuum," *Laser & Photonics Reviews* **17**, 2200308 (2023).

[147] C. Guo, J. Li, M. Xiao, and S. Fan, "Singular topology of scattering matrices," *Physical Review B* **108**, 155418 (2023).

[148] H. Tang, S. Fan, Y. Jie, H. S. Nguyen, E. Mazur, and Y. Cao, "Bilayer nonlocal flat optics," *eLight* **6**, 21 (2026).

[149] G. Alagappan, F. J. García-Vidal, and C. E. Png, "Fabry-perot resonances in bilayer metasurfaces," *Physical Review Letters* **133**, 226901 (2024).

[150] K. V. Semushev, Z. Zhao, A. Proskurin, M. Song, X. Liu, M. V. Rybin, E. E. Maslova, and A. A. Bogdanov, "Robustness of bound states in the continuum in bilayer structures against symmetry breaking," *Physical Review Applied* **25**, 014038 (2026).

[151] I. Toftul, P. Tonkaev, K. Koshelev, F. Lai, Q. Song, M. Gorkunov, and Y. Kivshar, "Chiral dichroism in resonant metasurfaces with monoclinic lattices," *Physical Review Letters* **133**, 216901 (2024).

[152] D. Gromyko, S. An, S. Gorelik, J. Xu, L. J. Lim, H. Y. L. Lee, F. Tjiptoharsono, Z.-K. Tan, C.-W. Qiu, Z. Dong, and L. Wu, "Unidirectional chiral emission via twisted bi-layer metasurfaces," *Nature Communications* **15**, 9804 (2024).

[153] N. Ustimenko, I. Fernandez-Corbaton, and C. Rockstuhl, "Singular value decomposition to describe bound states in the continuum in periodic metasurfaces," *Physical Review B* **113**, 235418 (2026).

[154] M. M. Sadafi, A. F. da Mota, and H. Mosallaei, "Dynamic control of light scattering in a single particle enabled by time modulation," *Applied Physics Letters* **123**, 101702 (2023).

[155] G. Oliveri, D. H. Werner, and A. Massa, "Reconfigurable electromagnetics through metamaterials—a review," *Proceedings of the IEEE* **103**, 1034 (2015).

[156] S. Molesky, Z. Lin, A. Y. Piggott, W. Jin, J. Vucković, and A. W. Rodriguez, "Inverse design in nanophotonics," *Nature Photonics* **12**, 659 (2018).

[157] J. Kim, J.-Y. Kim, J. Kim, Y. Hyeong, B. Neseli, J.-B. You, J. Shim, J. Shin, H.-H. Park, and H. Kurt, "Inverse design of nanophotonic devices enabled by optimization algorithms and deep learning: recent achievements and future prospects," *Nanophotonics* **14**, 121 (2025).

[158] J. Baxter and L. Ramunno, "Inverse design of optical pulse shapes for time-varying photonics," *Optics Express* **31**, 22671 (2023).

[159] J. Kim, D. Lee, S. Yu, and N. Park, "Unidirectional scattering with spatial homogeneity using correlated photonic time disorder," *Nature Physics* **19**, 726 (2023).

[160] Y. Long, L. Zou, L. Yu, H. Hu, J. Xiong, and B. Zhang, "Inverse design of topological photonic time crystals via deep learning," *Optical Materials Express* **14**, 2032 (2024).

[161] N. H. Phi, H. N. Bui, S.-Y. Moon, and J.-W. Lee, "Controlled synthesis of space–time modulated metamaterial for enhanced nonreciprocity by machine learning," *Advanced Intelligent Systems* **6**, 2300565 (2024).

[162] J. Bradbury, R. Frostig, P. Hawkins, M. J. Johnson, C. Leary, D. Maclaurin, G. Necula, A. Paszke, J. VanderPlas, S. Wanderman-Milne, and Q. Zhang, *JAX: composable transformations of Python+NumPy programs*, version 0.3.13, 2018.

[163] S. G. Johnson, *The NLopt nonlinear-optimization package*, 2007.

[164] C. C. Margossian, "A review of automatic differentiation and its efficient implementation," *WIREs Data Mining and Knowledge Discovery* **9**, e1305 (2019).

[165] P. I. Frazier, "A tutorial on bayesian optimization," *arXiv preprint*, `10.48550/arXiv.1807.02811` (2018).

[166] J. Kennedy and R. Eberhart, "Particle swarm optimization," in Proceedings of icnn'95-international conference on neural networks, Vol. 4 (ieee, 1995), p. 1942.

[167] W. Ma, Z. Liu, Z. A. Kudyshev, A. Boltasseva, W. Cai, and Y. Liu, "Deep learning for the design of photonic structures," *Nature Photonics* **15**, 77 (2021).

[168] S. Yu, X. Piao, and N. Park, "Machine learning identifies scale-free properties in disordered materials," *Nature Communications* **11**, 4842 (2020).

[169] M. Pelton, "Modified spontaneous emission in nanophotonic structures," *Nature Photonics* **9**, 427 (2015).

[170] P. E. Stamatopoulou and C. Tserkezis, "Role of emitter position and orientation on silicon nanoparticle-enhanced fluorescence," *OSA Continuum* **4**, 918 (2021).

[171] V. Giannini, A. I. Fernández-Domínguez, S. C. Heck, and S. A. Maier, "Plasmonic nanoantennas: fundamentals and their use in controlling the radiative properties of nanoemitters," *Chemical Reviews* **111**, 3888 (2011).

[172] J. Park, K. Lee, R.-Y. Zhang, H.-C. Park, J.-W. Ryu, G. Y. Cho, M. Y. Lee, Z. Zhang, N. Park, W. Jeon, J. Shin, C. T. Chan, and B. Min, "Spontaneous emission decay and excitation in photonic time crystals," *Physical Review Letters* **135**, 133801 (2025).

[173] R. Yu and S. Fan, "Manipulating coherence of near-field thermal radiation in time-modulated systems," *Physical Review Letters* **130**, 096902 (2023).

[174] G. Calajò, L. Rizzuto, and R. Passante, "Control of spontaneous emission of a single quantum emitter through a time-modulated photonic-band-gap environment," *Physical Review A* **96**, 023802 (2017).

[175] J. Ren, S. Franke, B. VanDrunen, and S. Hughes, "Classical purcell factors and spontaneous emission decay rates in a linear gain medium," *Physical Review A* **109**, 013513 (2024).

[176] A. Krasnok, A. Slobozhanyuk, C. Simovski, S. Tretyakov, A. Poddubny, A. Miroshnichenko, Y. Kivshar, and P. Belov, "Antenna model of the purcell effect," *Scientific reports* **5**, 12956 (2015).

[177] M. Blaber, M. Arnold, and M. Ford, "Search for the ideal plasmonic nanoshell: the effects of surface scattering and alternatives to gold and silver," *Journal of Physical Chemistry C* **113**, 3041 (2009).

[178] R. Carminati, J.-J. Greffet, C. Henkel, and J. Vigoureux, "Radiative and non-radiative decay of a single molecule close to a metallic nanoparticle," *Optics Communications* **261**, 368 (2006).

[179] L. Langguth, R. Fleury, A. Alù, and A. F. Koenderink, "Drexhage's experiment for sound," *Physical Review Letters* **116**, 224301 (2016).

[180] A. Kwadrin and A. F. Koenderink, "Gray-tone lithography implementation of drexhage's method for calibrating radiative and nonradiative decay constants of fluorophores," *The Journal of Physical Chemistry C* **116**, 16666 (2012).

[181] A. Rahimzadegan, R. Alaee, C. Rockstuhl, and R. W. Boyd, "Minimalist mie coefficient model," *Optics Express* **28**, 1651 (2020).

[182] A. S. Ansari, A. K. Iyer, and B. Gholipour, "Asymmetric transmission in nanophotonics," *Nanophotonics* **12**, 2639 (2023).

[183] H. B. Sedeh, H. M. Dinani, and H. Mosallaei, "Optical nonreciprocity via transmissive time-modulated metasurfaces," *Nanophotonics* **11**, 4135 (2022).

[184] D. Ramaccia, D. L. Sounas, A. V. Marini, A. Toscano, and F. Bilotti, "Electromagnetic isolation induced by time-varying metasurfaces: nonreciprocal bragg grating," *IEEE Antennas and Wireless Propagation Letters* **19**, 1886 (2020).

[185] M. Abramowitz and I. A. Stegun, *Handbook of mathematical functions* (Dover Publications Inc., 1967).

[186] K. Kim, "Symmetry relations of the translation coefficients of the spherical scalar and vector multipole fields," *Progress In Electromagnetics Research* **48**, 45 (2004).

[187] O. R. Cruzan, "Translational addition theorems for spherical vector wave functions," *Quarterly of Applied Mathematics* **20**, 33 (1962).

[188] S. Stein, "Addition theorems for spherical wave functions," *Quarterly of Applied Mathematics* **19**, 15 (1961).

A | Appendix

A.1. Definition of VSWs

Following the conventions used in [54], we define the VSWs as

$$\mathbf{F}^{(\iota)}_{lm0}(k\mathbf{r}) = \mathbf{X}_{lm}(\hat{\mathbf{r}}) z^{(\iota)}_{l0}(kr)\,, \tag{A.1a}$$

$$\mathbf{F}^{(\iota)}_{lm1}(k\mathbf{r}) = \Bigg(\hat{\mathbf{r}} \times \mathbf{X}_{lm}(\hat{\mathbf{r}}) \frac{1}{k}\frac{\partial}{\partial r}(kr z^{(\iota)}_{l0}(kr)) + \gamma_{lm}\hat{\mathbf{r}} l(l+1) P^m_l(\cos\theta) \frac{e^{im\phi}}{kr} z^{(\iota)}_{l0}(kr)\Bigg)\,, \quad \text{with} \tag{A.1b}$$

$$\mathbf{X}_{lm}(\hat{\mathbf{r}}) = \gamma_{lm}\left(i\hat{\boldsymbol{\theta}}\tau^{(1)}_{lm}(\theta) - \hat{\boldsymbol{\phi}}\tau^{(2)}_{lm}(\theta)\right) e^{im\phi}\,, \tag{A.1c}$$

$$\tau^{(1)}_{lm}(\theta) = \frac{m}{\sin\theta} P^m_l(\cos\theta),\ \tau^{(2)}_{lm}(\theta) = \frac{\partial}{\partial\theta} P^m_l(\cos\theta)\,, \tag{A.1d}$$

$$\gamma_{lm} = i\sqrt{\frac{(2l+1)}{4\pi l(l+1)}\frac{(l-m)!}{(l+m)!}}\,, \tag{A.1e}$$

where $P^m_l(x)$ are the associated Legendre polynomial functions [185], and $\{r, \theta, \phi\}$ are the polar coordinates of the vector $\mathbf{r}$.

A.2. Definition of unit vectors for PWs

The unit vectors for a PW of the form $e^{i(\mathbf{k}\cdot\mathbf{r}-\omega t)}\hat{\mathbf{e}}_\alpha(\mathbf{k})$ are defined as [54]:

$$\hat{\mathbf{e}}_0(\mathbf{k}) = -i\hat{\boldsymbol{\phi}}_{\mathbf{k}} = i\frac{k_y\hat{\mathbf{x}} - k_x\hat{\mathbf{y}}}{\sqrt{k_x^2+k_y^2}}\,, \tag{A.2a}$$

$$\hat{\mathbf{e}}_1(\mathbf{k}) = i\hat{\mathbf{k}} \times \hat{\mathbf{e}}_0(\mathbf{k}) = -\hat{\boldsymbol{\theta}}_{\mathbf{k}} = \frac{-k_xk_z\hat{\mathbf{x}} - k_yk_z\hat{\mathbf{y}} + (k_x^2+k_y^2)\,\hat{\mathbf{z}}}{k\sqrt{k_x^2+k_y^2}}\,. \tag{A.2b}$$

Note that these expressions are valid for $(k_x, k_y) \in \mathbb{R}^2$, and $(k_x, k_y) \neq (0,0)$. For $(k_x, k_y) = (0,0)$, we use

$$\hat{\mathbf{e}}_0(\mathbf{k}) = -i\hat{\mathbf{y}}\,, \tag{A.3a}$$

$$\hat{\mathbf{e}}_1(\mathbf{k}) = \mp\hat{\mathbf{x}}\,, \text{for } \Re(k_z) \gtrless 0\,. \tag{A.3b}$$

A.3. Symmetry relation for VSWs for negative frequencies

We use the following symmetry relation to derive various expressions involving negative frequencies (i.e., $\omega < 0$ and $k < 0$) [186]

$$[\mathbf{F}^{(\iota)}_{lms}(-k^*\mathbf{r})]^* = (-1)^{l+m+\delta_{s1}}\mathbf{F}^{(\iota)}_{l(-m)s}(k\mathbf{r})\,. \tag{A.4}$$

A.4. Incident field coefficients in the VSW basis

We expand a unit PW in a basis of regular VSWs as [49, 54]

$$e^{i(\mathbf{k}_{j\mathbf{g}\alpha d}\cdot\mathbf{r}-\omega_j t)}\hat{\mathbf{e}}_\alpha(\mathbf{k}_{j\mathbf{g}\alpha d}) = \sum_{lms} A^{\mathrm{inc}}_{jlms}(\omega_j, \mathbf{k}_{j\mathbf{g}\alpha d}, \hat{\mathbf{e}}_\alpha(\mathbf{k}_{j\mathbf{g}\alpha d}))\mathbf{F}^{(1)}_{lms}(k_j\mathbf{r})\mathrm{e}^{-i\omega_j t}\,. \tag{A.5}$$

The above expression holds for both $\omega_j > 0$ and $\omega_j < 0$. However, we can also derive a symmetry relation to compute the coefficients A^{inc}_{jlms} for $\omega_j < 0$ using those for $\omega_j > 0$. The details of such a derivation are in the following.

Using Eq. (A.4) in Eq. (A.5), we write

$$e^{i(\mathbf{k}_{j\mathbf{g}\alpha d}\cdot\mathbf{r}-\omega_j t)}\hat{\mathbf{e}}_\alpha(\mathbf{k}_{j\mathbf{g}\alpha d}) = \sum_{lms} A^{\mathrm{inc}}_{jlms}(\omega_j, \mathbf{k}_{j\mathbf{g}\alpha d}, \hat{\mathbf{e}}_\alpha(\mathbf{k}_{j\mathbf{g}\alpha d}))(-1)^{l+m+\delta_{s1}}\mathbf{F}^{(1)*}_{l(-m)s}(-k_j^*\mathbf{r})e^{-i\omega_j t}\,. \tag{A.6}$$

Complex conjugating both sides, we obtain

$$e^{-i(\mathbf{k}^*_{j\mathbf{g}\alpha d}\cdot\mathbf{r}-\omega_j^* t)}\hat{\mathbf{e}}^*_\alpha(\mathbf{k}_{j\mathbf{g}\alpha d}) = \sum_{lms} A^{\mathrm{inc}*}_{jlms}(\omega_j, \mathbf{k}_{j\mathbf{g}\alpha d}, \hat{\mathbf{e}}_\alpha(\mathbf{k}_{j\mathbf{g}\alpha d}))(-1)^{l+m+\delta_{s1}}\mathbf{F}^{(1)}_{l(-m)s}(-k_j^*\mathbf{r})e^{i\omega_j^* t}\,. \tag{A.7}$$

Expanding the PW on the L.H.S. according to Eq. (A.5) and substituting $m \to -m$ on the right-hand side (R.H.S.), we get

$$\begin{aligned}\sum_{lms} A^{\mathrm{inc}}_{jlms}(-\omega_j^*, -\mathbf{k}^*_{j\mathbf{g}\alpha d}, \hat{\mathbf{e}}^*_\alpha(\mathbf{k}_{j\mathbf{g}\alpha d}))\mathbf{F}^{(1)}_{lms}(-k_j^*\mathbf{r})e^{i\omega_j^* t} = \\ \sum_{lms} A^{\mathrm{inc}*}_{jl(-m)s}(\omega_j, \mathbf{k}_{j\mathbf{g}\alpha d}, \hat{\mathbf{e}}_\alpha(\mathbf{k}_{j\mathbf{g}\alpha d}))(-1)^{l-m+\delta_{s1}}\mathbf{F}^{(1)}_{lms}(-k_j^*\mathbf{r})e^{i\omega_j^* t}\,.\end{aligned} \tag{A.8}$$

By comparison, we find

$$A^{\mathrm{inc}}_{jlms}(-\omega_j^*, -\mathbf{k}^*_{j\mathbf{g}\alpha d}, \hat{\mathbf{e}}^*_\alpha(\mathbf{k}_{j\mathbf{g}\alpha d})) = (-1)^{l-m+\delta_{s1}} A^{\mathrm{inc}*}_{jl(-m)s}(\omega_j, \mathbf{k}_{j\mathbf{g}\alpha d}, \hat{\mathbf{e}}_\alpha(\mathbf{k}_{j\mathbf{g}\alpha d}))\,. \tag{A.9}$$

Next, we can rewrite

$$A^{\mathrm{inc}}_{jlms}(\omega_j, -\mathbf{k}^*_{j\mathbf{g}\alpha d}, \hat{\mathbf{e}}^*_\alpha(\mathbf{k}_{j\mathbf{g}\alpha d})) = (-1)^{l-m+\delta_{s1}} A^{\mathrm{inc}*}_{jl(-m)s}(-\omega_j^*, \mathbf{k}_{j\mathbf{g}\alpha d}, \hat{\mathbf{e}}_\alpha(\mathbf{k}_{j\mathbf{g}\alpha d}))\,. \tag{A.10}$$

Assuming $\omega_j \in \mathbb{R}$, we get

$$A^{\mathrm{inc}}_{jlms}(\omega_j, -\mathbf{k}^*_{j\mathbf{g}\alpha d}, \hat{\mathbf{e}}^*_\alpha(\mathbf{k}_{j\mathbf{g}\alpha d})) = (-1)^{l-m+\delta_{s1}} A^{\mathrm{inc}*}_{jl(-m)s}(-\omega_j, \mathbf{k}_{j\mathbf{g}\alpha d}, \hat{\mathbf{e}}_\alpha(\mathbf{k}_{j\mathbf{g}\alpha d}))\,. \tag{A.11}$$

Therefore, the incident field coefficients of the PW $e^{-i(\mathbf{k}^*_{j\mathbf{g}\alpha d}\cdot\mathbf{r}+\omega_j t)}\hat{\mathbf{e}}^*_\alpha(\mathbf{k}_{j\mathbf{g}\alpha d})$ are linked to those of the PW $e^{i(\mathbf{k}_{j\mathbf{g}\alpha d}\cdot\mathbf{r}-(-\omega_j)t)}\hat{\mathbf{e}}_\alpha(\mathbf{k}_{j\mathbf{g}\alpha d})$ by the symmetry relation in Eq. (A.11).

A.5. Symmetry relation for translation coefficients for negative frequencies

Here, we derive a symmetry relation that allows us to compute the translation coefficients of VSWs for negative frequencies from the corresponding expressions at positive frequencies. By definition, the translation coefficients $c^{\{lms\},\{l'm's'\}}$ satisfy [54, 187, 188]

$$\mathbf{F}^{(3)}_{l'm's'}(k(\mathbf{r}-\mathbf{R})) = \sum_{lms} c^{\{lms\},\{l'm's'\}}(-k\mathbf{R})\ \mathbf{F}^{(1)}_{lms}(k\mathbf{r}),\ \text{ for } r < R\,. \tag{A.12}$$

Using Eq. (A.4) in Eq. (A.12), we get

$$\mathbf{F}^{(3)}_{l'm's'}(k(\mathbf{r}-\mathbf{R})) = \sum_{lms} c^{\{lms\},\{l'm's'\}}(-k\mathbf{R})(-1)^{l+m+\delta_{s1}}\mathbf{F}^{(1)*}_{l(-m)s}(-k^*\mathbf{r})\,.$$

Complex conjugating both sides and replacing $m \to -m$ on the R.H.S., we get

$$\mathbf{F}^{(3)*}_{l'm's'}(k(\mathbf{r}-\mathbf{R})) = \sum_{lms} \left[c^{\{l(-m)s\},\{l'm's'\}}(-k\mathbf{R})\right]^* (-1)^{l-m+\delta_{s1}}\mathbf{F}^{(1)}_{lms}(-k^*\mathbf{r})\,.$$

Using Eq. (A.4) on the L.H.S., we get

$$(-1)^{l'+m'+\delta_{s'1}}\mathbf{F}^{(3)}_{l'(-m')s'}(-k^*(\mathbf{r}-\mathbf{R})) = \sum_{lms} \left[c^{\{l(-m)s\},\{l'm's'\}}(-k\mathbf{R})\right]^* (-1)^{l-m+\delta_{s1}}\mathbf{F}^{(1)}_{lms}(-k^*\mathbf{r})\,.$$

Again, using Eq. (A.12) on the L.H.S., we can write

$$\begin{aligned}&(-1)^{l'+m'+\delta_{s'1}}\sum_{lms} c^{\{lms\},\{l'(-m')s'\}}(k^*\mathbf{R})\mathbf{F}^{(1)}_{lms}(-k^*\mathbf{r})\\ =&\sum_{lms} \left[c^{\{l(-m)s\},\{l'm's'\}}(-k\mathbf{R})\right]^* (-1)^{l-m+\delta_{s1}}\mathbf{F}^{(1)}_{lms}(-k^*\mathbf{r})\,.\end{aligned}$$

Comparing both sides,

$$(-1)^{l'+m'+\delta_{s'1}}c^{\{lms\},\{l'(-m')s'\}}(k^*\mathbf{R}) = (-1)^{l-m+\delta_{s1}}\left[c^{\{l(-m)s\},\{l'm's'\}}(-k\mathbf{R})\right]^*,$$

hence,

$$c^{\{lms\},\{l'(-m')s'\}}(k^*\mathbf{R}) = (-1)^{l-l'-m-m'+\delta_{s1}-\delta_{s'1}}\left[c^{\{l(-m)s\},\{l'm's'\}}(-k\mathbf{R})\right]^*,$$

Replacing $m' \to -m'$,

$$c^{\{lms\},\{l'm's'\}}(k^*\mathbf{R}) = (-1)^{l-l'-m+m'+\delta_{s1}-\delta_{s'1}}\left[c^{\{l(-m)s\},\{l'(-m')s'\}}(-k\mathbf{R})\right]^*,$$

Replacing $k \to k^*$,

$$c^{\{lms\},\{l'm's'\}}(k\mathbf{R}) = (-1)^{l-l'-m+m'+\delta_{s1}-\delta_{s'1}}\left[c^{\{l(-m)s\},\{l'(-m')s'\}}(-k^*\mathbf{R})\right]^*,$$

Replacing $k \to -k$,

$$c^{\{lms\},\{l'm's'\}}(-k\mathbf{R}) = (-1)^{l-l'+m'-m+\delta_{s1}-\delta_{s'1}}\left[c^{\{l(-m)s\},\{l'(-m')s'\}}(-(-k^*)\mathbf{R})\right]^*.$$

The final expression is the desired symmetry relation for translation coefficients. For $k \in \mathbb{R}$, $c^{\{lms\},\{l'm's'\}}$ can be evaluated for $k < 0$ from the corresponding expressions at $k > 0$.

A.6. Symmetry relation for the S-matrix blocks of a static substrate

For the real-valued incident field of the form

$$\mathbf{E}_{\mathrm{r}}^{\mathrm{inc}}(\mathbf{r},t)=\sum_{j\mathbf{g}\alpha d}\frac{1}{2}\left(U_{j\mathbf{g}\alpha d}^{\mathrm{inc}}e^{i(\mathbf{k}_{j\mathbf{g}\alpha d}\cdot\mathbf{r}-\omega_j t)}\hat{\mathbf{e}}_\alpha(\mathbf{k}_{j\mathbf{g}\alpha d})+U_{j\mathbf{g}\alpha d}^{\mathrm{inc}*}e^{-i(\mathbf{k}_{j\mathbf{g}\alpha d}^{*}\cdot\mathbf{r}-\omega_j t)}\hat{\mathbf{e}}_\alpha^{*}(\mathbf{k}_{j\mathbf{g}\alpha d})\right), \tag{A.13}$$

the corresponding real-valued output field from a static substrate is given by

$$\mathbf{E}_{\mathrm{r}}^{\mathrm{out}}(\mathbf{r},t)=\sum_{j\mathbf{g}\alpha d}\frac{1}{2}\left(U_{j\mathbf{g}\alpha d}^{\mathrm{out}}e^{i(\mathbf{k}_{j\mathbf{g}\alpha d}\cdot\mathbf{r}-\omega_j t)}\hat{\mathbf{e}}_\alpha(\mathbf{k}_{j\mathbf{g}\alpha d})+U_{j\mathbf{g}\alpha d}^{\mathrm{out}*}e^{-i(\mathbf{k}_{j\mathbf{g}\alpha d}^{*}\cdot\mathbf{r}-\omega_j t)}\hat{\mathbf{e}}_\alpha^{*}(\mathbf{k}_{j\mathbf{g}\alpha d})\right). \tag{A.14}$$

By definition of the S-matrix (see Eq. (2.57)), we know that

$$\mathbf{U}_{jd}^{\mathrm{out}}=\mathbf{s}_{d\uparrow}^{\mathrm{subs}}(\omega_j,\mathbf{k}_\parallel)\mathbf{U}_{j\uparrow}^{\mathrm{inc}}+\mathbf{s}_{d\downarrow}^{\mathrm{subs}}(\omega_j,\mathbf{k}_\parallel)\mathbf{U}_{j\downarrow}^{\mathrm{inc}}. \tag{A.15}$$

Complex conjugating both sides,

$$\mathbf{U}_{jd}^{\mathrm{out}*}=\left[\mathbf{s}_{d\uparrow}^{\mathrm{subs}}(\omega_j,\mathbf{k}_\parallel)\right]^{*}\mathbf{U}_{j\uparrow}^{\mathrm{inc}*}+\left[\mathbf{s}_{d\downarrow}^{\mathrm{subs}}(\omega_j,\mathbf{k}_\parallel)\right]^{*}\mathbf{U}_{j\downarrow}^{\mathrm{inc}*}. \tag{A.16}$$

From Eqs. (A.13)–(A.14), we note that $\mathbf{U}_{jd}^{\mathrm{inc}*}$ and $\mathbf{U}_{jd}^{\mathrm{out}*}$ are incident and output field coefficients of the PWs with the Bloch wavevector $-\mathbf{k}_\parallel$ and frequency $-\omega_j$. Therefore, we can write

$$\mathbf{U}_{jd}^{\mathrm{out}*}=\mathbf{s}_{d\uparrow}^{\mathrm{subs}}(-\omega_j,-\mathbf{k}_\parallel)\mathbf{U}_{j\uparrow}^{\mathrm{inc}*}+\mathbf{s}_{d\downarrow}^{\mathrm{subs}}(-\omega_j,-\mathbf{k}_\parallel)\mathbf{U}_{j\downarrow}^{\mathrm{inc}*}. \tag{A.17}$$

Comparing Eqs. (A.15) and (A.17), we arrive at the symmetry relation

$$\mathbf{s}_{dd'}^{\mathrm{subs}}(\omega_j,\mathbf{k}_\parallel)=\left[\mathbf{s}_{dd'}^{\mathrm{subs}}(-\omega_j,-\mathbf{k}_\parallel)\right]^{*}. \tag{A.18}$$

A.7. Details of the convergence parameters used during simulations

For performing the simulations throughout this thesis, we used various convergence parameters. These parameters are the maximum multipolar orders $l_{\max}$ and l_{cut}, and the total number of scattered frequencies J. Note that, for computing the T-matrix of cylinders, using the dynamic EBCM, we use the maximum multipolar order l_{cut}. Here, $l_{\mathrm{cut}}>l_{\max}$ is chosen to ensure sufficient numerical convergence. However, after computing the T-matrix, we retain its terms only up to the order $l_{\max}$. Below we list the numerical values of these parameters.
Figures 4.2(b),(c): $l_{\max}=1$, $j_0=0,$and $J=1$.
Figures 4.2(d)–(j): $l_{\max}=1$, $j_0=-1,$and $J=3$.
Figures 4.3(b)–(e): $l_{\max}=1$, $j_0=-1,$and $J=3$.
Figures 4.4(a),(c),(d): $l_{\max}=4$, $j_0=0\,,$and $J=1$.
Figures 4.4(e)–(h): $l_{\max}=4$, $j_0=-3\,,$and $J=7$.
Figures 4.5(a)–(b): $l_{\max}=4$, $j_0=-3\,,$and $J=7$.
Figures 4.6(a)–(b): $l_{\mathrm{cut}}=10$, $l_{\max}=6$, $j_0=0\,,$and $J=1$.
Figures 4.7(b)–(c): $l_{\mathrm{cut}}=10$, $l_{\max}=6$, $j_0=0\,,$and $J=1$.

Figures 4.7(d)–(f): $l_{\text{cut}} = 10$, $l_{\max} = 6$, $j_0 = -3$, and $J = 7$.
Figure 5.1: $l_{\max} = 3$, $j_0 = -8$, and $J = 16$.
Figure 5.2: $l_{\max} = 3$, $j_0 = -8$, and $J = 16$.
Figure 5.3: $l_{\max} = 3$, $j_0 = -2$, $J = 4$, and $G = 5$.
Figure 5.4: $l_{\max} = 3$, $j_0 = -2$, $J = 4$, and $G = 5$.
Figure 5.5(b): $l_{\max} = 3$, $j_0 = 0$, $J = 1$, and $G = 1$.
Figures 5.5(c)–(d): $l_{\max} = 5$, $j_0 = -2$, $J = 4$, and $G = 9$.
Figure 5.6: $l_{\max} = 5$, $j_0 = -2$, $J = 4$, and $G = 9$.
Figures 5.7(c)–(e): $l_{\max} = 10$, $j_0 = -2$, $J = 4$, and $G = 5$.
Figure 5.7(f): $l_{\max} = 10$, $j_0 = -3$, $J = 6$, and $G = 5$.
Figure 6.2(b): $l_{\max} = 8$, $j_0 = -10$, $J = 21$.
Figure 6.3(a): $l_{\max} = 5$, $j_0 = 0$, $J = 1$.
Figure 6.3(b): $l_{\max} = 1$, $j_0 = 0$, $J = 1$.
Figure 6.3(c): $Q = 6$.
Figure 6.3(d): For the inverse simulation, we used $l_{\max} = 3$, $j_0 = -5$, $J = 11$, and $Q = 6$. On the other hand, for the forward simulation, we used $l_{\max} = 8$, $j_0 = -30$, and $J = 61$.
Figure 6.4(b): $l_{\max} = 5$, $j_0 = 0$, and $J = 1$.
Figure 6.4(c): $Q = 8$.
Figure 6.4(d): For the inverse simulation, we used $l_{\max} = 3$, $j_0 = -3$, $J = 7$, and $Q = 8$. On the other hand, for the forward simulation, we used $l_{\max} = 8$, $j_0 = -30$, and $J = 61$.
Figure 6.5(a) and (d): $l_{\max} = 8$, $j_0 = 0$, $J = 1$.
Figure 6.5(b)–(c) and (e)–(f): $l_{\max} = 8$, $j_0 = -30$, $J = 61$.

Acknowledgements

I would like to thank the many individuals who had a profound impact on shaping the research presented in this thesis. First and foremost, I am grateful to my supervisor, Prof. Carsten Rockstuhl, for giving me the opportunity to work on the topic of time-varying metamaterials in his group. Throughout my time as a PhD student, I always felt both independent and well supervised.

Next, I would like to thank Prof. Viktar Asadchy not only for agreeing to serve as the second referee of this thesis, but also for the amazing collaborations over the years, which played a major role in shaping this thesis into its present form.

I am thankful to Dr. Aristeidis Lamprianidis, who supervised my Master's thesis and taught me the fundamentals of scattering theory. It was by building upon Aris' PhD work that I carried out much of my own doctoral research.

I thank all my collaborators during my PhD for contributing to various exciting projects. I am also grateful to Dr. Thomas Sturges, Dr. Maria Paszkiewicz, Dr. Evangelos Almpanis, and Dr. David Globosits for proofreading various parts of this thesis.

I am thankful to all the past and present members of the TFP Photonics group, with whom I had the pleasure of interacting and working throughout my PhD. I would also like to acknowledge the administrative support of the TFP secretariat, which assisted me with various bureaucratic matters.

Finally, I thank Garima for her love, support, and patience, without which none of this would even exist.

Selbstständigkeitserklärung

Eidesstattliche Versicherung gemäß § 13 Absatz 2 Ziffer 3 der Promotionsordnung des Karlsruher Instituts für Technologie (KIT) für die KIT-Fakultät für Physik:

1. Bei der eingereichten Dissertation zu dem Thema
   "Resonant nanophotonics with time-varying metamaterials"
   handelt es sich um meine eigenständig erbrachte Leistung.

2. Ich habe nur die angegebenen Quellen und Hilfsmittel benutzt und mich keiner unzulässigen Hilfe Dritter bedient. Insbesondere habe ich wörtlich oder sinngemäß aus anderen Werken übernommene Inhalte als solche kenntlich gemacht.

3. Die Arbeit oder Teile davon habe ich wie bislang nicht an einer Hochschule des In- oder Auslands als Bestandteil einer Prüfungs- oder Qualifikationsleistung vorgelegt.

4. Die Richtigkeit der vorstehenden Erklärungen bestätige ich.

5. Die Bedeutung der eidesstattlichen Versicherung und die strafrechtlichen Folgen einer unrichtigen oder unvollständigen eidesstattlichen Versicherung sind mir bekannt.

Ich versichere an Eides statt, dass ich nach bestem Wissen die reine Wahrheit erklärt und nichts verschwiegen habe.

Ort und Datum Unterschrift